University of Memphis
University of Memphis Digital Commons

Electronic Theses and Dissertations

1-1-2020

SYNTHESIS, CHARACTERIZATION, AND REACTIVITY OF LATE TRANSITION METALALUMINUM HETEROBIMETALLICS

Timothy Yokley

Follow this and additional works at: https://digitalcommons.memphis.edu/etd

Recommended Citation
Yokley, Timothy, "SYNTHESIS, CHARACTERIZATION, AND REACTIVITY OF LATE TRANSITION METALALUMINUM HETEROBIMETALLICS" (2020). *Electronic Theses and Dissertations*. 2981.
https://digitalcommons.memphis.edu/etd/2981

This Dissertation is brought to you for free and open access by University of Memphis Digital Commons. It has been accepted for inclusion in Electronic Theses and Dissertations by an authorized administrator of University of Memphis Digital Commons. For more information, please contact khggerty@memphis.edu.

SYNTHESIS, CHARACTERIZATION, AND REACTIVITY OF LATE TRANSITION METAL—ALUMINUM HETEROBIMETALLICS

By

Timothy Wayne Yokley Jr.

A Dissertation

Submitted in Partial Fulfillment of the

Requirements for the Degree of

Doctor of Philosophy

Major: Chemistry

The University of Memphis

May 2020

DEDICATION

This doctoral thesis is dedicated to the people who believed in me when no one else did. First and foremost, my mother, Karen A. Weedo, who with unconditional love supported me as a single parent. This is for the better life we always dreamed of. I also dedicate this dissertation to my friend and mentor, Tanei J. Ricks, without whom I would have never had the direction or support to pursue a doctoral degree.

AKNOWLEDGMENT

This material is based upon work supported by the National Science Foundation under Grant No. CHE-1531466 and a grant from The University of Memphis College of Arts and Sciences Research Grant Fund. This support does not necessarily imply endorsement by the University of Memphis of research conclusions. I thank Dr. Timothy Brewster for being a patient mentor. I also thank Prof. Nathan J. DeYonker (University of Memphis) and Prof. D. Michael Heinekey (University of Washington) for helpful discussions. Prof. Paul S. Simone Jr. and Mr. Drake Williams (University of Memphis) are thanked for assistance with obtaining HRMS data. Prof. Nathan D. Schley (Vanderbilt University) is thanked for assistance with X-ray crystallography.

ABSTRACT

Yokley, Timothy Wayne. Ph.D. The University of Memphis. December 2019. Synthesis, Structure, and Reactivity of Late Transition Metal—Aluminum Heterobimetallics. Major Professor: Timothy P. Brewster, Ph.D.

Heterobimetallic systems have seen an increase in development over the last several years. These bimetallic systems typically involve two transition metals with unique properties used in tandem to activate chemical bonds. Many of these systems use transition metals, consisting of a soft, electron rich (low valent) metal and a harder, electron deficient (high valent) metal. These types of heterobimetallics can be exploited as an intramolecular Lewis acid—Lewis Base pair, which allows access to reactivity that may not be accessible to one transition metal alone.

Relatively unexplored is the use of a late transition metal (LTM) in tandem with a Lewis-acidic *p*-block (Group 13) metal. LTM-Lewis acid bimetallic complexes can be broadly categorized into two separate families, both capable of cooperative activation of a chemical bond. Among Group 13 Lewis acids specifically, aluminum is of particular interest to the Brewster laboratory due to it being earth-abundant and the most electropositive Group 13 element. Bimetallic complexes that contain an aluminum moiety are relatively unexplored compared to their boron analogs due to being highly reactive species and their synthetic difficulty. This has made their isolation and characterization quite challenging.

The goal of the Brewster lab is to develop bimetallic systems that contain aluminum and an electron-rich transition metal and to exploit cooperative reactivity between both metal centers. In this dissertation, we describe the successfully completed syntheses of bi- or tridentate ligands for our bimetallic aluminum complexes and their respective transition metal complexes. We report the experimental reactivity of the LTM complexes that contain a docking group for alkylaluminum or haloaluminum. Syntheses of these complexes follow a “ligand first” approach,

where the LTM complex is first synthesized and isolated, followed by the addition of the aluminum moiety. This synthetic route has been successful in the development of several bimetallic—aluminum complexes synthesized by the Brewster lab. We report the reactivity of the aluminum complexes with small molecules (i.e. H_2, CO_2, etc.). Varying the docking substituent attached to the aluminum moiety provides different reactivity. Experimental and computational investigation of the activation of CO_2 are reported.

TABLE OF CONTENTS

Chapter	Page
List of Figures	x
List of Abbreviations	xiii
List of Compounds	xvi
1. Introduction	1
1.1. Introduction to Heterobimetallics	1
1.2. Early/Late Bimetallic Complexes: Reactivity with Small Molecules	2
1.2.1. Alkene Hydrogenation Demonstrated by a Ta/Ir Heterobimetallic Complex	3
1.2.2. C-C Bond Formation Demonstrated by a Ru/Mn Heterobimetallic Complex	4
1.2.3. C-H Activation Demonstrated by a Zr/Rh Heterobimetallic Complex	5
1.2.4. H_2 Activation Demonstrated by a Zr/Ir Heterobimetallic Complex	6
1.2.5. CO_2 Oxidation Demonstrated by a Zr/Co Heterobimetallic Complex	7
1.2.6. O_2 Reduction Demonstrated by a M/Ru Heterobimetallic Complex	8
1.2.7. O_2 Activation Demonstrated by a Zr/Co Heterobimetallic Complex	9
1.3. Aluminum	9
1.4. Aluminum (III) Salt Redox Reactions	10
1.5. Bi- or Multidentate Redox Active Aluminum Complexes	11
1.5.1. Activation of CO_2 to formate using a redox-active aluminum catalyst	11
1.5.2. Activation of formic acid to CO_2 and H_2 using a redox-active aluminum catalyst	12
1.6. Early Transition Metal—Aluminum Bimetallics	13
1.6.1. Metallocene (M = Ti, Zr, Hf) – Aluminum Bimetallic Complexes	14

1.6.2. Bridged M-O-Al Bimetallic complexes (M = Ti, Zr) 16

1.6.3. Group 4 – Aluminum Heterobimetallic Complexes Featuring a Tetradentate Ligand 18

1.7 "Late Transition Metal—Aluminum Bimetallics" 19

1.7.1. Unsupported Bimetallic Aluminum Complexes 20

1.7.2. Unsupported "Z"-type Complexes 20

1.7.3. "Z-type" Ligand Supported Late Transition Metal-Aluminum Bimetallic Complexes 22

1.8. Overview of Chapter Contents 23

2. Synthesis and Characterization of Rhodium-Aluminum Heterobimetallic Complexes Tethered by a 1,3-Bis(diphenylphosphino)-2-propanoxy Group 25

2.1. Introduction 25

2.2. Synthesis and Characterization 26

2.3. Results and Discussion 27

2.4 Conclusions 38

2.5 Experimental Details 39

2.5.1. General Considerations 39

2.5.2. Synthesis 40

2.5.3. X-Ray Crystallography Data 42

3. Rhodium and Iridium NNO-Scorpionate Complexes: Synthesis, Structure, and Reactivity with Aluminum Alkyls 43

3.1 Introduction 43

3.2 Results and Discussion 44

3.2.1. Synthesis and Characterization of [Rh(cod)NNO]$_2$ and [Ir(cod)NNO]$_2$ 44

3.2.2. Synthesis and Characterization of [Ir(cod)NNO-H]BArF$_{24}$ 47

3.2.3. Reactivity of NNO Complexes with Aluminum Alkyls 48

3.3. Conclusion 50

3.4 Experimental Section 50

3.4.1. General Considerations 50

3.4.2. Synthesis 51

3.4.3. Procedures for Reactions with Aluminum Alkyl Reagents 52

3.4.4. X-Ray Crystallography Data 54

4. Activation of CO_2 Demonstrated by Aluminum Complexes Ligated by 2-Substituted Pyridines 55

4.1 Introduction 55

4.2. Results and Discussion 58

4.2.1. Reactivity of Heterobimetallic LTM-Aluminum Complexes with CO_2 58

4.2.2. Synthesis of Monometallic Aluminum Complexes 60

4.2.3 Reactivity of Monometallic Aluminum Complexes with CO_2 62

4.2.4 Computational Investigation 67

4.3 Conclusion 72

4.4 Experimental Details 73

4.4.1 General Considerations 73

4.4.2. Synthesis 73

4.4.3. Procedure for CO_2 Addition to Pyridonate Complex 77

4.4.4. X-ray Crystallography 77

4.4.5. Computational Details 78

5. Conclusions and Future Work 79

5.1 Summary of Work 79

5.2 Future Directions 80

References 83

Appendix A: Spectral Data for Chapter 2 98

Appendix B: Spectral Data for Chapter 3 118

Appendix C: Spectral Data for Chapter 4 130

LIST OF FIGURES

Figure Page

1.1. Proposed mechanism for ethylene hydrogenation by a Ta/Ir Heterobimetallic…… 3

1.2. Proposed mechanism for epoxide/CO_2 coupling by a Ru/Mn Heterobimetallic Complex. 4

1.3. Reactivity of a Zr/Rh Heterobimetallic Complex…… 5

1.4. H_2 activation across a Zr/Ir metal-metal bond…….... 6

1.5. CO_2 activation across a Zr/Co metal bond……... 7

1.6. Proposed mechanism of CO_2 reduction across a M-Ru bond…….. 8

1.7. O_2 activation demonstrated by a Zr/Co Complex…… 9

1.8. Mechanism of the Meerwein-Ponndorf-Verley Reduction……..10

1.9. CO_2 activation demonstrated by a redox-active aluminum complex……...11

1.10. Formic acid activation demonstrated by a redox-active catalyst……. 12

1.11. Generation of an active Zr catalysts using an aluminum activator……. 15

1.12. First structurally characterized Al-O-Zr complex by Roesky.[68,69]Representative Al-O-Zr aluminum heterobimetallic by Harder……. 17

1.13. Group 4-aluminum heterobimetallic reported by Nomura……. 18

1.14. Structurally Characterized Unsupported "Z"-type Complexes…… 20

1.15. Ligand Supported Late Transition Metal-Aluminum Heterobimetallics……. 22

2.1. Synthetic procedure for Rh(DPPE)(DPPP-O-Al^{i}Bu$_2$Cl) and Rh(DPPP-O-Al^{i}Bu$_2$)(DPPP-O-Al^{i}Bu$_2$Cl) ……...……... 26

2.2. Modeled (blue, above) and experimental (red, below) fine pattern of the $^{31}P\{^1H\}$ NMR spectrum for the two phosphorus atoms in the DPPE ligand (P_B, P_B' in table) in complex **1**… 29

2.3. Truncated $^{31}P\{^{1}H\}$ NMR spectrum of **2** showing the shift in the DP*P*P-O-R resonance on moving from R = H (bottom) to R = Al($^{i}Bu_2$)Cl (top)…… 30

2.4. Modeled and measured ^{1}H NMR spectrum of aluminum alkyl resonances in **2**…… 31

2.5. Top: ORTEP representations of **3-BArF**. Left: Carbons 2-6 of each phenyl ring omitted for clarity. Right: Full structure. Bottom: ORTEP representation of $[Rh(DPPP)_2][Cl]$……. 33

2.6. ORTEP representations of **5**. Ellipsoids shown at 50% probability. Hydrogen atoms and chloride counterion omitted for clarity. Left: Carbons 2-6 of each phenyl ring omitted for clarity. Right: Full structure…….. 33

2.7. Variable temperature $^{31}P\{^{1}H\}$ NMR of **4**. Temperature recorded across a range from -85°C to 65°C…….. 34

2.8. Possible diastereomers of **4**……..…….. 37

3.1 Previously reported Rh/Al and Ir/Al heterobimetallics from Brewster et al.[107]……...43

3.2. ORTEP representation of $[Rh(cod)NNO]_2$ **2**. Ellipsoids shown at 50% probability. Hydrogen atoms omitted for clarity……. 45

3.3. ORTEP representation of [Ir(cod)NNO-H]$BArF_{24}$ **4**. Ellipsoids shown at 50% probability. Hydrogen atoms and $BArF_{24}$ counterion omitted for clarity…….47

3.4. Representation of NNO binding to aluminum alkyls by Castro-Osma, Otero, and Lara-Sánchez et al.[131] (left) and proposed aluminum complex (right)…….. 48

4.1. Aluminum porphyrins reported by Inoue and coworkers (left) and Kusaga and coworkers (right)…… 56

4.2. Ligated aluminum complexes (1a-3b)…… 58

4.3. Formation of Al-pyridone-aluminum—alkoxide complex…… 59

4.4. ORTEP representation of **1b** (top), **2a** (left), and **2b** (right). Ellipsoids shown at 50% probability. Hydrogen atoms omitted for clarity……. 61

4.5. Stacked ^{1}H-NMR spectrum representative of 2a (bottom) and 2a after addition of 1 atm CO_2 (top) in benzene-d_6. Spectra referenced to residual solvent peak…….. 64

4.6. Computed reaction pathways for sequential CO_2 insertion into complex **10a**…….. 68

4.7. Computational structures of **10a** (left) and its counterpart **10a-cis** (right)…….. 69

4.8. Free energy diagram of proposed isomerization of reactant **10a** from trans to cis form…..70

4.9. Free energy diagram of proposed activation of CO_2 to the aluminum bound carboxylate where CO_2 insertion into alkyl group occurs first…….. 71

4.10. Free energy diagram of proposed activation of CO_2 to the aluminum bound carboxylate 72

5.1. Proposed ligand synthesis……. 80

5.2. Potential Z-type structures for proposed ligands……. 81

LIST OF ABBREVIATIONS

Å	Angstrom
Al	Aluminum
$AlCl_3$	Aluminum trichloride
$AlCl_4^-$	Aluminum tetrachloride ion
$AlEt_3$	triethylaluminum
$AlEt_2Cl$	diethylaluminum chloride
Al^iBu_3	triisobutylaluminum
Al^iPr_2Cl	diisopropylaluminum chloride
$BaRF_{24}$	Tetrakis[3,5-bis(trifluoromethyl)phenyl]borate
CH_2	methylene
CH_3	methyl
CO	Carbon Monoxide
CO_2	Carbon Dioxide
CO_3^{2-}	Carbonate ion
cod	1, 4–cyclooctadiene
Cp	cyclopentadienide
Cp^*	pentamethylcyclopentadienide
CS_2	Carbon Disulfide
Cl	Chloride ion
DCM	Dichloromethane
DFT	Density Functional Theory
DIPH	3,3'-bis(2-methylallyl)-[1,1'-biphenyl]-2,2'-bis(olate)

DIPH-H_2	3,3'-bis(2-methylallyl)-(1,1'-biphenyl)-2,2'-diol
DIPP	2,6-diisopropylphenyl
DOSY	Diffusion Ordered Spectroscopy
DPPE	ethylenebis(diphenylphosphine)
dppm	bis(dipheylphosphino)methane
DPPP	1,3-bis(diphenylphosphino)-2-propanoxy
DPPP-OH	bis(diphenylphosphino)-2-propanol
ESI-MS	Electrospray Ionization Mass Spectrometry
Et	Ethyl
FLP	Frustrated Lewis Pair
H	Hydride
H_2	Dihydrogen
HCOOH	Formic Acid
HCO_2^-	formate anion
HMBC	Heteronuclear Multiple Bond Correlation
HMQC	Heteronuclear Single Quantum Coherence Spectroscopy
HRMS	High Resolution Mass Spectrometry
^{i}Bu	isobutyl
Ir	Iridium
LTM	Late-Transition Metal
MAO	methyl aluminoxane
Mes	2,4,6-trimethylbenzyl
mg	milligrams

MHz	megahertz
μL	microliter
mL	milliliter
mmol	millimole
mPa	Megapascals
m/z	mass to charge ratio
Nacnac	β-diketiminato
nb	norbornene
nBuLi	n-butyl lithium
NEt_4^+	tetraethylammonium ion
NHC	N-heterocyclic carbene
NMR	Nuclear Magnetic resonance
NNO	bis(3,5-dimethyl-pyrazol-1-yl)acetate
OTf	Triflate ion
PCy_3	tricyclohexylphosphine
Ph	phenyl
$^{Ph}I_2P^{2-}$	(1E,1'E)-1,1'-(pyridine-2,6-diyl)bis(N-mesityl-1-phenylmethanimine)
PPh_3	Triphenylphosphine
Rh	rhodium
^{t}Bu	tert-butyl
THF	Tetrahydrofuran
v/v	volume to volume

LIST OF COMPOUNDS

Abbreviation	Compound Formula	Structure
1	Rh(DPPE)(DPPP-OH)Cl	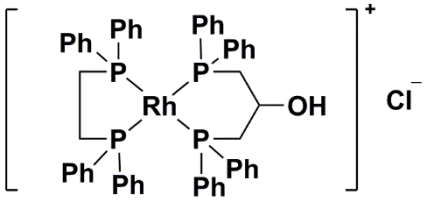
2	Rh(DPPE)(DPPP-OAl^{i}Bu$_2$Cl)	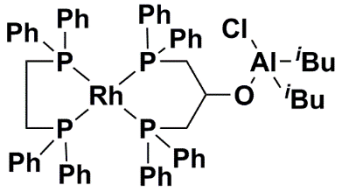
3	[Rh(DPPP-OH)$_2$][Cl]	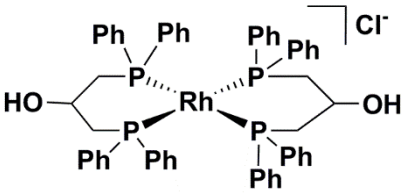
3-BArF	[Rh(DPPP-OH)$_2$][BArF$_{24}$]	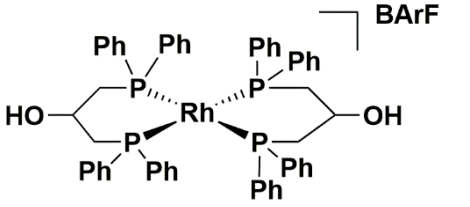
4	Rh(DPPP-OAl^{i}Bu$_2$)(DPPP-OAl^{i}Bu$_2$Cl)	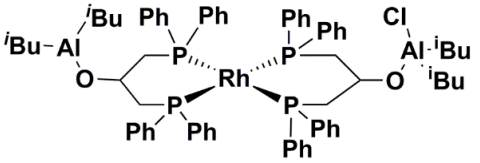

5	[Rh(DPPP-OH)$_2$(CO)][Cl]	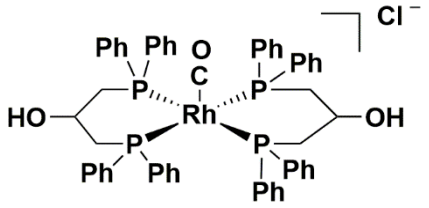
6	[Rh(cod)NNO]$_2$	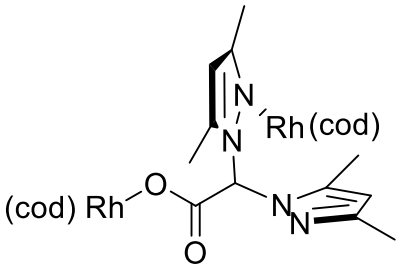

* Second bridging NNO ligand omitted for clarity

7	[Ir(cod)NNO]$_2$	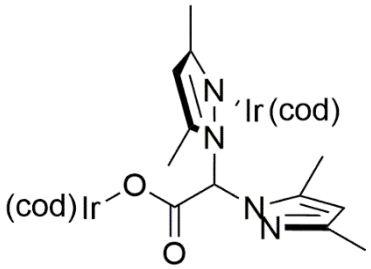

* Second bridging NNO ligand omitted for clarity

8	[Ir(cod)NNO-H] [BArF$_{24}$]	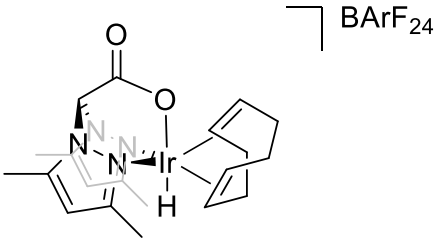
9a	2-pyridone[AlEt$_2$]	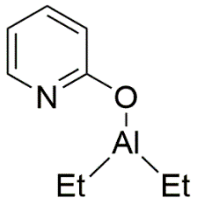

9b	2-pyridone[Al^{i}Bu$_2$]	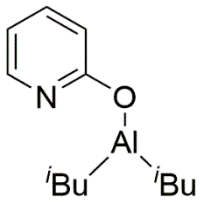
9c	2-pyridone[Al(OEt)Et]	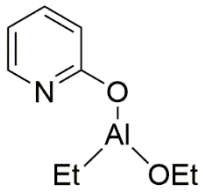
9d	2-pyridone[Al(O^{i}Bu)^{i}Bu]	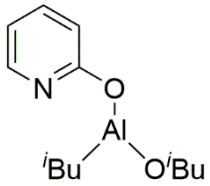
10a	Al(Et)(2-methylamino pyridine)$_2$	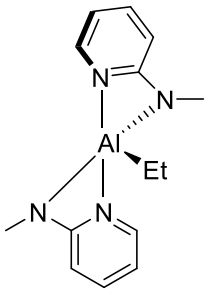
10b	Al(^{i}Bu)(2-methylamino pyridine)$_2$	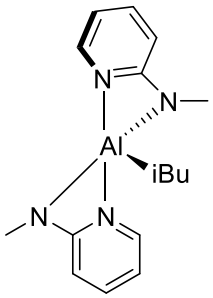

10c	(2-methylamino pyridine)$_2$Al(Et)(CO$_2$)$_2$	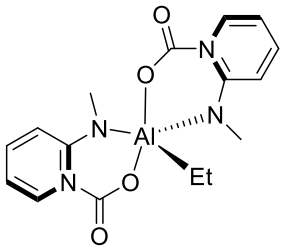
10d	(2-methylamino pyridine)$_2$Al(^{i}Bu)(CO$_2$)$_2$	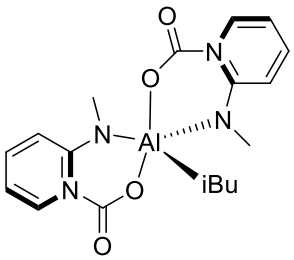
11a	Al(Et)$_2$(2-pyridinemethanol)	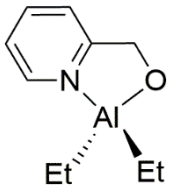
11b	Al(^{i}Bu)$_2$(2-pyridinemethanol)	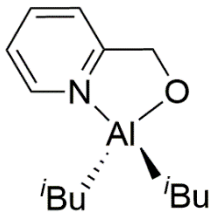

Chapter 1. INTRODUCTION

1.1 Introduction to Heterobimetallics

The development of heterodinuclear or heterobimetallic systems has shown a boom in interest over the past few decades. These bimetallic systems typically involve two transition metals with unique chemical properties.[1-4] A common construct consists of a soft, electron rich (low valent) metal and a harder, electron deficient (high valent) metal. In other words, these systems contain a comparatively Lewis basic metal with a formally low oxidation state in conjunction with a strongly Lewis acidic metal in a formally high oxidation state. The formation of a dative bond between two transition metal centers may occur by enforcing proximity between the nucleophilic metal center and the electrophilic metal. Traditionally, this type of interaction involves the donation from a filled *d*-orbital of the Lewis basic metal to an empty *d*-orbital of the Lewis acidic metal to form a net bonding interaction. This class of heterobimetallic can be exploited as an intramolecular Lewis acid—Lewis base pair, where reactivity of the complex is comparable to that of a Frustrated Lewis Pair (FLP).[5,6] In general, in the creation of a bimetallic complex one hopes to exploit synergistic or "cooperative" reactivity that may not be accessible to their mono- or homodinuclear counterparts.

The ability of the two metal centers to adopt different roles during "cooperative" reactivity has been the target of extensive study.[7-13] The Lewis acidic transition metal can often impart oxidative effects, while the Lewis basic transition metal can serve as a formal reductant. In other cases, the Lewis acidic (or basic) metal simply serves to electronically tune its counterpart which undergoes classical one-metal reactivity.[14] As mentioned above, in yet other instances the metals can work together to concertedly, heterolytically activate chemical bonds.

Finally, electrons may be stored in a heterobimetallic metal-metal multiple bond, suggesting the complexes may demonstrate unique redox behavior.[15] Because of the diversity in metal-metal interactions in heterobimetallic complexes, designing catalysts using this type of architecture will create a wave of discovery towards future exploration in catalysis research, allowing chemists to use various transition metal—transition metal or, in more recent years, transition metal—main group metal combinations to design more efficient catalysts to tackle some of the world's toughest problems.

The following sections review heterobimetallic complexes where both metals are needed to cooperatively activate small molecules. I will first review select early transition metal/late transition metal heterobimetallic complexes. Next, as an introduction to transition metal-main group metal bimetallics, I will briefly discuss aluminum, aluminum (III) salt reactions, and reactivity of aluminum supported by redox-active ligands. Specifically, I will be looking at the reactivity of CO_2 and formic acid with select complexes as this is directly relevant to the work described in ensuing chapters. The next section will discuss early transition metal/aluminum heterobimetallic complexes that demonstrate catalytic activity. This section will mainly discuss Group 4-aluminum bimetallic complexes that are used in olefin polymerization. Lastly, we will discuss late transition metal/aluminum heterobimetallics, giving a brief discussion of the reactivity towards small molecules.

1.2 Early/Late Bimetallic Complexes: Reactivity with Small Molecules

One of the more well-defined areas of catalysis using this type of metal-metal framework are early transition metal—late transition metal, or "early/late" heterobimetallic complexes. While the terms "early" and "late" are rather ambiguous, these terms typically reference either the left or right side of the *d*-block of the periodic table. In this discussion, "early" will refer to

the transition metals found in Groups 4-7 while "late" will refer to the transition metals found in Groups 8-12.

Small polar or polarizable substrates are particularly amendable to reaction with these types of Lewis acid/Lewis base bimetallic complexes. Hydrogenation of alkenes[16-18], C-C bond formation [19-22], C-H activation [23-27], H_2 activation [27-30], reduction or oxidation of CO_2 [31-33], and O_2 activation[34] are just a few of the diverse reaction types for which these systems have shown to be catalytically useful. However, there are many additional examples wherein the original complex cannot be regenerated after stoichiometric functionalization of the substrate at hand. Select examples of early/late heterobimetallic reactivity towards small molecules using will be given.

1.2.1. Alkene Hydrogenation Demonstrated by a Ta/Ir Heterobimetallic Complex

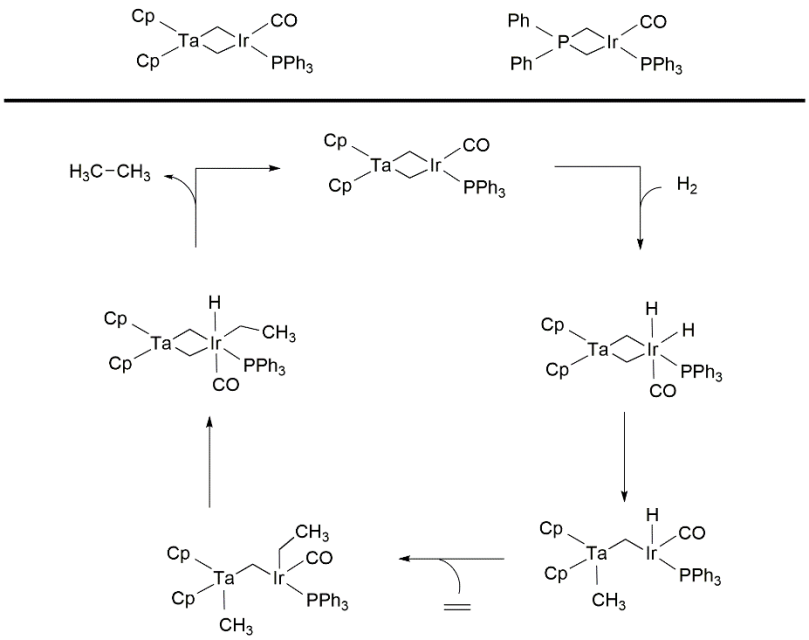

Figure 1.1. Proposed mechanism for ethylene hydrogenation by a Ta/Ir Heterobimetallic.[16]

A Ta/Ir heterobimetallic complex reported by Bergman et al.[16] $[Cp_2Ta(CH_2)_2Ir(CO)(PPh_3)]$ was able to demonstrate efficient activity in hydrogenation of ethylene. When the monometallic complex $Ph_2P(CH_2)_2Ir(CO)(PPh_3)$ was used under similar

reaction conditions, the reaction proceeded 150 times slower than the bimetallic analog. Extensive deuterium studies were performed to understand the catalytic mechanism between the two complexes. These studies revealed that the bimetallic complex underwent C-H reversible reductive elimination at the bridging CH_2 while incorporation of the deuterium into the monometallic complex was not observed, indicating this catalytic process occurs via different mechanisms. Computational studies supported these claims due to the higher calculated activation barrier for the monometallic complex compared to the bimetallic.

1.2.2. C-C Bond Formation Demonstrated by a Ru/Mn Heterobimetallic Complexes

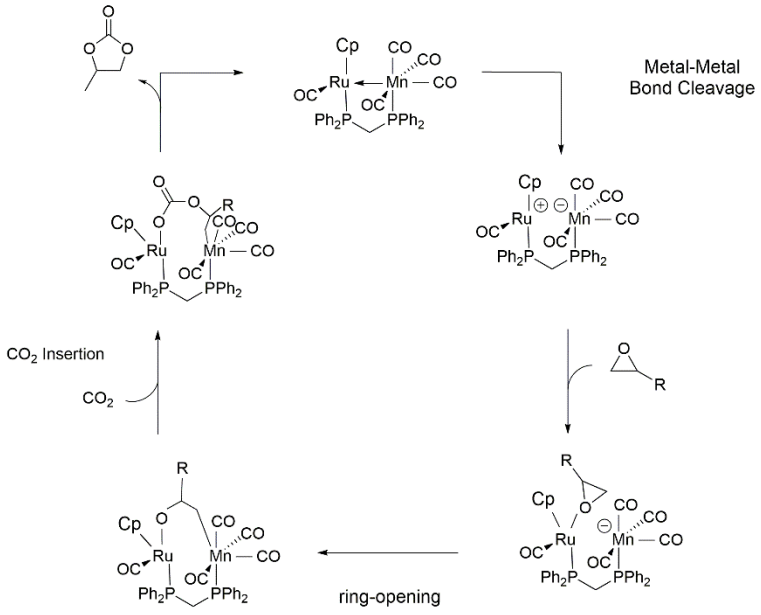

Figure 1.2. Proposed mechanism for epoxide/CO_2 coupling by a Ru/Mn Heterobimetallic Complex.[21]

Lau et al.[21] reports a pair of Ru/Mn heterobimetallic complexes [Cp(CO)Ru(μ-dppm)$Mn(CO)_4$] and [Cp*(CO)Ru(μ-dppm)(μ-$CO)_2Mn(CO)_3$] in the catalytic coupling of CO_2 and epoxides to yield cyclic carbonate products. In order for the bimetallic complex to demonstrate catalytic activity, the Ru—Mn metal-metal bond must break to generate the active Ru^{II} and Mn^- fragments. The electrophilic Ru binds to the epoxide, followed by a ring opening

attack by the nucleophilic Mn center, yielding a C-Mn bond. CO_2 insertion into the Ru-O bond, followed by a ring closure and reductive elimination of the cyclic carbonate product regenerates the Ru-Mn bond. Each metal center is necessary to yield the cyclic carbonate product and drive the reaction forward. The authors also report that the monometallic Mn complex was less active as compared to the bimetallic complexes. When the monometallic Ru complex was used, no reaction occurred.

1.2.3. C-H Activation Demonstrated by a Zr/Rh Heterobimetallic Complex

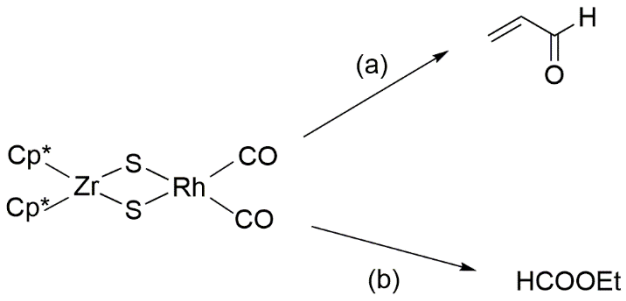

Figure 1.3. Reactivity of a Zr/Rh Heterobimetallic Complex.[33] (a) 5 eq PPh_3, 1 MPa Ethene 1MPa CO. (b) 5 eq PPh_3, 1 MPa Ethene, 1MPa CO, triethylorthoformate.

The direct carbonylation of ethylene to form the corresponding acrolein product using an early/late heterobimetallic complex $[AsPh_4][\ \eta\text{-}C_5Me_5)_2Zr(\mu\text{-}S)_2Rh(CO)_2]\bullet THF$ was demonstrated by Kalck and Gautheron et al.[33] The authors propose the formation of the acrolein product involves several multistep mechanisms and occur via a homogeneous process. These sequences involve the activation of ethene on the zirconium center to yield the vinyl species, the insertion of CO into the zirconium-carbon bond, reductive elimination of the acrolein product, and C-H activation of a CH_3 group from Cp* leading to the decomposition of the heterobimetallic complex (Figure 1.3. a). Catalytic carbonylation of ethene was achieved by addition of triethyl orthoformate with respect to the bimetallic complex (Figure 1.3b) but detection of the acrolein product was determined only in the gas phase.

1.2.4. H_2 Activation Demonstrated by a Zr/Ir Heterobimetallic Complex

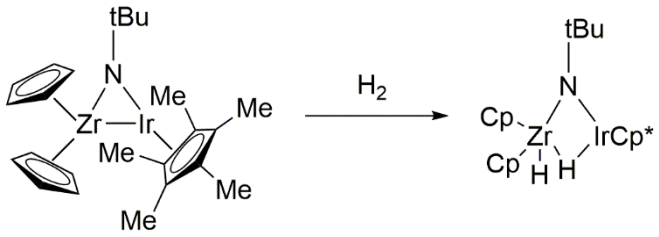

Figure 1.4. H_2 activation across a Zr/Ir metal-metal bond.[34]

Dihydrogen activation has been demonstrated with several early/late heterobimetallic complexes. For example, Bergman et al.[34] developed a heterobimetallic imido complex [$Cp_2Zr(\mu\text{-N-}t\text{-Bu})IrCp^*$] that led to the oxidative addition of H_2 at 25°C leading to the clean formation of the dihydride complex [$Cp_2Zr(H)(\mu\text{-N-}t\text{-Bu})(\mu\text{-H})\ IrCp^*$]. The dihydride complex demonstrates reversible oxidative addition of H_2 under vacuum and was found to be thermally unstable at 25°C over 24 hours. An analogous deuteride complex [$Cp_2Zr(D)(\mu\text{-N-}t\text{-Bu})(\mu\text{-D})IrCp^*$] was formed after reacting the complex with D_2 to determine hydride resonances. Deuterium incorporation into the Cp rings was observed by ^{2}H-NMR and small hydride peaks were observed by ^{1}H-NMR from the incorporation of hydrogen in the hydride position from the Cp rings. Addition of a 50/50 mixture of H_2 and D_2 to the imido complex resulted in the formation of H-D identifiable by ^{1}H-NMR. H-D exchange experiments were performed by addition of the dideuteride complex to the dihydride complex yielding two hydridodeuteride complexes. Attempts at catalytic hydrogenation of ethylene were performed, though thermal decomposition of the imido catalyst was reported.

1.2.5. CO_2 Oxidation Demonstrated by a Zr/Co Heterobimetallic Complex

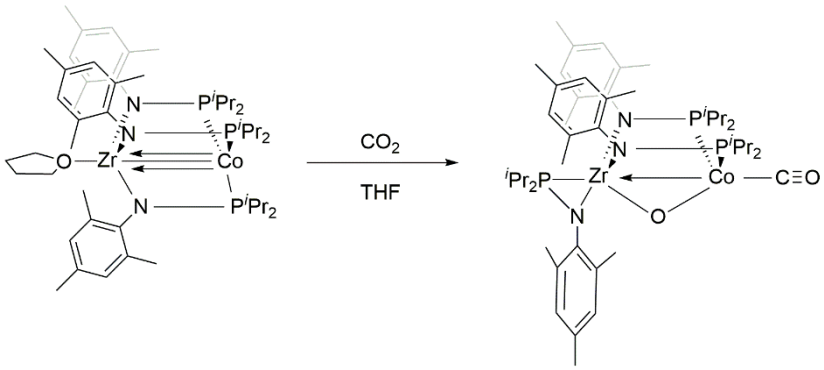

Figure 1.5. CO_2 activation across a Zr/Co metal bond.[35]

A zirconium/cobalt complex [Co(^{i}Pr$_2$PNMes)$_3$Zr(THF)] reported by Thomas et al.[35] demonstrates the stochiometric oxidative addition of CO_2 across the Zr—Co metal—metal multiple bond at room temperature to yield the complex [(OC)Co(^{i}Pr$_2$PNMes)$_2$-(μ-O)-Zr(^{i}Pr$_2$PNMes)] cleanly. The solid-state structure of the product reveals a bridged Zr—O—Co complex with a terminal CO group located on the Co metal center. The use of excess of CO_2 led to a mixture of intractable products attributed to the formation of CO_3^{2-} from a nucleophilic attack of the oxo bridge to a CO_2 molecule. The authors propose the reactivity of the Zr/Co bimetallic complex towards the stoichiometric activation of CO_2 can be explained by the hemilability of the phosphinoamide ligand, allowing the substrate to access the bimetallic multiple bond.

1.2.6. CO_2 Reduction Demonstrated by a M/Ru Heterobimetallic Complex

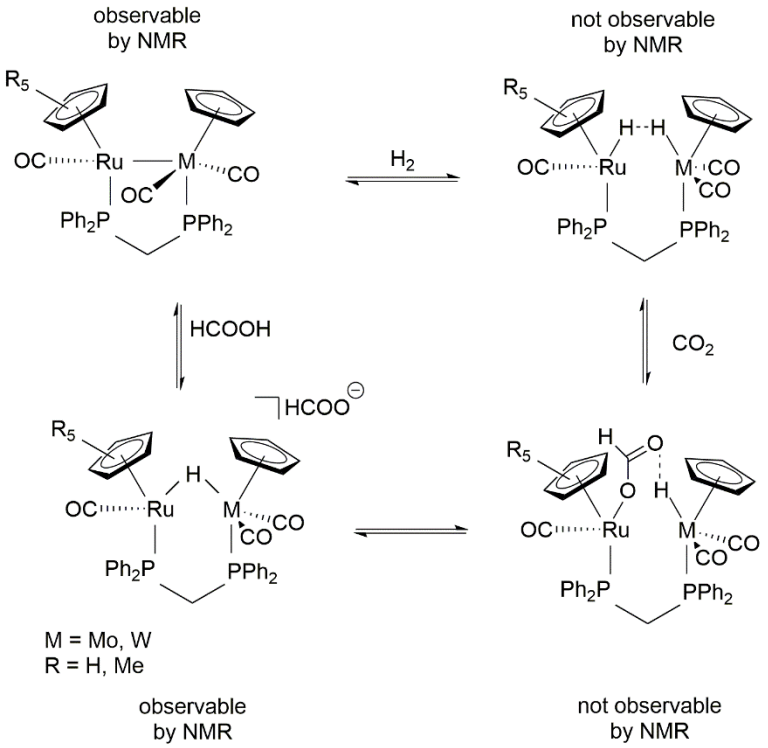

Figure 1.6. Proposed mechanism of CO_2 reduction across a M-Ru bond.[21]

Hydrogenation of CO_2 to formic acid using Group 6/Ru heterobimetallic species [(Cp)(CO)Ru(μ-dppm)M(CO)$_2$(Cp)] or [(Cp*)(CO)Ru(μ-dppm)M(CO)$_2$(Cp)] was reported. [21] Similarly, these complexes demonstrate activity for the decomposition of formic acid to CO_2 and H_2. The authors report the low catalytic activity of the bimetallic species, however, no catalytic activity was observed with the monometallic species, indicating the need for both metal centers to play a role in the reaction. A mechanism for the reversible hydrogenation of CO_2 (**Figure 1.6**) by the bimetallic M-Ru species was proposed, though very little experimental evidence for the mechanism was reported.

1.2.7. O_2 Activation Demonstrated by a Zr/Co Heterobimetallic Complex

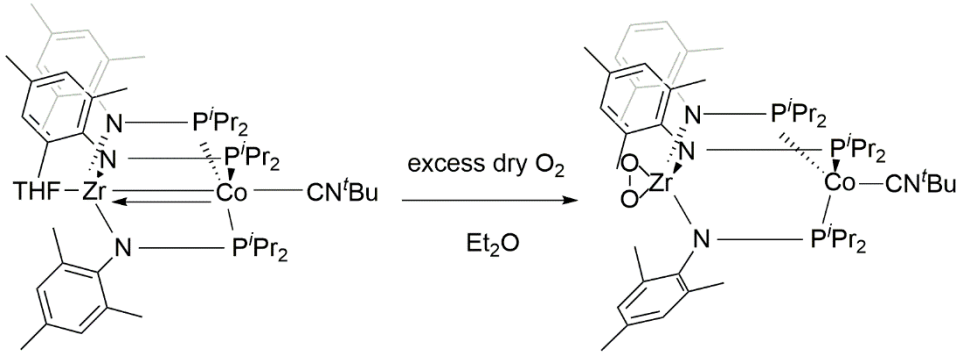

Figure 1.7. O_2 activation demonstrated by a Zr/Co Complex.[36]

A zirconium/cobalt complex [(THF)Zr(^{i}Pr$_2$PNMes)$_3$CoCN^{t}Bu] reported by Thomas et al.[36] was able to activate O_2 to yield the peroxo complex (O_2)Zr(^{i}Pr$_2$PNMes)$_3$CoCN^{t}Bu. The phosphinoamide ligand complex remains stable, where O_2 selectively binds to Zr to form the terminal peroxo complex. The authors propose a two electron oxidation of O_2 that occurs rapidly at the Zr^0 center while the pendant d^{10} Co center acts as a two-electron reductant; however, reactivity at the multiple metal bond was not reported.

1.3 Aluminum

A burgeoning area of research in the Brewster lab involves replacement of one of the transition metals in the early/late heterobimetallic construct with a Lewis acidic main group (Group 13) metal. Group 13 elements consist of boron, aluminum, gallium, indium, and thallium. These elements are considered *p*-block metals, where all s-orbitals are full and one electron is located in the p-orbital giving a ground state valence electron configuration ns^2np^1 (*n* = valence shell). Of the Group 13 metals, my work has focused primarily on the chemistry of aluminum. Aluminum is attractive because it is earth abundant, inexpensive, and relatively non-toxic. Aluminum is, in fact, the third most abundant element in the earth's crust (after oxygen and silicon), accounting for over 8% of its mass. Among Group 13 metals, aluminum is also the

most electropositive Group 13 element making it a particularly potent Lewis acid. The ensuing sections will first discuss some of the chemistry of aluminum itself and then transition into its limited application in heterobimetallic complexes.

1.4. Aluminum (III) Salt Redox Reactions

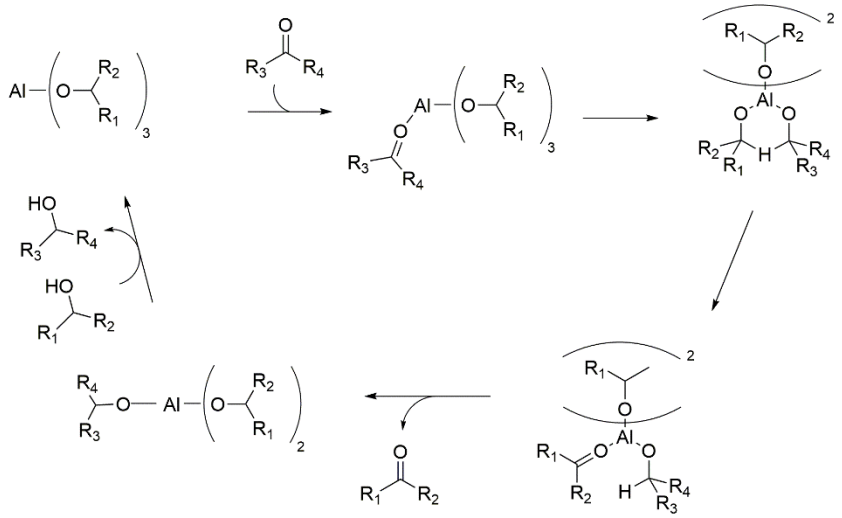

Figure 1.8. Mechanism of the Meerwein-Ponndorf-Verley Reduction

Aluminum has had a limited role in catalysis of oxidation/reduction, mainly due to the fact that aluminum exists almost exclusively in the +3 oxidation state outside of its elemental form.[37] Very few examples of a +1 oxidation state have been reported.[38-43] However, there are strategies to induce non-redox active metals to influence redox reactions. The first is direct addition of an aluminum (III) salt to enhance the activity of inorganic or organic oxidants and/or reductants. Coordination of aluminum (III) salts to an oxidant or reductant can directly impact the redox potential through electronic induction. One of the most recognized industrial processes that undergoes this direct addition are the classic electrophilic aromatic substitution reactions Friedel-Crafts alkylation and acylation, where the reaction is dependent on a strong Lewis acid such as aluminum trichloride. However, processes that are less likely to be familiar to the lay chemist are reactions that use aluminum to facilitate insertion and accelerate β-hydride transfer. For example, the Meerwein-Ponndorf-Verley reduction of ketones by secondary alcohols relies

on a beta-hydride transfer from the donating substrate via a six-membered aluminum metallocycle transition state. The coordination of aluminum increases the electrophilicity of the acceptor substrate allowing for the hydride transfer to form the secondary alcohol. Similarly, the Aufbau reaction is the aluminum catalyzed polymerization of ethylene by the repeated insertion of monomers into a growing polymer chain.

1.5. Bi- or Multidentate Redox Active Aluminum Complexes

While using a simple aluminum (III) salt may elicit a reaction of interest, substituting the salt with a bi- or multidentate ligand can often eliminate side reactions and increase selectivity in formation of target products.[37] Coordination of the aluminum center to a sterically bulky, redox-active ligands may additionally allow the redox-inert aluminum center to serve as a relevant redox partner in the reaction resulting in transition metal-like reactivity. This type of framework has led to the catalytic reduction of CO_2 and oxidation of formic acid mediated by an aluminum hydride. Select, representative, examples will be discussed in detail below as they demonstrate the concept and the current state of this subfield of aluminum chemistry.

1.5.1. Activation of CO_2 to Formate using a Redox-Active Aluminum Catalyst

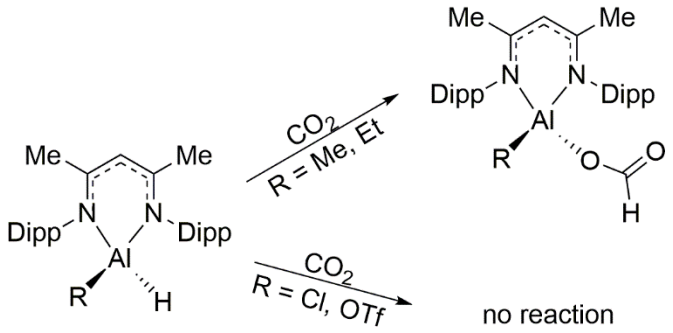

Figure 1.9. CO_2 activation demonstrated by a redox-active aluminum complex.[44]

In 2015, Aldridge et al. demonstrated the activation of CO_2 with a Nacnac supported gallium catalyst where CO_2 insertion into the metal hydride bond.[44] The authors were able to

release the derived formate product from the metal center and regenerate the metal hydride by using a sacrificial Lewis acid source. In 2018, Aldridge et. al.[45] reported several aluminum hydride analogs stabilized by a redox active Nacnac ligand framework capable of CO_2 insertion into the Al-H bond yielding the formate bound to the aluminum center. The authors report different reactivity depending on the R group adjacent to the hydride. Electron donating R groups (i.e. Me, Et) led to enhanced reactivity of CO_2 into the Al-H bond with 90% completion after 40 minutes for R = Me and 60 minutes for R= Et (rate constants = 7.16 x $10^{-4}s^{-1}$ and 6.16 x $10^{-4}s^{-1}$, respectively). Alternatively, when the R group is an electron withdrawing group (i.e. Cl, OTf) led to no observable reactivity. The authors propose the difference in reactivity is due to the weak Al—H bond (increase of hydricity caused by the electron donating group) leading to enhanced rates towards CO_2.

1.5.2. Activation of Formic Acid to CO_2 and H_2 using a Redox-Active Aluminum catalyst

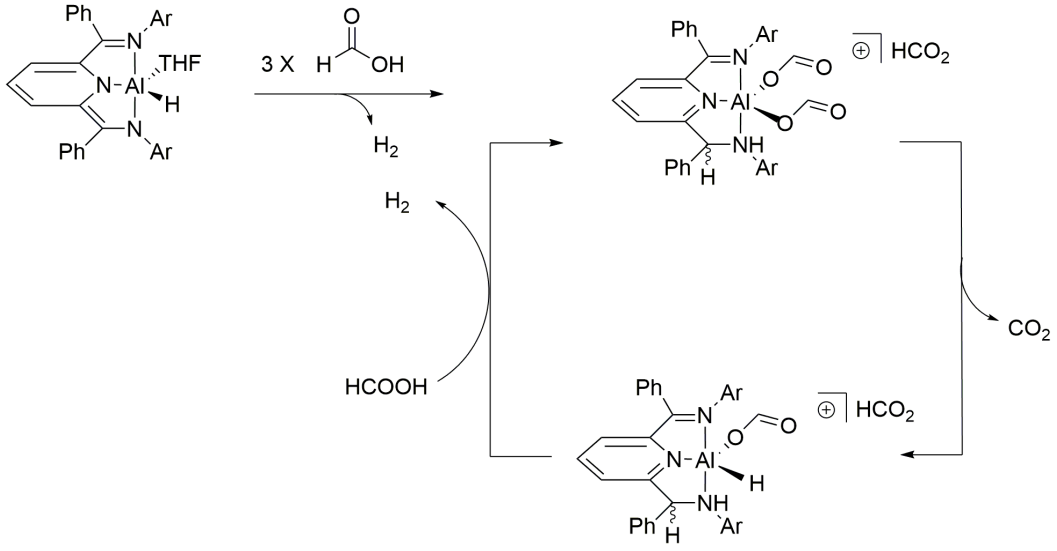

Figure 1.10. Formic acid activation demonstrated by a redox-active catalyst.[46]

Investigating the reverse reaction, Myers and Berben[46] reported the conversion of formic acid selectively into H_2 and CO_2 via a β-hydride elimination from the synthesized aluminum catalyst ($^{Ph}I_2P^{2-}$)Al(THF)H at an initial rate of 5200 turnovers per hour. It is proposed that the

steric bulk of the alkyl ligands promote the formation of aluminum-hydride product. The authors report a mechanism through which the catalytic dehydrogenation of formic acid occurs (**Figure 1.10**). Three equivalents of formic acid were introduced to, liberating one equivalent of H_2, protonation of the amine arm, and rearomatization of the pyridine ring, yielding two formate anions bound to the aluminum center to give a 4-coordinate intermediate. A β-hydride abstraction from one formate bound to the aluminum anion liberates CO_2 and regenerates the aluminum hydride. Introduction of one equivalent of formic acid to the catalytic cycle quickly liberates H_2 and regenerates the active catalyst.

Designing catalysts using less expensive and highly abundant metals is in high demand to lower the cost and increased sustainability of reactions. Although aluminum remains almost exclusively in the +3 oxidation state for most cases in coordination chemistry, there is still much that can be learned about using aluminum as a catalyst or redox partner to accelerate a variety of oxidation/reduction reactions. Coordination to a bi- or multidentate ligand with steric bulk and/or different electronic parameters (i.e. non-innocence) can affect the reactivity and selectivity of the reaction compared to using an aluminum (III) salt alone.

1.6. Early Transition Metal—Aluminum Bimetallics

Aluminum has found an emerging role as a component in bimetallic systems. Among the known metal—aluminum heterobimetallics, a small subset comprises early transition metal-aluminum systems.[47-60] Of the few known early transition metal-aluminum bimetallics, even fewer have been reported to catalyze reactions.[51, 57,59-61] Early transition metals and aluminum are both exceptional Lewis acids. As stated above, aluminum exists primarily in its most stable form of the +3 oxidation state. Early transition metals demonstrate similar properties where the thermodynamically stable form is generally the highest oxidation state (by noble gas

configuration). This similarity severely limits the types of reactivity for which these systems are employed.

Cooperative reactivity between both metal centers to function as a Lewis acid/Lewis base pair is unfavorable compared to the early/late systems, as both metals would prefer to serve as an electron pair acceptor, and in many cases have no valence electrons available to serve as a base. Polar substrates that demonstrate σ- and/or π-donation are subject to reaction with these Lewis acidic metals; however, catalytic turnover is often poor because the product, often a good Lewis base itself, has a strong affinity for one of the two metal sites. To prevent product inhibition, systems in which the product is an exceptionally poor ligand (relative to substrate) are under investigation. By far the most prevalent are systems for catalyzing olefin polymerization.[61] Early metal systems have long been used in this application with an aluminum source, methylalumoxane or MAO (MAO = $Al(CH_3)O)_n$) , often serving as a reaction initiator. Incorporation of aluminum into the framework is a potential route to having synthetic control over the activation step in this process. The remainder of this section will discuss early transition metal-aluminum bimetallic complexes that have been isolated and are used to catalyze olefin polymerization with or without an external aluminum activator.

1.6.1 Metallocene (M = Ti, Zr, Hf) – Aluminum Bimetallic Complexes

Group 4 early transition metal (M = Ti, Zr, Hf) - aluminum bimetallics have seen great success as catalysts for olefin polymerization.[61] These bimetallic catalysts generate an equilibrium mixture of coordinatively unsaturated species, usually cationic, that contain a reactive metal—alkyl bond capable of binding an olefin and transferring the alkyl to the monomer. The addition of an external cocatalyst (i.e. aluminum) serves as an activator to generate the active cationic catalyst.[62,63] These are typically bulky trialkyl aluminum (i.e. ^{i}Bu,

^{t}Bu) reagents and/or MAO due to the versatility of the reagent in the reaction. Typically, large quantities of these external cocatalysts are needed to function as an alkylating agent, an alkyl abstractor, a stabilizer for the generated transition metal cation, and a scavenger for impurities such as water that can inhibit the reactivity of the active catalyst.[61, 62] It is proposed that the aluminum cocatalyst may also act as a chain-transfer agent allowing for growth of the polymer chain.

Since the early 1950's, metallocene catalysts have been well established for olefin polymerization reactions. In particular, "metallocene catalysts" refer to zirconocene complexes that have been synthesized from either the metal-halide or metal-alkyl precursor. This is in part due to the instability of titanocene complexes at conventional polymerization temperatures and the cost to synthesize hafnium systems. These bis(cyclopentadienyl)group-IV metal complexes were introduced as a new generation of Ziegler-Natta catalysts for the polymerization of olefins. Specifically, these zirconocene catalysts can be modified to produce polyolefins with special stereoregularities and a high degree of tacticity.

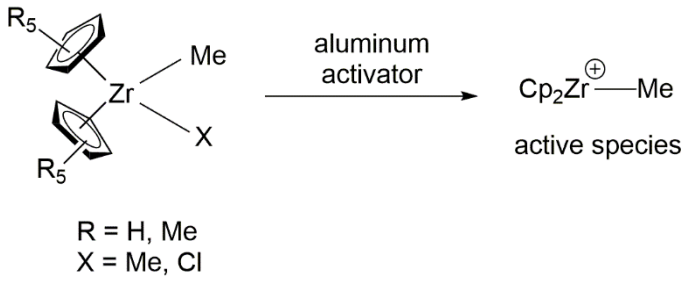

Figure 1.11. Generation of an active Zr catalysts using an aluminum activator.[61]

As stated above, an activation step using MAO is needed to generate the active catalyst. This occurs by transferring a methyl group to MAO to form a cationic aluminum species, generating an open site on the transition metal center $CpZrMe^+$.[61,62] There is no direct information on the structure of the metal-olefin preinsertion complexes, or about the monomer association equilibria. These sites are strongly Lewis acidic, allowing the association of olefins

and subsequent methyl transfer to occur. Metallocenes are typically homogeneous, allowing for the maximum number of open sites per molecule, making these catalysts more active than their heterogenous counterparts.

1.6.2. Bridged M-O-Al Bimetallic complexes (M = Ti, Zr)

Very few approaches to developing aluminum bimetallic complexes that demonstrate intramolecular activation of the early transition metal center have been reported. [51, 63-67] These bimetallic complexes would eliminate the need for an external aluminum activator and demonstrate high activity in catalysis. Unfortunately, activation of the transition metal complex is usually associated with a decrease in complex stability so having the activator in proximity can be challenging. Considerable attention has been given to the design and synthesis of ligands to prevent destabilization of the activated bimetallic complex. Ligands consisting of π-donor alkoxides and/or aryloxides have seen significant promise in these types of bimetallics due to both electronic and steric properties that the ligand has on the metal center (Figure 1.12). It is proposed that communication between metal centers through the oxygen bridge may be

beneficial by enhancing the Lewis acidity of the catalytic center or provide a vacant site for cocatalyst binding in these bimetallic systems.

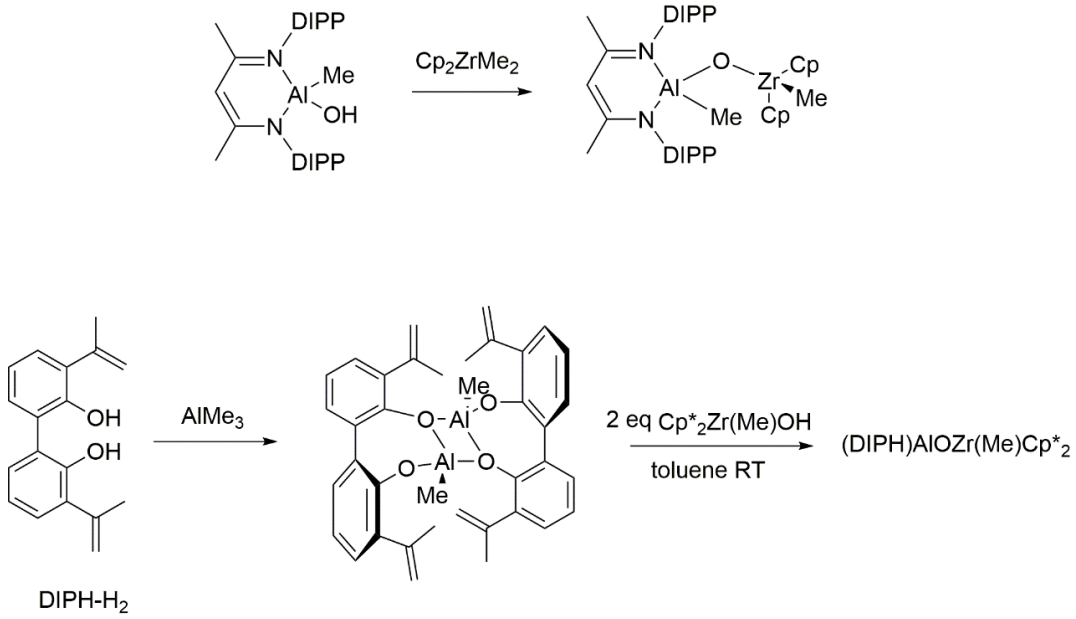

Figure 1.12. First structurally characterized Al-O-Zr complex (top).[68,69] Representative Al-O-Zr aluminum heterobimetallic containing a bidentate oxygen ligand (bottom).[70]

The first structurally characterized Al-O-Zr complex was obtained by Roesky et. al.[68,69] by reaction of the aluminum hydroxide precursor stabilized by the β-diketiminate ligand, DIPP-nacnac, with dimethyl-zirconocene (Figure 1.12, top). The obtained complex can be used towards olefin polymerization in the presence of small quantities of MAO. In a related study, Harder et. al.[70] proposed an Al-O-Zr catalyst with a preorganized vacant site that would be used to circumvent the use of MAO as a cocatalyst. However, both the solid-state structure and ^{1}H-NMR spectrum reveal a stable dimeric tetracoordinate aluminum complex where the oxygen atoms of the biphenolate ligand form a bridge between the aluminum centers. Reacting the biphenolate-aluminum dimer with two equivalents of Cp*Zr(Me)OH yielded the heterobimetallic (DIPH)AlOZr(Me)Cp*$_2$ dimer. The authors also report that the aluminum moiety does not contain a vacant site, though high reactivity of the complex for ethylene

polymerization can be achieved with the addition of MAO. DFT calculations show that the steric bulk of the Cp ligand and the biphenolate are unimportant, implying that less-hindered systems are unlikely to follow a bimetallic insertion mechanism. Harder proposes a sterically enforced six-membered transition state between M-CH_3-C during the insertion process is more likely where the M-CH_3 bond must break before the formation of the new CH_3-C bond can occur. They also show that heterobimetallic ethene insertion activation energies are so high that it is unlikely that this reaction can proceed below 100°C.

1.6.3. Group 4 – Aluminum Heterobimetallic Complexes Featuring a Tetradentate Ligand

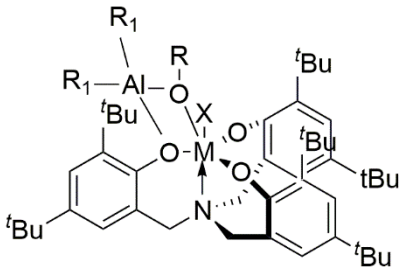

M = Ti, Zr
X = Me, Et, ^{t}Bu
R = ^{i}Pr, ^{t}Bu, DIPP, $CH(CF_3)_2$, C_6F_5, $C(CF_3)_3$
R_1= Me, Et, ^{t}Bu

Figure 1.13. Group 4-aluminum heterobimetallic reported by Nomura et al.[57, 71-74]

A series of bridged Group 4-aluminum heterobimetallic complexes were reported by Nomura et. al.[57, 71-74] using a tetradentate, trianionic atrane ligand that contains three aryloxide ligand and a neutral nitrogen atom that facilitates coordination to provide stabilization of the metal complex. For all synthesized heterobimetallics reported by Nomura et. al., he proposes the generation of the active transition metal catalyst occurs upon cleavage of the titanium -oxygen bond upon addition of MAO or small amounts of $AlMe_3$. In an exciting development, a titanium-aluminum bimetallic {TiMe[(O-2,4-$Me_2C_6H_2$-6-CH_2)$_2$(μ_2-OCH_2CH_2)N]}[Me_2Al(μ_2-O^{i}Pr)] by Nomura demonstrated autocatalytic polymerization of ethylene without the addition of any

external aluminum moiety, forming highly linear polymer with high molecular weight.[71] They propose the zwitterionic complex generated in equilibrium at 100°C is a plausible catalytic active species for linear polymerization though investigation of this phenomena is still ongoing.

1.7 Late Transition Metal—Aluminum Bimetallics

Also largely unexplored is the use of a late transition metal with a Lewis acidic *p*-block metal. Late transition metal-Lewis acid bimetallic complexes can be broadly categorized into two separate families, both capable of cooperative activation of a chemical bond. In the first, no dative bond forms between the transition metal and pendant metal, which allow them to function in a manner of a Frustrated Lewis Pair.[5,6] In the second, the late transition metal functions as a two-electron, σ-donor formally making the transition metal a Lewis base where a dative bond can form, making a "Z-type" interaction.[75,76] Z-type bonding can modulate reactivity at the transition metal or can be exploited in a manner similar to a traditional cooperative catalyst.[77,78] It is worth noting that very few aluminum complexes contain a Z-type interaction between the metal center and the aluminum moiety. Whether or not a Z-type bond forms is directly correlated to the design of the ligand and will be discussed in the latter sections. Though relatively rare, these bonding interactions have been observed with several late transition metal-boron[79-84] and only a few late transition metal-aluminum complexes that will be mentioned in this section of the dissertation. As stated in Section 1.3, aluminum is the most electropositive and earth abundant Group 13 *p*-block metal and of particular interest to our work. Bimetallic complexes that contain aluminum are relatively unexplored compared to their boron analogs to due to being highly reactive species and their synthetic difficulty. This has made their isolation and characterization quite challenging. The remainder of this section will elaborate on these complexes.

1.7.1. Unsupported Bimetallic Aluminum Complexes

Late transition metal-aluminum bonding ("Z-type bonding) has seen a recent boom in interest in the organometallic community. However, addition of an aluminum moiety to a late transition metal complex to form a metal-aluminum interaction is not a new concept. The most straightforward method to form a late transition metal-aluminum interaction is the simple addition of aluminum (III) reagent to a transition metal precursor. Information about the bonding interaction between both metal centers can be typically obtained by spectroscopy and computational methods. This unsupported ligand strategy has been successful in minimizing geometrical constraints between the metal and aluminum, but few examples exist due to co-ligands from the transition metal that can bind efficiently to aluminum.

1.7.2. Unsupported "Z"-type Complexes

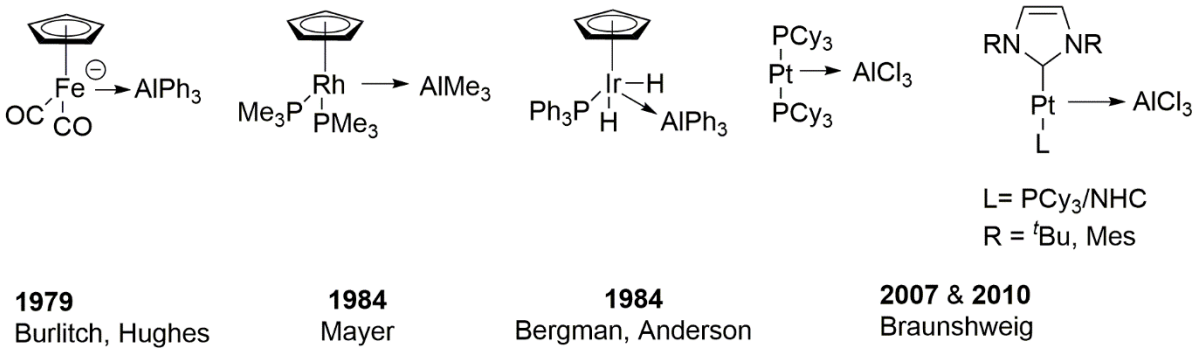

Figure 1.14. Structurally Characterized Unsupported "Z"-type Complexes.[85-89]

One of the earliest examples of unsupported late transition metal-aluminum bonding was demonstrated by Burlitch and Hughes[85] by reacting the anionic iron transition metal complex $Et_4N^+CpFe(CO)_2^-$ with an electron deficient, triaryl aluminum reagent to form an ionic metal-aluminum adduct $Et_4N^+Ph_3AlFe(CO)_2Cp^-$. Structural evidence of metal-metal bond formation was indicated by X-ray crystallography, where the Fe-Al bond was revealed to be 2.510 Å, and the geometry around the aluminum center was slightly distorted tetrahedron, consistent with single bond characteristic and an increase in coordination to the aluminum center. The bonding

interaction was also indicated by a slight shortening of the Fe-CO bond (1.151Å vs 1.18Å) though this is inconsistent with a "Z-type" interaction, where removal of electron density from the transition metal center caused by a Lewis acid would weaken the backbonding interaction between the transition metal and the carbonyl yielding a CO bond elongation.

Direct addition of the aluminum to transition metal complexes has been advantageous in the synthesis of other unsupported dative transition metal-aluminum bonding examples, where electron rich (formally low oxidation state) transition metal complexes were used. Mayer described an unsupported neutral Lewis acid/Lewis base pair when they generated the system $[CpRh(PMe_3)_2(AlMe_3)]$.[86] However, structural characterization of this system showed a significant zwitterionic contribution and the authors appropriately described it as a cationic $[CpRh(PMe_3)_2(AlMe_2)]^+$ with a weakly associated $[AlMe_2Cl_2]^-$. In 1998, Bergman and coworkers reported the complex $[(\eta\text{-}C_5Me_5)(Me_3P)IrH_2(AlPh_3)]$ where the complex demonstrates an Ir/Al interaction by an unsupported ligand scaffold; however, structural data suggests that the Ir-Al metal-metal bond is supported by two bridging hydrogens.[87] In 2007 and in 2010, Braunshweig et. al. demonstrated an unsupported Pt^0-Al dative bond in several linear platinum complexes $PtPCy_3$, $Pt(NHC)_2$, and $Pt(PCy_3)(NHC)$.[88,89] Braunshweig notes that the electron donating properties of the metal to the aluminum center can be tuned by increasing the donor strength of ligand coordinated to the transition metal center. The presence of strong transition metal-aluminum interactions is observed by crystallography**,** where the short transition metal-aluminum distances and pyramidalization of the aluminum are noticeable.

1.7.3. "Z-type" Ligand Supported Late Transition Metal-Aluminum Bimetallic Complexes

Development of ligands designed to contain multiple coordination sites that are selective for either the late transition metal or aluminum have been made in recent years. These ligands typically contain one or several donor ligands that bridge the aluminum moiety to the transition metal, providing stability and rigidity to prevent alternative coordination modes.

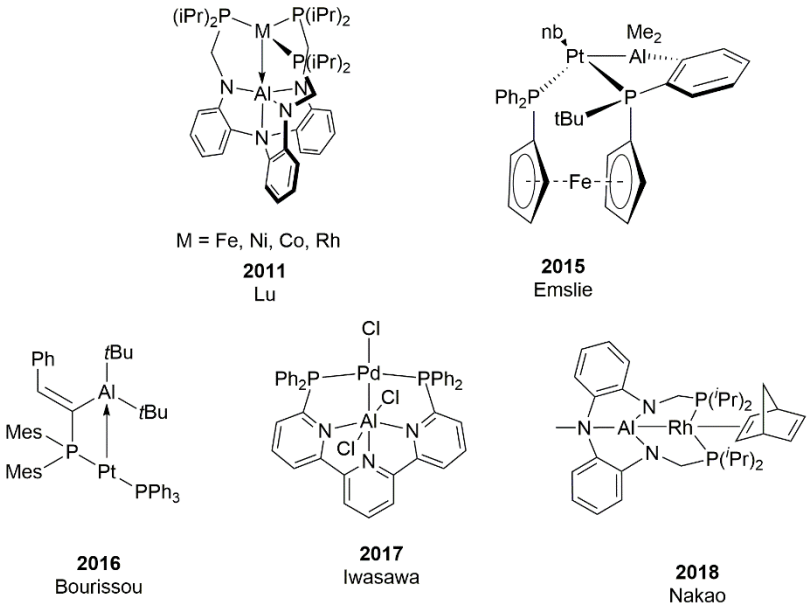

Figure 1.15. Ligand Supported Late Transition Metal-Aluminum Heterobimetallics.[90-94, 96]

As stated above, Z-type interactions are specific to ligand design that bridge aluminum to the late transition metal and have seen a degree of success in recent years. Lu and coworkers developed a dinucleating heptadentate ligand that cages aluminum and facilitates the formation of a Z-type bond.[90,91] Lu's aluminum complexes demonstrate N_2 activation, however, the aluminum moiety is completely caged by the ligand, limiting substrate access to the Lewis acid site. Bourissou[92] and Emslie[93] developed sterically accessible systems by forcing geometrically constrained phosphine-aluminum ligands in close proximity to low valent platinum metal centers. The complexes reported by Bourissou were able to cooperatively active CO_2. H_2, CS_2, and $PhCONH_2$, though no catalysis was reported. In Emslie's systems, a

1,1'-bis(phosphino)ferrocene ligand was employed to facilitate formation of a Pt-Al bond. The first Z-type late transition metal-aluminum bimetallic to demonstrate useful catalytic activity was synthesized by Iwasawa featuring a terpyridine pincer ligand with two coordinating arms to cage palladium and aluminum.[94] The resulting complex is capable of hydrosilylation of CO_2. Later, a Ni/Al[95] and Rh/Al[96] complexes reported by Nakao were found to facilitate ortho- C-H functionalization of pyridines. A formal metal-aluminum bond was not reported for the Ni/Al system; however, cooperative reactivity was achieved by the close proximity of the two metal centers.

1.8. Overview of Chapter Contents

The limited number of well characterized late transition metal-aluminum heterobimetallics, combined with their recently demonstrated catalytic utility, makes the development of new heterobimetallic constructs an area ripe for exploration for cooperative activation of small molecules. This dissertation will describe our endeavors toward this goal. A "transition metal first" synthetic strategy in which the reactive aluminum center is added to a pre-formed transition metal complex was developed to overcome the inherent synthetic difficult of working with moisture sensitive aluminum compounds. This strategy has been successful in developing several families of Rh/Al and Ir/Al bimetallic complexes which will be discussed in detail in the ensuing chapters. In addition to synthesis, the reactivity of a subset of the generated complexes will also be reported on.

In Chapter 2, we report the design and synthesis of a rhodium-aluminum heterobimetallic complex bridged using the tridentate ligand 1,3-bis(diphenylphosphino)-2-hydroxypropane. This bridging ligand is capable of binding both the transition metal and aluminum moiety selectively. Product identification was evaluated by various spectroscopic methods.

In Chapter 3, we describe the reactivity of a tripodal ligand, bis(3,5-dimethyl-pyrazol-1-yl)acetate (NNO), with late transition metals to form scorpionate rhodium and iridium complexes. We then report on the reactivity of these complexes with aluminum alkyls. Our efforts describe the synthesis of three new rhodium and iridium NNO complexes, which are dependent on the protonation state of the NNO ligand. These transition complexes were identified by various spectroscopic techniques. Reactivity of each of these transition metal complexes with triethyl and triisobutyl aluminum are described.

In Chapter 4, we demonstrate the reactivity of 2-substituted pyridine-aluminum alkyl complexes with CO_2. Joint experimental and computational mechanist studies suggest that CO_2 insertion occurs via a cooperative pathway. We demonstrate the first example of cooperative activation of CO_2 into a ligated aluminum alkyl at room temperature without the use of external base.

In Chapter 5, a summary of the results of the studies present in chapter 2-4 can be found. Here we identify and propose future studies to progress the work of late transition metal-aluminum bimetallics and their reactivity towards small molecules. Appendices A contains supplemental data pertaining to chapter 2, Appendices B contains supplemental data pertaining to chapter 3, and Appendices C contains supplemental data pertaining to chapter 4.

Chapter 2

Synthesis and Characterization of Rhodium-Aluminum Heterobimetallic Complexes Tethered by a 1,3-Bis(diphenylphosphino)-2-propanoxy Group

2.1 Introduction

Heterobimetallic complexes have gained intense attention due to their interesting structures, properties, and applications such as in theranostics,[97] medical imaging,[98] and catalysis.[99,100] In particular, early-late heterobimetallic complexes have been widely explored.[2, 101,102] The large polarity difference between metal centers make them nicely suitable for cooperative heterolytic bond activations.[11,103] In a similar fashion, as the most electropositive element in group 13, a highly Lewis acidic aluminum(III) center would be expected to impart significant polarity into a late transition metal heterobimetallic system.

Our laboratory has been exploring the synthesis of Ir-Al and Rh-Al heterobimetallic complexes, with the aim of exploiting these two metal centers for cooperative activation of small molecules in a manner reminiscent of a Frustrated Lewis Pair.[104-106] A " ligand first" synthetic strategy in which the reactive aluminum center is added to the bimetallic species following the synthesis of the transition metal component was developed to overcome the inherent synthetic difficulty of working with moisture sensitive compounds.[107] In recent experiments, discussed in more detail in Chapter 4, a proof-of-concept result has been obtained demonstrating that the heterobimetallic Ir-Al and Rh-Al complexes developed in our laboratory can facilitate the activation of small molecules.[108]

In this chapter, we report the synthesis and characterization of a new series of Rh-Al heterobimetallic complexes. In our initial paper,[107] we reported a slow, thermal decomposition of

the rhodium-containing heterobimetallic complexes. Analysis of a decomposition product informed us that dissociation of the bridging pyridone ligand from rhodium was responsible for the observed decomposition. To alleviate this concern, we envisioned replacing the pyridine moiety with a chelating phosphine ligand. In the work reported below, 1,3-bis(diphenylphosphino)-2-propanol (DPPP-OH)[109] has been utilized to tether rhodium and aluminum. As in our previous work, to ensure stable attachment, aluminum is linked to a bridging ligand through a thermodynamically strong Al-O bond.

2.2 Synthesis and Characterization

The general synthesis procedures are summarized in **Figure 2.1**. The overall strategy is similar to our reported procedure,[107] where aluminum was introduced at the end of the reaction sequence by reacting tri-isobutyl aluminum (Al^{i}Bu$_3$) with an aluminum-binding hydroxyl group on pre-assembled transition metal complexes, thereby taking advantage of the easy formation of aluminum-oxygen bonds and eliminating the need to further manipulate air- and moisture-sensitive aluminum compounds.

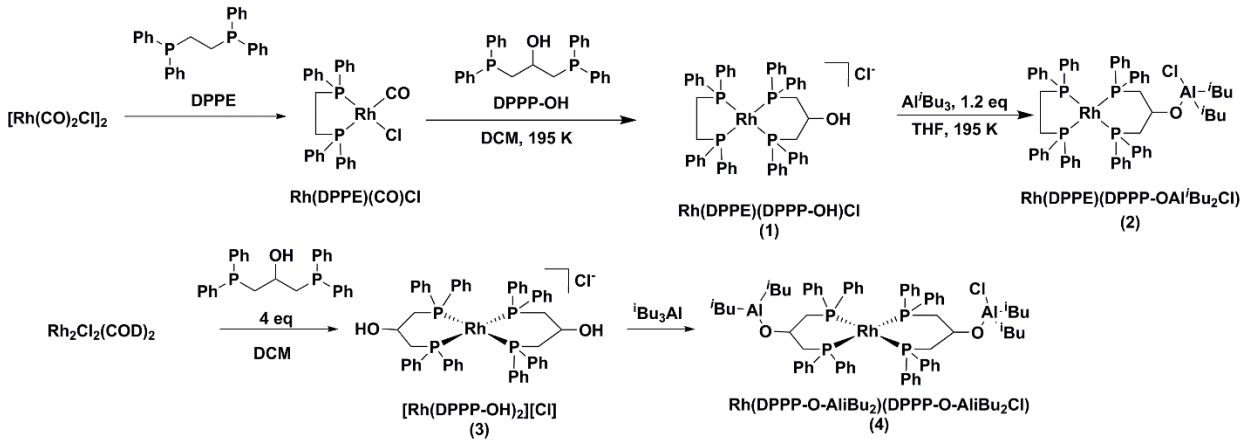

Figure 2.1. Synthetic procedure for Rh(DPPE)(DPPP-O-Al^{i}Bu$_2$Cl) and Rh(DPPP-O-Al^{i}Bu$_2$)(DPPP-O-Al^{i}Bu$_2$Cl)

2.3 Results and Discussion

In the synthesis of Rh(DPPE)(DPPP-OH)Cl (**1**), the assembly was designed to install DPPE and DPPP-OH sequentially on to rhodium from readily accessible $Rh_2(CO)_4Cl_2$.[110] The reaction conditions were empirically optimized and carefully controlled to avoid unintentional formation of $[Rh(DPPE)_2]^+$, $[Rh(DPPP\text{-}OH)_2]^+$, DPPP-OH bridged dimers,[111] or other species. First, Rh(DPPE)(CO)Cl was obtained by reacting DPPE with $[Rh(CO)_2Cl]_2$.[31] The $^{31}P\{^1H\}$ NMR spectrum of Rh(DPPE)(CO)Cl showed two sets of *dd* peaks that are characteristic of Rh-P and P-P splitting (see Figure A3 in Appendix A). Further treatment of Rh(DPPE)(CO)Cl with DPPP-OH resulted in the formation of **1**. The $^{31}P\{^1H\}$ NMR spectrum of **1** displayed a diagnostic, two signal pattern for the two phosphorus in DPPE and the two phosphorus in DPPP-OH respectively, as shown in Figure A6 in Appendix A. The two phosphorus centers in each DPPE or DPPP are chemically equivalent (δ 59.68 ppm and 16.78 ppm, respectively) but magnetically inequivalent, leading to an AA'MM'X spin system wherein each phosphorus atom is coupled to the other three and the $I = ½$ rhodium center.

The observed $^{31}P\{^1H\}$ coupling patterns within **1** are second-order as a result of the coupling between two nuclei with identical chemical shifts [$^2J_{P\text{-}P}$ >>>> 10*(Δδ)]. Thus, the coupling constants cannot be extracted by simply using peak spacing and relative peak intensity. However, the pattern can be effectively modeled based on parameterized chemical shift and coupling constants, as shown in **Figure 2.2**, allowing for full coupling analysis. As is often observed in highly second-order spin systems, the sign of the coupling constant *J* has a remarkable effect on the observed pattern. In this system, *syn* $^2J_{P\text{-}P}$ coupling constants were found to be negative (parallel spins lower in energy) while the *trans* $^2J_{P\text{-}P}$ coupling constants

were positive (opposite spins lower in energy). Measurement of negative $^{2}J_{P\text{-}P}$ values is not uncommon in bis-phosphine systems.[112]

Treatment of **1** with Al^{i}Bu$_3$ resulted in the target heterobimetallic complex Rh(DPPE)(DPPP-O-Al^{i}Bu$_2$Cl) (**2**). Unfortunately, the well-known complex [Rh(DPPE)$_2$]Cl[113,114] was formed as a byproduct during the synthesis of **2**. The two complexes are not easily separated, and the bis-DPPE impurity is present as a minor component in our product spectra (see Figure A7 in Appendix A). After extensive recrystallization, the mole percentage of [Rh(DPPE)$_2$]Cl could be reduced to below 5% (calculated from integration of the ^{31}P{^{1}H} NMR spectrum of the product mixture). The ^{31}P{^{1}H} NMR spectrum of **2** displayed a similar, diagnostic, coupling pattern to that observed in **1**. Aluminum coordination causes the second order multiplet for the DP*P*P-O-Al^{i}Bu$_2$Cl phosphorus resonance to shift slightly upfield to δ 13.90 ppm from the resonance observed in the parent complex (δ 16.78 ppm, see **Figure 2.2**). The DP*P*E resonance remains largely unchanged at δ 59.37 ppm. Full coupling constant information for this AA'MM'X system can be found in the Experimental Details and in Appendix A.

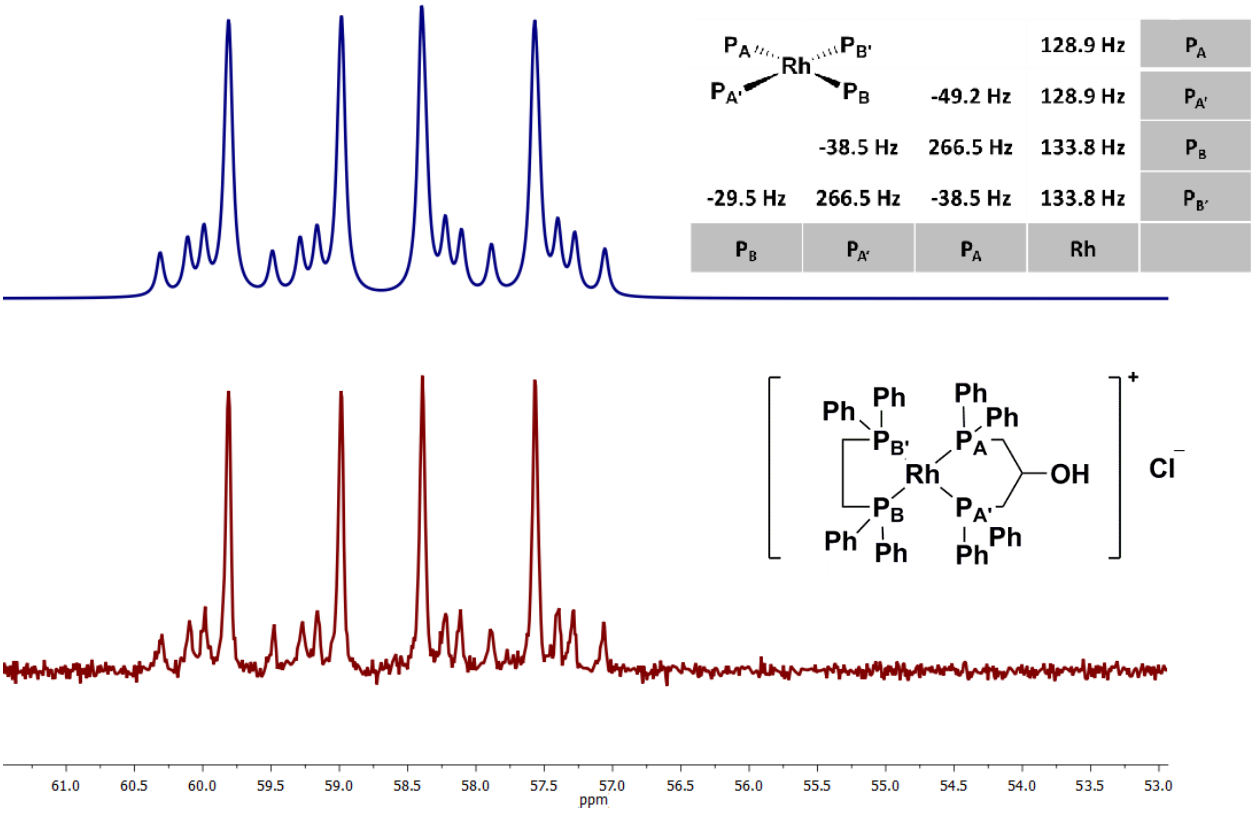

Figure 2.2. Modeled (blue, above) and experimental (red, below) fine pattern of the $^{31}P\{^{1}H\}$ NMR spectrum for the two phosphorus atoms in the DPPE ligand (P_B, P_B' in table) in complex **1**. An analogous peak is found for the DPPP-OH ligand. Inset: P-P and Rh-P coupling constants; P_A, $P_{A'}$ (DP***P***P-OH), P_B, $P_{B'}$ (DP***P***E). For full spectrum, see Figure A3 in the Appendix A.

The ^{1}H NMR spectrum of **2** also contains three critical diagnostic features that unambiguously confirm our assignment of the structure of the major reaction product. First, the integration of the signals corresponding to alane protons clearly indicated the loss of one equivalent of its alkane substituent. Second, the remaining methylene protons between δ 0.65 and 0.75 are now diastereotopic, coupled to each other with a geminal coupling constant of 13.6 Hz. This strongly indicates successful docking to the alkoxide *and* the formation of a tetrahedral aluminum center via chloride coordination. Third, the signal arising from the methine protons shifted downfield due to steric deshielding[115] after reaction between $^{i}Bu_3Al$ and the hydroxyl group on DPPP-OH. These phenomena are consistent with nitrate-bound aluminum centers in

the heterobimetallic complexes previously described in our laboratory.[107] The ^{1}H NMR spectrum was modeled using simple, coupling parameters to obtain the relevant coupling information (as shown in **Figure 2.3**). Full coupling parameters can be found in Figure A7 in Appendix A.

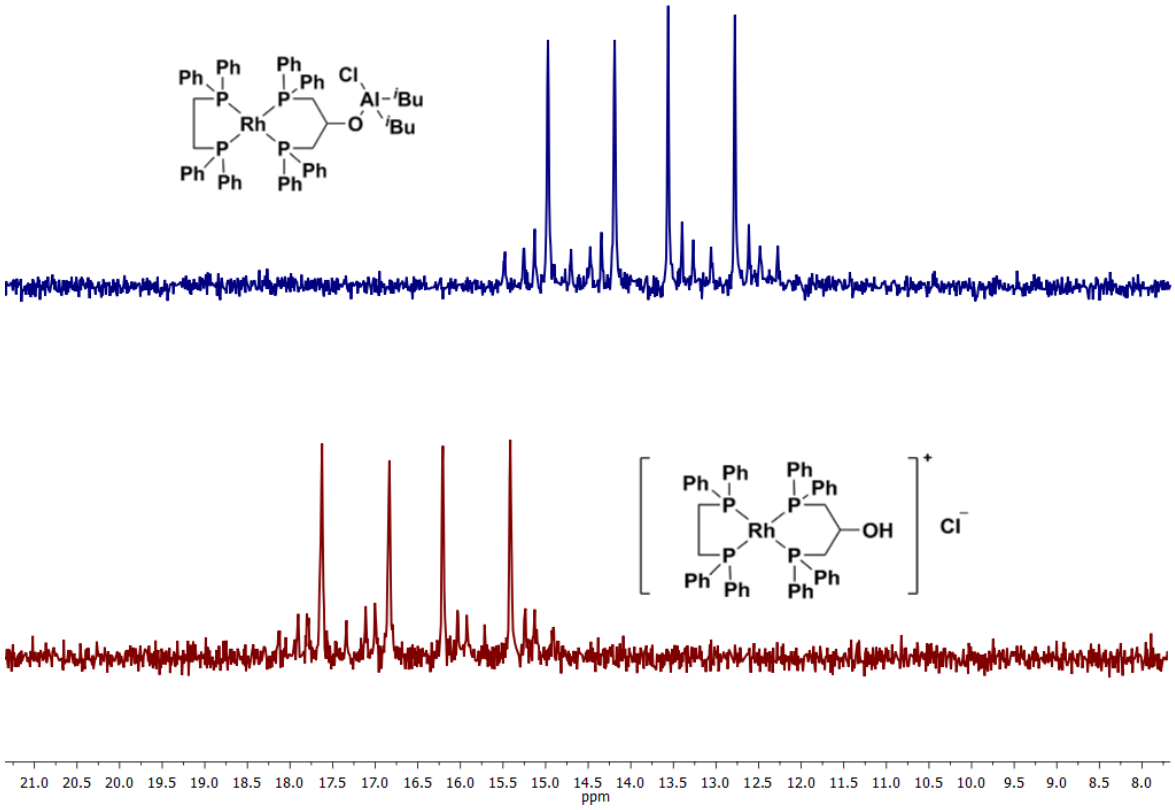

Figure 2.3. Truncated $^{31}P\{^{1}H\}$ NMR spectrum of **2** showing the shift in the DP*P*P-O-R resonance on moving from R = H (bottom) to R = Al($^{i}Bu_2$)Cl (top).

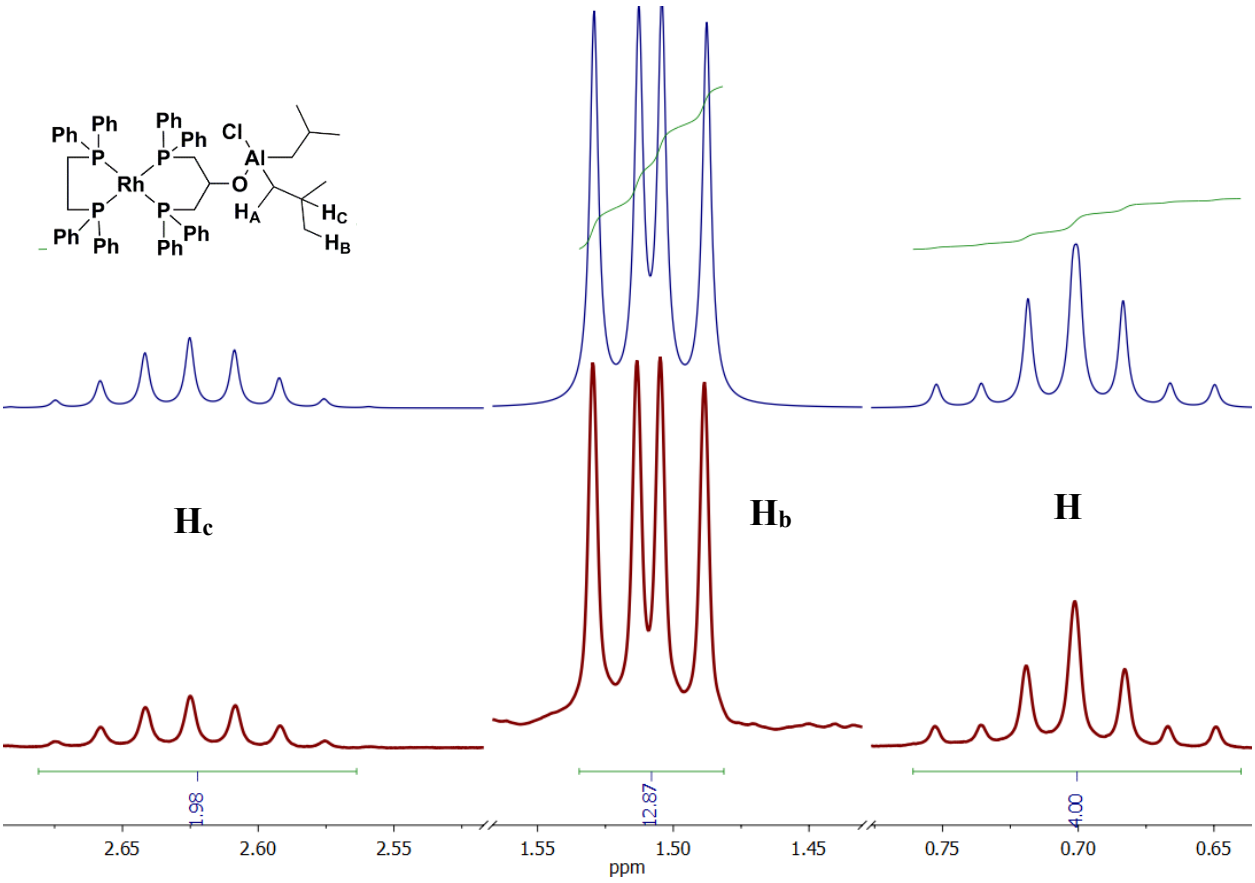

Figure 2.4. Modeled (top) and measured (bottom) ^{1}H NMR spectrum of aluminum alkyl resonances in **2**.

In an effort to eliminate the formation of unwanted inseparable byproducts, we then shifted our attention to the synthesis of a new target complex, Rh(DPPP-O-Al^{i}Bu$_2$)(DPPP-O-Al^{i}Bu$_2$Cl) (**4**), where we replaced the troublesome DPPE ligand with a second equivalent of DPPP-OH. The precursor, [Rh(DPPP-OH)$_2$]Cl (**3**), was synthesized in a straightforward manner by treating [Rh(COD)Cl]$_2$[110] with 4.2 equivalents of DPPP-OH followed by washing COD and excess DPPP-OH away with a mixed solvent system of pentane/dichloromethane (v/v = 5/1). Though we were unable to obtain X-ray quality crystals of the chloride complex, anion metathesis with Na(BArF$_{24}$) in dichloromethane followed by slow precipitation from a solution of [Rh(DPPP-OH)$_2$][BArF$_{24}$] (**3-BArF**) in chloroform layered with pentane did yield suitable crystals of the BArF$_{24}$ analogue (**Figure 2.5**). The complex is found to have a distorted square

planar geometry, with *syn* P-Rh-P angles of 88.51° and 88.18° within the metallacycles and 98.33° and 98.67° between the metallacycles (sum of angles = 373.69°). The two hydroxide functionalities also are located in equatorial positions of their respective pseudo-chair metallacycles and are found to be mutually *syn* within the spiro ring system. Interestingly, the deviation from planarity observed in the solid state structure of **3-BArF** is not observed in the solid state structure of $[Rh(DPPP)_2][Cl]$[116] structure found in Figure 2.5, sum of angles = 360.1°) suggesting that the steric demand of the hydroxyl group has a measurable impact on the observed structural metrics.

Interestingly, the synthesis of **3** from $[Rh(CO)_2Cl]_2$ was not successful. CO dissociation from Rh was found to be incomplete, leading to the formation of the penta-coordinate complex $[Rh(DPPP\text{-}OH)_2(CO)]Cl$ (**5**). An X-ray crystal structure of this unexpected product was obtained by layering a chloroform solution of the complex with pentane (**Figure 2.6**). Complex **5** displays a trigonal bipyramidal structure (sum of equatorial angles = 360.1°, P_{axial}-Rh-P_{axial} = 173.76°) with the carbonyl ligand occupying one of the equatorial positions. As in the structure of **3-BArF** above, the two hydroxide functionalities also are located in equatorial positions of their respective pseudo-chair metallacycles and are found to be mutually *syn* within the spiro ring system.

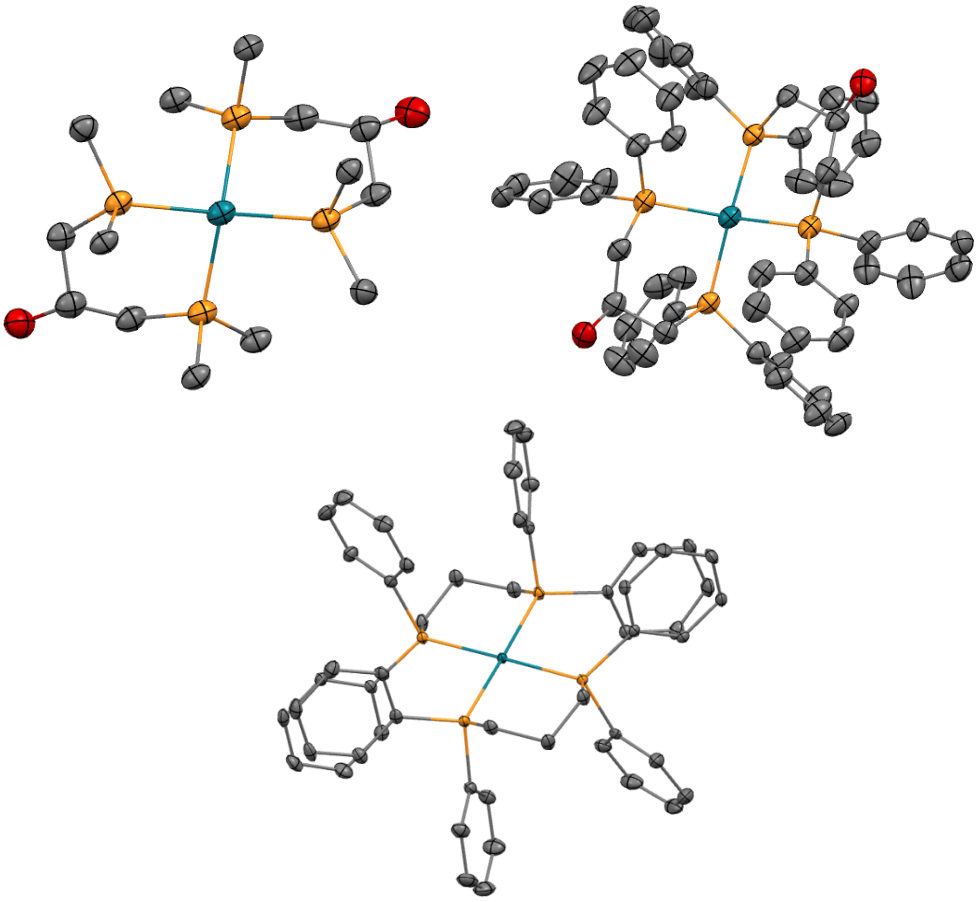

Figure 2.5. Top: ORTEP representations of **3-BArF**. Left: Carbons 2-6 of each phenyl ring omitted for clarity. Right: Full structure. Bottom: ORTEP representation of $[Rh(DPPP)_2][Cl]$. For all structures, ellipsoids shown at 50% probability. Hydrogen atoms and anion omitted from each structure for clarity.

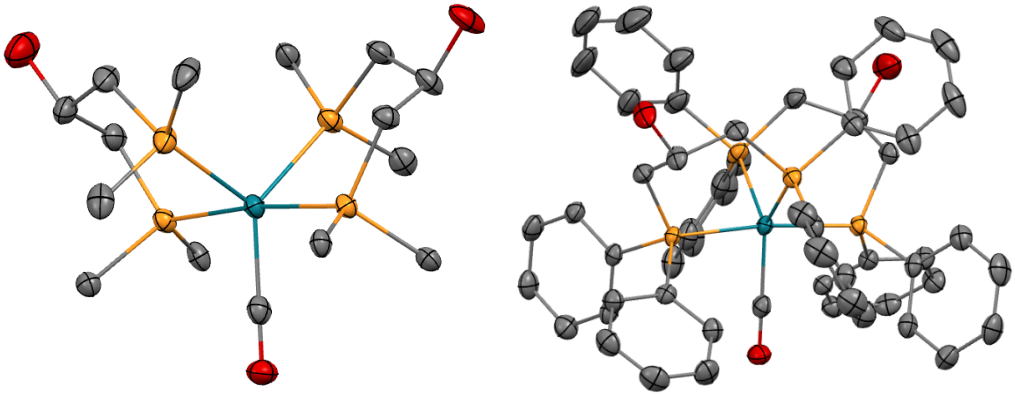

Figure 2.6. ORTEP representations of **5**. Ellipsoids shown at 50% probability. Hydrogen atoms and chloride counterion omitted for clarity. Left: Carbons 2-6 of each phenyl ring omitted for clarity. Right: Full structure.

Treatment of **3** with Al^iBu_3 resulted in the target heterobimetallic complex Rh(DPPP-O-Al^iBu_2)(DPPP-O-Al^iBu_2Cl) (**4**). Unfortunately, solid-state characterization of **4** has not been possible due to its dynamic nature and its intrinsically high reactivity. The ^1H NMR peaks (Figure A12 in Appendix A) are quite broad but features a number of upfield ($\delta < 0.5$ ppm) resonances consistent with the presence of the aluminum alkyl. The $^{31}P\{^1H\}$ NMR spectrum of **4** at room temperature features a sharp doublet and a broad secondary feature (as shown in Figure A11 in Appendix A). Variable temperature NMR in tetrahydrofuran-d_8 was carried out to further elucidate the observed broadness of the $^{31}P\{^1H\}$ spectrum, as shown in Figure 2.7, below.

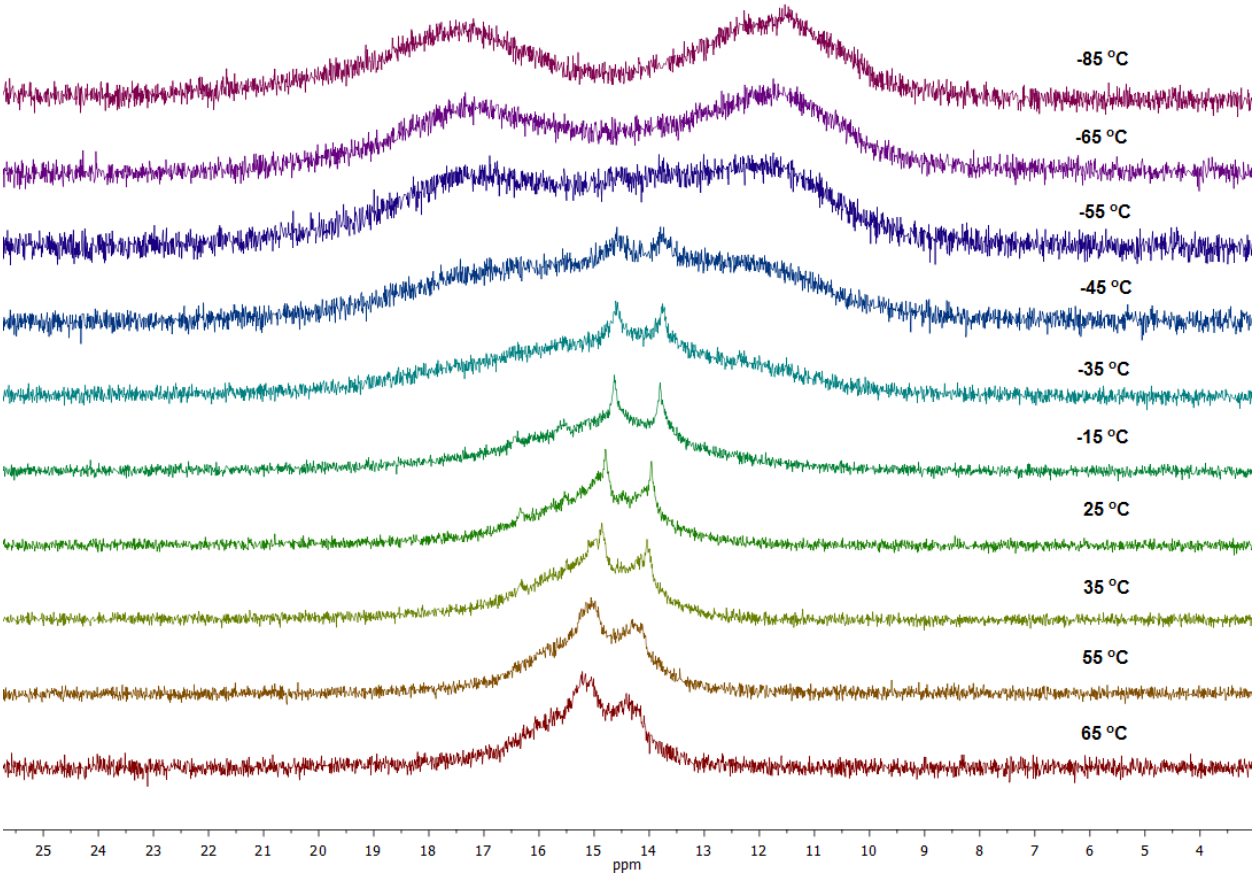

Figure 2.7. Variable temperature $^{31}P\{^1H\}$ NMR of **4**. Temperature recorded across a range from -85°C to 65°C.

Two processes were observed as temperature changes. The first process is evident at very low temperature. Two broad peaks (~ δ 17.44 and δ 11.72 ppm) with clear separation could be

observed at -85°C via $^{31}P\{^{1}H\}$ NMR spectroscopy. As the temperature is raised, these two peaks began to broaden and shift with coalescence observed at approximately -15°C. In the second dynamic process, a doublet with a coupling constant of 133 ppm, first observable at -55°C, first sharpens significantly with rising temperature. Above room temperature, this signal begins to broaden slightly and shift downfield. Though we were unable to increase the temperature above 65°C on our NMR spectrometer, it appears that the broad, underlying feature begins to coalesce with the sharp doublet at high temperature. The distinction between the two features is evident in the room temperature spectrum shown in Figure A11 (Appendix A). Importantly, signals arising from the precursor complex **3** are not observed in the product spectrum suggesting that the observed behavior is intrinsic to the reaction product mixture, **4**.

Though the exact nature of the equilibrating species in solution has not yet been rigorously established, we have significant evidence that the formulaic assignment of complex **4** is correct. First, ESI-MS (Figures A13 and A14 in Appendix A) of **4** under different ionization conditions showed different patterns that could be assigned as fragments arising from **4**. Under all ionization conditions, a peak at 960.08 from precursor $[Rh(DPPP\text{-}OH)_2]^+$ (*m/z* = 960) was seen suggesting the Al-O bond as a likely fragmentation location (the starting material was not observed by $^{31}P\{^{1}H\}$ NMR spectroscopy). Higher-mass fragments assignable to [Rh(DPPP-O-Al^{i}Bu)(DPPP-O-Al^{i}Bu)•H_2O]$^+$ (*m/z* = 1144, water arises from injection port contamination) and [Rh(DPPP-O-Al^{i}Bu$_2$)(DPPP-O-Al^{i}Bu$_2$)]$^+$ (*m/z* = 1144.17) were also easily identified, confirming that aluminum has docked successfully. High Resolution Mass Spectrometry provided further validation for the formation of the desired product (Fig A15, Appendix A). At no point in any ESI-MS experiment were mass fragments greater than the parent ion of **4** were identifiable that

corresponded to a potential dimeric product. This result strongly suggests that **4** is monomeric, rather than dimeric or oligomeric, in solution.

Further support for a monomeric product was obtained from DOSY (Figures A18 and A19, Appendix A), where a single diffusion coefficient was obtained for **4 (**molecular weight ≈ 1275, Diffusion = 10^0). Complexes in the product mixture **4** all diffuse at the same rate, indicating a uniform product size. Importantly, they also diffuse at the same rate as complex **3** (Diffusion = 10^0), which is known to be monomeric from the solid-state structure of **3-BArF** (Figure 2.5, right). This suggests that **3** and **4** are of similar size. Were **4** dimeric or oligomeric, it would be expected to diffuse much more slowly than **3**.

With this knowledge in hand, we propose a reasonable explanation for the dynamic behavior observed in the NMR spectra of **4**. We first postulate that the two distinct fluxional processes derive from two different, isomeric products. This is consistent with complex **3** which exists as a mixture of *syn* and *anti* isomers (**Figure 2.8**). It is quite likely, given the low temperature of the synthesis of **4** from **3** that interconversion between the *syn* and *anti* forms is not possible during synthesis. Thus, observing two distinct species with distinct dynamic behavior is not unexpected. At high temperatures, where dissociative interconversion may become feasible, the two species would be expected to interchange. This is consistent with the observed high temperature broadening in Figure 2.7. Notably, any dissociative pathways available above room temperature could also facilitate intramolecular scrambling of DPPP-O-Al^{i}Bu$_2$ ligands with DPPP-O-Al^{i}Bu$_2$Cl ligands further contributing to line broadening and complicating the analysis of the high-temperature spectra. We favor dissociative (as opposed to associative) ligand exchange as a mechanism due to precedent[117,118] and the steric bulk of the phosphines.

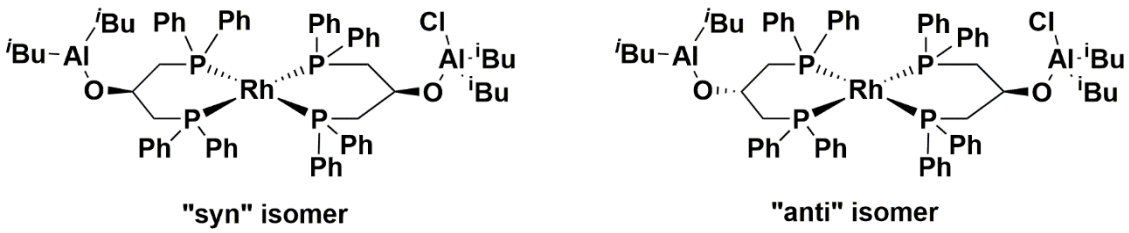

Figure 2.8. Possible diastereomers of **4**.

Additionally, we postulate that the low-temperature dynamic behavior observed for each isomer relates to chloride exchange between the aluminum centers. As can be clearly seen in Figure 2.7, the two DPPP-O-Al ligands in **4** should be chemically inequivalent, as one contains a bound chloride and the other does not. One would, thus, expect an AA'BB'X coupling pattern in the phosphorus NMR as was observed for complexes **1** and **2**. What is instead observed at room temperature is a sharp doublet (See A11 in Appendix A), indicating that all four phosphorus centers are equivalent (via exchange). The most likely explanation for this is chloride scrambling. The different molecular geometries of the *syn* and *anti* isomers would cause differential activation barriers to exchange, thus resulting in their unique dynamic behavior.

Though we believe that our explanation above is the most plausible given the data in hand, other possibilities for dynamic behavior exists. First, each diastereomer could undergo slow chair-chair interconversion. Given the significant preference for the bulky O-Al^{i}Bu$_2$Cl to occupy an equatorial position off the six-membered metallacycle, we believe that this is unlikely to be observed. Other potential dynamic behavior derives from the aluminum center itself. To maintain charge balance, at least one aluminum must be coordinatively unsaturated. It could then engage in a multitude of potential stabilizing interactions. First, it could dimerize via a bridging alkyl with a neighboring aluminum center. We consider this possibility unlikely due to the steric bulk of the isobutyl group (Al^{i}Bu$_3$ does not exist as a dimer), the DPPP-O ligand, and the lack of evidence for dimer formation by ESI-MS and DOSY. The aluminum center could also engage in

weak, intramolecular, Z-type bonding with the transition metal center. However, to attain such a geometry, the 6-membered metallacycle would be forced to adopt a boat geometry, which is likely energetically unfavorable even with a stabilizing Z-type bond.

Finally, we attempted to extend the synthetic protocols utilized here to other aluminum moieties. Interestingly, no other commercially available aluminum alkyls led to the formation of readily identifiable heterobimetallics. $AlEt_3$, $AlEt_2Cl$, and Al^iBu_2Cl, all facilitated transformation of the Rh precursors into a mixture of intractable products. The unique reactivity of Al^iBu_3 is attributed to the bulky size of isobutyl groups, which provide efficient steric protection of the Al center. Chloride, which in addition to its small steric profile can readily bridge between two aluminum centers, further complicates syntheses from $AlEt_2Cl$, and Al^iPr_2Cl.

2.4 Conclusions

Highly polarized heterobimetallic complexes are a promising catalyst family for the cooperative activation of polarizable substrates. In an effort to overcome the instability of the pyridone bridge in previously reported late transition metal-aluminum complexes from our laboratory[107] and prevent decomposition in the presence of a substrate, a synthetic route to a novel heterobimetallic complex, **2**, which is bridged via a ligand which chelates the transition metal was developed. Thorough spectroscopic characterization indicated the presence of a small amount of $[Rh(DPPE)_2]Cl$ in the product mixture. The thermodynamic stability of this undesired byproduct led us to develop a synthetic route to **4**. This complex was found to have a dynamic structure in solution. Application of these exciting complexes toward small molecule activation is now under investigation.

2.5 Experimental Details

2.5.1 General Considerations

Procedures were performed in a nitrogen-filled Inert Technologies glovebox or using standard Schlenk techniques unless otherwise specified. Extra dry benzene, pentane, tetrahydrofuran, diethyl ether, and dichloromethane were purchased from commercial suppliers and stored over molecular sieves in the glovebox prior to usage. Toluene was dried over calcium hydride and stored over molecular sieves in the glovebox. Deuterated solvents were purchased from Cambridge Isotope Laboratories, dried over molecular sieves, and stored in the glovebox prior to use. DPPE was purchased from Sigma-Aldrich. DPPP-OH was synthesized following literature procedure.[109] $NaBArF_{24}$ was synthesized by the method of Bergman[119] and purified using the modification reported by Peters.[120] All other reagents and solvents used were commercially available and used without further purification. Aluminum and phosphine reagents were stored in a nitrogen glovebox prior to use. ^{1}H and ^{13}C NMR spectra were recorded on a 400 MHz JEOL spectrometer and referenced to the residual solvent peak.[121] Additional NMR data were obtained on a 400 MHz JEOL spectrometer and referenced to an appropriate external standard (^{31}P: H_3PO_4 in D_2O (0.00 ppm)). Spectra were modeled using the MestReNova 10 software package. ESI-MS was measured on a ThermoFisher LTQ-XL ion trap mass spectrometer from dichloromethane or tetrahydrofuran solution. High resolution mass spectra were recorded on a Waters Synapt High Resolution Mass Spectrometer housed at the University of Memphis. Elemental analysis was performed by Atlantic Microlabs, Inc. and is reported as the average of duplicate runs.

2.5.2. Synthesis

Rh(DPPE)(CO)Cl This procedure was adapted from the synthetic protocol for the analogous iridium complex.[111] $RhCl_3 \cdot 3H_2O$ (1.37 g, 5 mmol) was dissolved in 100 mL methanol. The mixture was heated to reflux under CO for 24 hours. The bright yellow solution was cooled to room temperature and methanol was removed by vacuum. The dark red solid was dissolved in 50 mL benzene, to which a benzene solution (100 mL) of 1,2-bis(diphenylphosphino)ethane (2.0 g, 5 mmol) was added dropwise. The yellow precipitate was collected and recrystallized from dichloromethane/hexanes, affording 2.3 g yellow powder as product. Yield: 80%. ^{1}H NMR (400 MHz, $CDCl_3$) δ 7.71-7.83 (m, 8 H), 7.40 (m, 12 H), 2.42-2.49 (m, 2 H), 2.15-2.22 (m, 2 H). $^{31}P\{^1H\}$ NMR (162 MHz, $CDCl_3$) δ 71.17 (dd, J =159.6, 34.8 Hz), 49.46 (dd, J = 127.2, 34.8 Hz). Anal. Calc $C_{27}H_{24}OP_2RhCl$: C, 57.42; H, 4.28. Found: C, 57.39; H, 4.40.

Rh(DPPE)(DPPP-OH)Cl (1) To a stirred dichloromethane (5 mL) solution of DPPP-OH (215 mg, 0.5 mmol) at -78 °C, Rh(DPPE)(CO)Cl (280 mg, 0.5 mmol) in dichloromethane (10 mL) was added dropwise over a period of 1 hour. The mixture was allowed to stir for 16 hours as the temperature was slowly raised from -78 °C to room temperature. The crude product was purified by recrystallization from tetrahydrofuran at -35 °C. 370 mg yellow powder was collected as product. Yield: 77%. ^{1}H NMR (400 MHz, $CDCl_3$) δ 7.51 (m, 4H), 7.40 – 6.96 (m, 28H), 6.82 (m, 8H), 3.83 (s, 1 H), 3.66-3.69 (m, 1 H), 2.90 (m, 2H), 2.71 (m, 2H), 2.06 (m, 2H), 1.86 (m, 2H). $^{31}P\{^1H\}$ NMR (162 MHz, $CDCl_3$) δ 59.68 (DP*P*E, J_{Rh} = 133.8 Hz, J_{trans} = 266.5 Hz, $J_{cis,\ B\text{-}B'}$ = -29.5 Hz, $J_{cis,\ B\text{-}A'}$ = -38.5 Hz), 16.78 (DP*P*P-OH, J_{Rh} = 128.9 Hz, J_{trans} = 266.5 Hz, $J_{cis,\ A\text{-}A'}$ = -49.2 Hz, $J_{cis,\ A\text{-}B'}$ = -38.5 Hz). Anal. Calc $C_{53}H_{50}OP_4RhCl$: C, 65.95; H, 5.22. Found: C, 58.79; H, 5.02. Elemental consistent with two molecules of dichloromethane per formula unit (C, 58.20, H, 4.80).

Rh(DPPE)(DPPP-O-Al^{i}Bu$_2$Cl) (2) To a stirred tetrahydrofuran (3 mL) solution of Rh(DPPE)(DPPP-OH)Cl formed in situ from Rh(DPPE)(CO)Cl (141 mg, 0.25 mmol) and DPPP-OH (110 mg, 0.25 mmol) at -78 °C, ^{i}Bu$_3$Al (50 mg, 0.25 mmol) was added. The mixture was allowed to stir for 1 hour and warmed from -78 °C to room temperature. After the reaction, tetrahydrofuran was removed by vacuum. The resultant yellow powder was dissolved in 0.5 mL tetrahydrofuran and precipitated by the addition pentane. This recrystallization was repeated twice to remove [Rh(DPPE)$_2$]Cl and improve purity to greater than 95%. 170 mg bright yellow powder was collected as product. Impurity prevented acceptable microanalysis from being obtained. Yield: 62%. ^{1}H NMR (400 MHz, tetrahydrofuran-d$_8$) δ 6.60 – 7.36 (m, 56H), 5.36 (m, 1 H), 2.91 (m, 2H), 2.74 (m, 2 H), 2.62 (m, 2 H), 1.52 (d, J = 6.6 Hz), 1.50 (d, J = 6.6 Hz), 0.72 0.68 (dd, J_{gem} = 13.5 Hz, J = 6.6 Hz). ^{31}P{^{1}H} NMR (162 MHz, tetrahydrofuran-d$_8$) δ 59.37 (DP*P*E, J_{Rh} = 107.2 Hz, J_{trans} = 205.5 Hz, $J_{cis,\ B\text{-}B'}$ = -22.6 Hz, $J_{cis,\ B\text{-}A'}$ = -29.2 Hz), 58.20 (Rh(DP*P*E)$_2$Cl, d, J = 132.8 Hz), 13.90 (DP*P*P-OH, *ddd*, J_{Rh} = 101.2 Hz, J_{trans} = 205.5 Hz, $J_{cis\ A\text{-}A'}$ = -39.4 Hz, $J_{cis,\ A\text{-}B'}$ = -29.2 Hz). *J-values for these resonances were determined via modeling. Second order coupling modeled computationally. HRMS calculated for [$C_{53}H_{50}Al_2O_4P_4Rh$]$^{+}$ (product of alkyl hydrolysis) m/z calc: 971.1554. Found: 970.8866 (See Figures A17a and A17b in Appendix A).

[Rh(DPPP-OH)$_2$]Cl (3) To a stirred dichloromethane (5 mL) solution of Rh$_2$(COD)$_2$Cl$_2$ (49 mg, 0.1 mmol), DPPP-OH (170 mg, 0.4 mmol) in dichloromethane (5 mL) was added dropwise. The mixture was stirred at room temperature for 30 min before the solution was concentrated by vacuum to ~1 mL. The product was obtained via precipitation with pentane. The solid was washed with a mixed solvent system of pentane/dichloromethane (v/v = 5/1). This method was repeated twice to yield 122 mg of yellow powder. This product exists as a mixture of two

isomers, as determined by $^{31}P\{^{1}H\}$ NMR spectroscopy and confirmed by combustion analysis. Yield: 61%. $^{31}P\{^{1}H\}$ NMR (162 MHz, $CDCl_3$) δ 14.14 (d, J = 134 Hz), 13.39 (d, J = 134 Hz). Anal. Calc $C_{54}H_{52}O_2P_4RhCl$: C, 65.17; H, 5.27. Found: C, 64.88; H, 5.42.

Rh(DPPP-O-Al^{i}Bu$_2$)(DPPP-O-Al^{i}Bu$_2$Cl) (4) To a stirred tetrahydrofuran (3 mL) solution of [Rh(DPPP-OH)$_2$]Cl (50 mg, 0.05 mmol) at -35 °C, $^{i}Bu_3Al$ (22 mg, 0.11 mmol) was added. The solution was stirred for 10 minutes and tetrahydrofuran was removed by vacuum. The remaining solid was washed with cold pentane three times. The ^{1}H NMR spectrum is broadened due to probable isomeric mixture. ^{31}P NMR (162 MHz, tetrahydrofuran-d_8) δ 15.04 (d, J = 134 Hz). ESI-MS: m/z calc. for: $[C_{62}H_{70}Al_2O_3P_4Rh]^+$ ($[M\text{-}Cl]^+$): 1244.00. Found: 1244.17. HRMS for $[C_{54}H_{54}Al_2O_6P_4Rh]^+$ (product of alkyl hydrolysis during injection) m/z calc: 1079.1557. Found: 1079.0964. See Appendices for further ESI-MS analysis.

[Rh(DPPP-OH)$_2$(CO)]Cl (5) To a stirred dichloromethane (5 mL) solution of $[Rh(CO)_2Cl]_2$ (55 mg, 0.14 mmol), DPPP-OH (249 mg, 0.58 mmol) in dichloromethane (5 mL) was added dropwise. The mixture was stirred at room temperature for 30 min before the solution was concentrated by vacuum to ~1 mL. The product was obtained via precipitation with pentane. The solid was dissolved in chloroform and layered with pentane (1/4 = v/v) to obtain a crystal for X-ray analysis. Low complex purity has prevented bulk characterization.

2.5.3. X-Ray Crystallography Data

A suitable crystal of each sample was selected for analysis and mounted in a polyimide loop. All measurements were made on a Rigaku Oxford Diffraction Supernova Eos CCD with filtered Cu-Kα radiation at a temperature of 100 K. Using Olex2,[122] the structure was solved with the ShelXT structure solution program using Direct Methods and refined with the ShelXL refinement package[123] using Least Squares minimization.

Chapter 3
Rhodium and Iridium NNO-Scorpionate Complexes: Synthesis, Structure, and Reactivity with Aluminum Alkyls

3.1 Introduction

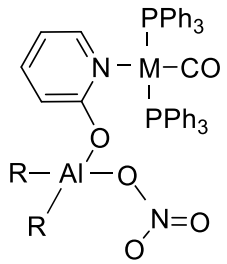

M = Rh: **I** R = ethyl: **a**
Ir: **II** isobutyl: **b**

Figure 3.1: Previously reported Rh/Al and Ir/Al heterobimetallics from Brewster et al.[107]

The Brewster lab recently reported the synthesis, characterization, and reactivity of a series of heterobimetallic Rh(I)/Al and Ir(I)/Al complexes wherein the metal centers are bridged by a simple, monodentate ligand, 2-pyridone (**Figure 3.1**).[107] While this series of complexes was found to be capable of facilitating hydrogen activation.[108] the long-term stability of the complexes prohibits their implementation in hydrogenation catalysis. One mechanism of decomposition, as determined by analysis of product mixtures, was found to be dissociation of the pyridone ligand from the transition metal center.[108] As a result, our recent efforts have focused on bridging ligands which bind the transition metal in a chelate fashion with the expectation that this binding mode will provide enhanced overall stability. As discussed in Chapter 2, a follow-up study in which the bridging ligand was changed to 1,3-bis(diphenylphosphino)-2-propanol was recently published.[124]

In this chapter, we describe our efforts to employ a different bridging ligand designed to form a bidentate N-N chelate at the transition metal, bis(3,5-dimethyl-pyrazol-1-yl)acetate **(NNO)**. Monometallic complexes of the NNO ligand with Ru(II), Rh(III), Ir(III), Pd(II) and Pt(II) are known in the literature.[125-130] However, the ability of NNO ligands to serve as a bridge in a heterobimetallic system has not been explored. We first describe the synthesis and characterization of a series of Ir and Rh NNO complexes. The oxidation state of the formed transition metal complex is found to be dependent on the protonation state of the NNO ligand during synthesis. Finally, we discuss the reactivity of our newly discovered Ir and Rh NNO complexes with aluminum alkyls.

3.2 Results and Discussion

3.2.1. Synthesis and Characterization of $[Rh(cod)NNO]_2$ and $[Ir(cod)NNO]_2$

Our laboratory commonly employs a "ligand first" synthetic strategy wherein an aluminum alkyl reagent is introduced to a pre-formed transition metal complex to form a heterobimetallic species. In that final step the aluminum alkyl interacts with a protic functionality installed in the transition metal complex ligand structure, releasing alkane gas and forming a new Al-X bond (X = N, O). Prior to this study, we had only explored the use of alcohols to form Al-O bonds but rationalized that carboxylic acids would be amenable to the reaction protocol. The resulting carboxylate could form either a κ^1 or κ^2-O,O complex at the aluminum center which may provide additional stability to the overall system.

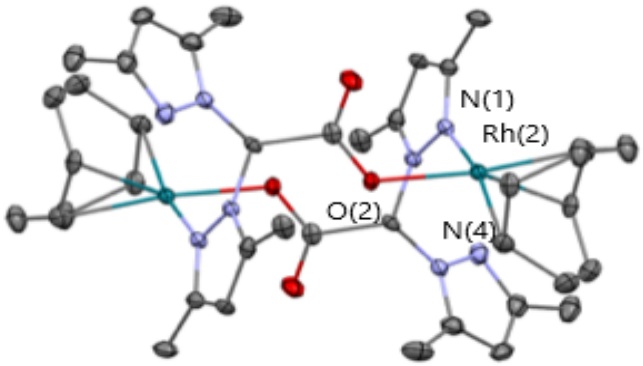

Figure 3.2. ORTEP representation of [Rh(cod)NNO]$_2$ **2**. Ellipsoids shown at 50% probability. Hydrogen atoms omitted for clarity. Selected bond lengths (Å): O(2)—Rh(2), 2.071; N(1)—Rh(2), 2.121; N(4)—Rh(2), 4.753.

Syntheses of low-valent rhodium and iridium-NNO complexes have not been previously reported. This is likely due, in part, to the high propensity of the ligand to undergo O-H oxidative addition when using the carboxylic acid precursor bis(3,5-dimethyl-pyrazol-1-yl)acetic acid **(NNO-H)**. Known rhodium or iridium NNO complexes show the ligand to bind the metal center in a κ^3-N,N,O fashion leading to the formal oxidation state of the metal being +3.[130] To avoid unwanted hydride formation and prevent oxidation of the metal center, we initially deprotonated NNO-H with potassium hydride to form potassium bis(3,5-dimethyl-pyrazol-1-yl) acetate [K-NNO] (**1**). Reacting **1** with [M(cod)Cl]$_2$ (M = Rh, Ir) in dichloromethane gives yield to new, low valent metal complexes [M(cod)NNO]$_2$ (M = Rh, **6** and M = Ir, **7)** formally in the +1 oxidation state, concomitant with precipitation of KCl. Newly obtained Rh(I) NNO and Ir(I)NNO complexes were fully characterized by ^{1}H NMR spectroscopy, ^{13}C{^{1}H} NMR spectroscopy, and High-Resolution Mass Spectrometry (HRMS).

The ^{1}H NMR spectrum of **6** and **7** show chemical shift resonances consistent with a highly symmetric species (see Figures B1 and B3 in Appendix B). The absence of two separate pyrazole proton peaks suggest that the two pyrazole rings are equivalent. This suggests that in

solution this complex most likely displays a similar structure to the known complex K[Pt(NNO)Me_2]; a monomeric species wherein the NNO ligand binds in a κ^2-N,N fashion.[129] $^{13}C\{^1H\}$ NMR data is also consistent with a solution formulation of C_s-symmetric monomer M(NNO)(cod).

An X-ray crystal structure was obtained for the rhodium variant, **6**, to gain further insight into its structure. Crystals were precipitated from a solution of **6** in dichloromethane with by layering with an excess of pentane. In the solid state, **6** presents as a dimeric, C_2-symmetric rhodium-rhodium structure. Each rhodium center is bound to two bridging NNO ligands, one via a pyrazole nitrogen and the other via a κ^1-carboxylate. The remaining pyrazole rotates 112.43° out of the ligand plane giving an internuclear Rh-N distance of 4.753 Å, much too long for a bonding interaction. The molecular geometry around the metal center preferentially remains square planar as would be expected for a d^8 rhodium(I) complex. Rh-N and Rh-O (2.121 Å & 2.071 Å, respectively) bonds are consistent with those found in the literature. The difference between the solid-state structure and that observed in solution is striking. Importantly, it demonstrates that the NNO ligand is sufficiently labile to rearrange prior to crystallization. The difference also stands in sharp contrast to the behavior of the analogous complex K[Pt(NNO)Me_2] which crystallizes as a monomer.[129] We ascribe this difference in reactivity to the presence of the potassium cation which effectively sequesters the carboxylate functionality and prevents dimerization. Unfortunately, X-ray quality crystals of **7** could not be obtained for direct comparison with **6**. As a result, we are unsure as to whether **7** dimerizes on precipitation or retains its solution form.

3.2.2. Synthesis and Characterization of [Ir(cod)NNO-H]$BArF_{24}$

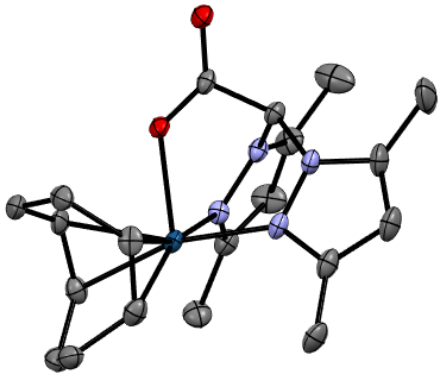

Figure 3.3. ORTEP representation of [Ir(cod)NNO-H]$BArF_{24}$ **8**. Ellipsoids shown at 50% probability. Hydrogen atoms and $BArF_{24}$ counterion omitted for clarity.

We then sought to further explore the reactivity of the NNO ligand with Ir. Reacting NNO-H with $[Ir(cod)_2]BArF_{24}$ gave the oxidative addition product [Ir(cod)NNO(H)]$BArF_{24}$ (**8**) in moderate yield. Formation of the hydride product is confirmed via ^{1}H-NMR spectroscopy; a diagnostic singlet resonance is observed at δ -15.95 ppm. The solid-state structure of (**8, Figure 3.3**) shows the NNO ligand bound in a κ^3 fashion to the iridium center. Interestingly, the hydride is located *trans* to the carboxylate functionality in the octahedral Ir(III) complex. This suggests that an ionic oxidative addition mechanism involving initial protonation of the metal center is likely to be in operation. Alternatively, dissociative ligand rearrangement following a traditional, concerted oxidative addition may occur rapidly, allowing for isomerization from the kinetic *cis* product to the thermodynamically preferred *trans* geometry.

3.2.3. Reactivity of NNO Complexes With Aluminum Alkyls

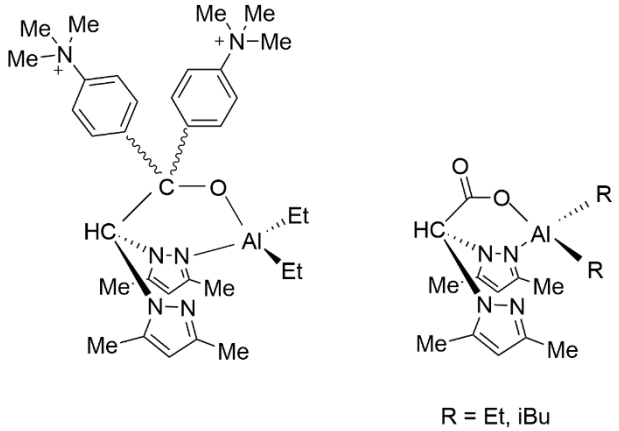

Figure 3.4. Representation of NNO binding to aluminum alkyls by Castro-Osma, Otero, and Lara-Sánchez et al.[131] (left) and proposed aluminum complex (right).

Our laboratory has had success in forming heterobimetallic Rh/Al and Ir/Al by reacting transition metal complexes bearing oxygen-containing ligands with aluminum alkyl precursors. While our previous efforts have relied on protonolysis of an aluminum alkyl to form the Al-O bond, we hypothesized that the oxophilicity of aluminum would be sufficient to form an Al-O bond from our neutral rhodium(I) and iridium(I) complexes. Unfortunately, reacting the dimeric complexes **6** and **7** directly with either triethyl or triisobutyl aluminum at room temperature did not yield the desired bimetallic, but rather resulted in the loss of the NNO ligand from the transition metal complex. The obtained products were investigated by mass spectrometry. We were able to identify the species $[(AlEtOH_2)NNO]^+$ (m/z = 321.1530, hydrolysis of one equivalent of aluminum alkyl occurs from injection port contamination), confirming that the aluminum center abstracted the NNO ligand from the late transition metal, forming the complex $Al(Et_2)(NNO)$. This is consistent with ligand lability observed in solution and with the inherent preference for the hard pyrazole and carboxylate ligands to bind to the hard aluminum center. The Al-NNO product is highly soluble in pentane and could not be isolated via precipitation, even at low temperature. It is also difficult to separate from triethylaluminum, added in excess during the reaction, which prevents us from reporting a yield for this process. However, the

iridium product precipitates from solution and does not contain any NNO ligand suggesting a near-quantitative reaction.

The identity of the aluminum product was further confirmed via independent synthesis. $Al(NNO)Et_2$ was synthesized directly by adding 1 equivalent of the triethylaluminum to 1 equivalent of NNO-H. High resolution mass spectral characterization of this material matched well with the species described above (m/z = 321.1524). Attempts to grow crystals of the NNO-aluminum complex from a saturated solution of pentane or diethyl ether have been unsuccessful, even at low temperature. However, based on data in hand we postulate that our obtained aluminum-NNO complex is structurally similar to an aluminum complex reported by Castro-Osma, Otero, and Lara-Sánchez et al.[131] where κ^3-N,N,O coordination through a single carboxylate oxygen and one nitrogen from each pyrazole is favored.

Additional attempts at synthesizing the target heterobimetallic complexes were then made. Notably, reaction of the iridium and rhodium precursors **6** and **7** with trialkylaluminum starting materials in dilute THF at -78°C resulted in similar decomposition of the metal complex. Based on this result, we conclude that dissociation of the NNO ligand from the late transition metal and chelation to aluminum is rapid and thermodynamically favored relative to the target bridged complex. Similarly, no other commercially available aluminum alkyls led to the formation of readily identifiable heterobimetallics. $AlEt_2Cl$ and Al^iPr_2Cl all facilitated the loss of the NNO ligand from the synthesized rhodium or iridium-NNO complex.

We then wanted to explore the difference in reactivity between Ir(I) precursor **7** and Ir(III) precursor **8.** As a direct comparison, **8** was reacted with both triethylaluminum and triisobutylaluminum. In both cases, reacting the metal hydride complex with trialkyl aluminum resulted in the immediate formation of the corresponding alkane gas indicating that the iridium

hydride is sufficiently acidic to facilitate alkyl protonolysis. Evaluation of the post-reaction ^{1}H-NMR spectrum indicates the loss of the hydride signal at (δ -15.95 ppm) and confirms that this reaction had occurred. Unfortunately, the ^{1}H NMR spectrum of the iridium-containing product also indicated loss of the NNO proton signals suggesting that, once again, the NNO ligand was abstracted from the transition metal center by the aluminum center.

3.3. Conclusion

Three new iridium and rhodium NNO complexes were synthesized and characterized by ^{1}H and ^{13}C{^{1}H} NMR spectroscopy, mass spectrometry and X-ray diffraction. Deprotonation of the NNO ligand prior to reaction with [M(cod)Cl$_2$] (M = Ir, Rh) led to Rh(I) and Ir(I) species **6** and **7**. In contrast, reacting NNO-H with [Ir(cod)$_2$]BArF$_{24}$ resulted in the formation of monomeric iridium (III) hydride complex, **8**. Reacting complexes **6**, **7**, and **8** with trialkylaluminum resulted in the abstraction of the NNO ligand from the metal complex. Chelation of the NNO ligand to aluminum is, thus, thermodynamically favored over a bridging late transition metal—aluminum bimetallic complex.

3.4 Experimental Section

3.4.1. General Considerations

Syntheses and manipulations were performed in a nitrogen-filled Inert Technologies glovebox or using standard Schlenk techniques unless otherwise specified. Deuterated solvents were purchased from Cambridge Isotope Laboratories, dried over molecular sieves and stored in the glovebox over molecular sieves prior to use. All other reagents and solvents used were commercially available and used without further purification unless specified. [Rh(cod)Cl]$_2$ and [Ir(cod)Cl]$_2$ were prepared according to standard literature procedures.[132,133] Bis(3,5-dimethyl-pyrazol-yl) acetate (NNO-H) was prepared by an adaptation of the literature procedure provided

by Reger.[134] Potassium bis(3,5-dimethyl-pyrazol-yl) acetate (K-NNO) was prepared according to literature procedures provided by Goldberg.[129] $[Ir(cod)_2]BArF_{24}$ was prepared from literature procedures reported by Bower.[135] $NaBArF_{24}$ was synthesized by the method of Bergman[119] and purified using the modification reported by Peters.[120] Aluminum reagents were purchased from commercial sources and stored in a nitrogen glovebox prior to use. ^{1}H NMR and $^{13}C\{^{1}H\}$ NMR spectra were recorded on a 400 MHz JEOL spectrometer and referenced to the residual solvent peak.[121] High resolution mass spectra were obtained on a Waters Synapt High Resolution Mass Spectrometer.

3.4.2. Synthesis

[Rh(cod)NNO] (**6**) - Solid $[Rh(cod)Cl]_2$ (101 mg, 0.205 mmol) was added to a solution of K-NNO (117 mg, 0.410 mmol) in 5 mL of dichloromethane and stirred for 24 hours inside the glovebox at room temperature. The golden solution was filtered directly into a 20 ml vial through a Celite-packed polyethylene frit. The product was obtained by precipitation with pentane. Crystals suitable for X-ray analysis were obtained by layering the dichloromethane solution with excess pentane (v:v, 1:3) at room temperature. Yield: 139 mg, 74 %. ^{1}H NMR (400 MHz, CD_2Cl_2) δ 6.34 (s, 1H), 5.90 (s, 2H), 4.48 (bs, 4H), 2.54 (m, 4H), 2.33 (s, 12H), 1.78 (m, 4H). $^{13}C\{^{1}H\}$ NMR (101 MHz, CD_2Cl_2) δ 151.00, 142.56, 107.89, 81.95, 81.81, 70.26, 30.36, 14.80, 11.74. (absence of carboxylate carbon due to slow relaxation). HRMS calculated for $[C_{28}H_{39}Rh_2N_4O_2]^+$ (Loss of NNO ligand occurs at the lowest ionization energy) ($M\text{-}NNO^+$) *m/z* calc.: 669.1183. Found: 669.1194.

[Ir(cod)NNO] (**7**) - Solid $[Ir(cod)Cl]_2$ (104 mg, 0.155 mmol) was added to a solution of K-NNO (89 mg, 0.311 mmol) in 5 mL of dichloromethane and stirred for 24 hours inside the glovebox at room temperature. The golden solution was filtered directly into a 20 ml vial through a Celite-

packed polyethylene frit. The solid product was then obtained by precipitation with pentane. Yield: 111 mg, 65 %. ^{1}H NMR (400 MHz, CD_2Cl_2) δ 6.24 (s, 1H), 6.01 (s, 2H), 4.28 (bs, 4H), 2.43 (s, 6H), 2.37 (s, 6H), 2.32 (m, 4H), 1.52 (m, 4H). $^{13}C\{^{1}H\}$ NMR (101 MHz, CD_2Cl_2) δ 151.00, 142.56, 107.89, 81.95, 81.81, 70.26, 30.36, 14.80, 11.74. HRMS calculated for $[C_{20}H_{27}IrN_4O_2]^+$ ($M+H^+$) *m/z* calc.: 548.1763. Found: 547.1816.

[Ir(cod)NNO(H)]BArF$_{24}$ (8) - Inside the glovebox, **8** was prepared by adding solid NNO-H (59.4 mg, 0.240 mmol) to a dark purple solution of $[Ir(cod)_2]BArF_{24}$ (304 mg, 0.239 mmol) in dichloromethane. The solution changed instantly from dark purple to golden yellow. The solution was allowed to stir for 3 hours at room temperature inside the glovebox. The volume was reduced to ~1 mL of solvent. The solid product was then obtained by precipitation with diethyl ether. Crystals suitable for X-ray analysis were obtained by layering the dichloromethane solution with excess diethyl ether (v:v, 1:3) at -35°C overnight under nitrogen atmosphere. Yield: 203 mg, 60%. ^{1}H NMR (400 MHz, CD_2Cl_2) δ 7.71 (br s, 8H), 7.55 (br s, 4H), 6.45 (s, 1H), 6.08 (s, 2H), 5.66 (m, 2H), 4.86 (m, 2H), 2.91-2.81 (m, 2H), 2.71-2.61 (m, 2H), 2.43-2.45 (m, 8H), 2.33 (s, 6H), 1.98 (m, 2H), -15.95, (s, 1H). $^{13}C\{^{1}H\}$ NMR (101 MHz, CD_2Cl_2) δ 162.70, 155.23, 144.85, 135.23, 129.14, 126.33, 123.62, 117.88, 110.61, 91.63, 87.11, 69.28, 32.78, 27.74, 16.22, 11.71. $^{19}F\{^{1}H\}$ NMR (376 MHz, CD_2Cl_2) δ -62.78. HRMS calculated for $[C_{20}H_{28}IrN_4O_2]^+$ *m/z* calc.: 549.1841. Found 549.1823.

3.4.3. Procedures for Reactions with Aluminum Alkyl Reagents

Attempt 1: Inside the glovebox, approximately 100 mg of **6**, **7**, or **8** was dissolved in 10 mL of THF at room temperature. One equivalent of $AlEt_3$ or Al^iBu_3 was added via a microliter syringe. The solution turned dark immediately. Solvent was removed in vacuo and the solid produced

was washed with pentane. The products were dried and analyzed by NMR spectroscopy. The pentane layer was analyzed by High Resolution Mass Spectrometry.

Attempt 2: Inside the glovebox, approximately 100 mg of **6**, **7**, or **8** was dissolved in 10 mL of THF and cooled to -78°C using a dry ice/acetone bath. One equivalent of $AlEt_3$ or Al^iBu_3 was added via a microliter syringe. The flask was removed from the dry ice/acetone bath and allowed to warm to room temperature. Upon warming to room temperature, the solution turned orange and then dark immediately. Solvent was removed in vacuo and the solid produced was washed with pentane. The products were dried and analyzed by NMR spectroscopy.

Attempt 3: Inside the glovebox, approximately 100 mg of **6**, **7**, or **8** was dissolved in 10 mL of THF and placed inside the cryochamber. One equivalent of Al^iBu_3 dissolved in 5 mL of THF was layered on top of the frozen solution. The flask was removed from the cryochamber and allowed to warm to room temperature. Upon warming to room temperature, the solution turned orange and then dark immediately. Solvent was removed in vacuo and the solid produced was washed with pentane. The products were dried and analyzed by NMR spectroscopy.

Attempt 4: Inside the glovebox, approximately 15 mg of **6**, **7**, or **8** was dissolved in 500 μL of CD_2Cl_2 at room temperature. One drop of Al^iBu_3 was added using a 10 μL syringe. The solution turned dark immediately. The solution was immediately analyzed by NMR spectroscopy.

Attempt 5: Inside the glovebox, approximately 34 μL of $AlEt_3$ was added dropwise to a solution of NNO-H (63 mg) in 5 mL of THF. Gas evolution was immediate, and the solution was allowed to stir at 1 hour at room temperature. The solution was analyzed by High Resolution Mass Spectrometry.

3.4.4. X-Ray Crystallography Data

A suitable crystal of each sample was selected for analysis and mounted in a polyimide loop. All measurements were made on a Rigaku Oxford Diffraction Supernova Eos CCD with filtered Cu-Kα radiation at a temperature of 100 K. Using Olex2,[122] the structure was solved with the ShelXT structure solution program using Direct Methods and refined with the ShelXL refinement package[123] using Least Squares minimization.

Chapter 4

Activation of CO_2 Demonstrated by Aluminum Complexes Ligated by 2-Substituted Pyridines

4.1 Introduction

The effect of greenhouse gases in the atmosphere has been an important topic of discussion for many years in media, politics, and the science community worldwide.[137,138] The concentration of atmospheric carbon dioxide has increased remarkably since the onset of the industrial revolution and continued increase in concentration of this greenhouse gas will have long lasting effects on climate and the natural environment.[139] The increase in CO_2 concentration is largely due to combustion of fossil fuels for energy purposes. Efforts to quell the rising tide of CO_2 emission has led to extensive research into alternative energy sources,[140] carbon capture technology,[141] and biomass utilization.[142] While the direct effect on atmospheric CO_2 levels may be negligible, the possibility of using CO_2 as a chemical feedstock is intriguing.[143] CO_2 presents an readily available, environmentally friendly alternative to the use of CO as a C_1 source,[144,145] which is commonly produced in the energy intensive processes of coal gasification[146] or methane steam reforming.[147] Unfortunately, the utilization of CO_2 as a chemical feedstock has proven to be problematic due to its thermodynamic stability and the relative kinetic inertness of the small molecule.[143,148,149] Processes that involve CO_2 typically require highly reactive substrates or severe reaction conditions, limiting the scope of desired transformations.

In nature, the Mg-containing Rubisco enzyme catalyzes CO_2 fixation during the Calvin Cycle.[150] Inspired by biological precedent, intense focus has been given to the development of organometallic catalysts that can insert CO_2 into metal-ligand bonds to generate chemically useful materials such as carbonates,[151,152] carbamates,[153,154] and carboxylic acids.[155] CO_2 has

been observed to insert into the metal-alkyl bond of several *d*-block transition metal alkyl complexes and mono-metallic (M = Al, Fe, Zn, In, Co, Ru, Mn) porphyrin systems.[156-162]

Of particular interest to the Brewster lab is the reactivity of aluminum complexes with CO_2, as the high Lewis acidity and oxophilic nature of the aluminum center make it likely to interact favorably with the substrate. In fact, the ability of CO_2 to insert into simple aluminum alkyls has been known since the 1960s, though not widely explored.[163-165] These early examples were neither particularly efficient nor selective, but nonetheless demonstrated the potential of aluminum-based complexes for CO_2 fixation.

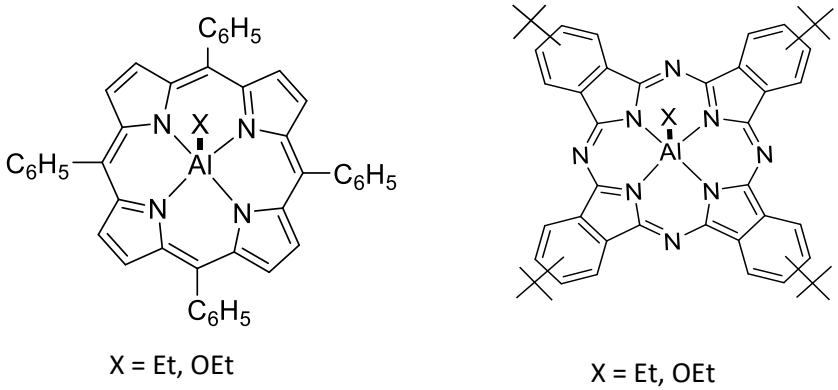

Figure 4.1. Aluminum porphyrins reported by Inoue and coworkers[156] (left) and Kusaga and coworkers[162] (right).

Alternative complex platforms have been pursued to increase yield and specificity in aluminum-promoted CO_2 insertion reactions. The earliest report of a migratory CO_2 insertion into alkyl groups appended to a metalloporphyrins was demonstrated by Inoue and coworkers using (tetraphenylporphinato)aluminum ethyl ((TPP)AlEt) or (tetraphenylporphinato)aluminum alkoxide ((TPP)AlOR) (Figure 4.1, left).[156] In this system, the respective carboxylate or carbonate product is generated in the presence of visible light and 1-methylimidazole (MeIm) at room temperature. Kusaga and coworkers also demonstrated migratory CO_2 insertion at room temperature to yield carbonate species by photoexcitation of an aluminum porphyrin using

visible light and a tenfold excess of external base (Figure 4.1, right).[162] Conversion to the target carbonate product was found to increase with increased temperature; however, this reaction also does not proceed without photoinduction and/or external base.

More recently, aluminum-containing Frustrated Lewis Pairs (FLPs) have also been observed to react productively with CO_2. Menard and Stephan demonstrated the successful capture and reduction of CO_2 at room temperature using sterically bulky phosphines in combination with aluminum trihalides, providing an alternate reduction pathway to form CO or methanol.[166] Other complexes containing an aluminum metal center have been shown to activate CO_2. For example, Aldridge et al. have reported the synthesis of various β-diketiminate stabilized aluminum hydrides [(Nacnac)Al(R)H ; R = Me, Et , Cl, OTf], that demonstrate facile CO_2 insertion into the Al-H bond when R is an electron donating group (See Section 1.5.1).[45]

The Brewster lab is interested in developing bimetallic late transition metal-aluminum heterobimetallic complexes in which the late transition metal (LTM) center can function as a Lewis base for cooperative activation of substrates; reaction methodology highly reminiscent of Frustrated Lewis Pair (FLP) of Stephan noted above. This metal-metal cooperative activity has been observed previously in systems developed by Bourissou,[92] Iwasawa,[94] Nakao,[95,96] and Cramer.[168] Of particular interest to us was the report from Iwasawa, in which a Pd-Al Z-type complex catalyzed the hydrosilylation of CO_2 under 1 atm. CO_2 with a turnover frequency (TOF) of 19300 h^{-1}, making it among the most efficient known catalysts for this transformation.[94] Our laboratory designed a series of rhodium-aluminum and iridium-aluminum analogs of Vaska's complex, $[M(PPh_3)_2(CO)(2\text{-pyridone-}AlR_2)][NO_3]$ (M = Rh, Ir; R = ethyl, isobutyl) (See Figure

3.1)[107] with the thought that they, too, would be able to cooperatively activate small molecules. These complexes have since been shown to facilitate hydrogen activation and hydrogenolysis.[108]

Control reactions using complex **9** led us to discover a series of simplified (Figure 4.2), monometallic aluminum complexes which also facilitate CO_2 functionalization. In the case of **10a**, insertion into an aluminum-alkyl bond was observed. Joint experimental and computational mechanistic studies suggest that CO_2 activation occurs via a cooperative pathway in which a nitrogen atom from an associated pyridine works in tandem with the aluminum center to trap the CO_2 molecule.

4.2 Results and Discussion

4.2.1. Reactivity of Heterobimetallic LTM-Aluminum Complexes with CO_2

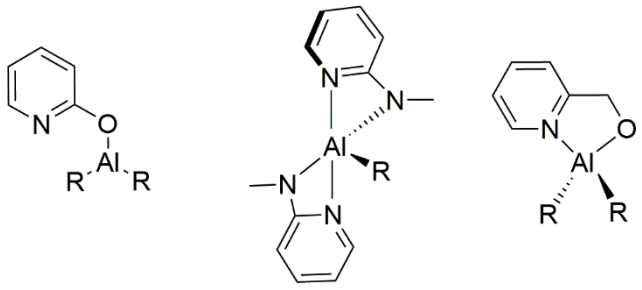

9 **10** **11**

R = ethyl (**a**), isobutyl (**b**)

Figure 4.2. Ligated aluminum complexes (**9a-11b**).

We first set out to investigate the reactivity of $[M(PPh_3)_2(CO)(2\text{-pyridone-}AlR_2)][NO_3]$ (M = Rh, Ir; R = ethyl, isobutyl) with CO_2. After bubbling CO_2 through a benzene solution of the bimetallic complex, we were excited to see that a small degree of thermal insertion of CO_2 into the aluminum alkyl occurred. Insertion was confirmed by the presence of a new signal in the ^1H NMR spectrum between δ 3.7-3.6 ppm. This signal, a quartet for reactions of **Ia** and **IIa**, and a doublet for reactions of **Ib**, and **IIb** (See Chapter 3, Figure 3.1), is assigned to the methylene

protons originating from an ethyl ligand to aluminum or isobutyl ligand to aluminum, respectively, that has undergone an insertion process. It was later discovered via independent synthesis that the newly formed signal corresponds to an alkoxide generated from CO_2 after extrusion of CO (*vide infra*). Unfortunately, the reaction yield, as determined by ^1H NMR integration, was quite low (<5%) and a considerable amount of an unknown precipitate was formed. With a thought to improve reaction efficiency, we began to investigate the mechanism.

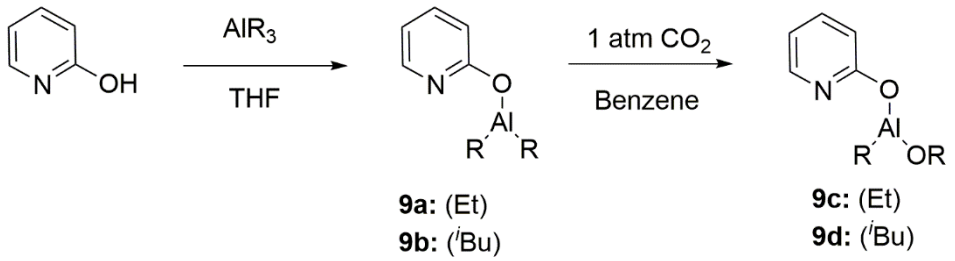

Figure 4.3. Formation of Al-pyridone-aluminum—alkoxide complex.

We first sought to validate our heterobimetallic design by demonstrating the role of both metals in the reaction. To do so, we reacted 2-pyridone-[AlR_2] (R = ethyl, isobutyl; **9a** and **9b**, Figure 4.3) with CO_2. We were surprised to observe the same downfield alkyl signal in the ^1H NMR spectrum (*vide infra*), indicating that insertion of CO_2 had occurred in the absence of the LTM center. Further computational investigation into potential bimetallic activation pathways confirmed that the transition metal center does not participate in the activation of CO_2, rather that insertion in our bimetallic system most likely occurs after the dissociation of the organo-aluminum moiety from the transition metal complex and without involvement of the LTM. Excitingly, while our bimetallic system does not react as initially designed, through careful control experiments we have been able to demonstrate a unique example of CO_2 insertion into a cheaper, more easily synthesized monometallic aluminum alkyl species. The remainder of this

chapter will discuss our efforts to expand upon this reactivity and understand the mechanism of CO_2 insertion in our monometallic systems.

4.2.2. Synthesis of Monometallic Aluminum Complexes

Monometallic aluminum systems reported on here are derivatives of 2-pyridone-[AlR_2]. Each complex contains one or two alkyl ligands at aluminum and one or two 2-substituted pyridines as supporting ligands. Syntheses of 2-pyridone[$AlEt_2$]**(9a)** and 2-pyridone[Al^iBu_2]**(9b)** were accomplished using a modification of the literature procedure reported by Barron et. al.[169] One equivalent of solid 2-pyridone was added to one equivalent of trialkyl aluminum ($AlEt_3$ or Al^iBu_3) diluted in THF at room temperature (**Figure 4.3**). Similarly, treatment of 2-(methylamino)pyridine (2.05 equivalents) with one equivalent of trialkyl aluminum at room temperature yields the di-amino pyridine-ligated aluminum alkyl complex (**10a** and **10b**) in 55-80% yield. Attempts to synthesize and isolate the monomeric aminopyridine-aluminum complexes directly analogous to **9a** and **9b** were then made. However, when the synthesis is repeated with a 1:1 ratio of aminopyridine to aluminum, analytically pure di-ligated products **10a** and **10b** are still obtained following recrystallization. This implies that the second addition of aminopyridine is rapid. Recrystallization of **9b, 10a,** and **10b** using a concentrated solution of each in pentane -35°C allowed for recovery of pure white solids and the formation of X-ray quality crystals. Each complex has been characterized by standard spectroscopic and analytical techniques (See Appendix C), and their molecular structures determined by X-ray crystallography (Figure 4.4).

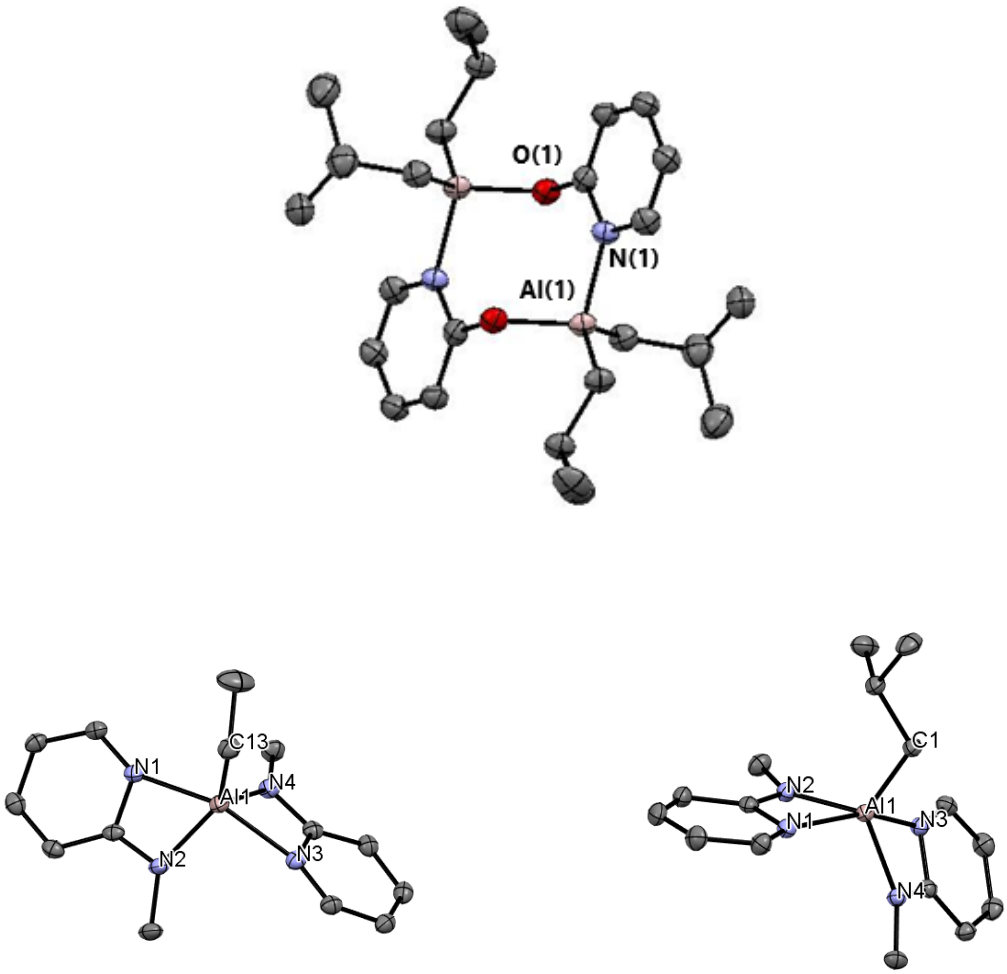

Figure 4.4. ORTEP representation of **9b** (top), **10a** (left), and **10b** (right). Ellipsoids shown at 50% probability. Hydrogen atoms omitted for clarity. Select bond distances Å and angles (deg): (**10a)** $N(1)_{pyridine}$-Al(1) 2.06(9), $N(3)_{pyridine}$-Al(1) 2.11(0), N(2)-Al(1)-N(4) 119.33, C(13)-Al(1)-N(4) 117.26, C(13)-Al(1)-N(2) 123.23. (**10b)** $N(1)_{pyridine}$-Al(1) 2.085, $N(3)_{pyridine}$-Al(1) 2.088, N(2)-Al(1)-N(4) 119.03, C(1)-Al(1)-N(2) 119.88, C(1)-Al(1)-N(4) 121.09.

10a and **10b** are found to be monomeric in the solid state. The molecular geometry about aluminum is that of a distorted trigonal bipyramid (**Figure 4.4, left** and **right)** where the sum of the equatorial angles (C13, N2, and N4, and C1, N1 and N3 occupy equatorial positions in **10a** and **10b**, respectively) about aluminum in **10a** and **10b** are 359.82° and 360°. In contrast, **9b** in

Figure 4.4 crystallizes to yield a dimeric solid-state structure. As expected for a tetradentate Al(III) complex, a distorted tetrahedral geometry around is observed about each aluminum center. Two distinct 2-pyridone ligands bridge between two $Al(iBu)_2$ moieties, resulting in an eight membered cyclic structure. Similar pyridone-aluminum alkyl structures have been reported by Barron and coworkers.[169] The Al(1)-O(1) and Al(1)-N(1a) bond lengths observed in our structure of **9b** (1.978 Å and 1.805 Å, respectively) are comparable to those previously reported. In the case of **9a**, ^{1}H-NMR evidence at room temperature is consistent with a dynamic structure. The ethyl groups are found to be chemically equivalent, as opposed to diastereotopic which one would expect for a static tetrahedral dimer. This stands in sharp contrast to the diastereotopic alkyl resonances observed for **IIa** and **IIb**, which are known to exist as monomers tetrahedral about aluminum both in the solid state and solution.[169]

4.2.3 Reactivity of Monometallic Aluminum Complexes with CO_2

We then set out to investigate, in detail, the reactivity of CO_2 with 2-substiuted pyridine-aluminum alkyls. We tested the reactivity of each complex (**9a-10b**) with 1 atm of CO_2 at room temperature. Each complex reacted productively, though the exact nature of the eventual product was dependent on the substituent located at the two position of the pyridine and the alkyl group employed.

As mentioned above, we began our investigation into monometallic aluminum complexes with 2-pyridone ligated complexes **9a** and **9b**. Two methods were employed in testing: 1) bubbling CO_2 through a solution of the pyridonate complex dissolved in 600 μL of benzene-d_6 in a screw-cap NMR tube for 5 minutes, and 2) dissolving the pyridonate complex in 5 mL of anhydrous benzene in a Schlenk flask and passing dry CO_2 through the flask (1 atmosphere) for 5 minutes before sealing the flask and stirring vigorously for 24 hours. In either case, the

formation of a new species (**9c** or **9d**) (**Figure 4.3**) can be observed in the ^{1}H-NMR spectrum. The product is readily identifiable from a diagnostic signal of appropriate multiplicity (quartet for ethyl precursors, doublet for isobutyl precursors) between δ 3.71 and δ 3.68 ppm in the ^{1}H-NMR spectrum. The weak intensity of this signal suggests that product formation proceeds slowly at room temperature. To distinguish whether the observed products **9c** and **9d** are carboxylates (resulting from direct CO_2 insertion into the aluminum alkyl) or alkoxides (resulting from insertion followed by loss of CO), 1 equivalent of the appropriate alcohol was reacted with 1 equivalent of the aluminum pyridonate precursor. Identical chemical shifts with appropriate multiplicities were identified for each of the new species, suggesting that the observed products are alkoxides. As further supporting evidence, reaction of **9a** and **9b** with isotopically labelled $^{13}CO_2$ (δ 124 ppm reference) did not yield a signal in the ^{13}C NMR spectrum consistent with ^{13}C incorporation into the final product. This leads us to believe that the formation of the alkoxy occurs via insertion of CO_2, followed by decarbonylation. Unfortunately, we were not able to directly observe the formation of the ^{13}CO byproduct due to the low yield for production of alkoxide (~ 1% by ^{1}H-NMR integration) and transfer of CO_2 to the head space of the NMR tube. Finally, based on our independent synthesis, we believe that the reaction terminates after a single insertion of CO_2 to form alkoxide. Oxygen-ligated alane complexes have been shown to decrease in electrophilicity as the number of oxygen atoms bound to aluminum increases. This is no doubt due to the π-donor character of the oxygen-bound ligand. In our case, the consequence of decreased electrophilicity is an inability to react further with CO_2. Attempts to increase the yield of the alkoxide product through extended reaction times at increased temperature, unfortunately, proved fruitless. Solutions of **9a** and **9b** were heated to 80 °C for 5 days and no observable increase to yield of **9c** and **9d** was observed.

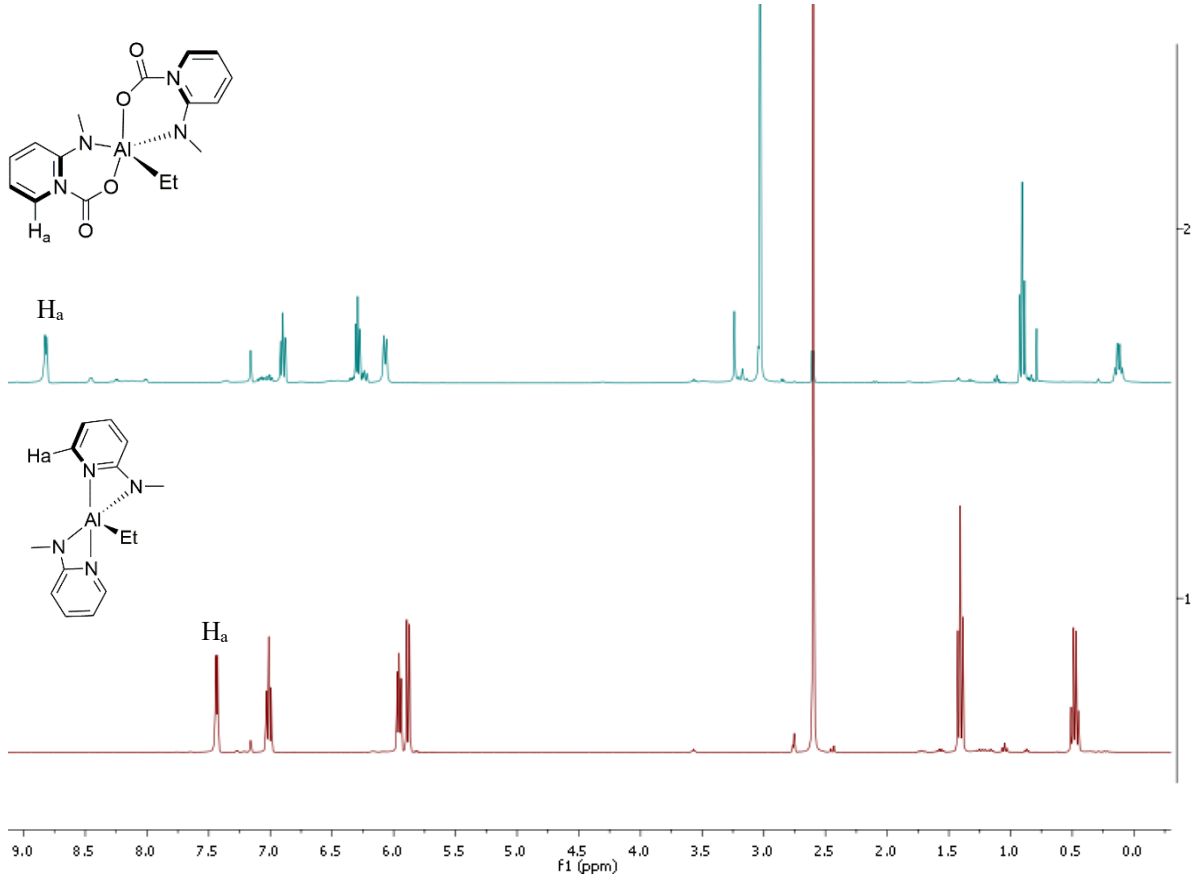

Figure 4.5. Stacked ^{1}H-NMR spectrum representative of **10a** (bottom) and *in situ* generation of **10c** (top) in benzene-d_6. Spectra referenced to residual solvent peak.

To investigate the generality of our observed reaction we then turned our attention to aminopyridine derivatives **10a** and **10b**. Bubbling CO_2 for 5 minutes through a solution of **10a** or **10b** dissolved in 600 µL of benzene-d_6 in a screw-cap NMR tube led to the clean formation of a new species in high NMR yield after 90 minutes. Though we have not been able to isolate this product in the solid state, spectroscopic evidence suggests that the obtained product is a cyclic carbonate resulting from CO_2 insertion into the Al-$N_{pyridine}$ bond rather than an alkyl insertion product. Initial evidence for the formation of this product derives from ^{1}H NMR spectroscopy. The methylene signal attributed to the ethyl group remains in the far upfield region (δ 0.10 ppm) associated with carbon ligands directly bound to electropositive atoms. Additionally, pyridine

proton H_A (**Figure 4.5**) shifts dramatically downfield from δ 7.5 ppm to δ 8.8 ppm. This suggests that the pyridine moiety is the most likely site of the observed reaction.

Further evidence for the identity of **10c** and **10d** the product was obtained from ^{13}C NMR spectroscopy. A new downfield peak, observed at δ 154 ppm in the ^{13}C-NMR spectrum, is indicative of the corresponding carbamate product. This peak is enhanced when the reaction is undertaken with isotopically labelled $^{13}CO_2$ suggesting that it must derive from CO_2 insertion. HMQC and HMBC data further supports the pyridine as the site of insertion (see Appendix C). In the HMBC, No proton-carbon coupling between the carbon signal at δ 154 ppm and the alkyl -CH_2 proton resonances located at approximately δ 0.6 ppm are apparent in either spectrum further indicating that the alkyl-aluminum moiety is not the site of direct insertion (See Appendix C24 for **10c** and C37 for **10d**).

In an attempt to observe further reactivity beyond cyclic carbonate formation, we monitored the reaction progress with isotopically labelled $^{13}CO_2$ over extended times. After 48 hours, a new, isotopically enhanced, peak was observed to appear at δ 173 ppm in the ^{13}C-NMR spectrum. We suspect that this new peak arises from an alkyl migration from the aluminum center to the electrophilic carbon to form an aluminum bound propionate. After 72 hours, the new carbonyl peak remains prominent in the ^{13}C-NMR suggesting the compound is stable at room temperature and does not decarbonylate to produce the alkoxide. The stability of this compound is supported by our computational investigation, where the migration or decarbonylation of the carboxylate to form the alkoxide was found to be energetically disfavored (*vide infra*).

Subjecting the isobutyl derivative **10b** to similar reaction conditions does not yield the corresponding butanoate. The carbamate remains stable for several days (96 hours monitored by

^{1}H & ^{13}C-NMR) before the complex degrades into an undesirable side product. Upon analysis of the product spectra, we believe that the eventual decomposition product is the hydrolyzed form of the aluminum carbamate species (See Appendix C). To verify this hypothesis, we intentionally reacted the generated carbonate with 10 μL of water and compared the resultant ^{1}H NMR spectrum with that of the final decomposition product (Appendix C, C39 and C40). A distinct doublet located at δ 8.21 ppm serves as a diagnostic resonance for the hydrolysis product. This directly matches a resonance observed in our CO_2 insertion experiments 5 hours after the addition of CO_2 (~ 13% by ^{1}H-NMR integration). Additionally, the appearance of a doublet located at δ 0.86 ppm corresponding to the methyl protons of isobutane increases over the course of our CO_2 insertion experiments indicating hydrolysis of the alkyl is occurring over time. Reaction of aluminum alkyls with adventitious water is well known to occur rapidly under most conditions, thus slow contamination of our reaction mixture through the NMR septum cap would be expected to result in formation of this byproduct over time.

The combined results from the reactions described above led us to hypothesize a mechanistic theory as to how CO_2 inserts into 2-substituted pyridine ligated aluminum alkyls. First, pyridine dissociates from the aluminum center. This is quite likely due to the geometrically strained 4-membered ring formed on κ^2 binding of 2-pyridone or 2-methylaminopyridine. As mentioned above, spectroscopic evidence for pyridine lability derives from the alkyl protons of **9a** and **9b** being equivalent rather than diastereotopic in the ^{1}H NMR spectrum. Following pyridine dissociation, CO_2 is cooperatively activated to generate a cyclic carbamate at the sterically congested aluminum center created by the two methylaminopyridine ligands. This cooperative reactivity is reminiscent of that described by Stephan for Al-P FLPs.[167]

In contrast, the sterically open environment about the 2-oxypyridine congener facilitates insertion into the alkyl ligand.

To further support our mechanistic hypothesis, we synthesized **11a** and **11b**. Similar to complexes reported by Barron et. al.[169] the pyridinemethanol ligands employed in **11a** and **11b** are expected to form 5-membered rings on chelation to aluminum. This favorable, unstrained geometry is not expected to be labile under our reaction conditions, thereby preventing cooperative CO_2 activation. As evidence for a static structure, the alkyl ligands are found to be diastereotopic in the ^{1}H NMR spectra of **11a** and **11b**. Gratifyingly, exposure of **11a** and **11b** to CO_2 by the methods previously described resulted in no observable change in the ^{1}H-NMR spectrum.

4.2.4 Computational Investigation

To further elucidate the observed reactivity, a computational study was undertaken to investigate potential CO_2 insertion pathways for **10a**. A variety of mechanisms were investigated. The primary variable involved order of CO_2 insertion – into which ligand is insertion favored? Pathways for CO_2 migration between ligands were also considered, though no transition states could be located computationally. Thus, the computed pathways (Figure 4.6) involved (1) insertion of CO_2 into the alkyl, followed by insertion into the pyridine to form a carbamate, (2) insertion into a single pyridine ligand followed by insertion into the alkyl, followed by insertion into the second pyridine, and (3) insertion into successive pyridine ligands followed by insertion into the alkyl. Experimental evidence strongly suggests against pathways 1 and 2. The intermediate formed following insertion of CO_2 into two pyridine ligands has been observed spectroscopically (complex **10c**), though if carbamate formation were reversible these pathways could be accessible.

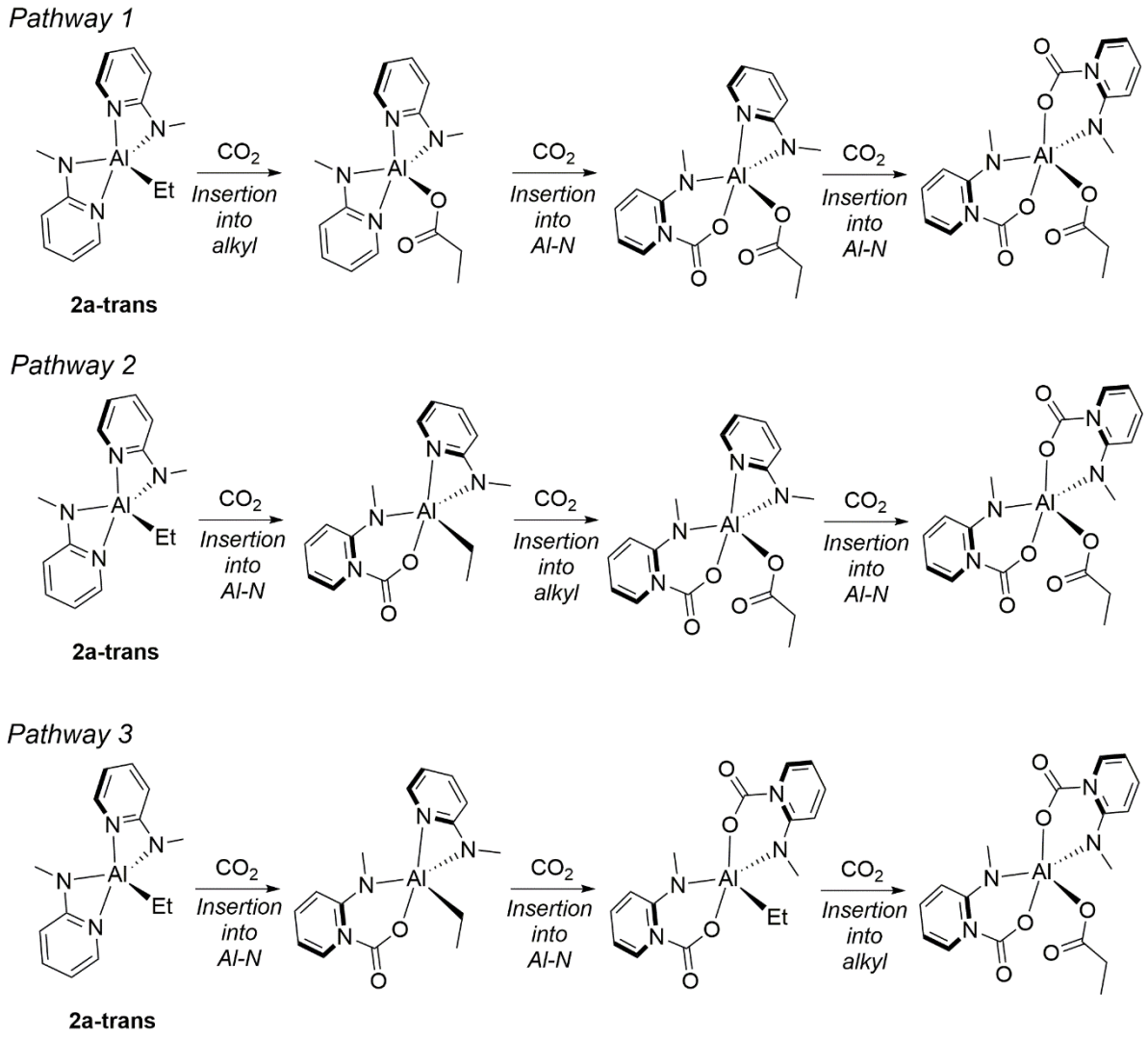

Figure 4.6. Computed reaction pathways for sequential CO_2 insertion into complex **10a.**

Further complicating our ability to propose a chemical mechanism for CO_2 insertion is the ability of the aluminum complex to stereochemically isomerize. The pyridine nitrogen atoms can exist in the two axial positions of the trigonal bipyramid (**10a-trans**, as seen in the crystal structure of 2a), 2 equatorial positions, or one axial and one equatorial (**10a-cis**). In solution, the two methylaminopyridine ligands are found to be chemically equivalent on the NMR timescale, but this does not preclude rapid isomerization from occurring. In Figure 7, the optimized 3D structure of **10a-trans** and **10a-cis** are shown. Theoretically, **10a-cis** is only 2.2 kcal/mol higher

in free energy than **10a-trans**. In Figure 4.8, a free energy diagram is provided, showing that the **10a-trans** form can isomerize to **10a-cis** through a high-energy intermediate (**10a-i)**. The rate-limiting step has a barrier of 12.6 kcal/mol, and the reverse activation free energy from **10a-cis** to **10a-i** is 9.0 kcal/mol. Accordingly, this interconversion should be rapid at the experimental conditions.

Though incompatible with our observed NMR data, "cis" versions of CO_2-inserted intermediates have also been identified computationally for completeness. The cis version of the final product is only 1.9 kcal/mol higher in free energy than complex **10a**. For brevity, we have opted to avoid mapping out the complete reaction network of proposed cis/trans interconversion mechanisms. Unlike studies where examination of the full reaction network contributes greatly to an understanding of the observed kinetics and thermodynamics,[170,171] the ability of the various stereoisomeric forms of each complex to interconvert is simply assumed to be possible. The lowest energy "trans" complexes accurately reflect the experimental data and are presented in detail below.

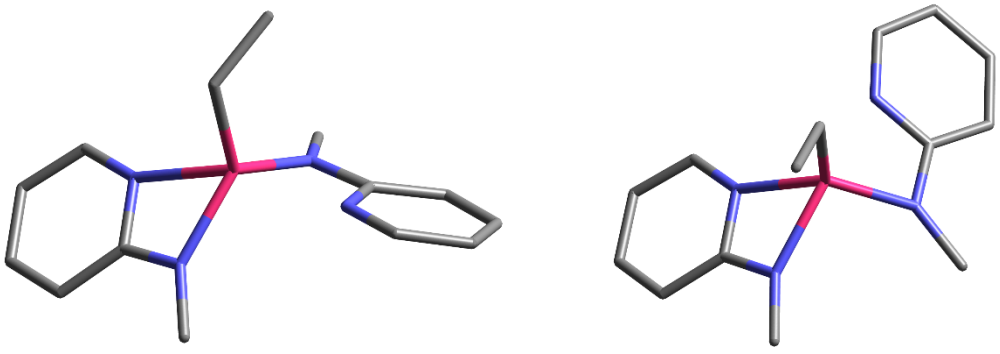

Figure 4.7. Computational structures of **10a** (left) and its counterpart **10a-cis** (right), where the methyl substituents of the aminomethylpyridine are sterically unfavored.

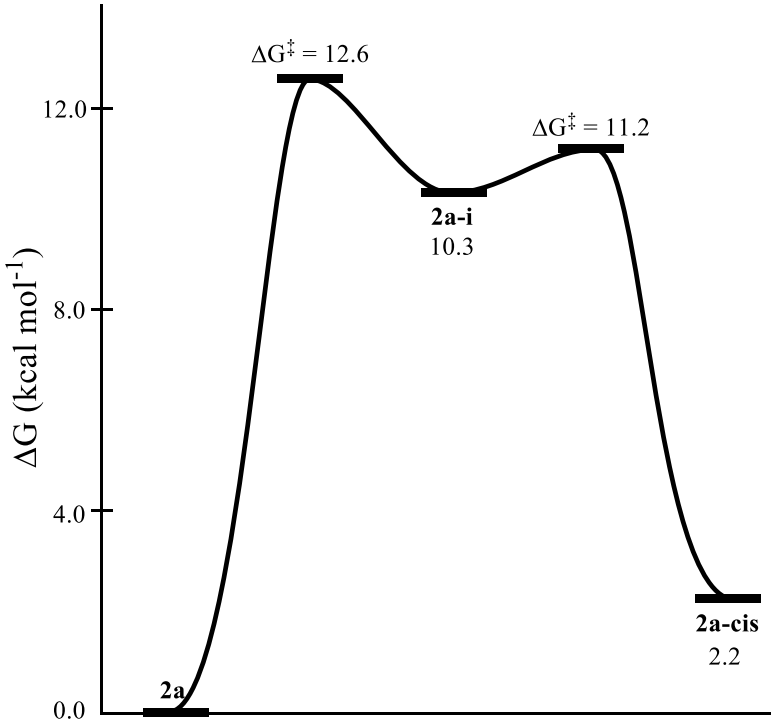

Figure 4.8. Free energy diagram of proposed isomerization of reactant **10a** from trans to cis form. The reference free energy (in kcal/mol) is that of the **10a** structure.

Computations on complex **10a** suggest that at each insertion step, insertion into the alkyl was found to have a higher barrier than cooperative activation to form the carbamate, which computationally rules out proposed pathways 1 and 2. The trajectory of approach of the CO_2 toward the sterically crowded aluminum center must be more open for the cooperative, FLP-like activation. Thus, pathway 3 was found to be the most likely to be in operation.

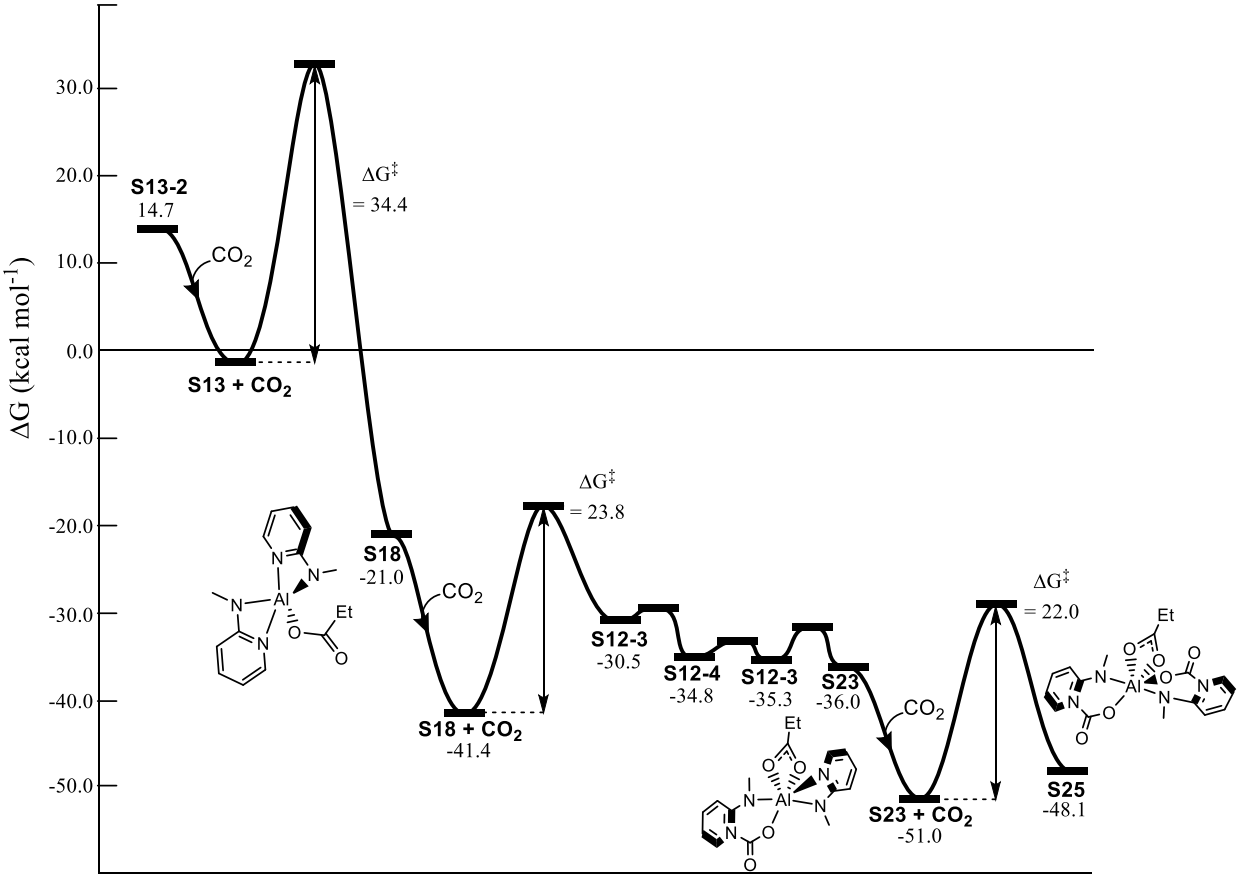

Figure 4.9. Free energy diagram of proposed activation of CO_2 to the aluminum bound carboxylate where CO_2 insertion into alkyl group occurs first. The baseline free energy (in kcal/mol) is complex S13 + the free energy of CO_2 at infinite separation.

Figure 4.10 displays the energy diagram for the most plausible pathway of cooperative activation of CO_2 using **10a**. The reference free energy value (**S13 + CO_2**) in the free energy diagram is the sum of **10a** and CO_2 at infinite separation. The first insertion of CO_2 into an Al-N bond was found to have an effective barrier below 20 kcal/mol consistent with rapid room temperature reaction. The second insertion was found to have a lower absolute barrier than the first, consistent with the experimental observation of only the symmetric, doubly inserted product after 5 hours.

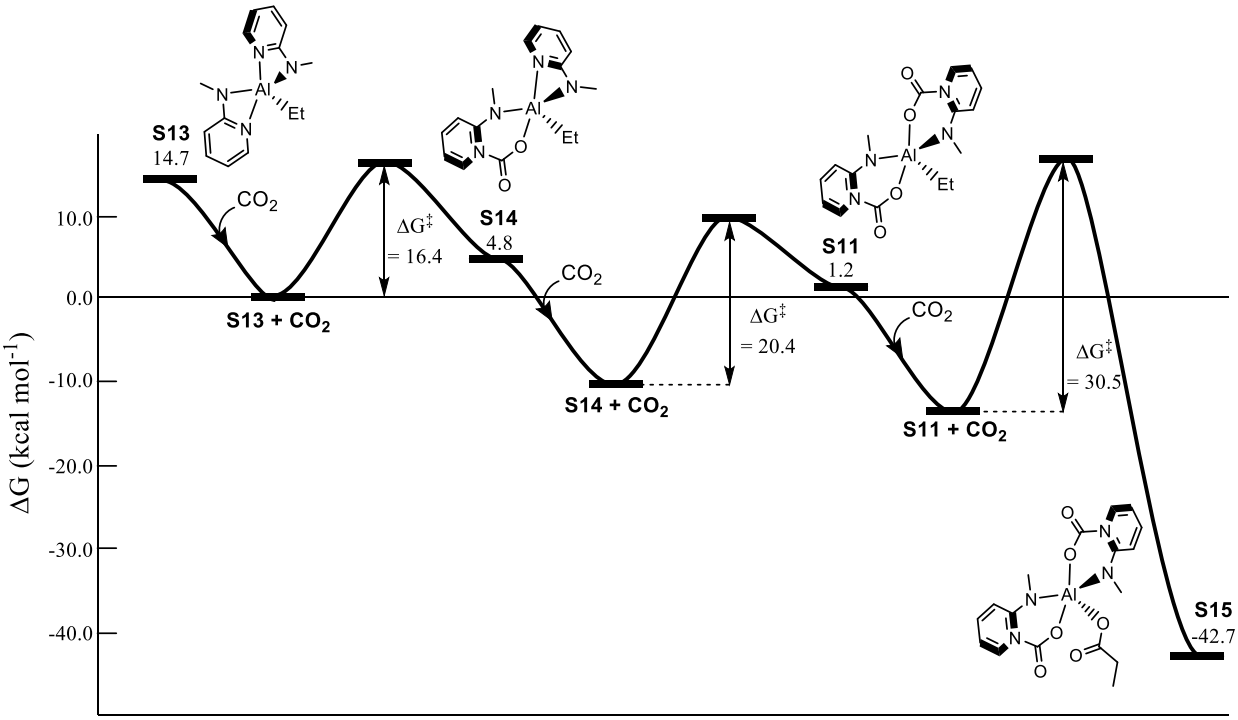

Figure 4.10. Free energy diagram of proposed activation of CO_2 to the aluminum bound carboxylate. The baseline free energy (in kcal/mol) is complex S14 + the free energy of CO_2 at infinite separation.

The high barrier for this step is not surprising, as this step was found experimentally to be quite slow and low yielding. The final insertion is thermodynamically highly favorable, consistent with experimental observation.

4.3 Conclusion

We have demonstrated the ability to cooperatively activate CO_2 using simple organoaluminum complexes at room temperature. Changing the ortho- substituent on pyridine (i.e. -NHMe, OH, CH_2OH) led to divergent reactivity. Addition of CO_2 to 2-pyridonate[AlR_2] (R = Et, ^{i}Bu) led to the low-yielding formation of an aluminum-alkoxy product (approximately 1%) while addition of CO_2 to (2-(methylamino)pyridine)$_2$AlR (R = Et, ^{i}Bu) led to the clean formation of a bis-metalocyclic carbamate product after 5 hours. In the case of 2-(methylamino)pyridine)$_2$AlEt, we were able to observe additional insertion of CO_2 into the

aluminum ethyl moiety at long reaction times. We conclude that the final product forms by way of direct CO_2 insertion into the aluminum alkyl yielding an aluminum bound propionate product. Computational data supports the proposed reaction pathway and product formulation.

4.4 Experimental Details

4.4.1 General Considerations

Syntheses and manipulations were performed in a nitrogen-filled Inert Technologies glovebox or using standard Schlenk techniques unless otherwise specified. Deuterated solvents were purchased from Cambridge Isotope Laboratories, dried over molecular sieves or calcium hydride, and stored in the glovebox over molecular sieves prior to use. CO_2 was passed through a Drierite column to remove trace water. $^{13}CO_2$ was purchased from Sigma-Aldrich. All other reagents and solvents used were commercially available and used without further purification unless specified. Aluminum reagents and 2-pyridone were stored in a nitrogen glovebox prior to use. Al(2-pyridone)Et_2 (**9a**) was synthesized as described elsewhere[108]. NMR spectra were recorded on a 400 MHz JEOL and referenced to the residual solvent peak.[121]

4.4.2. Synthesis

Synthesis of 2-pyridone[Al(^{i}Bu)$_2$]. (9b)

In the glovebox, solid 2-pyridone 356 mg (3.7 mmol) 2-pyridone was added to a solution of Al(^{i}Bu)$_3$ (1 mL, 4.1 mmol) in 10 mL of THF. Rapid bubbling was observed, indicating liberation of isobutane gas. A pale-yellow solution resulted after ten minutes. The solution was then allowed to stir at room temperature overnight in the glovebox. Solvent was removed *in vacuo* to give a light-colored oil. Colorless crystals suitable for X-ray analysis were obtained by dissolving the crude oil in dry pentane and placing inside the glovebox freezer at -35°C overnight. Yield: 0.76 g, 82%. ^{1}H NMR (400 MHz, Benzene-d_6) δ 7.69 (d, J = 7.7 Hz, 1H), 6.90 (t, J = 8.7 Hz 1H), 6.57

(d, J = 8.4 Hz, 1H), 6.10 – 6.05 (t, J = 6.9 Hz, 1H), 2.11 (non, 2H), 1.16 (d, J = 6.9 Hz, 12H) 0.41(d, J = 7.0 Hz, 4H). $^{13}C\{^{1}H\}$ NMR (101 MHz, Benzene-D_6) δ 166.152, 143.20, 142.95, 118.13, 114.54, 28.58, 26.72, 22.01 (br). HRMS calculated for $[C_5H_6AlNO_3]^+$ (product of alkyl hydrolysis) *m/z* calc.: 155.0163. Found: 156.0848.

Synthesis of Al(Et)(2-methylamino pyridine)$_2$. (10a)

In the glovebox, a solution of $Al(Et)_3$ (1 mL, 3.96 mmol) in 10 mL of THF was prepared. The solution was removed from the glovebox and 2-methylamino pyridine 1.578 g (1.5 mL, 7.92 mmol) was added. Rapid bubbling was observed, indicating liberation of ethane gas. A pale-yellow solution resulted after ten minutes. The solution was then allowed to stir at room temperature for 24 hours. Solvent was removed *in vacuo* to yield a pale yellow solid. The solid was washed with pentane (3 x 3 mL) and dried *in vacuo*. A second crop of product crystals was grown by placing the pentane wash in the glovebox freezer (-35°C) overnight. Yield: 1.3024 g, 66%. ^{1}H NMR (400 MHz, Benzene-d_6) δ 7.43 (dt, J = 5.1, 1.1 Hz, 2H), 7.01 (dd, J = 7.0, 1.6 Hz, 2H), 5.95 (m, 2H), 5.88 (d, J = 8.6 Hz, 2H), 2.60(s, 6H) 1.42 (t, J = 8.1 Hz, 3H) 0.48 (q, J = 8.4 Hz, 2H). $^{13}C\{^{1}H\}$ NMR (101 MHz, Benzene-D_6) δ 167.47, 143.70, 140.30, 107.54, 102.67, 29.51, 10.25. HRMS calculated for $[C_{12}H_{16}AlN_4O]^+$ $[M+H]^+$ (product of alkyl hydrolysis) *m/z* calc.: 259.1140. Found: 259.1333.

Synthesis of Al(^{i}Bu)(2-methylamino pyridine)$_2$. (10b)

In the glovebox, a solution of $Al(^iBu)_3$ (1 mL, 3.96 mmol) in 10 mL of THF was prepared. The solution was removed from the glovebox and 0.857 g 2-methylamino pyridine (0.81 mL, 7.92 mmol) was added. Rapid bubbling was observed, indicating liberation of isobutane gas. A pale-yellow solution resulted after ten minutes. The solution was then allowed to stir at room temperature for 24 hours. Solvent was removed *in vacuo* to yield a pale yellow solid. The solid

was washed with pentane (3 x 3mL) and dried *in vacuo*. A second crop of product crystals was grown by placing the pentane wash in the glovebox freezer (-35°C) overnight. Yield: 0.95 g, 80%. ^{1}H NMR (400 MHz, Benzene-d_6) δ 7.40 (d, J = 5.3 Hz, 2H), 6.95 (dd, J = 7.2, 1.7 Hz, 2H), 6.00-5.89 (m, 2H), 5.80 (d, J = 8.6 Hz, 2H), 2.59 (s, 6H), 2.05 (nonet, J = 6.6 Hz, 1H), 1.21 (d, J = 6.5 Hz, 6H), 0.53 (d, J = 6.9 Hz, 2H),. ^{13}C{^{1}H} NMR (101 MHz, Benzene-d_6) δ 167.36, 143.60, 140.28, 107.55, 102.70, 29.37, 28.02, 27.02. * Aluminum alkyl CH_2 absent from ^{13}C-NMR due to fast relaxation time. HRMS calculated for $[C_{16}H_{23}AlN_4]^+$ *m/z* calc.: 298.1738. Found: 298.1624.

Generation of (2-methylamino pyridine)$_2$Al(Et)(CO$_2$)$_2$ (10c) *in situ*

In the glovebox, approximately 12 mg of **2a** was weighed inside a vial, dissolved in 600 µL of benzene-d_6, and transferred inside a screw cap NMR tube. The tube was removed from the box and dry CO_2 was bubbled through the solution for 5 minutes. ^{1}H NMR (400 MHz, Benzene-d_6) δ 8.78 (dd, J = 5.8, 1.6 Hz, 2H), 6.97 (m, 2H), 6.33 (m, 2H), 6.14 (d, J = 8.7 Hz, 2H), 3.05 (s, 6H). 0.88 (t, J = 8.1 Hz, 3H), 0.10 (q, J = 8.1 Hz, 2H). ^{13}C{^{1}H} NMR (101 MHz, Benzene-D_6) δ 154.11, 152.71, 145.83, 140.62, 116.48, 111.93, 34.37, 9.85.

Generation of (2-methylamino pyridine)$_2$Al(^{i}Bu)(CO$_2$)$_2$ (10d) *in situ*

In the glovebox, approximately 12 mg of **2b** was weighed inside a vial, dissolved in 600 µL of benzene-d_6, and transferred inside a screw cap NMR tube. The tube was removed from the box and dry CO_2 was bubbled through the solution for 5 minutes. ^{1}H NMR (400 MHz, Benzene-d_6) δ 8.87 (dd, J = 5.8, 1.6 Hz, 2H), 6.86 (ddd, J = 9.0, 7.3, 2.0 Hz, 2H), 6.28 (ddd, J = 6.9, 5.7, 1.0 Hz 2H), 6.14 (d, J = 8.7 Hz, 2H), 3.05 (s, 6H), 1.38 (m, 1H), 0.97 (d, J = 6.5 Hz, 6H), 0.10 (br, 2H). ^{13}C{^{1}H} NMR (101 MHz, Benzene-D_6) δ154.46, 152.94, 146.39, 116.72, 112.15, 34.64, 26.74.

Synthesis of $Al(Et)_2$(2-pyridinemethanol). (11a)

In the glovebox, a solution of $Al(Et)_3$ (1.0 mL, 7.3 mmol) was dissolved in 10 mL of THF inside a Schlenk flask. The solution was removed from the glovebox and 2-pyridinemethanol (0.64 mL, 6.6 mmol) was added under a constant flow of nitrogen. Rapid bubbling occurred immediately. The resulting solution was allowed to stir at room temperature overnight in the glovebox. Solvent was removed *in vacuo* to give an off white solid. Biphasic recrystallization using benzene/pentane (v/v = 1/2) produced a pure white solid. Yield: 1.3289 g, 94%. ^{1}H NMR (400 MHz, Benzene-d_6) δ 8.29 (d, J = 5.2 Hz, 1H), 6.79 (td, J = 7.7, 1.5 Hz, 1H), 6.46 (m, 1H), 6.25 (d, J = 7.9 Hz, 1H), 4.90 (s, 2H), 1.42 (t, J = 8.1 Hz, 6H), 0.42 (m, 4H). ^{13}C{^{1}H} NMR (101 MHz, Benzene-D_6) δ 159.32, 145.16, 137.69, 122.48, 119.89, 63.20, 11.12. HRMS calculated for $[C_6H_{10}AlNO_3]^+$ M-H^+ (product of alkyl hydrolysis) *m/z* calc.: 171.0476. Found: 171.1027.

Synthesis of $Al(iBu)_2$(2-pyridinemethanol). (11b)

In the glovebox, a solution of $Al(iBu)_3$ (1.0 mL, 4.0 mmol) in 10 mL of THF inside a Schlenk flask. The solution was removed from the glovebox and 2-pyridinemethanol (0.35 mL, 3.6 mmol) was added under a constant flow of nitrogen. Rapid bubbling immediately occurred. The resulting solution was allowed to stir at room temperature overnight in the glovebox. Solvent was removed *in vacuo* to give an off white solid. Biphasic recrystallization using benzene/pentane (v/v = 1/2) produced a pure white solid. Yield: 0.7866 g, 87%. ^{1}H NMR (400 MHz, Benzene-d_6) δ 8.35 (d, J = 5.4 Hz, 1H), 6.76 (td, J = 7.6, 1.4 Hz, 1H), 6.51-6.41 (m, 1H), 6.25 (d, J = 7.9 Hz, 1H), 4.99 (s, 2H). 2.10 (nonet, 2H), 1.28 (d, J = 6.4 Hz, 6H), 1.16 (d, J = 6.4 Hz, 6H), 0.39 (m, 4H). ^{13}C{^{1}H} NMR (101 MHz, Benzene-D_6) δ 158.97, 145.37, 137.78, 122.43, 120.01, 63.08, 29.67, 28.82, 27.58. Anal. Calc. $C_{14}H_{24}AlNO$: 67.44; H, 9.70; N, 5.62. Found: C, 64.36; H, 9.15; N, 5.90. *Purity of compound was determined based on ^{1}H-NMR data.

4.4.3. Procedure for CO_2 Addition to Ligated Pyridine-Aluminum Complexes

1) Approximately 100 mg of **9a** or **9b** was weighed inside the glovebox and placed inside a 20 mL Schlenk flask. The solid was dissolved in 5 mL of benzene and removed from the glovebox. Dry CO_2 was allowed to pass through the flask for 5 minutes before closing the flask off and removal of the bubbler. The solution was stirred for 24 hours at room temperature. After 24 hours, the solvent was removed producing a pale yellow oil.

2) Inside the glovebox, approximately 10 mg of **9a** or **9b** was weighed inside a vial, dissolved in 600 μL benzene-d_6 and transferred to a screw cap NMR tube. The tube was removed from the box and dry CO_2 was bubbled through the solution for 5 minutes.

Inside the glovebox, approximately 10 mg of **10a** or **10b** was weighed inside a vial, dissolved in 600 μL benzene-d_6 and transferred to a screw cap NMR tube. The tube was removed from the box and dry CO_2 was bubbled through the solution for 5 minutes.

3) Inside the glovebox, approximately 100 mg of **11a** or **11b** was weighed inside a vial, dissolved in 5 mL of benzene, and placed inside a 25 mL Schlenk flask. Dry CO_2 was allowed to pass through the flask for 5 minutes before closing the flask off and removal of the bubbler. The solution was stirred for 24 hours at room temperature. After 24 hours, the solvent was removed producing a white solid.

4) Inside the glovebox, approximately 100 mg of **11a** or **11b** was weighed inside a vial, dissolved in 600 μL benzene-d_6 and transferred to a screw cap NMR tube. The tube was removed from the box and dry CO_2 was bubbled through the solution for 5 minutes.

4.4.4. X-ray Crystallography

A suitable crystal of each sample was selected for analysis and mounted in a polyimide loop. All measurements were made on a Rigaku Oxford Diffraction Supernova Eos CCD with

filtered Cu-Kα radiation at a temperature of 100 K. Using Olex2,[122] the structure was solved with the ShelXT structure solution program using Direct Methods and refined with the ShelXL refinement package[123] using Least Squares minimization.

4.4.5. Computational Details

All computations were performed using the Gaussian16 software package.[172] Gas-phase energies, optimized geometries, and unscaled harmonic vibrational frequencies were obtained using Density Functional Theory (DFT).[173] The pure hybrid B3LYP functional was used with default grid parameters.[174] The basis set for aluminum was the standard Hay and Wadt basis set and effective core potential (ECP) combination (LANL2DZ)[175,176] All carbon, nitrogen, oxygen, and hydrogen atoms utilized the 6-31G(d') basis set.[177] Spherical harmonic d functions were used throughout; i.e., there are five angular basis functions per d function. The Hessian of the energy was computed at all stationary points to confirm if they were minima (no imaginary vibrational frequencies) or transition states (only one imaginary vibrational frequency). Unscaled harmonic vibrational frequencies, zero-point energies (ZPE) and thermal enthalpy/free energy corrections were computed at 1 atm and 298.15 K. Solvation energies were computed using the CPCM model with standard cavity parameters for benzene.[178,179]

Chapter 5

Conclusions and Future Research Recommendations

5.1. Summary

In this dissertation we have reported, in Chapter 2, the successful synthesis and characterization of a new class of late transition metal-aluminum heterobimetallic complexes. A bridging ligand which both chelates the transition metal and binds the aluminum *via* an alkoxide was employed to impart stability to the bimetallic system. Novel rhodium-aluminum heterobimetallic complexes Rh(DPPE)(DPPP-O-Al^{i}Bu$_2$Cl) and Rh (DPPP-O-Al^{i}Bu$_2$) (DPPP-O-Al^{i}Bu$_2$Cl) are synthesized and spectroscopically identified.

In Chapter 3, the synthesis of rhodium and iridium NNO complexes was demonstrated. Complexes have been fully characterized by ^{1}H and ^{13}C{^{1}H} NMR spectroscopy, mass spectrometry and X-ray diffraction. Addition of K(NNO) to [M(cod)Cl]2 resulted in formation of a bimetallic M(I)-M(I)dimer bridged by two NNO ligands. In contrast, addition of the protic starting material NNO-H to [Ir(cod)$_2$][BArF$_{24}$] resulted in the Ir(III) hydride species [Ir(cod)(NNO)(H)]BArF$_{24}$. Finally, the reactivity of the newly synthesized complexes with alkyl aluminum reagents, AlR$_3$ (R = Et, iBu) was explored. Unfortunately, removal of the ligand after the addition of the aluminum alkyl reagents was observed.

In Chapter 4, we demonstrate the ability to activate CO_2 using simple organoaluminum complexes. Addition of CO_2 to 2-pyridonate[AlR$_2$] (R = Et, ^{i}Bu) led to the formation of the aluminum-alkoxy product (approximately 1%) identified by ^{1}H-NMR. Addition of CO_2 to (2-(methylamino) pyridine)$_2$AlR (R = Et, ^{i}Bu) led to the clean formation of the cyclic carbamate product after 5 hours identified by ^{1}H-NMR and ^{13}C-NMR. After 48 hours, formation of a new

product with the generic formula (2-(methylamino) pyridine)$_2$AlCO$_2$Et was identified by ^{13}C-NMR. The newly formed product remains in solution for up to 96 hours. Computational investigation into the formation of the alkoxy and carboxylate product has been performed. A unique cooperative mechanism for CO_2 incorporation is proposed based on joint experimental/theoretical data.

5.2. Future Direction

The goal of the Brewster lab is to develop transition metal systems that successfully dock aluminum to form a heterobimetallic species. Ultimately, we would like to utilize an electron-rich transition metal to exploit cooperative reactivity between both metal centers. A potential future direction for the Brewster lab would involve the synthesis of a ligand capable of binding the aluminum moiety in a tridentate fashion with additional functionality to coordinate electron rich metal (**Figure 5.1.**).

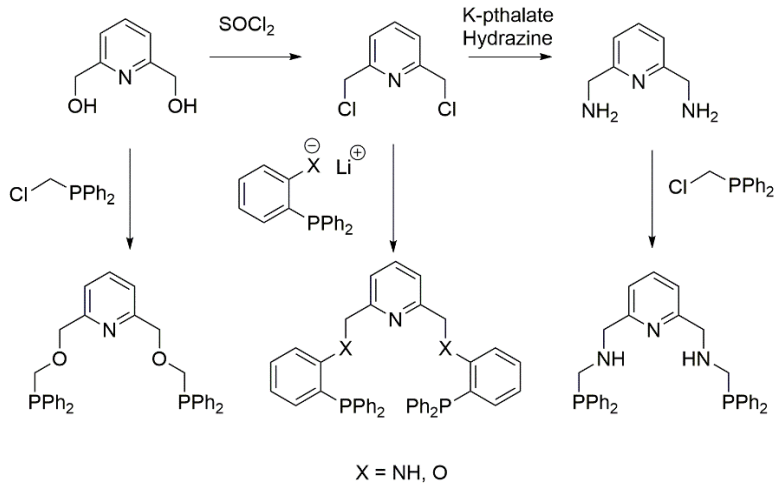

Figure 5.1. Proposed ligand synthesis

Using ligands of this scaffold would provide several advantages. The first is site selectivity for the aluminum center and transition metal center. Synthesis of related organoaluminium species has been successfully employed by Lu[91], Takaya[94], and Nakao[96] (see section 1.7.2.) allowing for

easy isolation of the target ligand. Following a synthetic protocol akin to that of Takaya, we propose that the direct addition to the ethereal-pyridine ligand would provide a stable 5- coordinate -ate species. In the case of the amine containing ligands, salt metathesis of the aluminum after deprotonation using nBuLi would provide a 4-coordinate aluminum species. This approach has been successfully utilized by Lu[91] and Nakao[96]. Successful docking of aluminum to the ligand will be identified by ^{27}Al-NMR spectroscopy and X-ray crystallography. Subsequent introduction of the appropriate transition metal precursor will yield the desired heterobimetallic complexes.

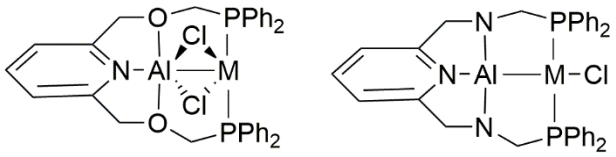

Figure 5.2. Potential Z-type structures for proposed ligands.

The second advantage would be metal-metal proximity after formation of the heterobimetallic species. As seen in several examples throughout this dissertation, addition of the late transition metal material to phosphorous-containing ligands has shown selectivity for binding of the transition metal, as opposed to aluminum, to the phosphorous arms. Specifically, we will be using low valent, late transition metals that demonstrate a d^8-square planar or d^{10}-tetrahedral configuration (Rh^I, Ir^I, Pd^0, or Pt^0). In theory, this type of scaffold would facilitate formation of a "Z"-type interaction between the metal centers (**Figure 5.2.**). Using either Rh^I or Pt^0 would allow additional spectroscopy techniques to identify and electronically characterize the interaction (^{103}Rh or ^{195}Pt NMR Spectroscopy).

The final advantage of this ligand scaffold is the "flexibility" of the ligand. In several cases of "Z"-type complexes, the ligand employed is part of a conjugated system or is otherwise rigid. The rigidity and may limit the ability for cooperative small molecule activation with Z-type complexes. In the case of this work, we propose ligands that are unconjugated that would allow

for conformational changes at both of the metal centers to provide stability when the substrate is activated.

This demonstration would be the first "Z"-type complex of aluminum to contain an oxygen supporting ligand. However, the coordination between the ethereal oxygen and aluminum may not provide the thermodynamic stability imparted by the X-type amine ligand. It is also important to note that reactivity of aluminum decreases with the number oxygens bound. This is attributed to oxygen being an excellent π-donor. In our case, however, the geometric constraints imparted by the overall chelate system will diminish the ability of oxygen to function in this fashion. Thus, the inductive effect of oxygen will likely dominate, making the aluminum center more Lewis acidic. Therefore, the strength of the interaction between the transition metal and aluminum would be increased. It is predicted that the unique structure of this ligand scaffold will impart both an interesting structural study into Z-type bonding and allow for cooperative activity with small molecules in an FLP-like fashion *across the two metal centers,* analogous to the mechanism to the complex described in Chapter 4 wherein the pyridine ligand served as an internal base.

References

1. Gade, L. H. Highly Polar Metal-Metal Bonds in "Early-Late" Heterobimetallic Complexes. *Angew. Chem. Int. Ed.* **2000***, 39*, 2658-2678.

2. Cooper, B.; Napoline, J. W.; Thomas, C. M. Catalytic Applications of Early/Late Heterobimetallic Complexes. *Catalysis Reviews: Science and Engineering* **2012***, 54*, 1-40.

3. Powers, D. C.; Ritter, T. Bimetallic Redox Synergy in Oxidative Palladium Catalysis. *Acc. Chem. Res.* **2012***, 45*, 840-850.

4. van den Beuken, Esther K; Feringa, B. L. Bimetallic catalysis by late transition metal complexes. *Tetrahedron* **1998***, 54*, 12985-13011.

5. Stephan, D. W. Frustrated Lewis Pairs: From Concept to Catalysis. *Acc. Chem. Res.* **2015***, 48*, 306-316.

6. Stephan, D. W. Frustrated Lewis pairs: a new strategy to small molecule activation and hydrogenation catalysis. *Dalton Trans.* **2009**, 3129-3136.

7. Gade, L. H., Memmler, H.; Kauper, U.; Schneider, A.; Fabre, S.; Bezougli, I.; Lutz, M.; Galka, C.; Scowen, I.J.; McPartlin, M. Cooperative Reactivity of Early-Late Heterodinuclear Transition Metal Complexes with Polar Organic Substrates. *Chem. Eur. J.* **2000***, 6*, 692.708.

8. Zhou, W.; Marquard, S. L.; Bezpalko, M. W.; Foxman, B. M.; Thomas, C. M. Catalytic Hydrosilylation of Ketones Using a Co/Zr Heterobimetallic Complex: Evidence for an Unusual Mechanism Involving Ketyl Radicals. *Organometallics* **2013***, 32*, 1766-1772.

9. Leelasubcharoen, S.; Zhizhko, P. A.; Kuzmina, L. G.; Churakov, A. V.; Howard, J. A. K.; Nikonov, G. I. Niobium/Rhodium Bimetallic Complexes: Synthesis, Structure, and Catalytic Hydrosilylation of Acetophenone and Benzaldehyde. *Organometallics* **2009***, 28*, 4500-4506.

10. Comte, V.; Le Gendre, P.; Richard, P.; Moïse, C. [TiPHOS(Rh)]+: A Fortuitous Coordination Mode and an Effective Hydrosilylation Bimetallic Catalyst. *Organometallics* **2005***, 24*, 1439-1444.

11. Zhang, H.; Wu, B.; Marquard, S. L.; Litle, E. D.; Dickie, D. A.; Bezpalko, M. W.; Foxman, B. M.; Thomas, C. M. Investigation of Ketone C═O Bond Activation Processes by Heterobimetallic Zr/Co and Ti/Co Tris(phosphinoamide) Complexes. *Organometallics* **2017***, 36*, 3498-3507.

12. Chiu, H. C.; Koley, A.; Dunn, P. L.; Hue, R. J.; Tonks, I. A. Ethylene Polymerization Catalyzed by Bridging Ni/Zn Heterobimetallics. *Dalton Trans.* **2017***, 46*, 5513-5517.

13. Mankad, N. P. Diverse Bimetallic Mechanisms Emerging from Transition Metal Lewis Acid/Base Pairs: Development of co-catalysis with Metal Carbenes and Metal Carbonyl Anions. *Chem. Commun.* **2018***, 54*, 1291-132.

14. Cotton, F.A.; James, C.A.; Luck, R.L. Synthesis and Characterization of the 1st Multiply Bonded Heteronuclear Edge-Sharing Bioctahedral Complex, $MoWCl_4(\mu\text{-}Cl)$ $(\mu\text{-}H)$ $(\mu\text{-}dppm)_2$. *Inorg. Chem*. **1991**, *30*, 4370-4373.

15. Greenwood, B.P.; Forman, S.I.; Rowe, G.T.; Chen, C.-H.; Foxman, B.M.; Thomas, C.M. Multielectron Redox Activity Facilitated by Metal-Metal Interactions in Early/Late Heterobimetallics: Co/Zr Complexes Supported by Phosphinoamide Ligands. *Inorg. Chem.* **2009**, *48*, 6251-6260.

16. Hostetler, M.J.; Bergman, R.G. Synthesis and Reactivity of $Cp_2Ta(CH_2)_2Ir(CO)_2$: An Early-Late Heterobimetallic Complex that Catalytically Hydrogenates, Isomerizes, and Hydrosilates Alkenes. *J. Am. Chem. Soc.* **1990**, *112*, 8621-8623.

17. Hostetler, M.J.; Butts, M.D.; Bergman, R.G. Scope and Mechanism of Alkene Hydrogenation/Isomerization Catalyzed by Complexes of the Type $R_2E(CH_2)_2M(CO)(L)$ (R = Cp, Me, Ph; E = P, Ta; M = Rh, Ir; L = CO, PPh_3). *J. Am. Chem. Soc.* **1993**, *115*, 2743-2752.

18. Karunananda, M.k.; Mankad, N.P. E-selective Semi-Hydrogenation of Alkynes by Heterobimetallic Catalysis. *J. Am. Chem. Soc.* **2015**, *137*, 14598-14601.

19. Chiu, H. C.; Koley, A.; Dunn, P. L.; Hue, R. J.; Tonks, I. A. Ethylene polymerization catalyzed by bridging Ni/Zn Heterobimetallics. *Dalton Trans.* **2017***, 46*, 5513-5517.

20. Coombs, J.; Perry, D.; Kwon, D.; Thomas, C. M.; Ess, D. H. Why Two Metals Are Better Than One for Heterodinuclear Cobalt–Zirconium-Catalyzed Kumada Coupling. *Organometallics* **2018***, 37*, 4195-4203.

21. Man, M. L.; Lam, K. C.; Sit, W. N.; Ng, S. M.; Zhou, Z.; Lin, Z.; Lau, C. P. Synthesis of heterobimetallic Ru-Mn complexes and the coupling reactions of epoxides with carbon dioxide catalyzed by these complexes. *Chem. Eur. J.* **2006***, 12*, 1004-1015.

22. Lindenberg, F.; Shribman, T.; SIeler, J.; Hey-Hawkins, E.; Eisen, M. S. Dinuclear phosphido- and arsenido-bridged early/late metal complexes. Efficient catalysts for ethylene polymerization. *J. Organomet. Chem.* **1996***, 515*, 19-25.

23. Oishi, M.; Kato, T.; Nakagawa, M.; Suzuki, H. Synthesis and Reactivity of Early-Late Heterobimetallic Hydrides of Group 4 Metals and Iridium Supported Mono(η^5-C_5Me_5) Ancillary Ligands: Bimetallic Carbon-Hydrogen Bond Activation. *Organometallics* **2008**, *27*, 6046-6049.

24. Braunstein, P.; Chetcuti, M.J.; Welter, R. Bimetallic-Induced Tail-to-Tail Dimerization and C-H Activation of Methyl Acrylate. *Chem. Commun.* **2001**, 2508-2509.

25. Oishi, M.; Suzuki, H. Zirconocene—Iridium Hydrido Complexes: Arene Carbon—Hydrogen Bond Activation and Formation of a Planar Square Zr_2Ir_2 Complex. *Inorg. Chem.* **2009**, *48*, 2349-2351.

26. Greenwood, B.P.; Rowe, G.T.; Chen, C.-H.; Foxman, B.M.; Thomas, C.M. Metal-Metal Multiple Bonds Early/Late Heterobimetallics Support Unusual Trigonal Monopyramidal Geometries at Both Zr and Co. *J. Am. Chem. Soc.* **2010**, *132*, 44-45.

27. Thomas, C.M.; Napoline, J.W.; Rowe, G.T.; Foxman, B.M.; Oxidative Addition Across Co/Zr Multiple Bonds in Early/Late Heterobimetallic Complexes. *Chem*. *Commun*. **2010**, *46*, 5790-5792.

28. Gramigna, K.M..; Dickie, D.A.; Foxman, B.M.; Thomas, C.M. Cooperative H_2 Activation across a Metal-Metal Multiple Bond and Hydrogenation Reactions Catalyzed by a Zr/Co Complexes. *ACS Catal*. **2019**, *9*, 3153-3164.

29. Riddlestone, I.M.; Rajabi, N.A.; Lowe, J.P.; Mahon, M.F.; Macgregor, S.A.; Whittlesey, M.K. Activation of H_2 over the Ru-Zn Bond in the Transition Metal-Lewis Acid Heterbimetllic Species $[Ru(IPr)_2(CO)ZnEt]^+$. *J. Am. Chem. Soc.* **2016**, *138*, 11081-11084.

30. Baranger, A.M.; Bergman, R.G. Cooperative Reactivity in the Interaction of X-H Bonds with a Zirconium-Iridium Bridging Imido Complex. *J. Am. Chem. Soc.* **1994**, *116*, 3822-3835.

31. Steffey, B.D.; Vites, J.C.; Cutler, A.R. Reduction of the Heterobimetallic μ-η^1(C): η^2(O, O')-CO_2 Complex $Cp(CO)_2Ru(CO_2)Zr(Cl)Cp_2$ to its μ-η^1(C): η^1(O)-Formaldehyde Derivative $Cp(CO)_2Ru(CH_2O)Zr(Cl)Cp_2$: Hydride Transfer Occurs at Ligated Carbon Monoxide. *Organometallics* **1991**, *10*, 3432-3435.

32. Krogman, J.P.; Bezpalko, M.W.; Foxman, B.M.; Thomas, C.M. Synthesis, Structure, and Reactivity of an Anionic Zr—Oxo Relevant to CO_2 Reduction by a Zr/Co Heterobimetallic Complex. *Inorg*. *Chem*. **2013**, *52*, 3022-3031.

33. Kalck, P.; Serra, C.; Machet, C.; Broussier, R.; Gautheron, B.; Delmas, G.; Trouvé, G.; Kubicki, M. Carbonylation of Ethene to Acrolein in the Presence of Early-Late Heterobimetallic Complex $[AsPh_4][\ \eta\text{-}C_5Me_5)_2Zr(\mu\text{-}S)_2Rh(CO)_2]$•THF. *Organometallics* **1993**, *12*, 1021-1022.

34. Baranger, A.M.; Bergman, R.G. Cooperative Reactivity in the Interactions of X-H Bond with a Zirconium-Iridium Bridging Imido Complex. *J. Am. Chem. Soc.* **1994**, *116*, 3822-3835.

35. Krogman, J.P.; Foxman, B.M.; Thomas, C.M. Activation of CO_2 by a Heterobimetallic Zr/Co Complex. *J. Am. Chem. Soc.* **2011**, *133*, 14582-14585.

36. Zhang, H.; Hatzis, G.P.; Moore, C.E.; Dickie, D.A.; Bezpalko, M.W.; Foxman, B.M.; Thomas, C.M. O_2 Activation by a Heterobimetallic Zr/Co Complex. *J. Am. Chem. Soc.* **2019**, *141*, 9516-9520.

37. Goldsmith, C.R. Aluminum and Gallium Complexes as Homogenous Catalysts for Reduction/Oxidation reactions. *Coord. Chem. Rev.* **2018**, *377*, 209-224.

38. Dohmeier, C.; Robl, C.; Tacke, M.; Schnöckel, H. The Tetrameric Aluminum (I) Compound [{Al(η-C_5Me_5)}$_4$] *Angew. Chem. Int. Ed. Eng.* **1991**, *30,* 564-565.

39. Cui,C.; Roesky, W.; Schmidt, H.-G.; Noltemeyer, M.; Hao, H.; Cimpoesu, F. Synthesis and Structure of a Monomeric Aluminum (I) Compound [{HC(CMeNAr)$_2$Al] (Ar=2,6-$iPr_2C_6H_3$): A Stable Aluminum Analogue of a Carbene. *Angew. Chem. Int.Ed.* **2000**, *112*, 4444-4446.

40. Bag, P.; Porzelt, A.; Altmann, P.J.; Inoue, S. A Stable Neutral Compound with an Aluminum-Aluminum Double Bond. *J. Am. Chem. Soc.* **2017**, *139*, 14384-14387.

41. Hicks, J.; Vasko, P.; Goicoechea, J.M.; Aldridge, S. Synthesis, Structure and Reaction Chemistry of a Nucleophilic Aluminyl Anion. *Nature* **2018**, *557*, 92-95.

42. Hormann, A.; Pranckevicus, C.; Tröster, T.; Braunschweig, H. Aluminum (I)/Boron(III) Redox Reactions. *Angew. Chem. Int. Ed.* **2019**, *58*, 3625-3629.

43. Mellerup, S.K.; Cui, Y.; Fantuzzi, F.; Schmid, P.; Goettel, J.T.; Bélanger-Chabot, G.; Arrowsmith, M.; Krummenacher, I.; Ye, Q.; Engel, V.; Engels, B.; Braunschweig, H. Lewis-Base Stabilization of the Parent Al(I) Hydride Under Ambient Conditions. *J. Am. Chem. Soc.* **2019**, *141*, 16954-16960.

44. Abdalla, J.A.B; Riddlestone, I.M.; Tirfoin, R.; Aldridge, S. Cooperative Bond Activation and Catalytic Reduction of Carbon Dioxide at a Group 13 Metal Center. *Angew. Chem.* **2015**, *127*, 5187-5191.

45. Caise, A.; Jones, D.; Kolychev, E.L.; Hicks, J.; Goicoechea, J.M.; Aldridge, S. On the Viability of Catalytic Turnover via Al—O/B—H Metathesis: The Reactivity of β-Diketiminate Aluminum Hydrides towards CO_2 and Boranes. *Chem. Eur. J.* **2018**, *24*, 13624-13635.

46. Myers, T.W.; Berben, L.A. Aluminum-Ligand Cooperation Promotes Selective Dehydrogenation of Formic Acid to H_2 and CO_2. *Chem. Sci.* **2014**, *5*, 2771-2777.

47. Albrecht, M.; Erker, G.; Nolte, M., Krüger, C. Planar Tetracoordinate Carbon Stabilized in a Dimetallic Hafnium/Aluminum Compound: Formation and Crystal Structure of $Cp_2Hf[\mu\text{-}\eta^1 : \eta^2\text{-}MCC(C_6H_{11})][\mu\text{-}CC(C_6H_{11})]AlMe_2$. *J. Organomet. Chem.* **1992**, *427*, C21-C25.

48. Grant, L.N.; Kriegel, B.M.; Arnold, J. Formation of a Niobium-Aluminum Heterobimetallic Complex via Supporting Ligand Exchange. *Polyhedron* **2016**, *114*, 53-55.

49. Parfenova, L.V.; Kovyazin, P.V.; Tyumkina, T.V.; Islamov,, D.N.; Lyapina, A.R.; Karchevsky, S.G.; Ivchenko, P.V. Reactions of Bimetallic Zr,Al- Hydride Complexes with Methylaluminoxane: NMR and DFT Study. *J. Organomet. Chem.* **2017**, *851*, 30-39.

50. Schröder, L.; Brintzinger, H.-H. rac-Me_2Si(2-Me-4-*t*-Bu-$C_5H_2)_2ZrMe^+$: An alkyl Zirconocenium Cation Stabilized by Steric Shielding Against Interaction with Ancillary Ligands. *Organometallics* **2005**, *24*, 867-871.

51. Kulangara, S.V.; Jabri, A.; Yang, Y.; Korobkov, I.; Gambarotta, S.; Duchateau, R. Synthesis, X-Ray Structural Analysis, and Ethylene Polymerization Studies of Group IV Metal Heterobimetallic Aluminum-Pyrrolyl Complexes. *Organometallics* **2012**, *31*, 6085-6094.

52. Turevskaya, E.P.; Berdyev, D.V.; Turoba, N.Y.; Starikova, Z.A.; Yanovsky, A.I.; Strchkov, Y.T.; Belokon, A.I. Bimetallic Alkoxides of Aluminum-Hafnium and Aluminum Zirconium. X-Ray Structure of $Al_2Hf(OPr^i)_{10}$. *Polyhedron* **1997**, *16*, 663-670.

53. Wisniewska, D.; Janas, Z.; Sobota, P.; Jerzykiewics, L.B. Dimethyl Group IV Metal Complexes of the OSO-Type Ligand Bearing $AlMe_2$ Moieties. *Organometallics* **2006**, *25*, 6166-6169.

54. Bryliakov, K.P.; Talsi, E.P.; Voskoboynikov, A.Z.; Lancaster, S.J.; Bochmann, M. Formation and Structures of Hafnocene Complexes in MAO- and $Al^iBu_3/CPh_3[B(C_6F_5)_4]$-Activated Systems. *Organometallics* **2008**, *27*, 633-6342.

55. Khan, K.; Raston, C.L., McGrady, J.E.; Skelton, B.W.; White, A.H. Hydride-Bridged Heterobimetallic Complexes of Zirconium and Aluminum. *Organometallics* **1997**, *16*, 3252-3254.

56. Bolton, P.D.; Clot, E.; Cowley, A.R.; Mountford, P. $AlMe_3$ and $ZnMe_2$ Adducts of A Titanium Imido Methyl Cation: A Combined Crystallographic, Spectroscopic, and DFT Study. *J. Am. Chem. Soc.* **2006**, *128*, 15005-15018.

57. Gurubasavarj, P.M.; Nomura, K. Hetero-bimetallic Complexes of Titanatranes with Aluminum Alkyls: Synthesis, Structural Analysis, and Their Use in Catalysis for Ethylene Polymerization. *Organometallics* **2010**, *29*, 3500-3506.

58. Bolton, P.D.; Clot, E.; Cowley, A.R.; Mountford, P. Well-defined Imidotitanium Alkyl Cations: Agostic Interactions, Migratory Insertion vs [2+2] Cycloaddition, and the First Structurally Authenticated $AlMe_3$ Adduct of Any Transition Metal Alkyl Cation. *Chem. Commun.* **2005**, 3313-3315.

59. Jabri, A.; Korobkov, I.; Gambarotta, S.; Duchateau, R. Single-Site, Single-Component Catalysts for Very High Molecular Weight Polyethylene: A Robust "Ready-To-Go"

Vanadium π-Bonded Complex Without A Preformed V—C Bond. *Angew. Chem. Int. Ed.* **2007**, *46*, 6119-6122.

60. Janas, Z.; Godbole, D.; Nerkowski, T.; Szczegot, K. Zirconium and Hafnium Complexes of the thio(bisphenolato) Ligand: Synthesis, Structural Characterization and Testing as 1-hexene Polymerization Catalysts. *Dalton Trans*. **2009**, 8846-8853.

61. Bochmann, M. The Chemistry of Catalyst Activation: The Case of Group 4 Polymerization Catalysts. *Organometallics* **2010**, *29*, 4711-4740.

62. Chen, E.Y.X.; Marks, T.J. Cocatalysts for Metal-Catalyzed Olefin polymerization: Activators, Activation Processes, and Structure-Activity Relationships. *Chem. Rev.* **2000**, *100,* 1391-1434.

63. Bochmann, M. Kinetic and Mechanistic Aspects of Metallocene Polymerization Catalysts. *J. Organomet. Chem.* **2004**, *689*, 3982-3998.

64. Nikiforov, G.B.; Roesky, H.W.; Schulz, T.; Stalke, D.; Whitt, M. On the Quest for New Mixed-Metal μ-Oxo-Bridged Complexes: Synthesis of Compounds Containing Transition Metal—Oxygen—Main Group Metal Motifs M—O—M^1 (M = Ti, Zr; M^1 = Al, Ga) Without Cyclopentadienyl Ligands. *Inorg. Chem.* **2008**, *47*, 6435-6443.

65. Brown, A.C.; Altman, A.B.; Lohrey, T.D.; Hohloch, S.; Arnold, J. Hydride Oxidation from a Titanium-Aluminum Bimetallic Complex: Insertion, Thermal and Electrochemical Reactivity. *Chem. Sci.* **2017**, *8*, 5153-5160.

66. Gurubasavaraj, P.M.; Roesky, H.W.; Nekouelshahkraki, B.; Pal, A. Herbst-Irmer, R. From Unstable to Stable: Half-Metallocene Catalysts for Olefin Polymerization. *Inorg. Chem.* **2008**, *47*, 5324-5331.

67. Vidyaratne, I.; Nikiforov, G.B.; Gorelsky, S.I.; Gambarotta< S.; Duchateau, R.; Korobkov, I. Isolation of a Self-Activating Ethylene Trimerization Catalyst. *Angew. Chem. Int. Ed.* **2009**, *48*, 6552-6556.

68. Bai, G.; Singh, S.; Roesky, H.W.; Noltemeyer, M.; Schmidt, H.-G. Mononuclear Aluminum Hydroxide for the Design of Well-Defined Homogenous Catalysts. *J. Am. Chem. Soc.* **2005**, *127*, 3449-3455.

69. Askevold, B.; Roesky, H.W.; Schneider, S. Learning from the Neighbors: Improving Homogeneous Catalysts with Functional Ligands Motivated by Heterogenous and Biocatlysis *ChemCatChem* **2012**, *5*, 307-320

70. Boulhom C.; Zijlstra, H.S.; Harder, S. Oxide-Bridged Heterobimetallic Aluminum/Zirconium Catalysts for Ethylene Polymerization. *Eur. J. Inorg. Chem.* **2015**, 2132-2138.

71. Padmanabhan, S.; Katao, S.; Nomura, K. Synthesis and Structure of Titanatranes Containing Tetradentate Trianionic Donor Ligands of the Type [(O-2,4-$R_2C_6H_2$-6-$CH_2)_2(OCH_2CH_2)]N^{3-}$ and their use in Catalysis for Ethylene Polymerization. *Organometallics* **2007**, *26*, 1616-1626.

72. Takii, Y.; Gurubasavarj, P.M.; Katao, S.; Nomura, K. Effect of Terminal Aryloxo Ligands in Ethylene Polymerization Using Titanatranes of the Type, [Ti(OAr){O-2,4-$R_2C_6H_2$)-6-$CH_2\}_3$N]: Synthesis and Structural Analysis of the Heterobimetallic Complexes of Titanatranes with $AlMe_3$. *Organometallics* **2012**, *31*, 8237-8248.

73. Tewasekson, U.; Tsutsumi, K.; Nomura, K.; Synthesis and Structural Analysis of Zr-Al Heterobimetallic Complexes, [ZrX{(O-2,4-$^tBu_2C_6H_2$-6-$CH_2)_3$(μ_2-O-2,4-$^tBu_2C_6H_2$-6-CH_2)}N][R_2Al μ_2-O^{i}Pr)][X = Cl, Et, ^{i}Bu; R=Me, Et, ^{i}Bu]. Unique Reactivity of the ^{i}Bu Complex. *Organometallics* **2016**, *35*, 866-874.

74. Takii, Y.; Inagaki, A.; Nomura, K. Synthesis, Structural Analysis of the Hetero-bimetallic Complexes MMe[(O-2,4-$^tBu_2C_6H_2$-6-$CH_2)_2$(μ_2-O-2,4-$^tBu_2C_6H_2$-6-CH_2)}N][R_2Al μ_2-O^{i}Pr)][M = Zr, Hf] and their use in Catalysis for Ethylene Polymerization. *Dalton Trans*. **2013**, *42*, 11632-11639.

75. Amgoune, A.; Bourissou, D. σ-Acceptor, Z-type Ligands for Transition Metals. *Chem. Commun*. **2011**, *47*, 859-871.

76. Kuzu, I.; Krummenacher, I.; Meyer, J.; Armbruster, F.; Breher, F. Multidentate Ligand Systems Featuring Dual Functionality. *Dalton Trans.* **2008**, 5836-5865.

77. Devillard, M.; Bouhadir, G.; Bourissou, D. Cooperation between Transition Metals and Lewis Acids: A Way To Activate H_2 and H—E bonds. *Angew. Chem. Int. Ed.* **2015***, 54*, 730-732.

78. Owen, G. R. Hydrogen atom storage upon Z-class borane ligand functions: an alternative approach to ligand cooperation. *Chem. Soc. Rev.* **2012***, 41*, 3535-3546.

79. Hill, A. F.; Owen, G. R.; White, A. J.; Williams, D. J. The Sting of the Scorpion: A Metallaboratrane. *Angew. Chem. Int. Ed.* **1999***, 38*, 2759-2761.

80. Landry, V. K.; Melnick, J. G.; Buccella, D.; Pang, K.; Ulichny, J. C.; Parkin, G. Synthesis and Structural Characterization of [κ^3-B,S,S-B(mim^R)3]Ir(CO)(PPh_3)H (R = Bu^t, Ph) and [κ^4-B(mim^{But})$_3$]M(PPh_3)Cl (M = Rh, Ir): Analysis of the Bonding in Metal Borane Compounds. *Inorg. Chem.* **2006***, 45*, 2588-2597.

81. Bontemps, S.; Bouhadir, G.; Miqueu, K.; Bourissou, D. On the versatile and unusual coordination behavior of ambiphilic ligands o-R2P(Ph)BR'2. *J. Am. Chem. Soc.* **2006***, 128*, 12056-12057.

82. Sircoglou, M.; Bontemps, S.; Bouhadir, G.; Saffon, N.; Miqueu, K.; Gu, W.; Mercy, M.; Chen, C. H.; Foxman, B. M.; Maron, L.; Ozerov, O. V.; Bourissou, D. Group 10 and 11 Metal Boratranes (Ni, Pd, Pt, CuCl, AgCl, AuCl, and Au^{+}) Derived from a Triphosphine−Borane. *J. Am. Chem. Soc.* **2008***, 130*, 16729-16738.

83. Harman, W. H.; Peters, J. C. Reversible H_2 Addition Across a Nickel-Borane Unit as a Promising Strategy for Catalysis. *J. Am. Chem. Soc.* **2012***, 134*, 5080-5082.

84. Segawa, Y.; Yamashita, M.; Nozaki, K. Syntheses of PBP Pincer Iridium Complexes: A Supporting Boryl Ligand. *J. Am. Chem. Soc.* **2009***, 131*, 9201-9203.

85. Burlitch, J.M.; Leonowicz, M.E.; Petersen, R.B.; Hughes, R.E. Coordination of Metal Carbonyl Anions to Triphenyaluminum, -gallium, and -indium and the Crystal Structure of Tetraethylammonium Triphenyl ((η^5-cyclopentadienyl)dicarbonyliron)aluminate(Fe-Al). *Inorg. Chem.* **1979**, *18*, 1097-1105.

86. Mayer, J.M.; Calabrese, J.C. Reactions of Alkylaluminum Reagents with Basic and Acidic Rhodium Compounds. X-ray Crystal and Molecular Structure of (η-C_5H_5)Rh(PMe_3)$_2$($Al_2Me_4Cl_2$), a Rhodium-Lewis Acid Adduct. *Organometallics* **1984**, 3, 1292-1298.

87.Golden, J.T.; Peterson, T.H.; Holland, P.L.; Bergman, R.G.; Andersen, R.A. Adduct Formation of Single and Double Deprotonation of Cp*(PMe_3)Ir$(H)_2$ with Main Group Metal Alkyls and Aryls: Synthesis and Structure of Three Novel Ir—Al and Ir—Mg Heterobimetallics. *J. Am. Chem. Soc.* **1998**, *120*, 223-224.

88.Braunschweig, H.; Gruss, K.; Radacki, K. Interaction between d- and p-Block Metals: Synthesis and Structure of Platinum-Alane Adducts. *Angew. Chem. Int. Ed*. **2007**, *46,* 7782-7784.

89. Bauer, J.; Braunschweig, H.; Brenner, P.; Kraft, K.; Radacki, K.; Schwab, K. Late-Transition-Metal Complexes as Tunable Lewis Bases. *Chem. Eur. J.* **2010**, 16, 11985-11992.

90. Rudd, P. A.; Liu, S.; Gagliardi, L.; Young, J., Victor G; Lu, C. C. Metal-Alane Adducts with Zero-Valent Nickel, Cobalt, and Iron. *J. Am. Chem. Soc.* **2011***, 133*, 20724-20727.

91. Moore. James, T.; Smith, N. E.; Lu, C. C. Structure and Dynamic NMR behavior of Rhodium Complexes supported by Lewis Acidic Group 13 Metallatranes. *Dalton Trans.* **2017***, 46*, 5689-5701.

92. Devillard, M.; Declercq, R.; Nicolas, E. C.; Ehlers, A. W.; Backs, J.; Merceron-Saffon, N.; Bouhadir, G.; Slootweg, J. C.; Uhl, W.; Bourissou, D. A Significant but Constrained Geometry Pt→Al Interaction: Fixation of CO_2 and CS_2, Activation of H_2 and $PhCONH_2$. *J. Am. Chem. Soc.* **2016***, 138*, 4917-4926.

93. Cowie, B.E.; Tsao, F.A.; Emslie, D.J. Synthesis and Platinum Complexes of an Alane-Appended 1,1'-Bis(phosphino)ferrocene Ligand. *Angew. Chem. Int. Ed.* **2015**, *54*, 2165-2169.

94. Takaya, J.; Iwasawa, N. Synthesis, Structure, and Catalysis of Palladium Complexes Bearing a Group 13 Metalloligand: Remarkable Effect of an Aluminum-Metalloligand in Hydrosilylation of CO_2. *J. Am. Chem. Soc.* **2017***, 139*, 6074-6077.

95. Nakao, Y.; Kanyiva, K.S.; Hiyama, T. A Strategy for C—H Activation of Pyridines: C-2 Selective Alkenylation of Pyridines by Nickel/Lewis Acid Catalysis. *J. Am. Chem. Soc.* **2008**, *130*, 2448-2449.

96. Hara, N. Saito, T.; Semba, K. Kuriakose, N.; Zheng, H.; Sakaki, S.; Nakao, Y. Rhodium Complexes Bearing PAlP Pincer Ligands. *J. Am. Chem. Soc.* **2018**, *140*, 7070-7073.

97. Fernández-Moreira, V.; Concepción Gimeno, M. Heterbimetallic Complexes for Theranostic Applications *Chem. Eur. J.* **2018**, *24*, 3345-3353.

98. Desbois, N.; Pacquelet, S.; Dubois, A.; Michelin, C.; Gros, C.P. Easy Access to Heterobimetallic Complexes for Medical Imaging Applicactions via Microwave-Enhanced Cycloaddition. *Beilstein J. Org. Chem.* **2015**, *11*, 2202–2208.

99. Böhmer, M.; Kampert, F.; Tan, T.; Guisado-Barrios, G.; Peris, E.; Hahn, F.E. Ir^{III}/Au^{I} and Rh^{III}/Au^{I} Heterobimetallic Complexes as Catalysts for the Coupling of Nitrobenzene and Benzylic Alcohol. *Organometallics* **2018**, *37*, 4092-4099.

100. Wu, B.; Bezpalko, M.W.; Foxman, B.N.; Thomas, C.M. A Heterobimetallic Complex Featuring a Ti-Co Multiple Bond and its Application to the Reductive Coupling of Ketones to Akenes. *Chem. Sci.* **2015**, *6*, 2044-2049.

101. Wheatley, N.; Kalck, P. Structure and Reactivity of Early-Late Heterobimetallic Complexes. *Chem. Rev.* **1999**, *99*, 3379−3420.

102. Bodio, E.; Picquet, M.; Le Gendre, P. *Homo- and Heterobimetallic Complexes in Catalysis*, **2015**, 139−186.

103. Culcu, G.; Iovan, D. A.; Krogman, J. P.; Wilding, M. J. T.; Bezpalko, M. W.; Foxman, B. M.; Thomas, C. M. Heterobimetallic Complexes Comprised of Nb and Fe: Isolation of Coordinatively Unsaturated Nb^{III}/Fe^{0} Bimetallic Complex Featuring a Nb≡Fe Triple Bond. *J. Am. Chem. Soc.* **2017**, *139*, 9627-9636.

104. Stephan, D.W.; Erker, G. Frustrated Lewis Pairs: Metal-Free Hydrogen Activation and More. *Angew. Chem. Int. Ed.* **2010**, *49*, 46-76.

105. Miller, A.J.M.; Labinger, J.A.; Bercaw, J.E. Homogenous CO Hydrogenation: Ligand Effects on the Lewis Acid-Assisted Reductive Coupling of Carbon Monoxide. *Organometallics* **2010**, *29*, 4499–4516.

106. Miller, A.J.M.; Labinger, J.A.; Bercaw, J.E. Homogenous CO Hydrogenation: Dihydrogen Activation Involves Frustrated Lewis Pair Instead of a Platinum Complex. *J. Am. Chem. Soc.* **2010**, *132*, 3301–3303.

107. Brewster, T.P.; Nguyen, T.H.; Li, Z.; Eckenhoff, W.T.; Schley, N.D.; DeYonker, N.J. Synthesis and Characterization of Heterobimetallic Iridium-Aluminum and Rhodium-Aluminum Complexes. *Inorg. Chem.* **2018**, *57*, 1148−1157.

108. Charles III, R.M.; Yokley, T.W.; Schley, N.D.; DeYonker, N.J.; Brewster. T.P. Hydrogen Activation and Hydrogenolysis Facilitated by Late Transition Metal-Aluminum Heterobimetallic Complexes. *Inorg. Chem.* **2019**, *58*, 12635-12645.

109. Karas, J.; Huttner, G.; Heinze, K.; Rutsch, P. Zsolnai. Preparation of Enantiomerically Pure Chelate Ligands $L_2 = XCH_2CH(OH)CH_2Y$ from Epichlorohydrin – Conformation of their $L_2Rh(COD)^+$ Derivatives and Enantioselective Hydrogenation by $L_2Rh(COD)^+$. *Eur. J. Inorg. Chem.* **1999**, 405-420.

110. McCleverty, J.A.; Wilkinson, G. *Inorg. Syn.* **1966**, *8*, 211-214.

111. Fischer, B.J.; Eisenberg, R. Mono- and Binuclear Iridium Carbonyl Hydrides Containing Bis(tertiary phosphine) Ligands. *Inorg. Chem.* **1984**, *23*, 3216-3222.

112. Bertrand, R.D.; Ogilvie, F.B.; Verkade, J.G. Signs of Phosphorous-Phosphorous Coupling Constants in Coordination Compounds. *J. Am. Chem. Soc.* **1970**, *92*, 1908-1915.

113. Pilloni, G.; Vecchi, E.; Martelli, M. Electrochemistry of Coordination Compounds: II. Electrochemical Reduction of di-(1,2-bisdiphenylphosphinoethane)M(I) Chloride: A New Route to hydrido di-(1,2-bisdiphneylphosphinoethane)M(I)(M =Rh, Ir). *J. Electroanal. Chem. Interfacial Electrochem.* **1973**, *45*, 483-485.

114. Teo, B.K.; Ginsberg, A.P.; Kalabrese, K.C. A Remarkable Epoxide Opening. AN Expeditious Synthesis of Vernolepin and Vernomenin. *J. Am. Chem. Soc.* **1976**, *98*, 3027-3029.

115. Zong, J.; Mague, J.T.; Pascal Jr., R.A. Exceptional Steric Congestion in an *in, in*-Bis(hydrosilane) *J. Am. Chem. Soc.* **2013**, *135*, 13235-13237.

116.Brady, R.; Miller, W.V.; Vaska, L. Luminescence of d^8 Complexes of Iridium and Rhodium, and its Quenching by Molecular Oxygen and Other Gases. *J. Chem. Soc., Chem. Commun.* **1974**, 393-394.

117. Halpern, J.; Wong, C.S. Hydrogenation of tris(triphenylphosphine)chlororhodium(I). *J. Chem. Soc., Chem. Commun.* **1973**, 629-630.

118. Hartwig, J. *Organotransition Metal Chemistry: From Bonding to Catalysis*, University Science Books: Sausalito, CA. 2010.

119. Lesley, M.J.G.; Norman, N.C.; Rice, C.R.; Reger, D.L.; Little, C.A.; Lamba, J.J.S.; Brown, K.J.; Peters, J.C.; Thomas, J.C.; Sahasrabudhe, S. et al., Main Group Compounds. *Inorg. Synth.* **2004**, *34*, 1−48.

120. Del Castillo, T.J.; Thompson, N.B.; Peters, J. C. A Synthetic Single-Site Fe Nitrogenase: High Turnover, Freeze-Quench ^{57}Fe Mössbauer Data, and a Hydride Resting State. *J. Am. Chem. Soc.* **2016**, *138*, 5341−5350.

121. Fulmer, G.R.; Miller, A.J.M.; Sherden, N.H.; Gottlieb, H.E.; Nudelman, A.; Stoltz, B.M.; Bercaw, J.E.; Goldberg, K.I. NMR Chemical Shifts of Trace Impurities: Common Laboratory Solvents, Organics, and Gases in Deuterated Solvents Relavent to the Organometallic Chemist. *Organometallics* **2010**, *29*, 2176−2179.

122. Dolomanov, O.V.; Bourhis, L.J.; Gildea, R.J.; Howard, J.A.K., Puschmann, H. OLEX2: A Complete Structure Solution, Refinement and Analysis. *J. Appl. Crystallogr.* **2009**, *42*, 339-341.

123. Sheldrick, G. A Short Histroy of SHLEX. *Acta Crystallogr. Sect. A* **2008**, *64*, 112-122.

124. Li, Z.; Yokley, T.W.; Tran, S.L.; Zong, J.; Schley, N.D.; Brewster, T.P. Synthesis and Characterization of Rhodium-Aluminum Heterobimetallic Complexes Tethered by a 1,3-bis(diphenylphosphino)-2-popanoxy Group. *Dalton Trans*. **2019**, *48*, 8782-8790.

125. Yogi, A.; Oh, J.H.; Nishiokam T.; Tanakam, R.; Asato, E.; Kinoshita, I.; Takara, S. Synthesis and Structural Characterization of Novel Ruthenium(II) Complexes Featuring an N, N,O-Scorpionate Ligand: A Versitle Synthetic Precursor for Open-Face Scorpionatoruthenium(II) Complexes. *Polyhedron* **2010**, *29*, 1508–1514.

126. López-Hernández, A.; Müller, R.; Kopf, H.; Burzlaff, N. Bis9pyrazol-1-yl)acetato Ligands in Ruthenium Chemistry: Syntheses and Structures of Ruthenium(II) and Ruthenium(III) Complexes with bpza and bdmpza. *Eur. J. Inorg. Chem*. **2002**, 671-677.

127. Marchetti, F.; Pettinari, C.; Cerquetella, A.; Cingolani, A.; Pettinari, R.; Monari, M.; Wanke, R.; Kuznetsov, M.L.; Pombeiro, A.J.L. Switching Between κ^2 and κ^3 Bis(pyrazol-1-yl)acetate Ligands by Tuning Reaction Conditions: Synthesis, Spectral, Electrochemical, Structural, and Theoretical Studies on Arene-Ru-(II) Derivatives of Bis(azol-1-yl)acetate Ligands. *Inorg. Chem.* **2009**, *48*, 6096-6108.

128. Keter, F.K.; Ojwach, S.O.; Oyetunji, O.A.; Guzei, I.A.; Darkwa, J. Bis(pyrazolyl) Palladium(II), Platinum(II), and Gold(II) Complexes: Syntheses Molecular Structures and Substitution Reactions with L-Cysteine. *Inorg. Chim. Acta*. **2009**, *362*, 2595-2602.

129. Prantner, J.D.; Kaminsky, W.; Goldberg, K.I. Methylplatinum(II) and Molecular Oxygen: Oxidation to Methylplatinum(IV) in Competition with Methyl Group Transfer to Form Dimethylplatinum(IV). *Organometallics* **2014**, 3227-3230.

130. Rhinehart, J.L.; Manbeck, K.A; Buzak, S.K.; Lippa, G.M.; Brennessel, W.W.; Goldberg, K.I.; Jones, W.D. Catalytic Arene H/D Exchange with Novel Rhodium and Iridium Complexes. *Organometallics*, **2012**, 31, 1943-1952.

131. de la Cruz-Martinez, F.; Martinez, J.; Goana, M.A.; Fernandez-Baeza, J.; Sanchez-Barba, L. F.A.; Rodriguez, M.; Castro-Osma, J.A.; Otero, A.; Lara-Sanchez, A. Bifunctional Aluminum Catalysts for the Chemical Fixation of Carbon Dioxide into Cyclic Carbonates. *ACS Sustainable Chem. Eng.*, **2018**, 6, 5322-5332.

132. Herde, J.L.; Lambert, J.C.; Senoff, C.V. *Inorg. Synth*. **1974**, *15*, 18-19.

133. Giordano, G.; Crabtree, R.H. *Inorg. Synth.*, **1990**, *28*, 88-90.

134. Reger, D.L.; Foley, E.A.; Semeniuc, R.F.; Smith, M.D. Structural Comparisons of Silver(I) Complexes of Third-Generation Ligands Built from Tridentate ($O\text{-}C_6H_4[CH_2OCH_2C(pz)_2]_2$) (pz = Pyrazolyl Ring). *Inorg. Chem.* **2007**, 46, 11345-11355.

135. Crisenza, G.E.M.; McCreanor, N.G.; Bower, J.F. Branch-Selective, Iridium-Catalyzed Hydroarylation of Monosubstituted Alkenes via a Cooperative Destabilization Strategy. *J. Am. Chem. Soc.*, **2014**, 136, 10258-10261.

136. Soon, W. Implications of the Secondary Role of Carbon Dioxide and Methane Forcing in Climate Change. *Physical Geography* **2007**, *28*, 97-125.

137. *Carbon Dioxide as Chemical Feedstock* (Ed.: M. Aresta), Wiley-VCH, Weinhein, **2010**.

138. Song, C. Global Challenges and strategies for Control, Conversion and Utilization of CO_2 for Sustainable Development Involving Energy, Catalysis, Absorption and Chemical Processing. *Catal Today* **2006**, *115*, 2-32.

139. Kohut, R. The Long Term Effects of Carbon Dioxide on Natural Systems: Issues and Research Needs. *Environment International* **2003**, *29*, 171.-180.

140. Mohtasham, J. Review Article-Renewable Energies. *Energy Procedia* **2015**, *74*, 1289-1297.

141. Liu, Y; Wang, Z.U.; Zhaou, H.C. Recent Advances in Carbon Dioxide Capture with Metal-Organic Frameworks. *Greenhouse Gas Sci. Technol.* **2012**, 239-259.

142. Pang. S. Fuel Flexible Gas Production: Biomass, Coal, and Bio-Solid Wastes. *Fuel Flexible Energy Generation* (Ed. J. Oakey), Woodhead Publishing, **2016**, 241-269.

143. Aresta, M.; Dibenedetto, A. Utilisation of CO_2 as a Chemical Feedstock: Opportunities and Challenges. *Dalton Trans.* **2007**, 2975-2992.

144. Liu, Q.; Wu, L.; Jackstell, R.; Beller, M. Using Carbon Dioxide as a Building Block in Organic Synthesis. *Nat. Commun.* **2015**, *6*, 5933.

145. Behr, A. Carbon Dioxide as an Alternative C_1 Synthetic Unit: Activation by Transition-Metal Complexes. *Angew. Chem. Int. Ed.* **1988**, *100*, 681-698.

146. Self, S.J.; Reddy, B.V.; Rosen, M.A. Review of Underground Coal Gasification Technologies and Carbon Capture. *Int. J. Energy Environ. Eng*. **2012**, *13*, 16.

147. Van Hook, J.P. Methane-Steam Reforming. *Catalysis Reviews* **1980**, *21*, 1-51.

148. Arakawa, H. *et al*. Catalysis Research of Relevance to Carbon Management: Progress, Challenges, and Opportunities. *Chem. Rev.* **2001**, *101*, 953-996.

149. Benson, E.E.; Kubiak, C.P, Sathrum, A.J.; Smieja, J.M. Electrocatalytic and Homogeneous Approaches to Conversion of CO_2 to Liquid Fuels. *Chem. Soc. Rev.* **2009**, *38, 89-99.*

150. Andersson, I.; Backlund, A. Structure and Function of Rubisco. *Plant Physiology and Biochemistry* **2008**, *46*, 275-291.

151 Zevenhoven, R.; Eloneva, S.; Teir, S. Chemical Fixation of CO_2 in Carbonates: Routes to Valuable Products and Long-Term Storage. *Catalysis Today* **2006**, *115*, 73-79.

152. Sakakura, T.; Kohno, K. The Synthesis of Organic Carbonates from Carbon Dioxide. *Chem. Commun*. **2009**, 1312-1330.

153. Zhang, Q.; Yuan, H.-Y.; Fukaya, N.; Yasuda, H.; Choi, J.-C. Direct Synthesis of Carbamate from CO_2 Using a Task-Specific Ionic Liquid Catalyst. *Green Chem.* **2017**, *19*, 5614-5624.

154. Ion, A.; Van Doorslaer, C.; Parvulescu, V.; Jacobs, P.; De Vos, D. Green Synthesis of Carbamates from CO_2, Amines and Alcohols. *Green Chem*. **2008**, *10*, 111-116.

155. Liu, A.-H.; Yu, B.; He, L.-N. Catalytic Conversion of Carbon Dioxide to Carboxylic Acid Derivatives. *Greenhouse Gas Sci Technol.* **2014**, 1-17.

156. Aida, T.; Inoue, S. Activation of Carbon Dioxide with Aluminum Porphyrin and Reaction with Epoxide. Studies on Tetraphenylprophinato)aluminum Alkoxide Having a Long Oxyalkylene Chain as the Alkoxide Group. *J. Am. Chem. Soc.* **1983**, *105*, 1304-1309.

157. Arafa, I.M.; Shin, K.; Goff, H.M. Carbon Monoxide and Carbon Dioxide Carbon-Metal Bond Insertion Chemistry of Alkyliron(III) Porphyrin Complexes. *J. Am. Chem. Soc.* **1988**, *110*, 5228-5229.

158. Cocolious, P.; Guilard, R.; Bayeul, D.; Lecomte, C. Carbon Dioxide Insertion Into the Methyl-Indium σ Bond of Methylindium(III) Porphyrins. Molecular Sterochemistry of (Acetato)(2,3,7,8,12,13,17,18-octaethylporphyrinato)indium(III). *Inorg. Chem.* **1985**, *24*, 2058-2062.

159. Arai, T.; Sato, Y.; Inoue, S. Reaction of Carbon Dioxide with (Porphyrinato)aluminum Thiolates. *Chem. Lett.* **1990**, 551-554.

160. Ema, T.; Miyazaki, Y.; Koyama, S.; Yano, Y.; Sakai, T. A Bifunction Catalyst for Carbon Dioxide Fixation: Cooperative Double Activation of Epoxides for the Synthesis of Cyclic Carbonates. *Chem. Commun.* **2012**, *48*, 4489-4491.

161. Jin, L.; Jing, H.; Chang, T.; Bu, X.; Wang, L.; Liu, Z. Metal Poryphyrin/phenyltrimethylammonium tribromide: High Efficient Catalysts for Coupling Reaction of CO_2 and Epoxides. *J. Mol. Catal. A Chem.* **2007**, *261*, 262-267.

162. Kasuga, K.; Mariwaki, N; Handa, M. Reaction of Caron Dioxide with tetra-t-butylphtalocyaninato-aluminum(III) -ethylate or -ethoxide. *Inorg. Chim.. Acta.* **1996**, *244*, 137-139.

163. Weidlein, J. CO_2-Einshciebungsreaktionen bei Aluminum-, Gallium, und Indiumalkylverbidungen. *Zeitschrift für Anorganische und Allgemeine Chemie* **1970**, *378*, 245-262.

164. Ziegler, Karl. Metallorganische Verbindungen, XLI Reaktionen der Aluminumtrialkyle mut Kohlendioxyd und Schwefeldioxyd. *Justus Liebigs Annalen der Chemie* **1960,** *629*, 251.

165. Reaction of aluminum trialkyls with carbon dioxide. *Izvestiya Akademii Nauk SSSR, Seriya Khimicheskaya* **1974**, 853-856

166. Mömming, C.M.; Otten, E.; Kehr, G.; Fröhlich, R.; Grimme, S.; Stephan, D.W.; Erker, G. Reversible Metal-Free Carbon Dioxide Binding by Frustrated Lewis Pairs. *Angew. Chem. Int. Ed.* **2009**, *48*, 6643-6646.

167. Ménard, G. Stephan, D.W. Room Temperature of CO_2 to Methanol by Al-Based Frustrated Lewis Pairs and Ammonia Borane. *J. Am. Chem. Soc.* **2010**, *132*, 1796-1797.

168. Donets, P.A; Cramer, N. Diaminophoshine Oxide Ligand Enabled Asymmetric Nickel-Catalyzed Hydrocarbamoylations of Alkenes. *J. Am. Chem. Soc.* **2013**, *135*, 11772-11775.

169. Francis, J.A.; Bott, S.G.; Barron, A.R. Aluminum Compounds Containing Bidentate Ligands: Chelate Ring Size and Rigid Conformation Effects. *Dalton Trans.* **1998**, 3305-3310.

170. DeYonker, N.J., Webster, C. E. The trans-cis isomerization of Ni(η^2-TEMPO)$_2$: Interconnections and conformational complexity. *Inorg. Chim. Acta*. **2015**, 436, 220-229.

171. Habershon, S. Automated Prediction of Catalytic Mechanism and Rate Law Using Graph-Based Reaction Path Sampling. *J. Chem. Theory. Comput.* **2016**, 12, 1786-1798.

172. Frisch, M. J.; Trucks, G. W.; Schlegel, H. B.; Scuseria, G. E.; Robb, M. A.; Cheeseman, J. R.; Scalmani, G.; Barone, V.; Petersson, G. A.; Nakatsuji, H.; Li, X.; Caricato, M.; Marenich, A. V.; Bloino, J.; Janesko, B. G.; Gomperts, R.; Mennucci, B.; Hratchian, H. P.; Ortiz, J. V.; Izmaylov, A. F.; Sonnenberg, J. L.; Williams-Young, D.; Ding, F.; Lipparini, F.; Egidi, F.; Goings, J.; Peng, B.; Petrone, A.; Henderson, T.; Ranasinghe, D.; Zakrzewski, V. G.; Gao, J.; Rega, N.; Zheng, G.; Liang, W.; Hada, M.; Ehara, M.; Toyota, K.; Fukuda, R.; Hasegawa, J.; Ishida, M.; Nakajima, T.; Honda, Y.; Kitao, O.; Nakai, H.; Vreven, T.; Throssell, K.; Montgomery, J. A.; Peralta, J. E.; Ogliaro, F.; Bearpark, M. J.; Heyd, J. J.; Brothers, E. N.; Kudin, K. N.; Staroverov, V. N.; Keith, T. A.; Kobayashi, R.; Normand, J.; Raghavachari, K.; Rendell, A. P.; Burant, J. C.; Iyengar, S. S.; Tomasi, J.; Cossi, M.; Millam, J. M.; Klene, M.; Adamo, C.; Cammi, R.; Ochterski, J. W.; Martin, R. L.; Morokuma, K.; Farkas, O.; Foresman, J. B.; Fox, D. J. GAUSSIAN 16, Revision B.01; Gaussian Inc., Wallingford, CT. **2016**.

173. Parr, R. G.; Yang, W. Density Functional Theory of Atoms and Molecules; Oxford University Press: New York, **1989**.

174. Becke, A. Density-Functional Thermochemistry. 3. the Role of Exact Exchange. *J. Chem. Phys.* **1993**, *98*, 5648−5652.

175. Hay, P.; Wadt, W. Abinitio Effective Core Potentials for Molecular Calculations - Potentials for K to Au Including the Outermost Core Orbitals. *J. Chem. Phys.* **1985**, *82*, 299−310.

176. Hay, P.; Wadt, W. Abinitio Effective Core Potentials for Molecular Calculations - Potentials for the Transition-Metal Atoms Sc to Hg. *J. Chem. Phys.* **1985**, *82*, 270−283.

177. Hariharan, P. C.; Pople, J. A. Influence of Polarization Functions on Molecular-Orbital Hydrogenation Energies. *Theor. Chim. Acta* **1973**, *28*, 213−222.

178. Barone, V.; Cossi, M. Quantum Calculation of Molecular Energies and Energy Gradients in Solution by a Conductor Solvent Model. *J. Phys. Chem. A* **1998**, *102*, 1995−2001.

179. Cossi, M.; Rega, N.; Scalmani, G.; Barone, V. Energies, Structures, and Electronic Properties of Molecules in Solution with the C-PCM Solvation Model. *J. Comput. Chem.* **2003**, *24*, 669−681.

Appendix A: Spectral Data for Chapter 2

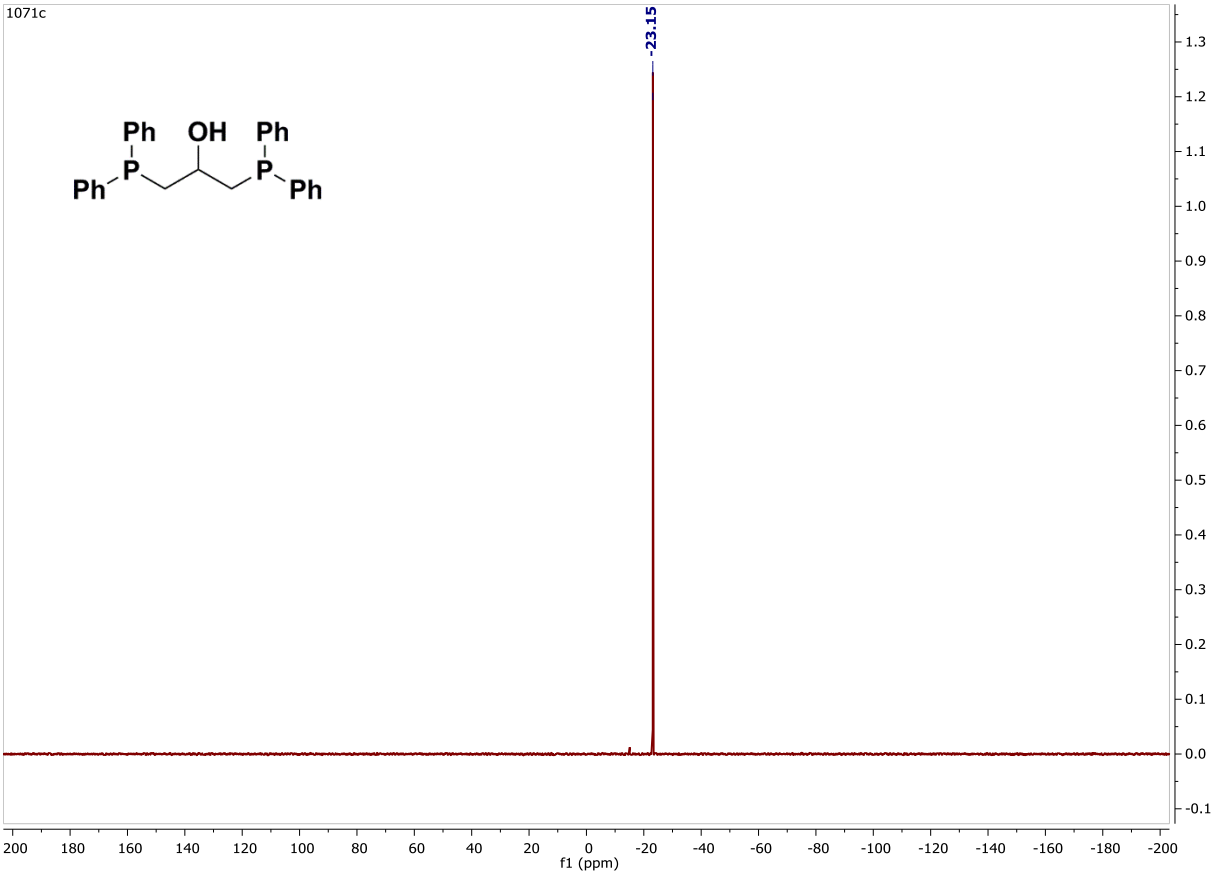

Figure A1. $^{31}P\{^{1}H\}$ NMR spectrum of DPPP-OH in $CDCl_3$.

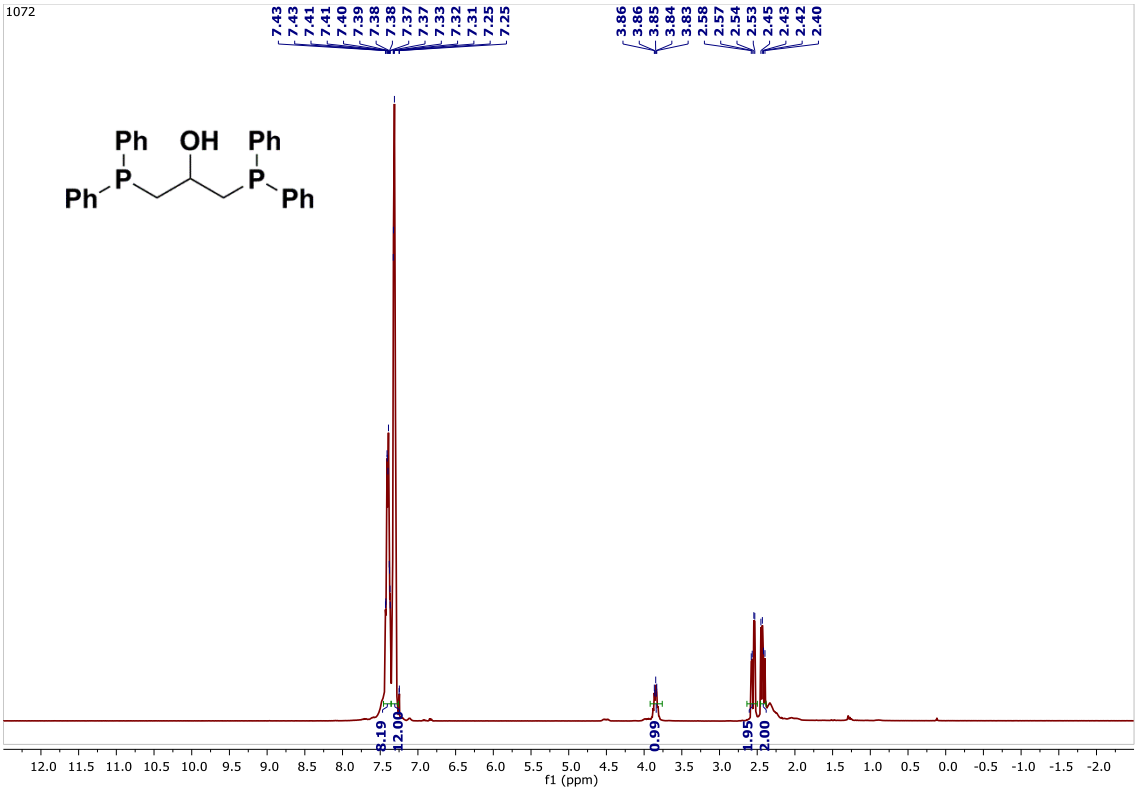

Figure A2. ^{1}H NMR spectrum of DPPP-OH in $CDCl_3$.

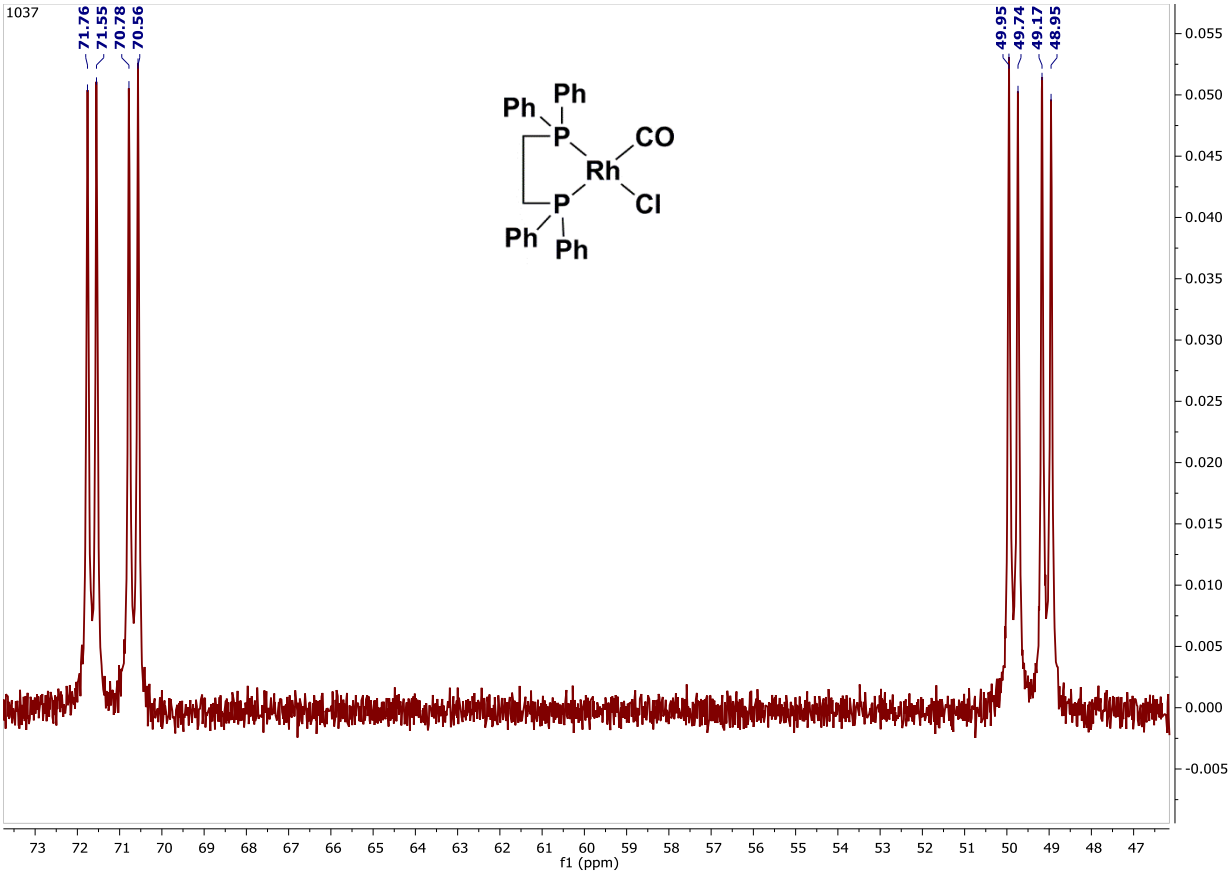

Figure A3. $^{31}P\{^{1}H\}$ NMR spectrum of Rh(DPPE)(CO)Cl in $CDCl_3$.

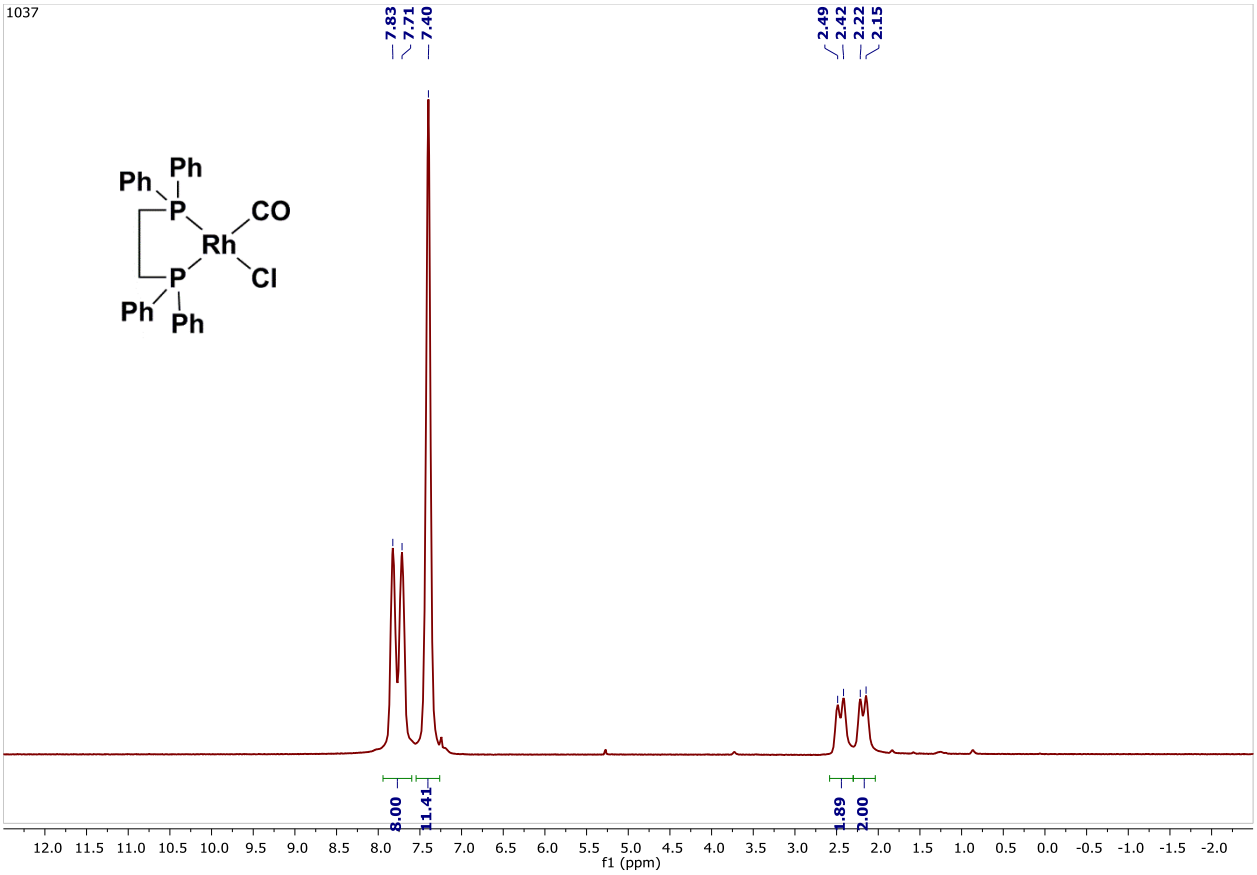

Figure A4. ^{1}H NMR spectrum of Rh(DPPE)(CO)Cl in $CDCl_3$.

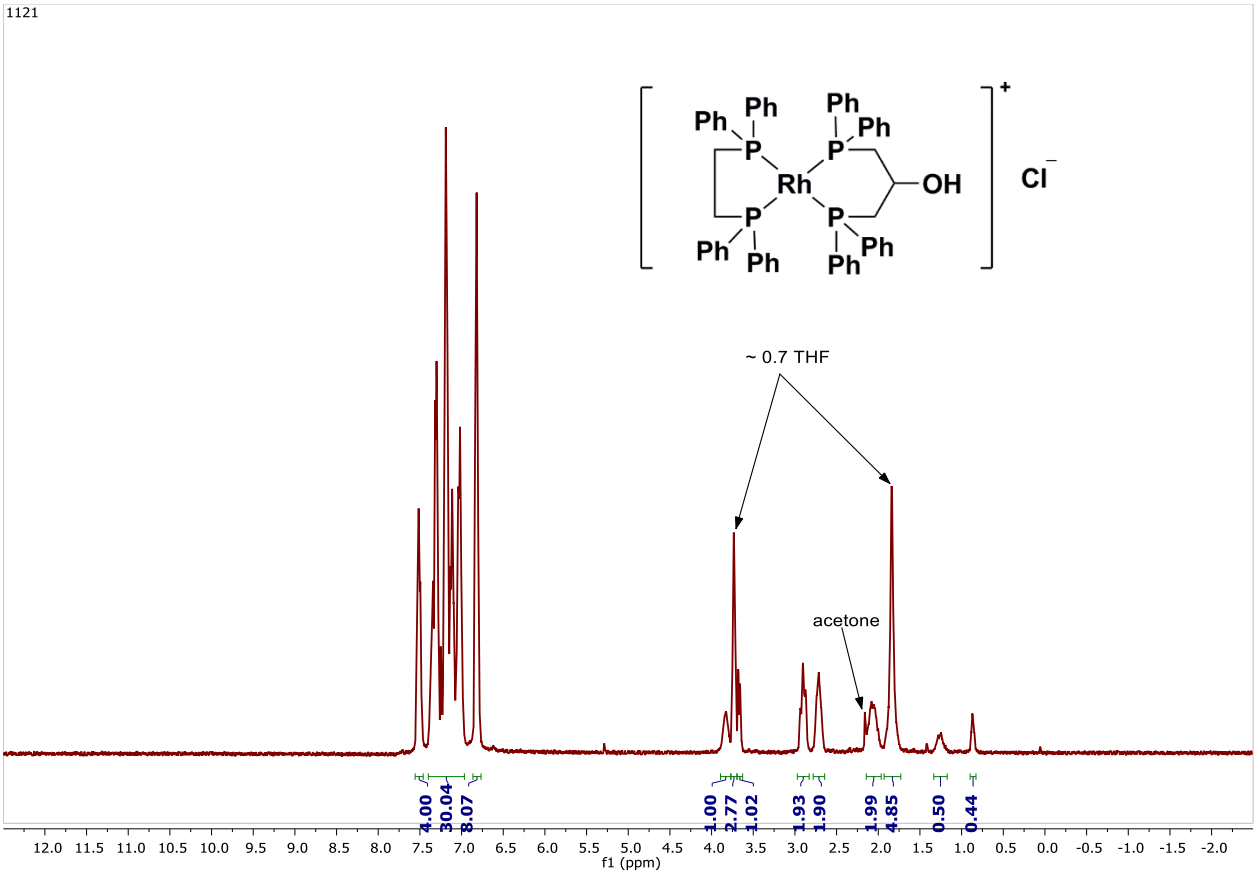

Figure A5. ^{1}H NMR spectrum of Rh(DPPE)(DPPP-OH)Cl (**1**) in $CDCl_3$.

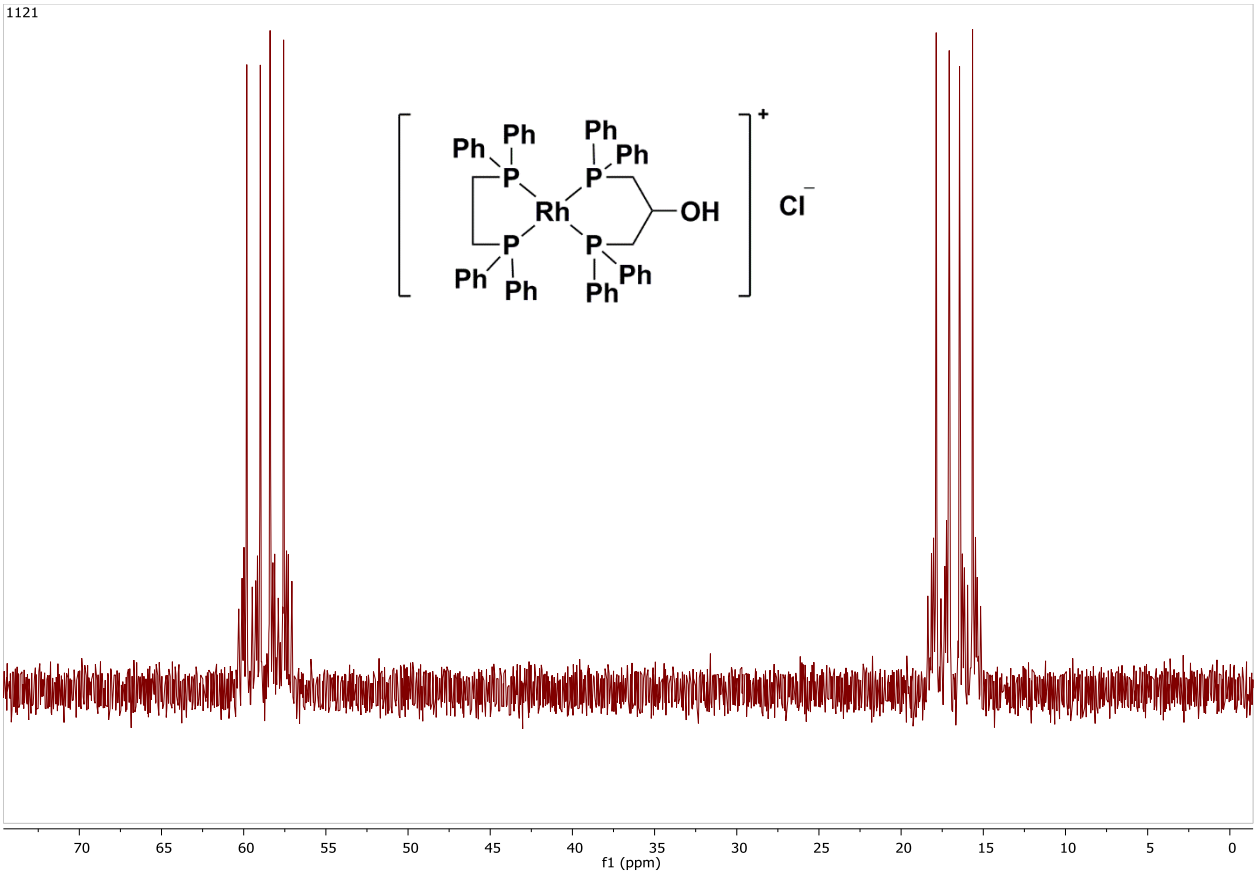

Figure A6. $^{31}P\{^{1}H\}$ NMR spectrum of **1** in $CDCl_3$.

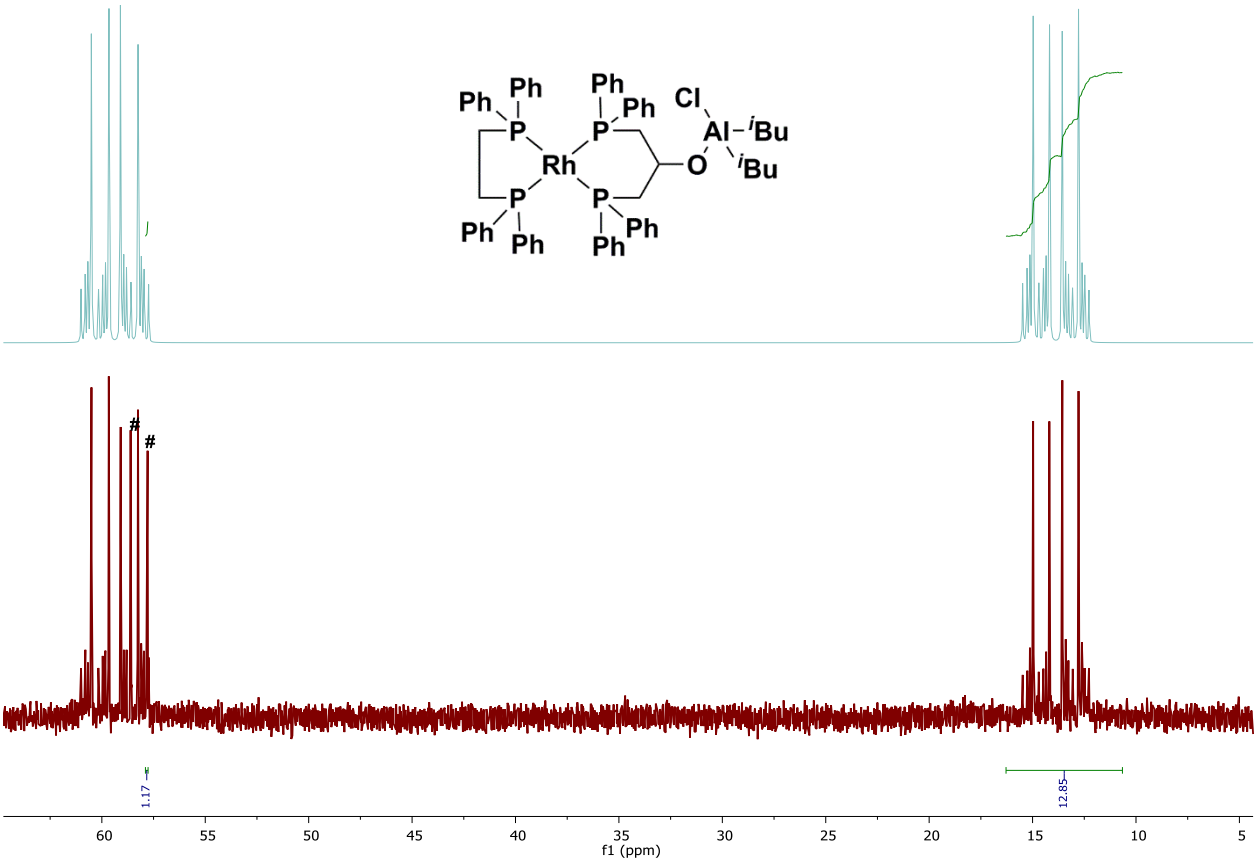

Figure A7. Modeled (top) and measured (bottom) $^{31}P\{^{1}H\}$ NMR spectra of Rh(DPPE)(DPPP-O-Al^{i}Bu$_2$Cl) (**2**). The peaks for byproduct Rh(DPPE)$_2$Cl are denoted with #. Integration values used to quantify by product.

List of peaks and coupling constants in **2**: $^{31}P\{^{1}H\}$ NMR (162 MHz, tetrahydrofuran-d$_8$) δ 59.37 (DP*P*E, J_{Rh} = 107.2 Hz, J_{trans} = 205.5 Hz, $J_{cis,\ B\text{-}B'}$ = -22.6 Hz, $J_{cis,\ B\text{-}A'}$ = -29.2 Hz), 58.20 (Rh(DP*P*E)$_2$Cl, d, J = 132.8 Hz), 13.90 (DP*P*P-OH, J_{Rh} = 101.2 Hz, J_{trans} = 205.5 Hz, $J_{cis\ A\text{-}A'}$ = -39.4 Hz, $J_{cis,\ A\text{-}B'}$ = -29.2 Hz).

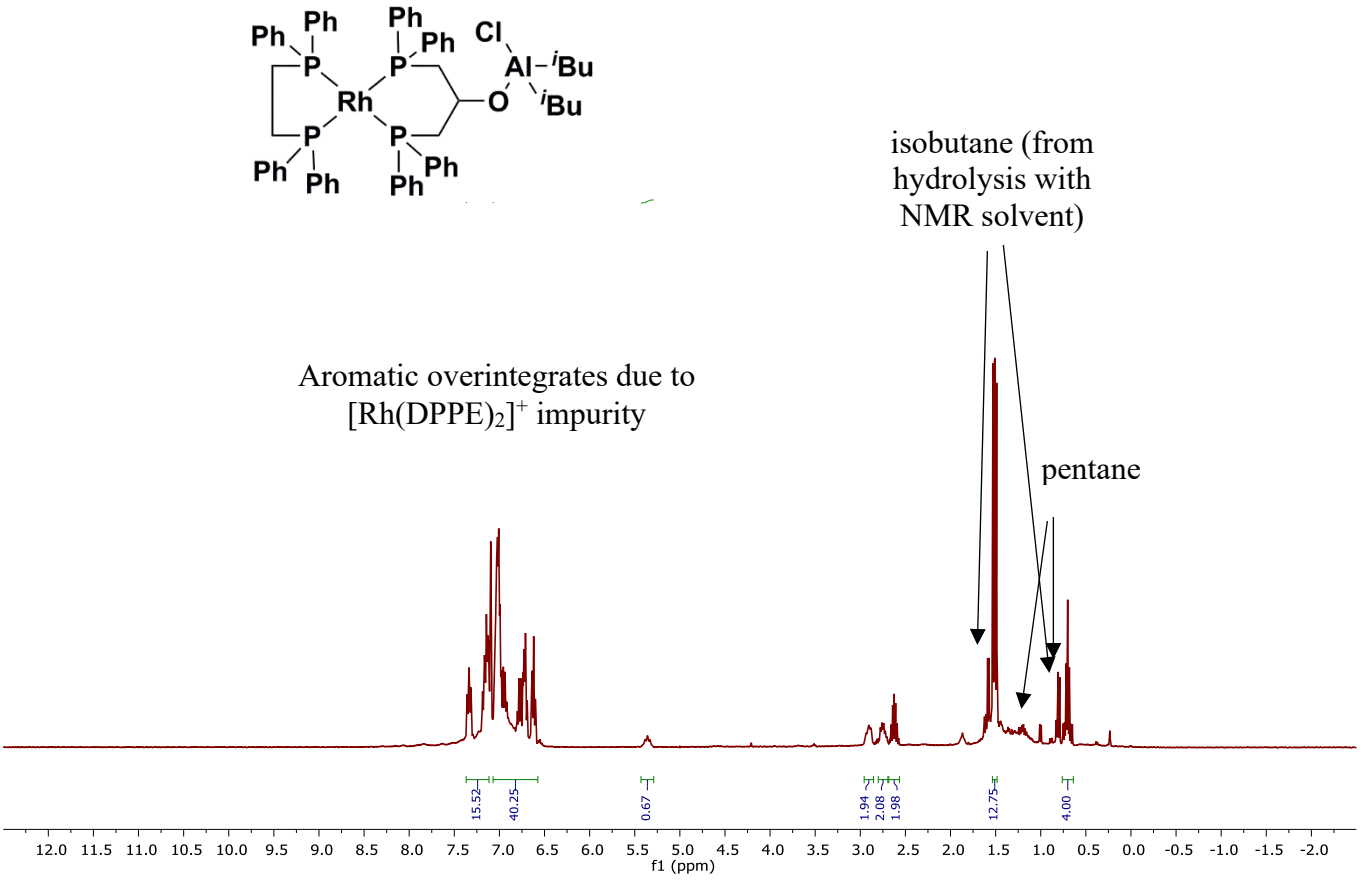

Figure A8. ^{1}H NMR spectrum of **2** in tetrahydrofuran-d_8. Impurity in alkyl region is pentane. Overintegration of aromatic signals due to 5% [Rh(DPPE)$_2$]Cl impurity.

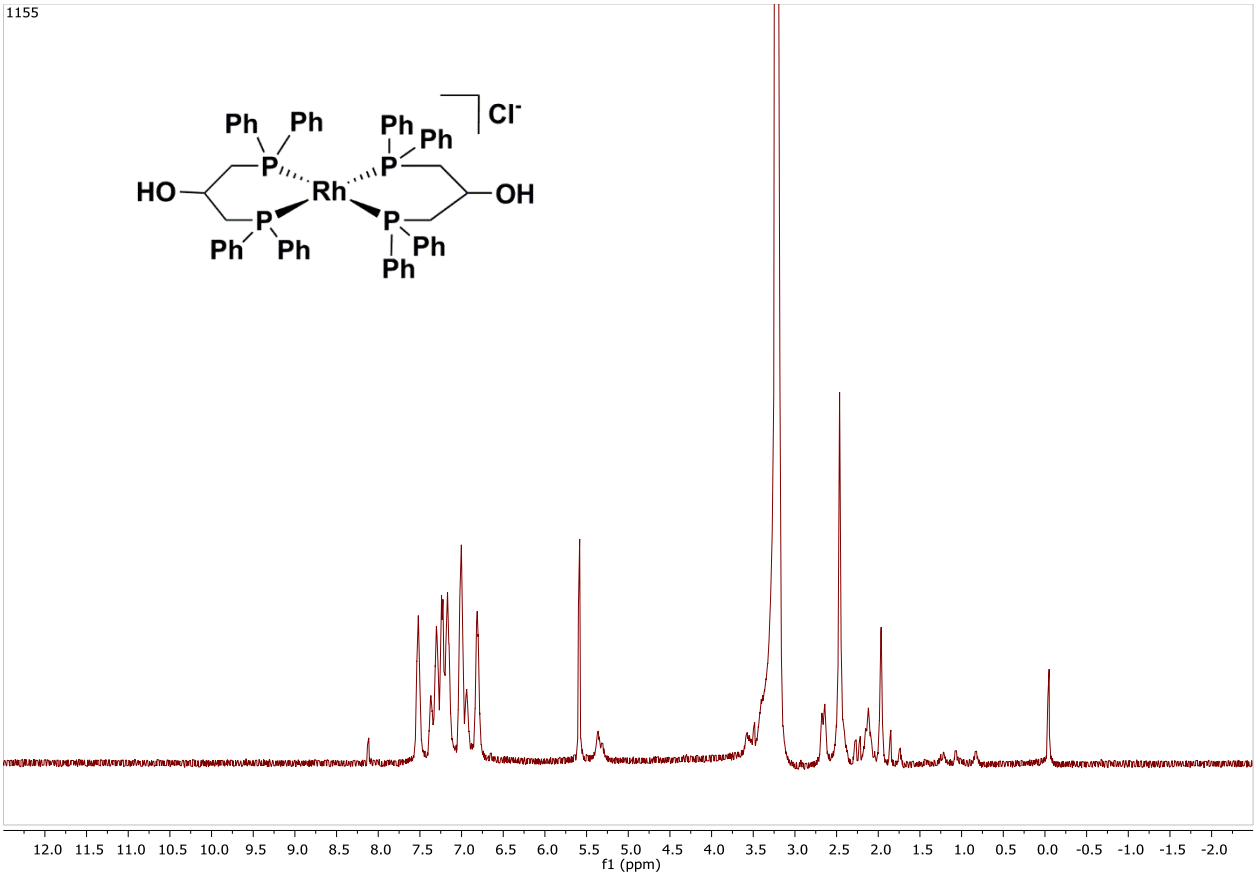

Figure A9. ^{1}H NMR spectrum of isomeric mixture of Rh(DPPP-OH)$_2$Cl (**3**) in DMSO-d_6.

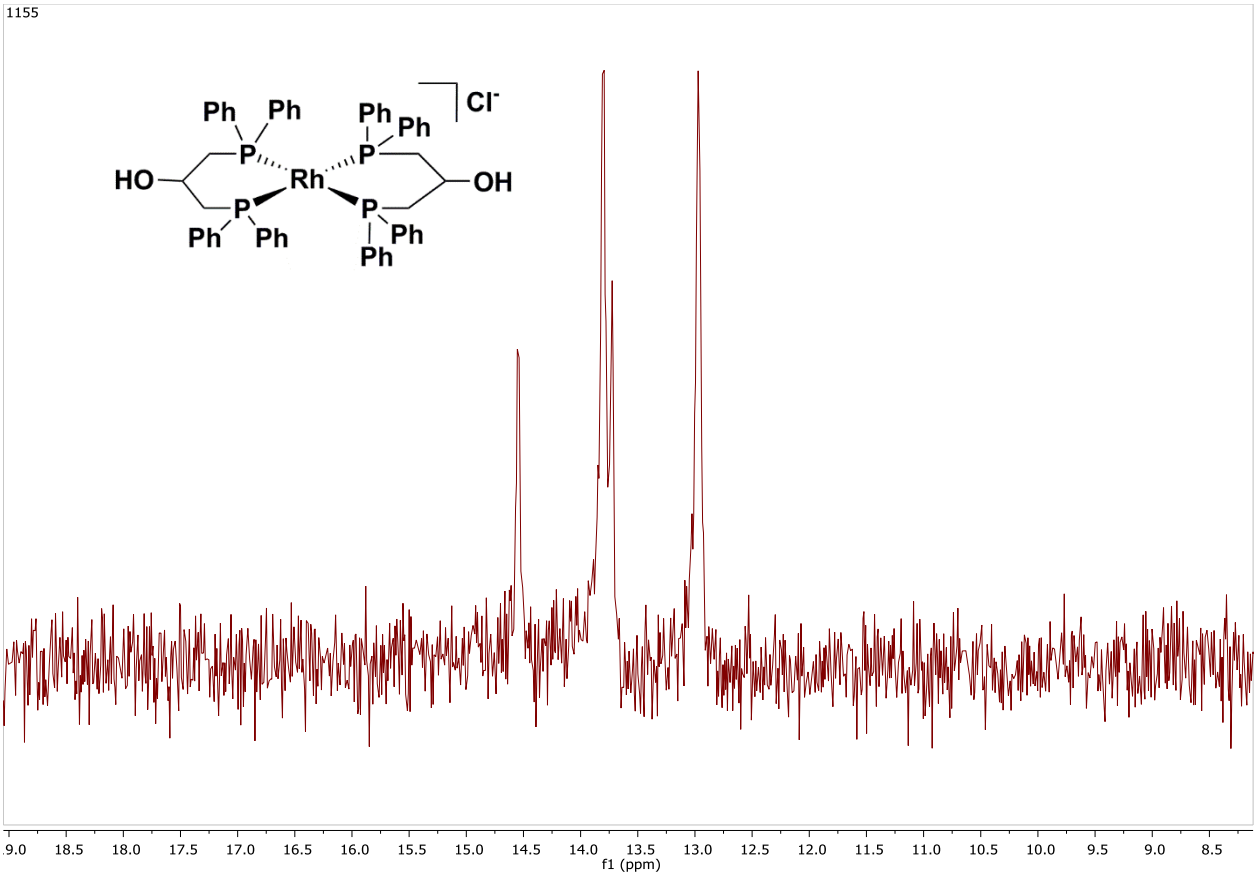

Figure A10. $^{31}P\{^{1}H\}$ NMR spectrum of isomeric mixture **3** in DMSO-d_6.

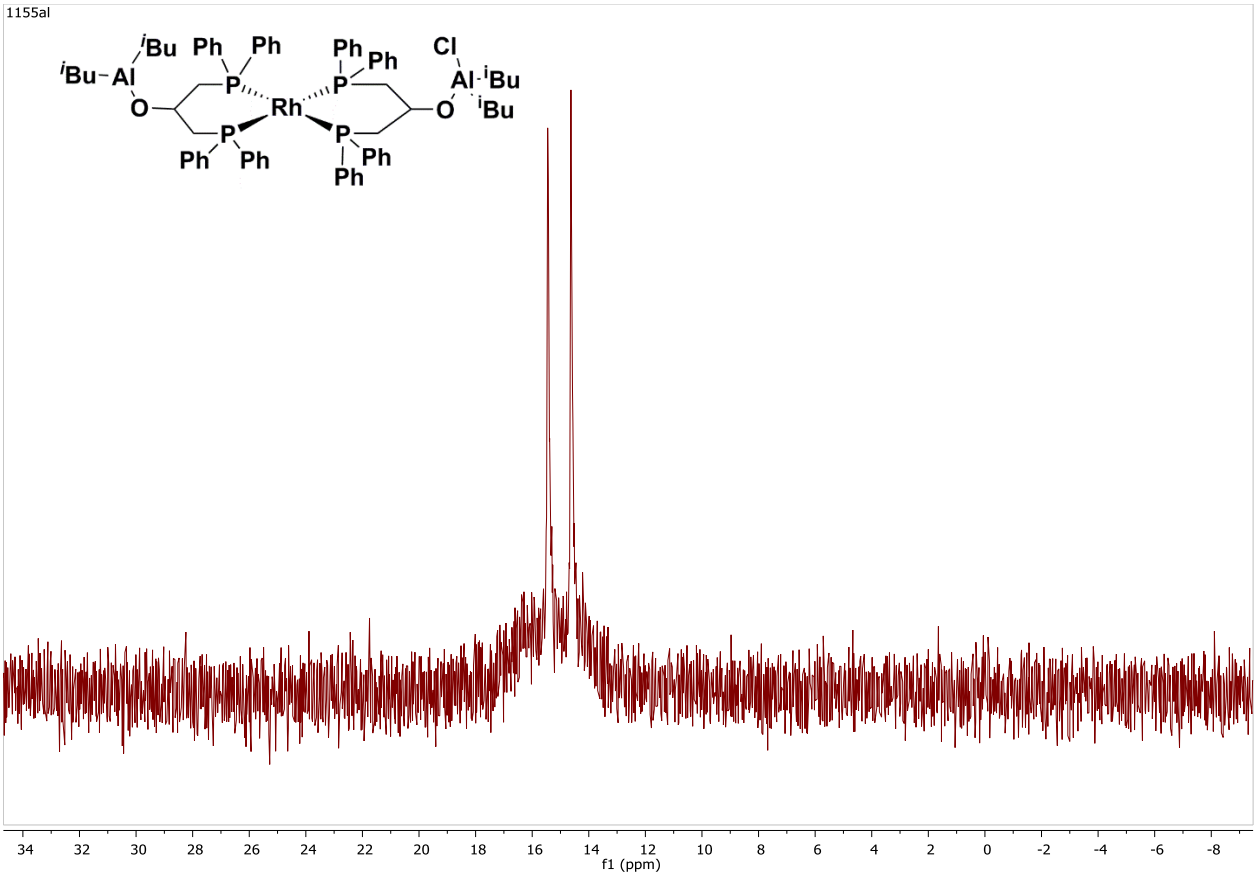

Figure A11. Room temperature $^{31}P\{^{1}H\}$ NMR spectrum of Rh(DPPP-O-Al^{i}Bu$_2$)(DPPP-O-Al^{i}Bu$_2$Cl) (**4**) in CD_2Cl_2.

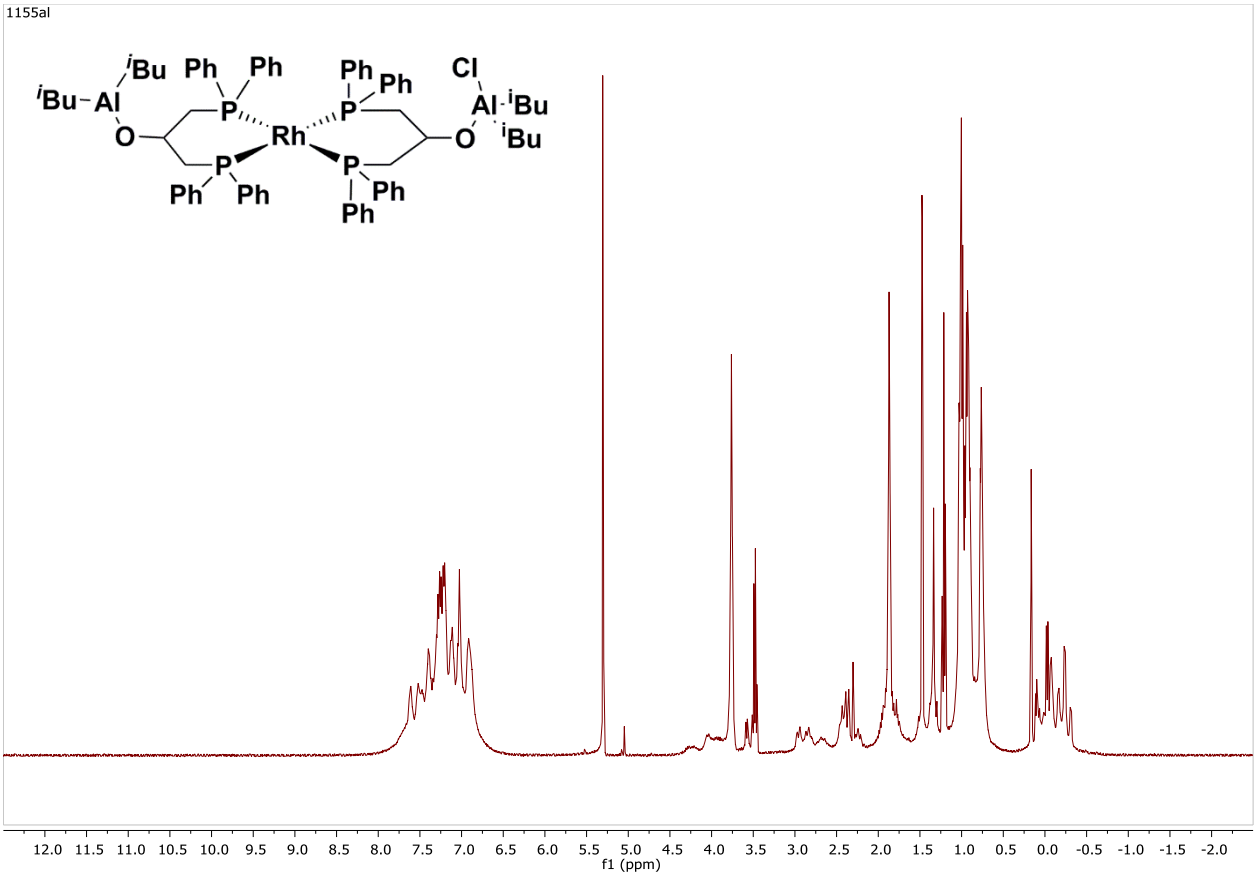

Figure A12. ^{1}H NMR of **4** product mixture in CD_2Cl_2.

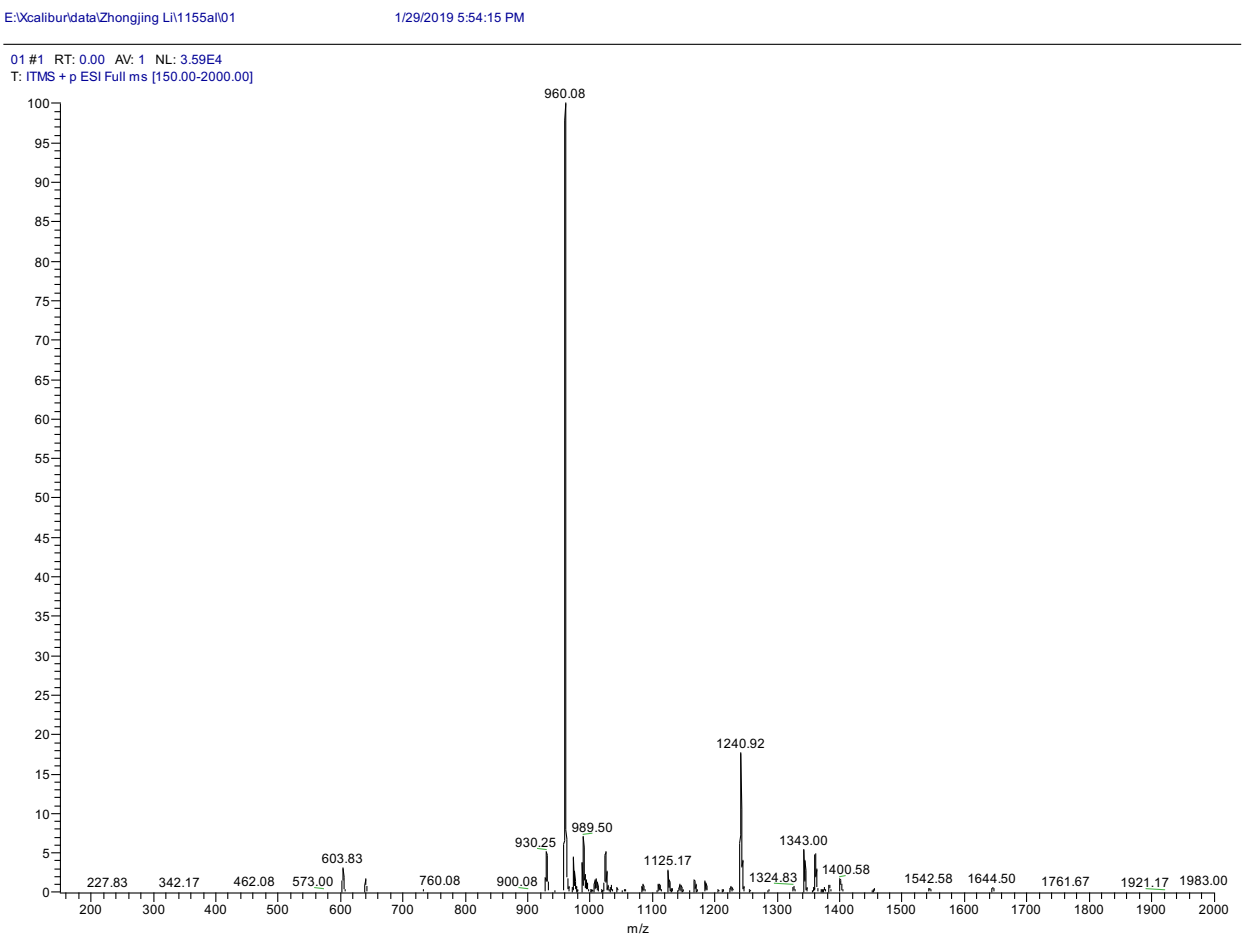

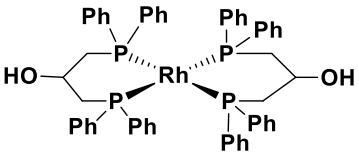

A

Chemical Formula: $C_{54}H_{52}O_2P_4Rh$
Exact Mass: 959.20
Molecular Weight: 959.81
m/z: 959.20 (100.0%), 960.20 (58.4%), 961.20 (16.7%), 962.21 (2.3%)

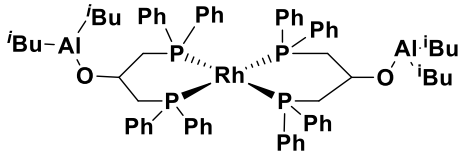

B

Chemical Formula: $C_{70}H_{86}Al_2O_2P_4Rh$
Exact Mass: 1239.43
Molecular Weight: 1240.22
m/z: 1239.43 (100.0%), 1240.43 (75.7%), 1241.43 (28.3%), 1242.44 (6.7%), 1243.44 (1.3%)

Figure A13. ESI-MS data for **4**. The base peak (m/z = 960 corresponds to fragment A above. The high mass peak (m/z =1144) corresponds to fragment B above. Isotope pattern from high-resolution experiment can be found in Figure A15, below.

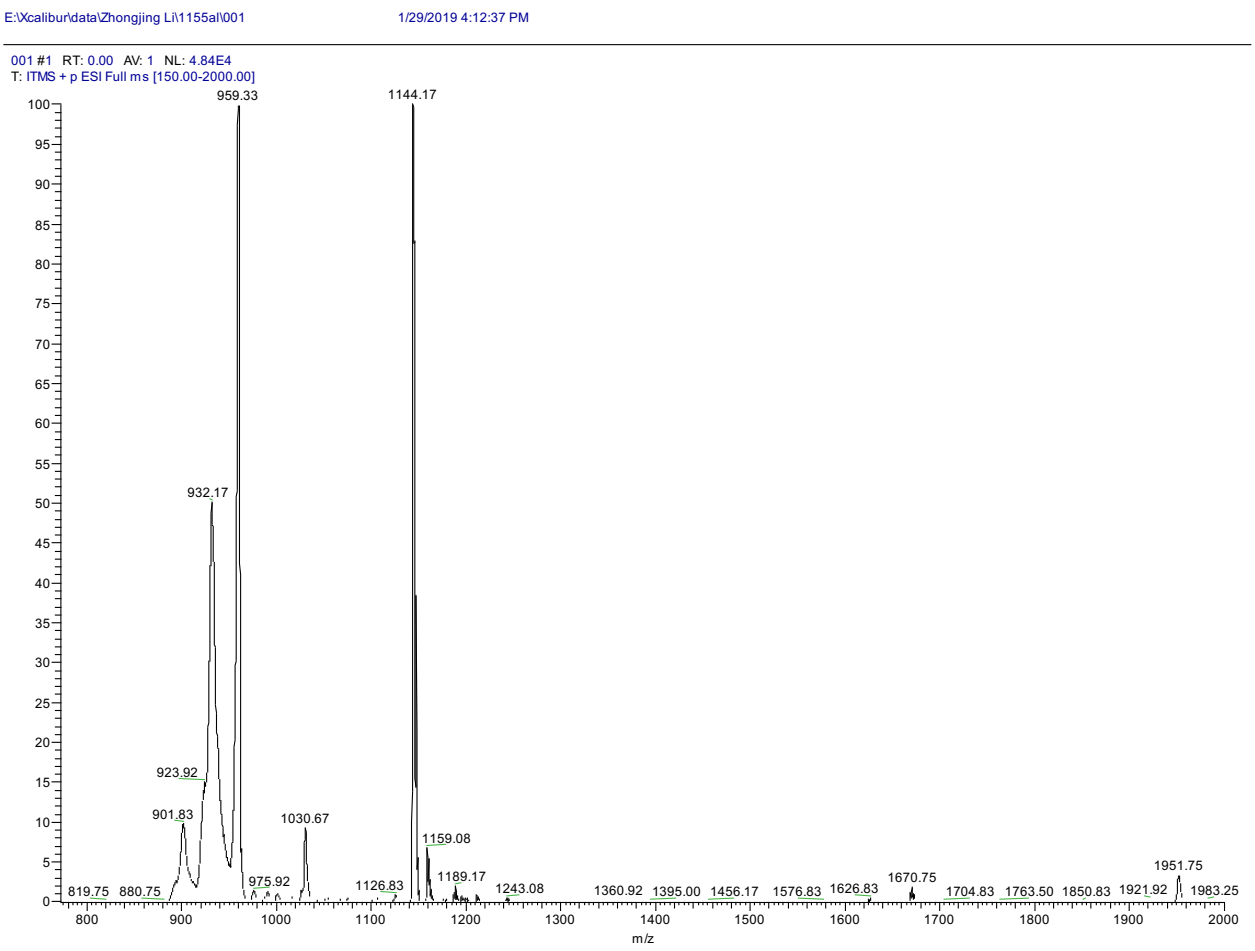

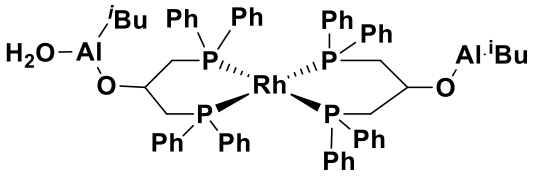

Chemical Formula: $C_{62}H_{70}Al_2O_3P_4Rh$
Exact Mass: 1143.30
Molecular Weight: 1144.00
m/z: 1143.30 (100.0%), 1144.30 (67.1%), 1145.30 (22.1%), 1146.31 (4.8%)

Figure A14. ESI-MS data for **4**. The base peak (m/z = 960 corresponds to fragment A in Figure A13 above. The high mass peak (m/z =1144) corresponds to the fragment above, a hydrated fragment generated (water acquired during the injection).

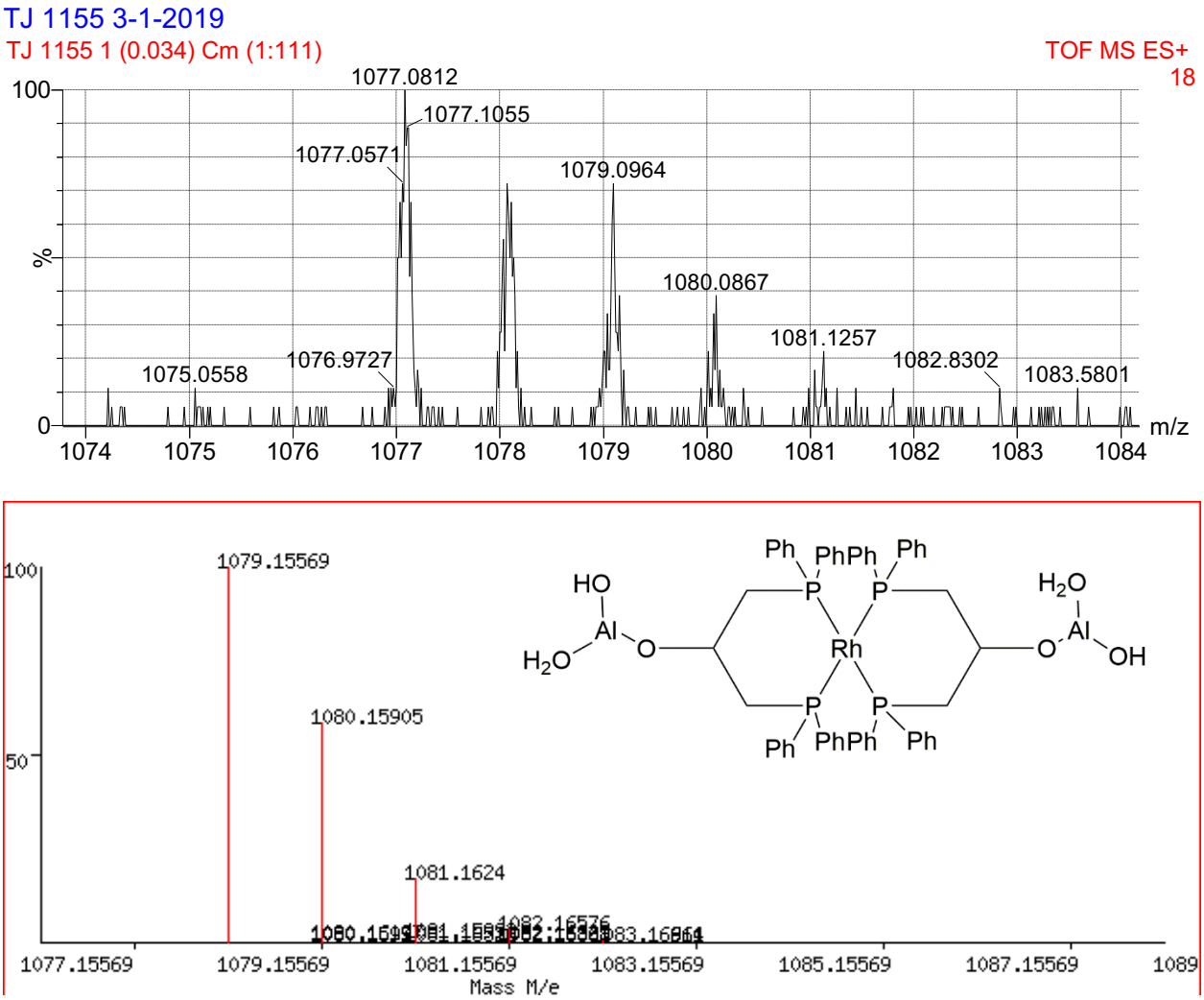

Figure A15. HRMS data for **4**. Top: measured data. Bottom: predicted isotope pattern. Value calculated for $[C_{54}H_{54}Al_2O_6P_4Rh]^+$ (product of alkyl hydrolysis) m/z calc: 1079.1557. Found: 1079.0964. Peaks at 1077 and 1078 correspond to hydrolysis product less two or one hydrogen atoms, respectively.

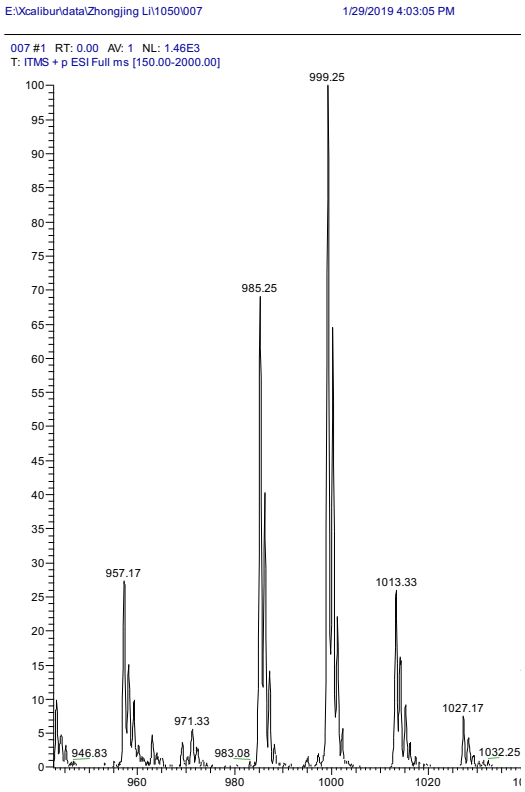

Figure A16. ESI-MS data for **2**. Corresponding fragments are shown below.

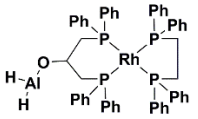

Chemical Formula: $C_{53}H_{51}AlOP_4Rh$
Exact Mass: 957.18
Molecular Weight: 957.77
m/z: 957.18 (100.0%), 958.18 (57.3%), 959.18 (14.5%), 960.19 (2.7%), 959.18 (1.7%)

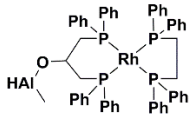

Chemical Formula: $C_{54}H_{53}AlOP_4Rh$
Exact Mass: 971.19
Molecular Weight: 971.80
m/z: 971.19 (100.0%), 972.20 (58.4%), 973.20 (15.1%), 974.20 (2.8%), 973.20 (1.7%)

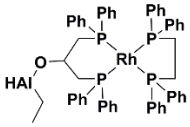

Chemical Formula: $C_{55}H_{55}AlOP_4Rh$
Exact Mass: 985.21
Molecular Weight: 985.83
m/z: 985.21 (100.0%), 986.21 (59.5%), 987.21 (15.7%), 988.22 (3.0%), 987.21 (1.7%)

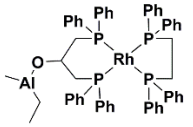

Chemical Formula: $C_{56}H_{57}AlOP_4Rh$
Exact Mass: 999.22
Molecular Weight: 999.85
m/z: 999.22 (100.0%), 1000.23 (60.6%), 1001.23 (16.4%), 1002.23 (3.1%), 1001.23 (1.7%)

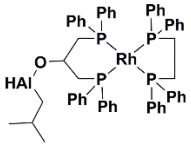

Chemical Formula: $C_{57}H_{59}AlOP_4Rh$
Exact Mass: 1013.24
Molecular Weight: 1013.88
m/z: 1013.24 (100.0%), 1014.24 (61.6%), 1015.25 (17.0%), 1016.25 (3.3%), 1015.25 (1.7%)

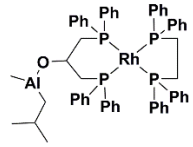

Chemical Formula: $C_{58}H_{61}AlOP_4Rh$
Exact Mass: 1027.25
Molecular Weight: 1027.91
m/z: 1027.25 (100.0%), 1028.26 (62.7%), 1029.26 (17.7%), 1030.26 (3.9%), 1029.26 (1.7%)

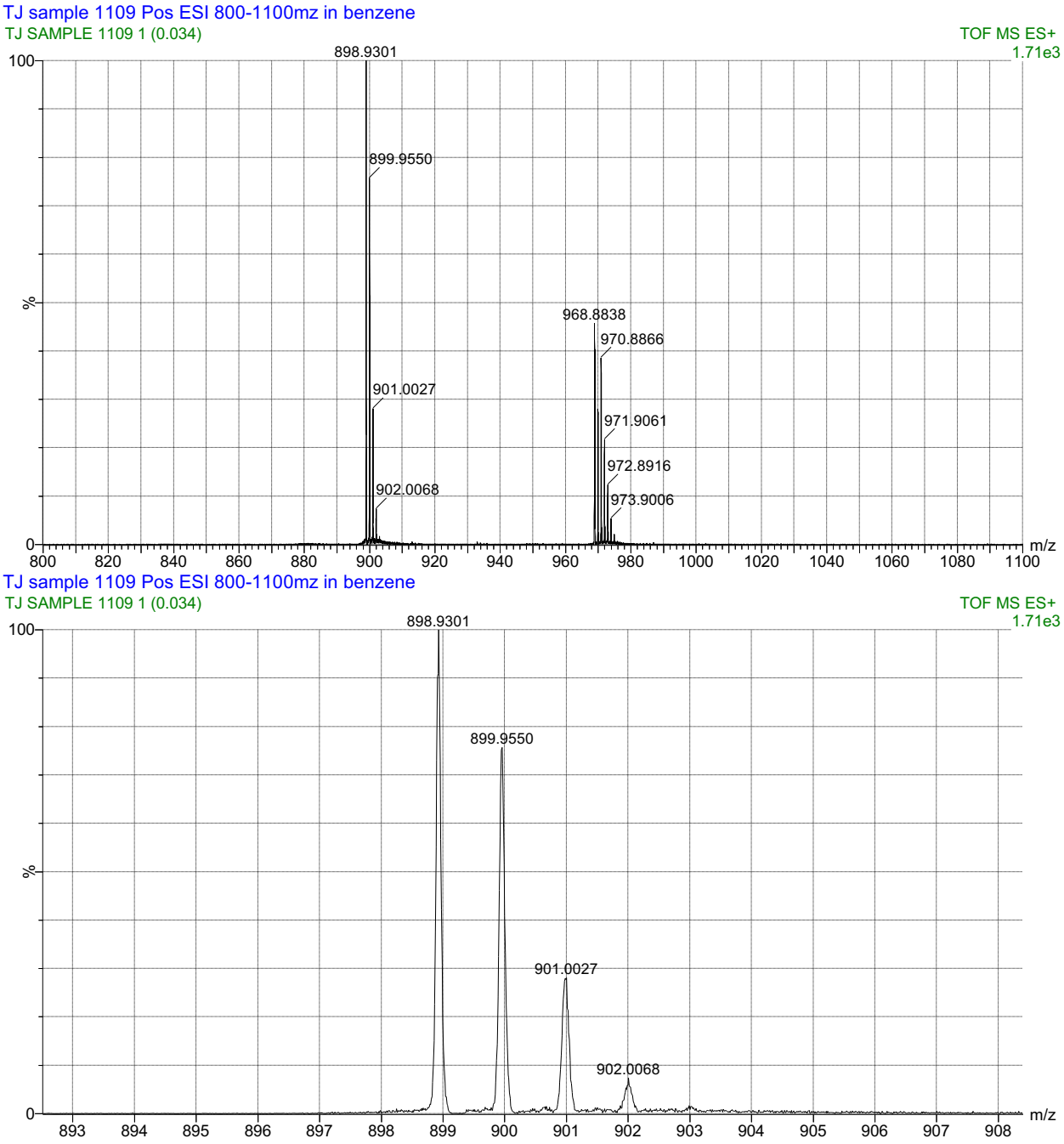

Figure A17a. HRMS data for **2**. Top: Full measured mass spectrum. Bottom: Observed isotope pattern for major impurity [Rh(DPPE)$_2$][Cl]. Value calculated for $[C_{52}H_{48}P_4Rh]^+$ (M-Cl$^+$) m/z calc: 899.1761. Found: 898.9301.

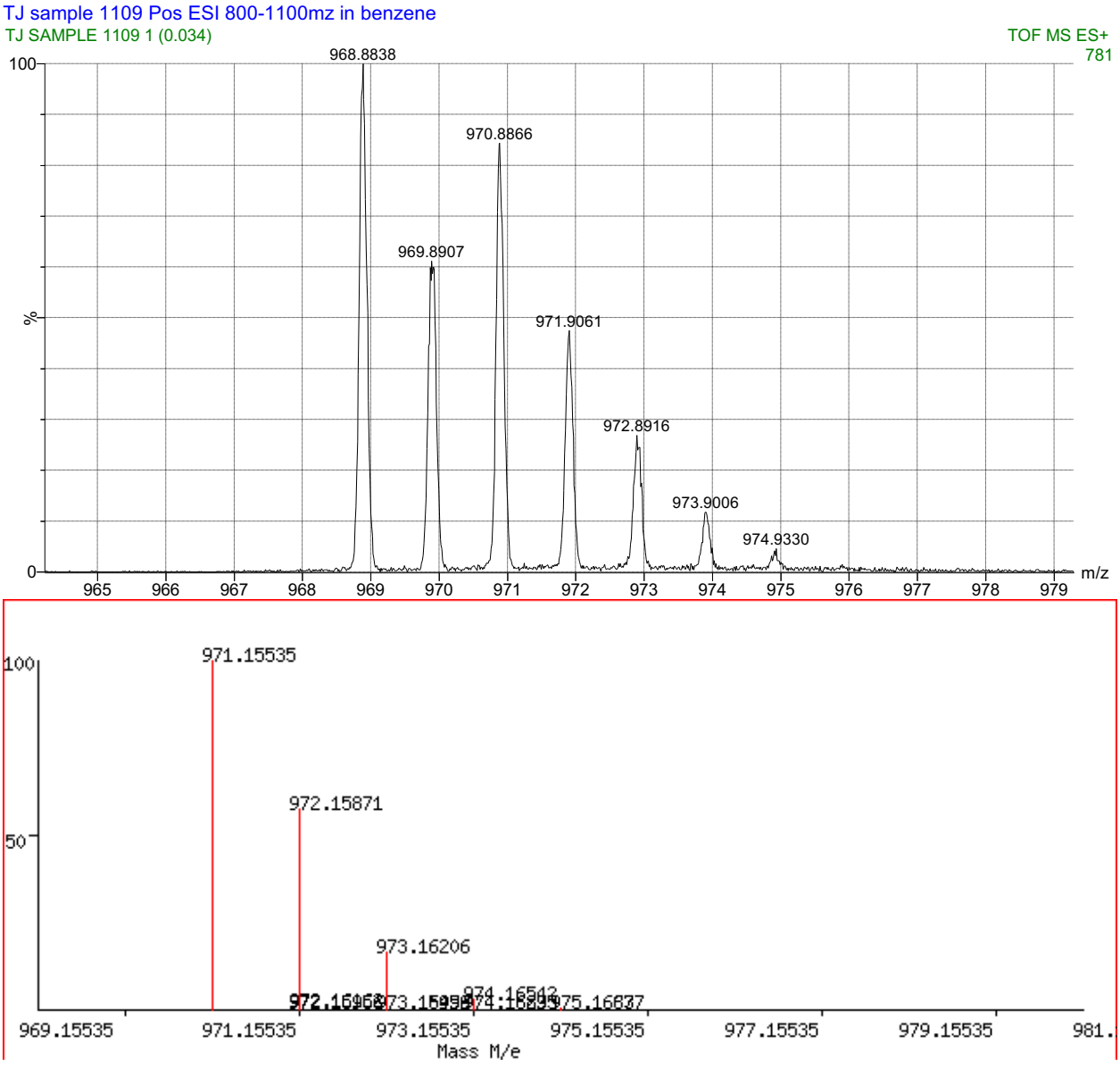

Figure A17b. HRMS data for **2**. Top: measured data. Bottom: predicted isotope pattern. Value calculated for $[C_{53}H_{50}Al_2O_4P_4Rh]^+$ (product of alkyl hydrolysis) m/z calc: 971.1554. Found: 970.8866. Peaks at 969 and 970 correspond to hydrolysis product less two or one hydrogen atoms, respectively.

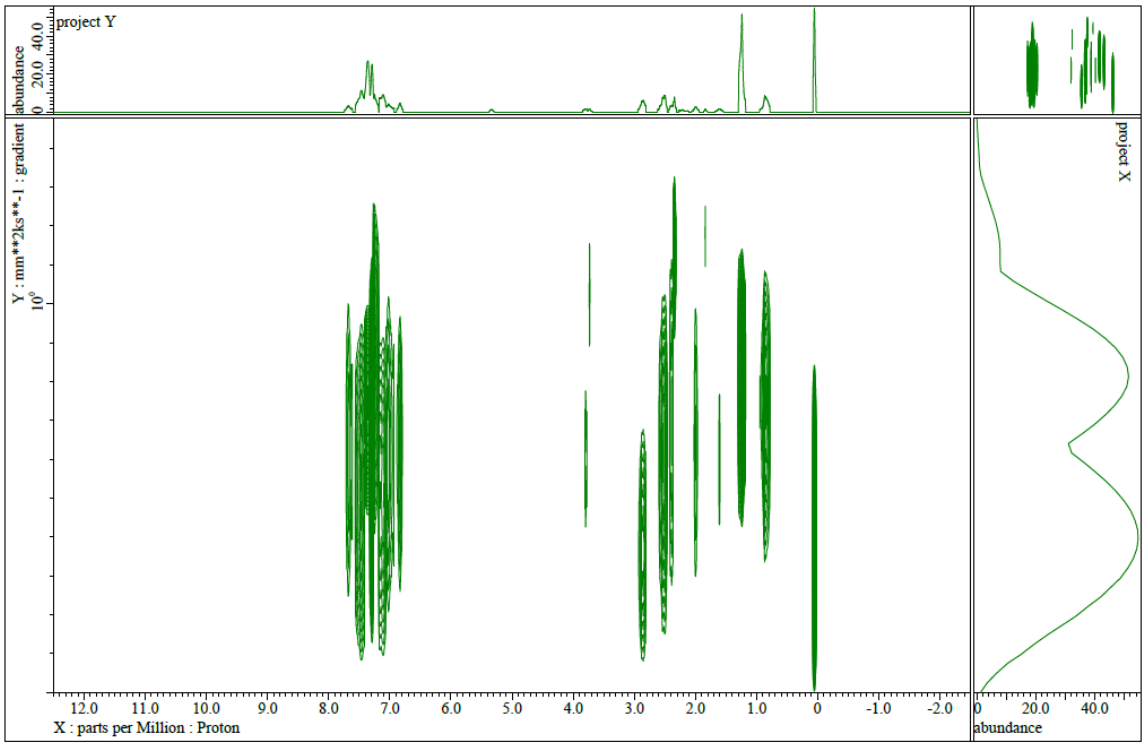

Figure A18: DOSY of [Rh(DPPP-OH)$_2$][Cl] (**3**).

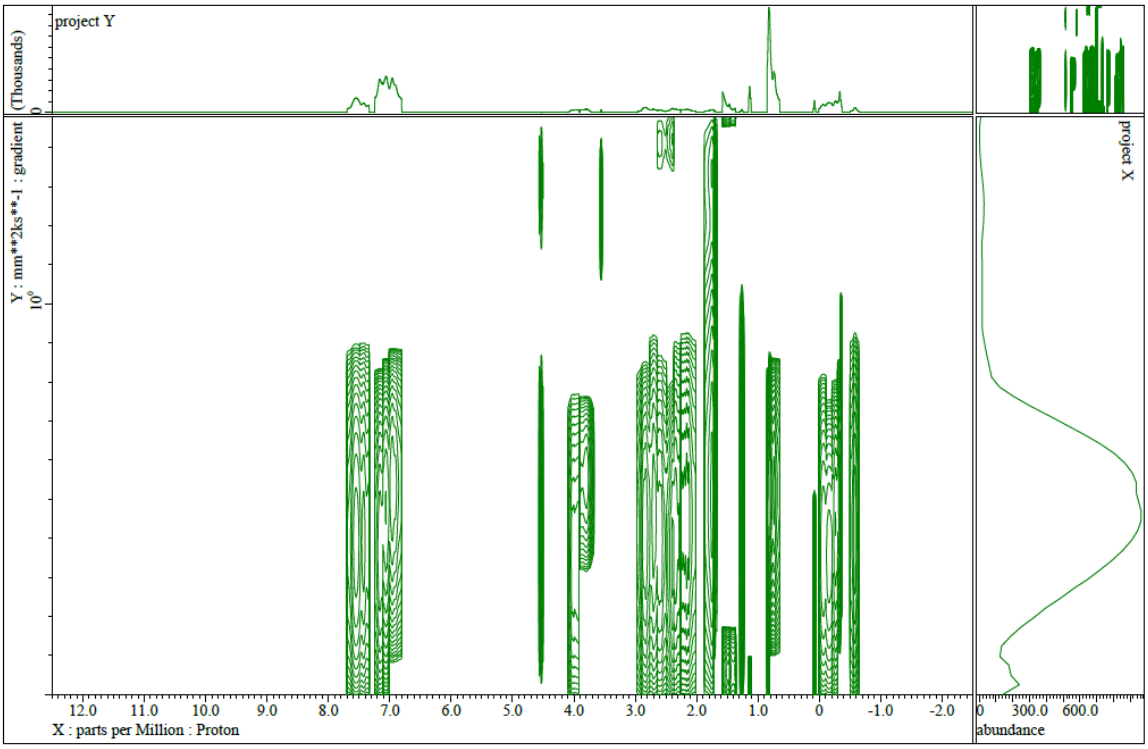

Figure A19: DOSY of Rh(DPPP-OAl^{i}Bu$_2$)(DPPP-OAl^{i}Bu$_2$Cl) (**4**).

X-Ray Crystallography

$Rh(DPPP\text{-}OH)_2(CO)Cl$ (ZL-0048)

The disordered chloroform molecule was modeled over two positions with similarity restraints placed on the C-Cl bond lengths. A single, highly-disordered dichloromethane was modeled over 3 positions using the fragment based approach as Guzei, I. A. (2014). J. Appl. Crystallogr. 47, 806-809. The thermal parameters of all disordered solvent molecules were modeled with similarity restraints.

$[Rh(DPPP\text{-}OH)_2][BArF_{24}]$ (ZL-0051)

Three disordered chloroform molecules were modeled over two positions each with similarity restraints placed on the C-Cl bond lengths and atom thermal parameters. A disordered trifluoromethyl group of the $BAr^F{}_4$ anion was modeled over two positions with similarity restraints placed on the C-F bond lengths and atom thermal parameters.

$[Rh(DPPP)_2][Cl]$ (z1dppe)

The structure was modeled without restraint.

Appendix B: Spectral Data for Chapter 3

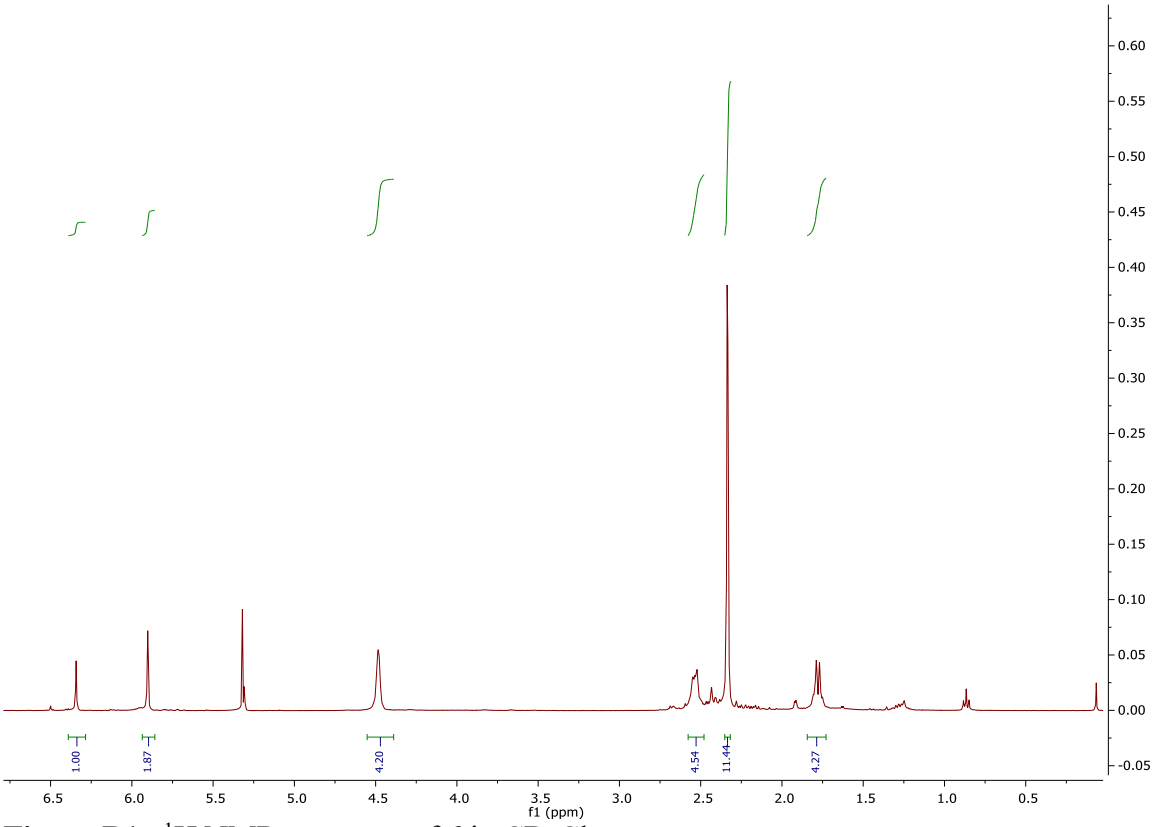

Figure B1. ^{1}H NMR spectrum of **6** in CD_2Cl_2.

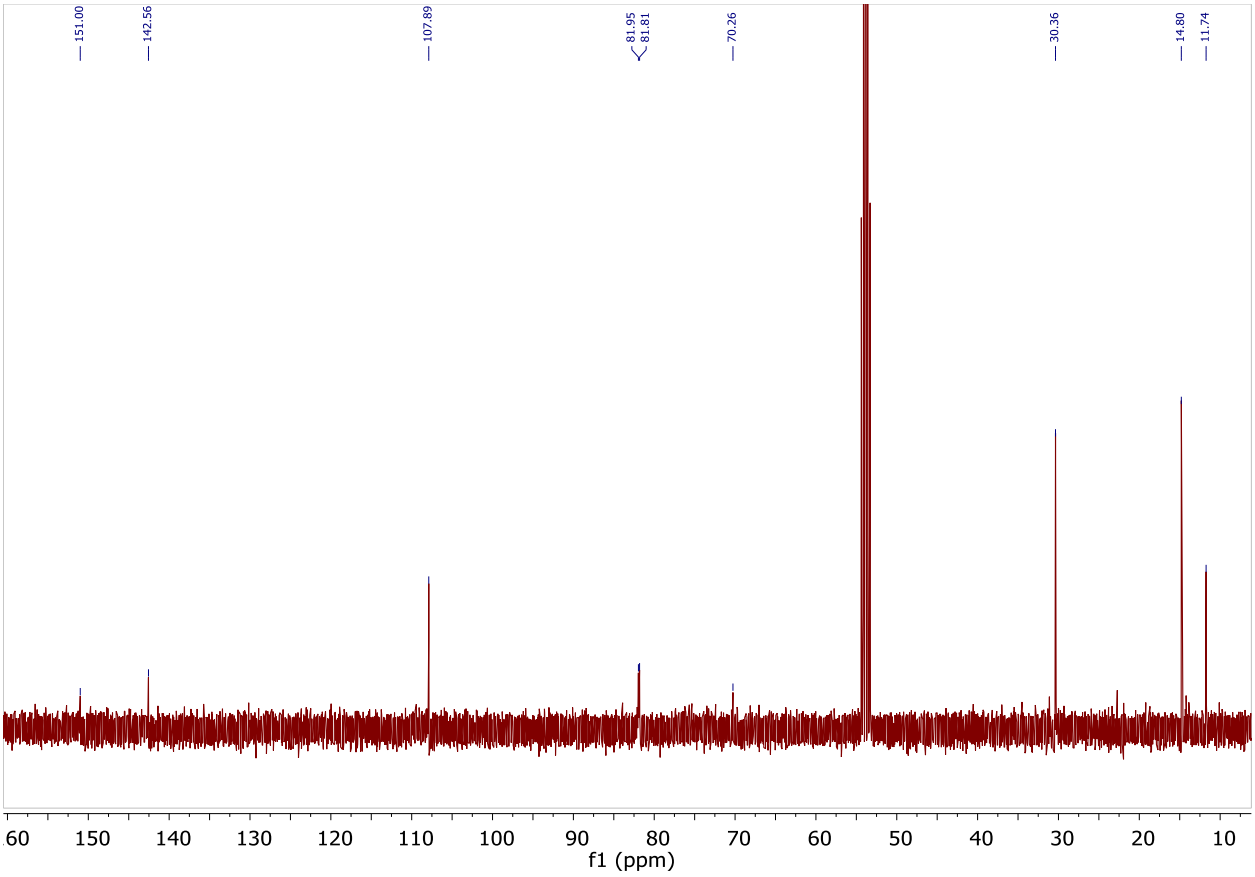

Figure B2. ^{13}C NMR spectrum of **6** in CD_2Cl_2

.

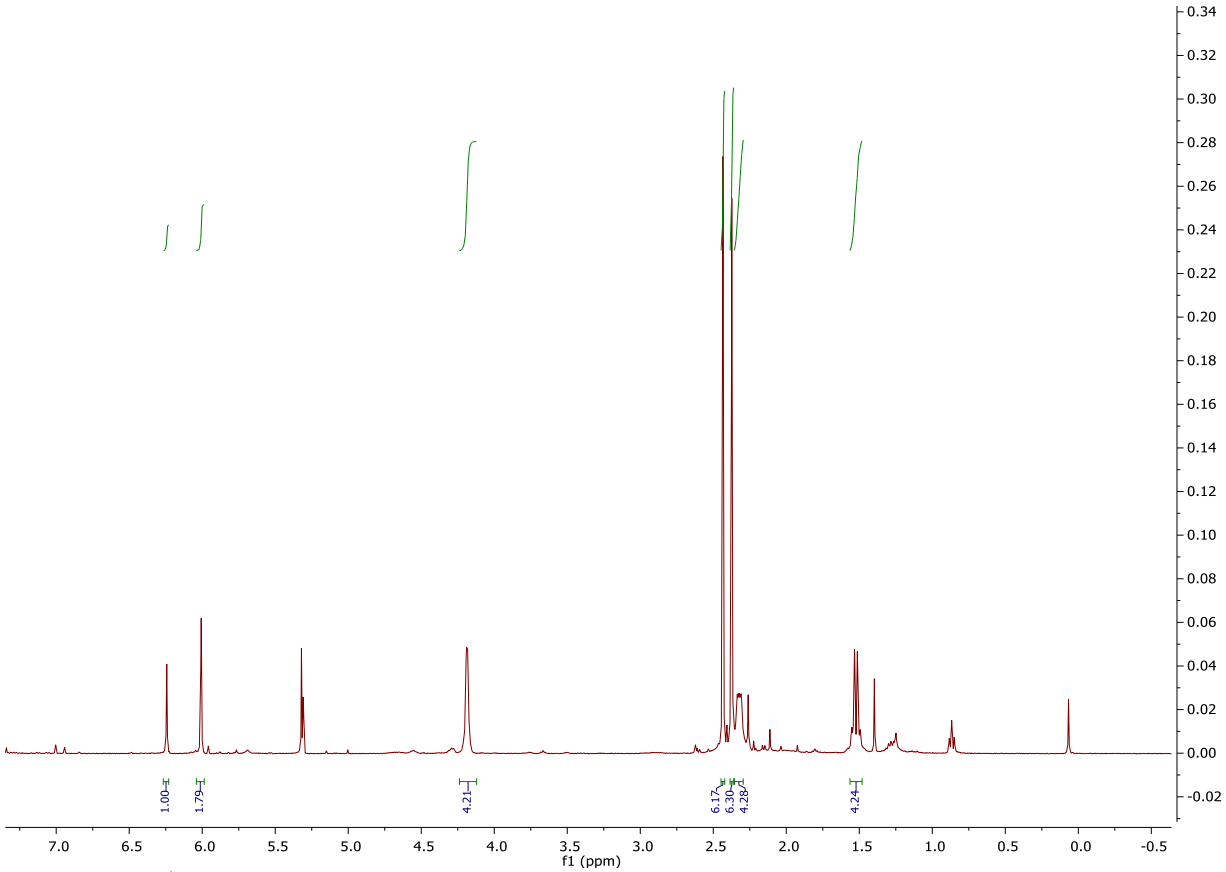

Figure B3. ^{1}H NMR spectrum of **7** in CD_2Cl_2.

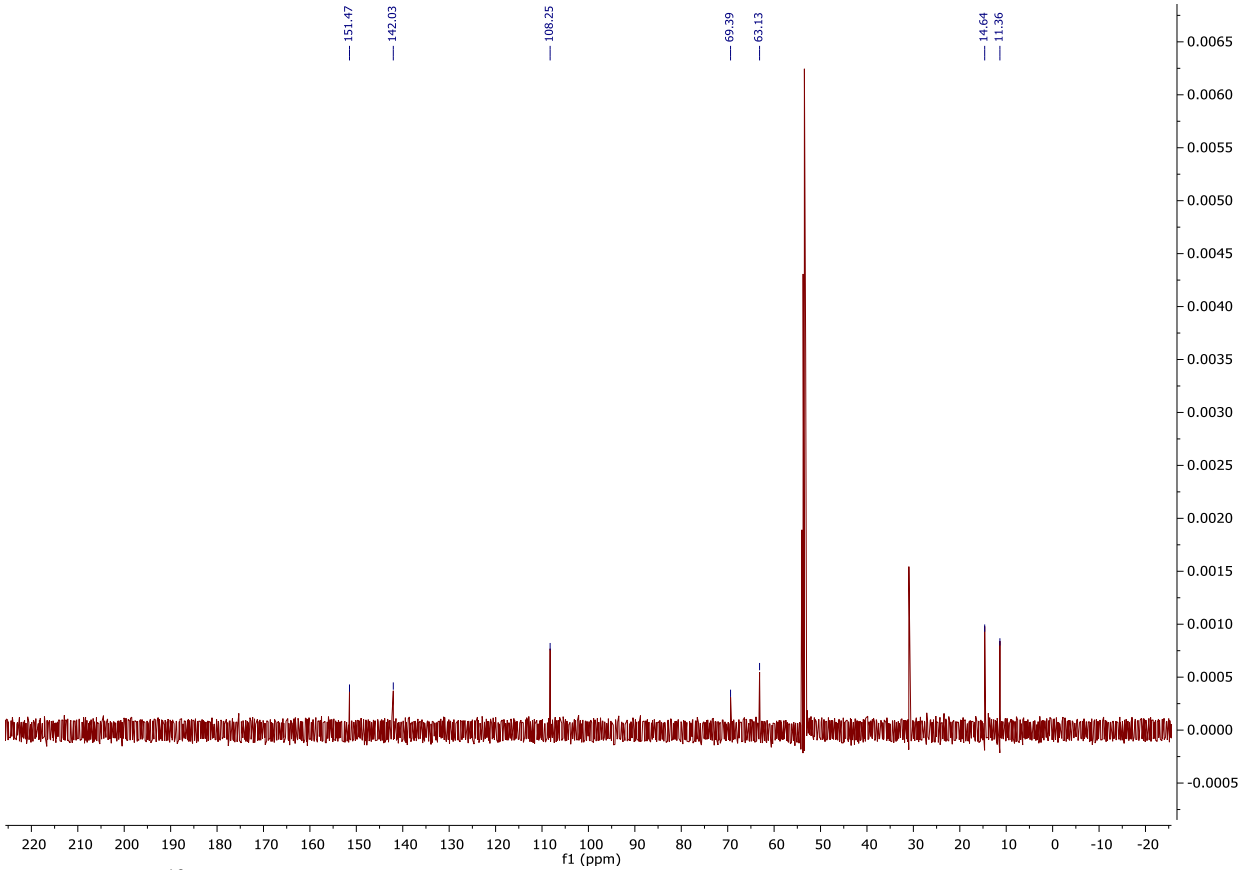

Figure B4. ^{13}C NMR spectrum of **7** in CD_2Cl_2.

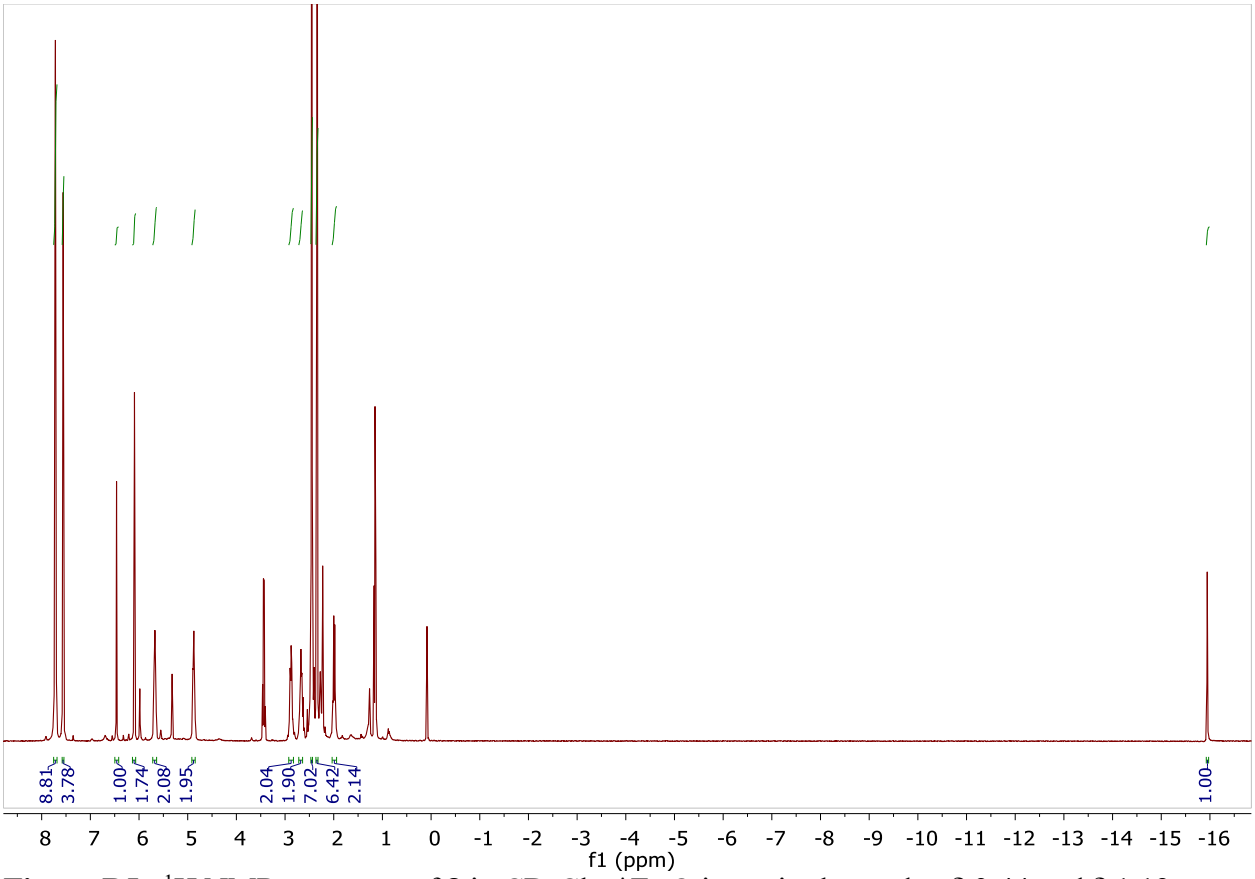

Figure B5. ^{1}H NMR spectrum of **8** in CD_2Cl_2. *Et_2O impurity located at δ 3.44 and δ 1.12 ppm.

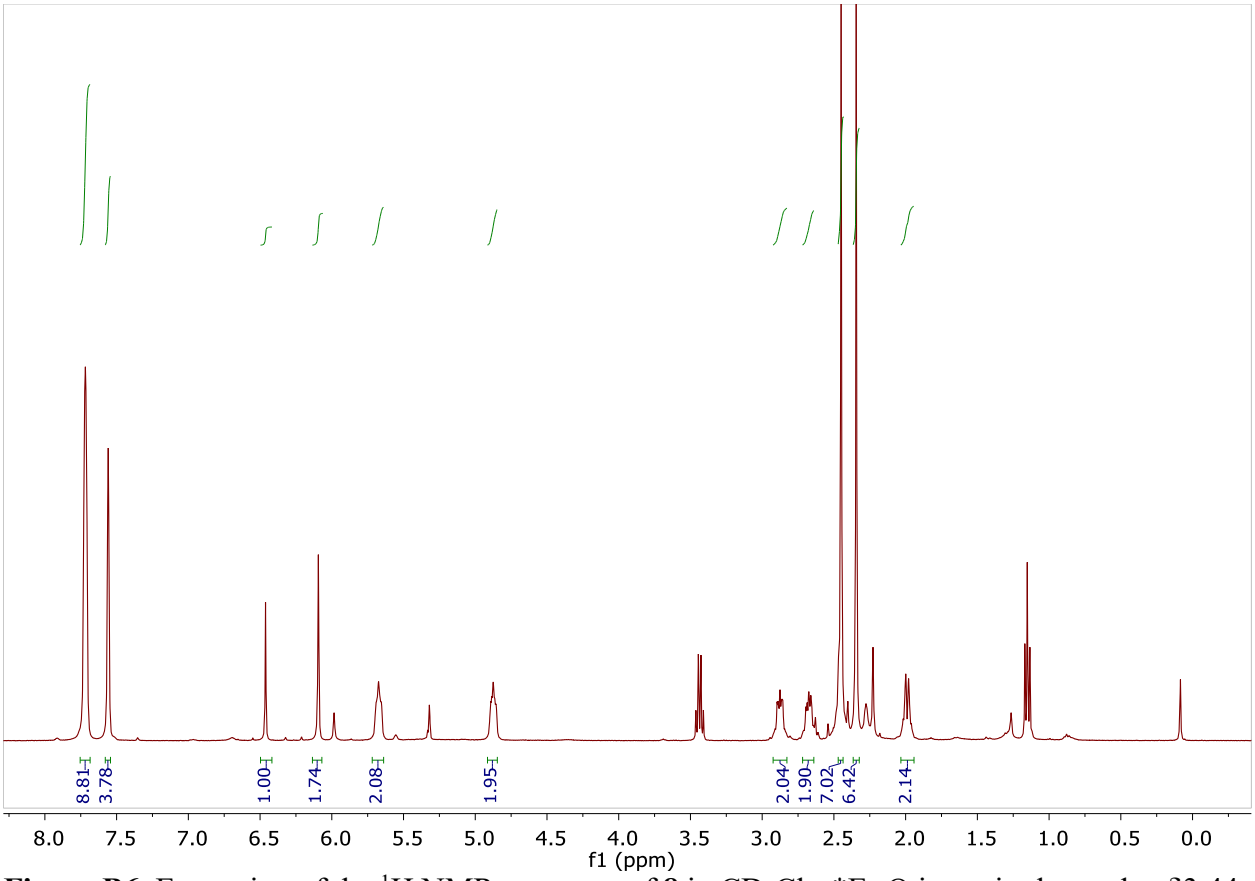

Figure B6. Expansion of the ^{1}H NMR spectrum of **8** in CD_2Cl_2. *Et_2O impurity located at δ3.44 and δ 1.12 ppm.

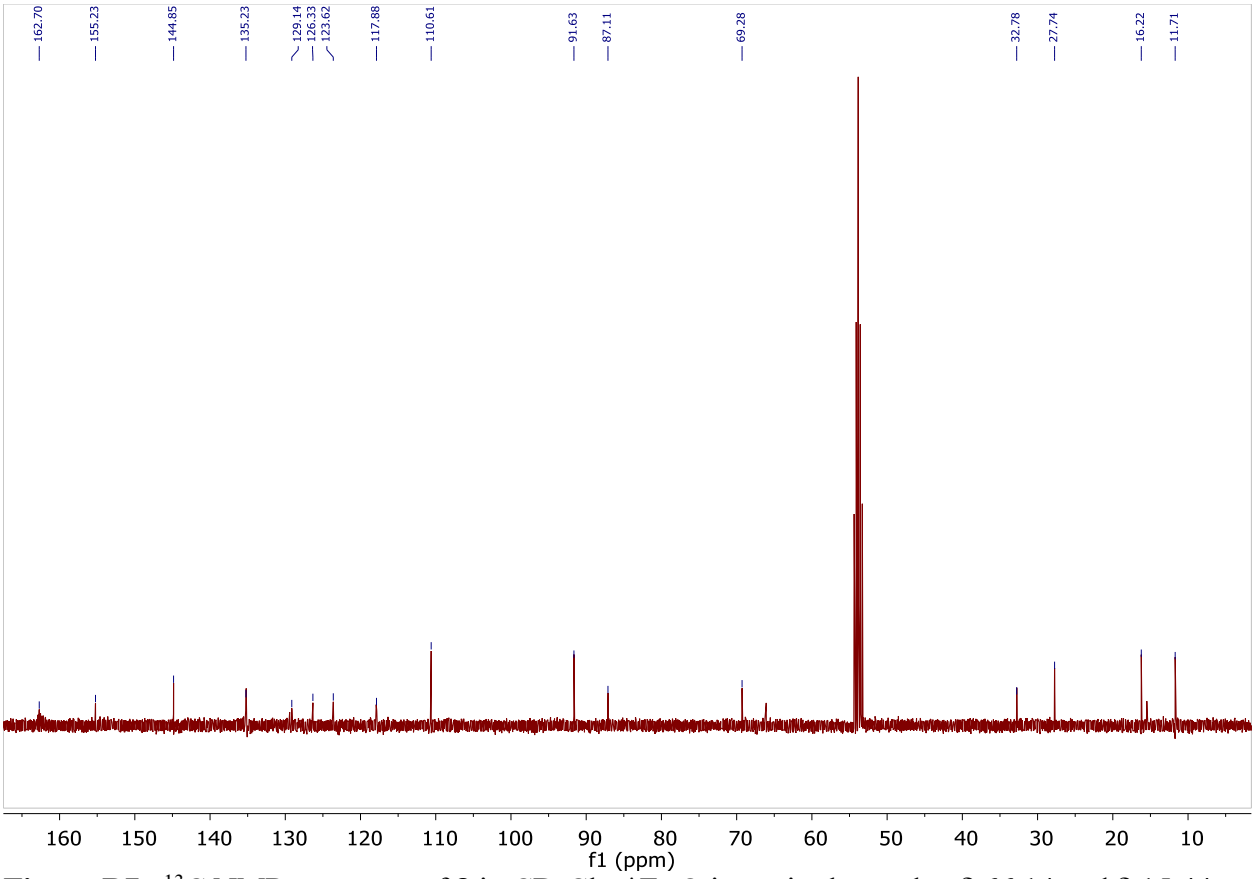

Figure B7. ^{13}C NMR spectrum of **8** in CD_2Cl_2. *Et_2O impurity located at δ 66.14 and δ 15.44 ppm.

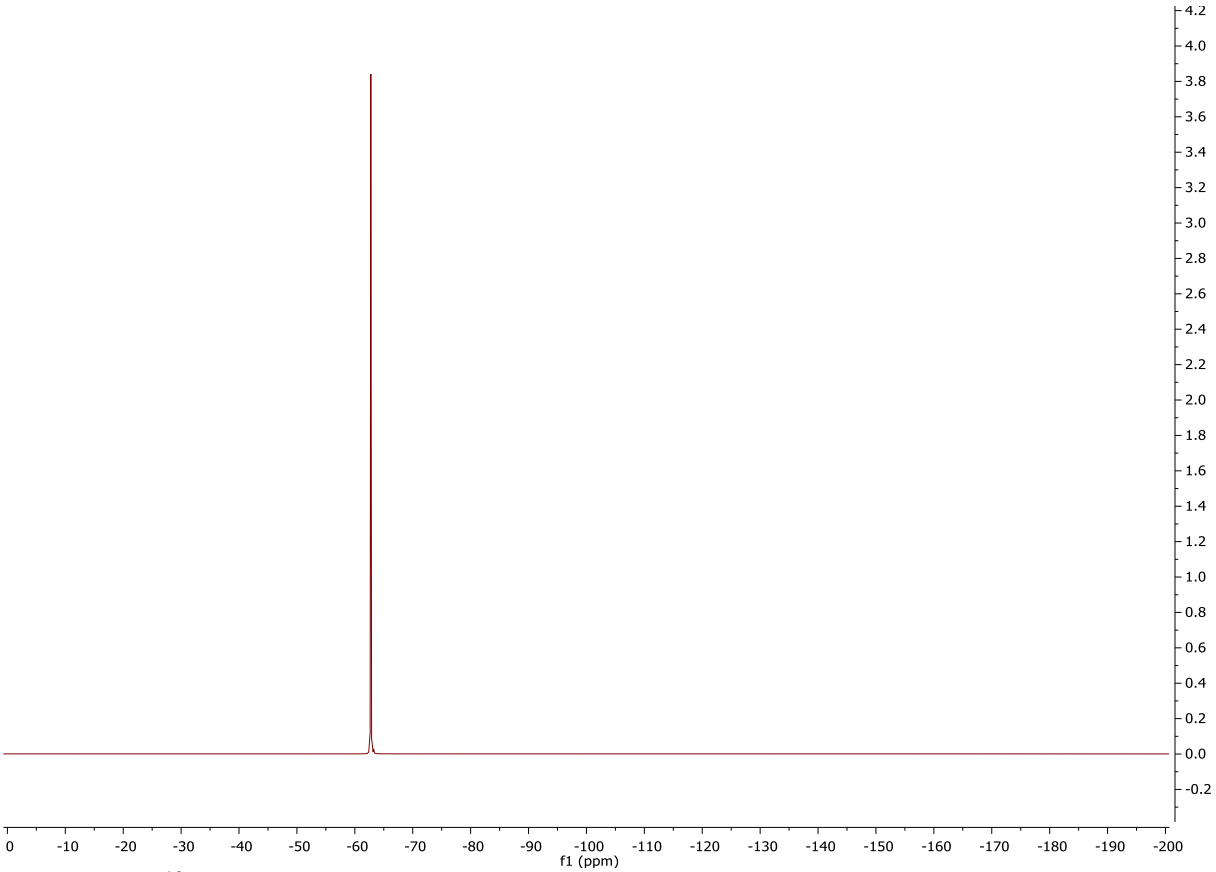

Figure B8. ^{19}F NMR spectrum of **8** in CD_2Cl_2.

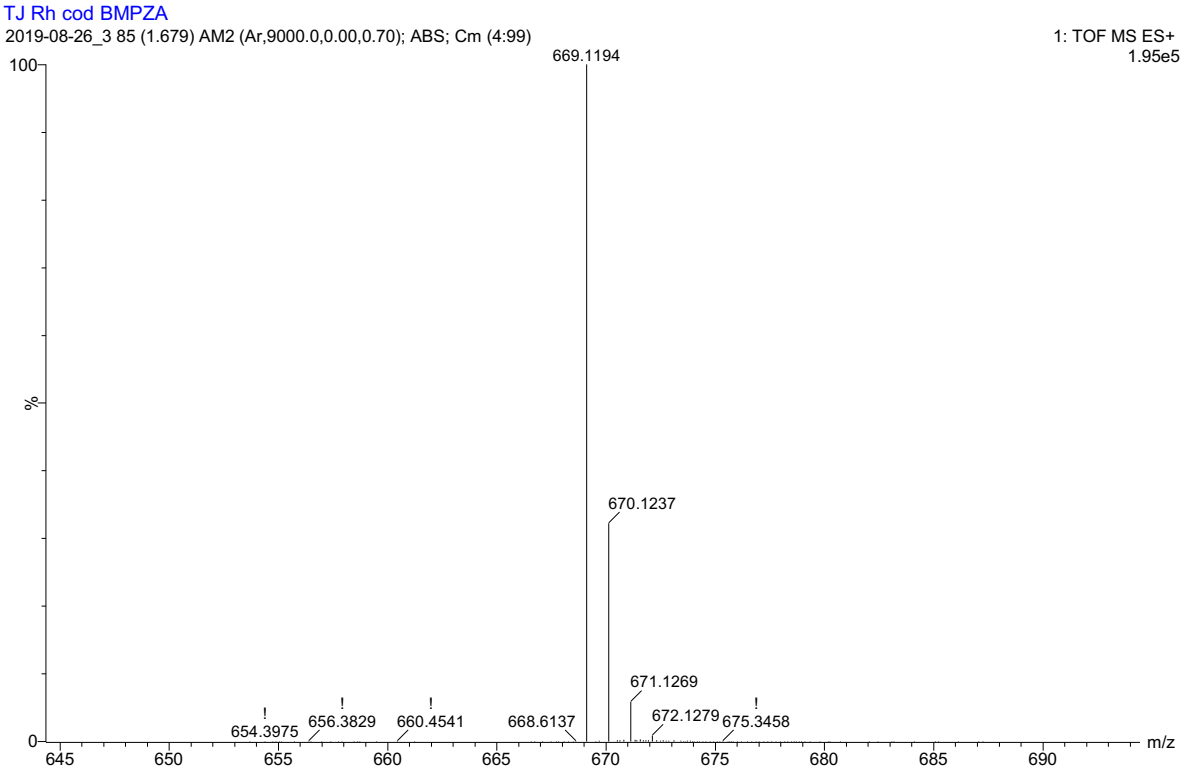

Figure B9. HRMS spectrum of **6.**

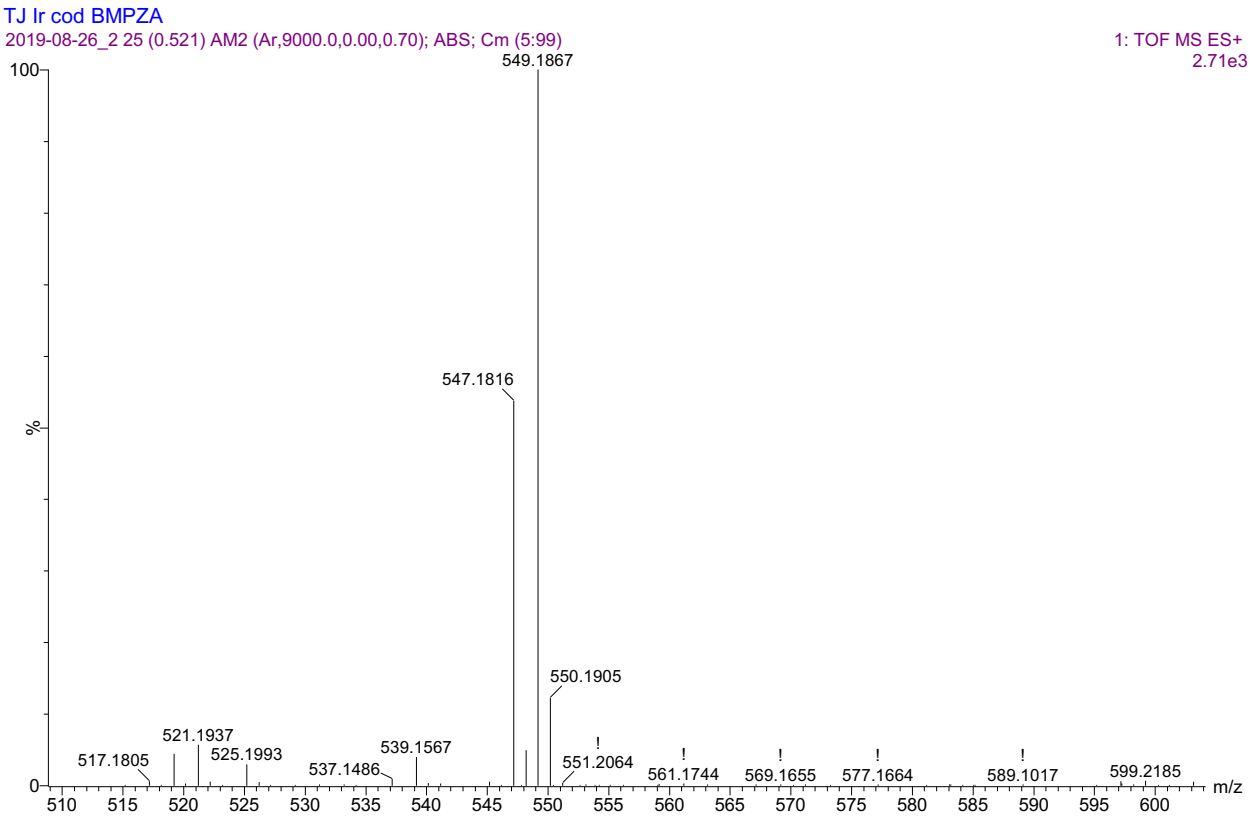

Figure B10. HRMS spectrum of **7.**

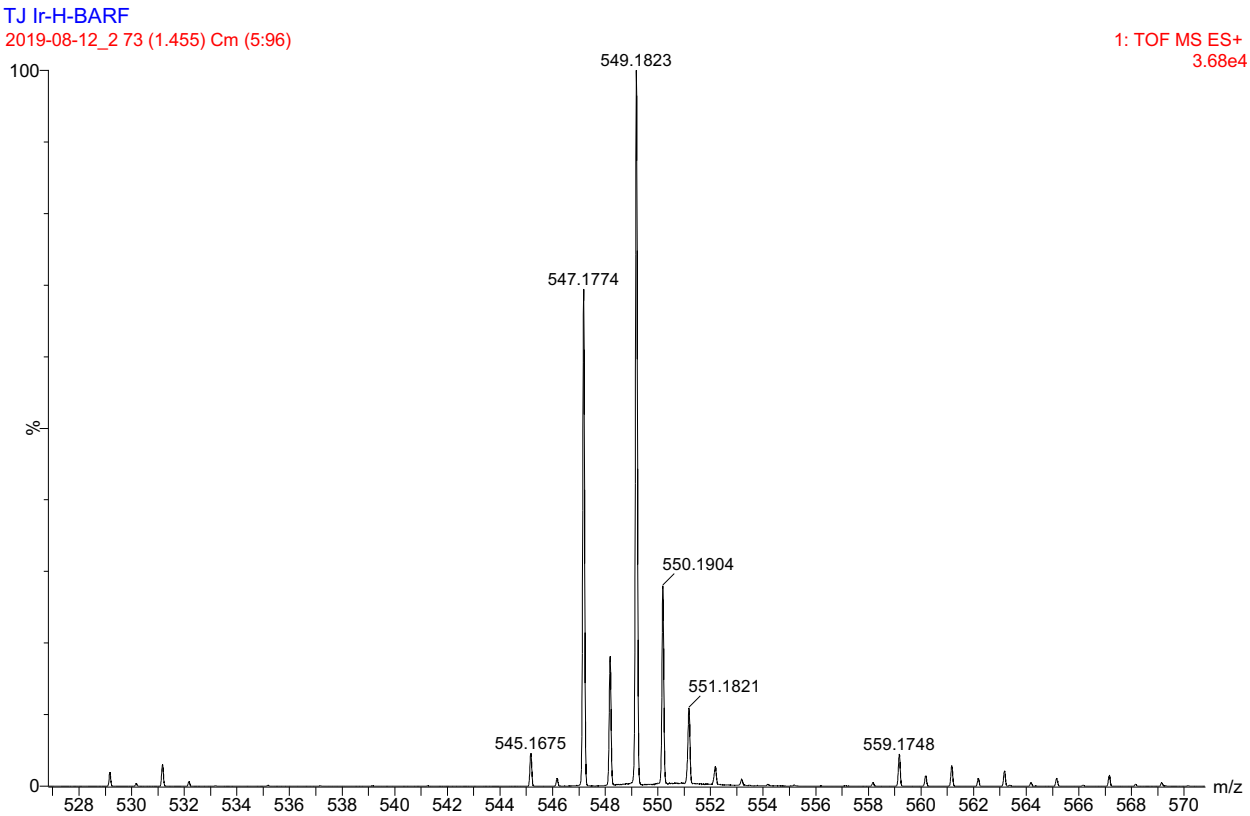

Figure B11. HRMS spectrum of **8.**

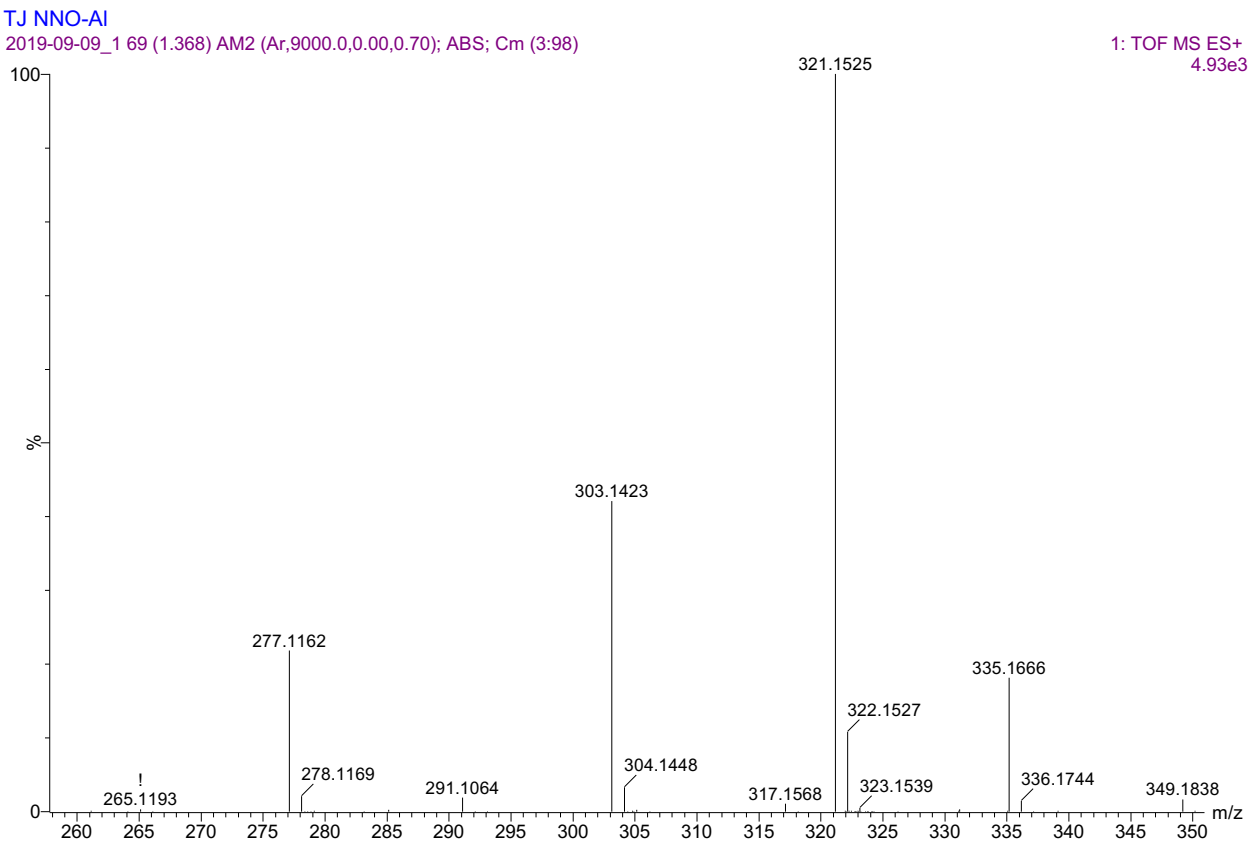

Figure B12. HRMS spectrum of aluminum-NNO complex by direct synthesis.

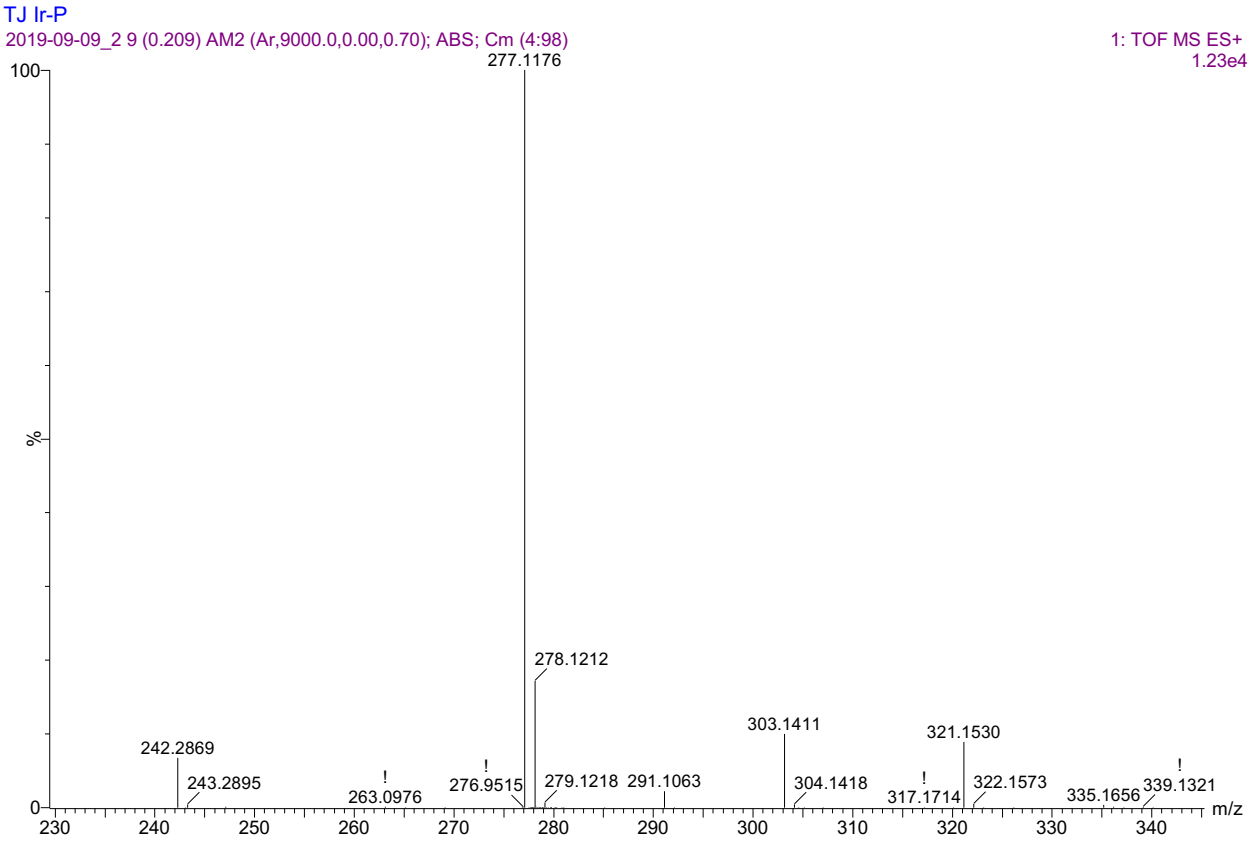

Figure B13. HRMS spectrum of pentane layer after reacting **6** with $AlEt_3$.

Appendix C: Spectral Data for Chapter 4

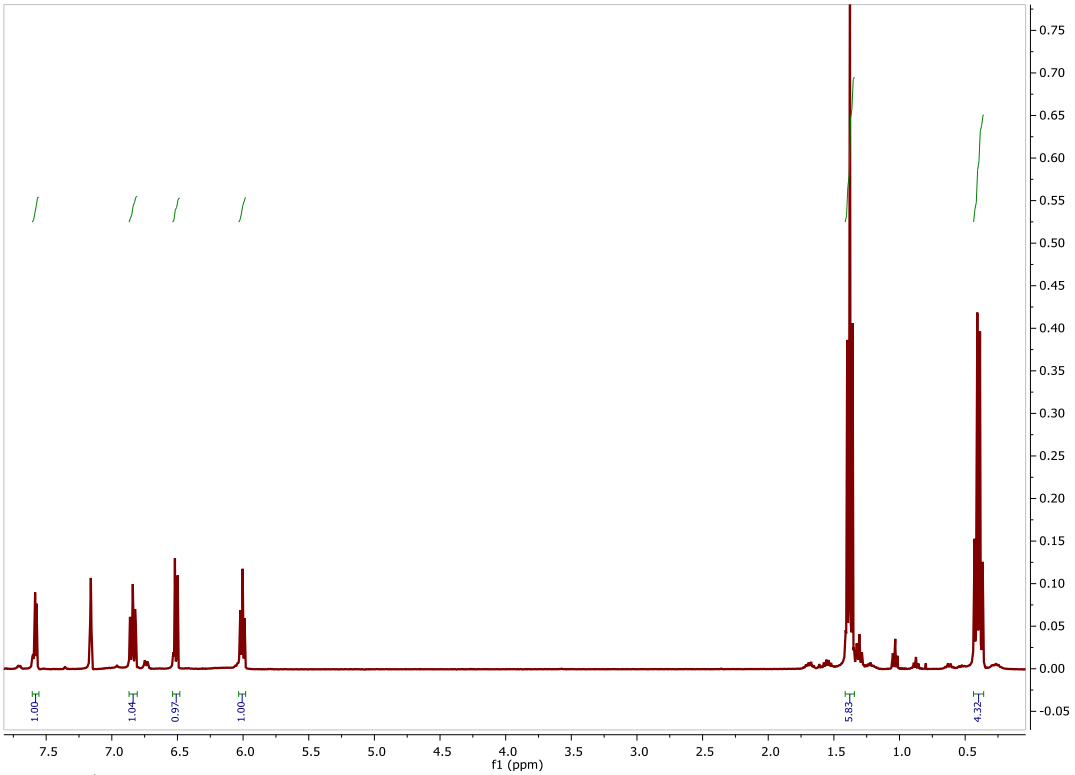

Figure C1. ^{1}H NMR spectrum of (2-pyridone-AlEt$_2$) (**9a**) in C_6D_6.

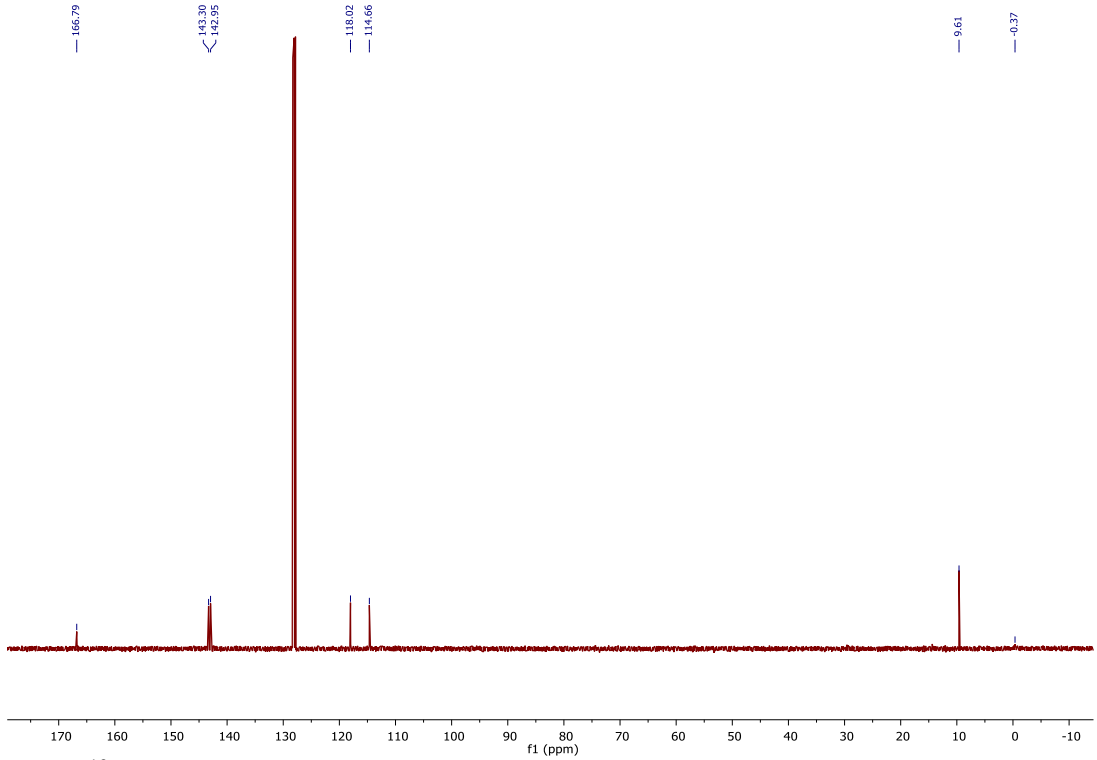

Figure C2. ^{13}C NMR spectrum of (2-pyridone-AlEt$_2$) (**9a**) in C_6D_6.

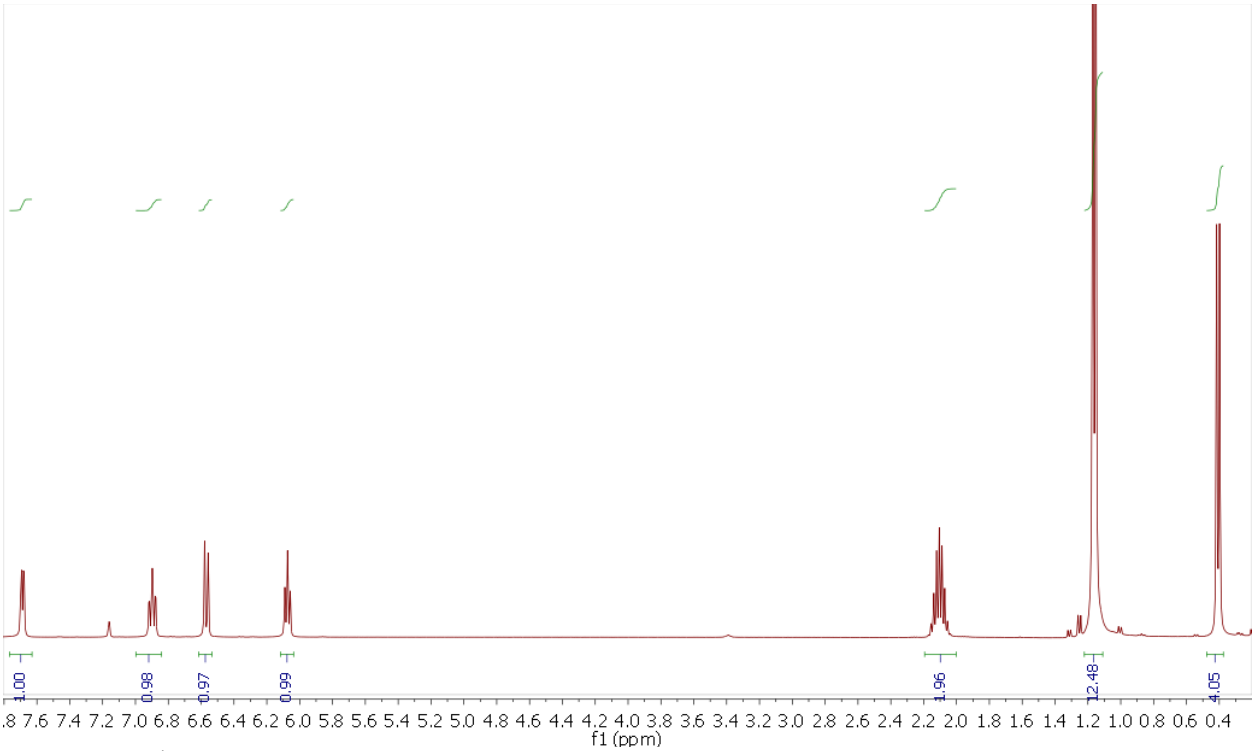

Figure C3. ^{1}H NMR spectrum of (2-pyridone-Al^{i}Bu$_2$) (**9b**) in C_6D_6.

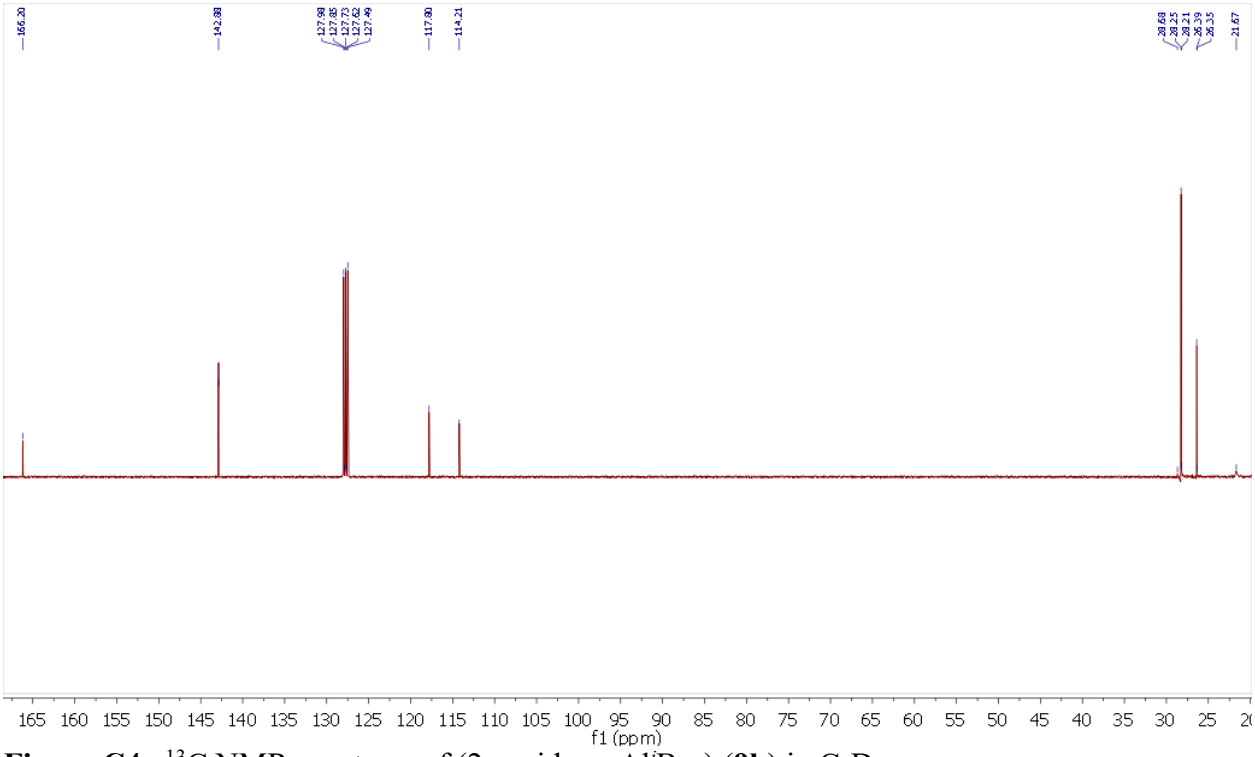

Figure C4. ^{13}C NMR spectrum of (2-pyridone-Al^{i}Bu$_2$) (**9b**) in C_6D_6.

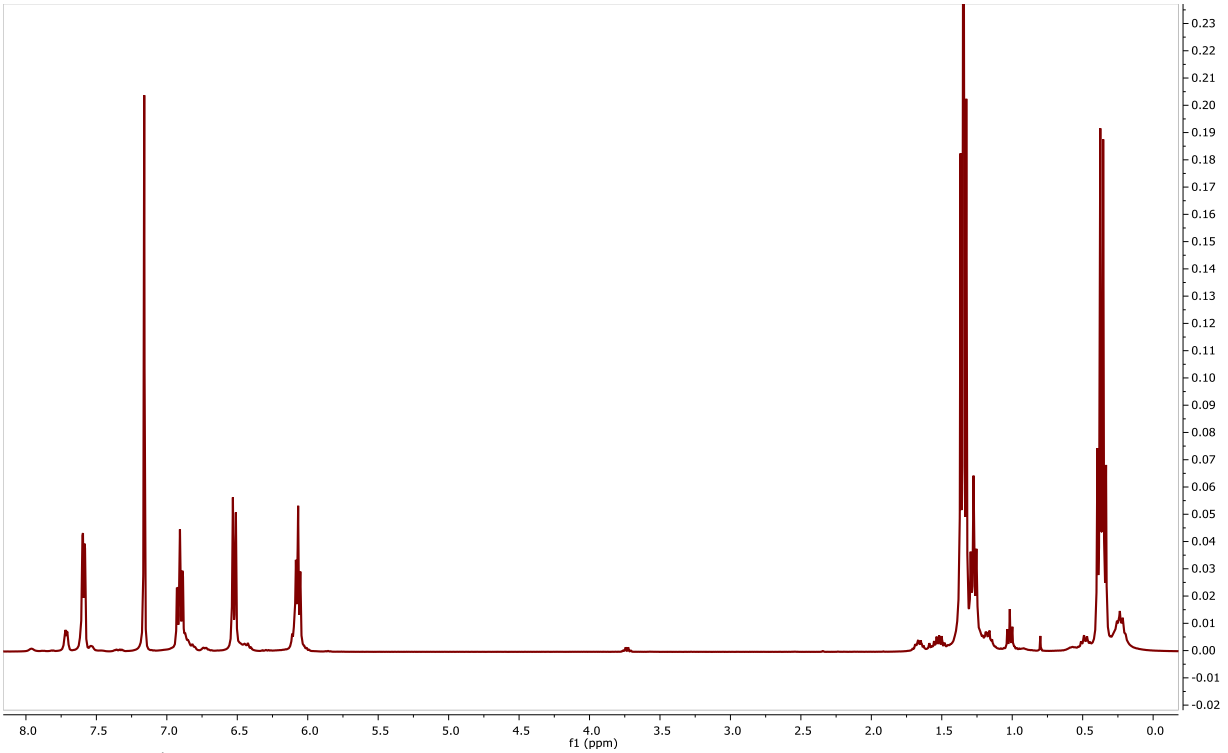

Figure C5. ^{1}H NMR spectrum of (2-pyridone-AlEt$_2$) after CO_2 addition (**9c**) in C_6D_6.

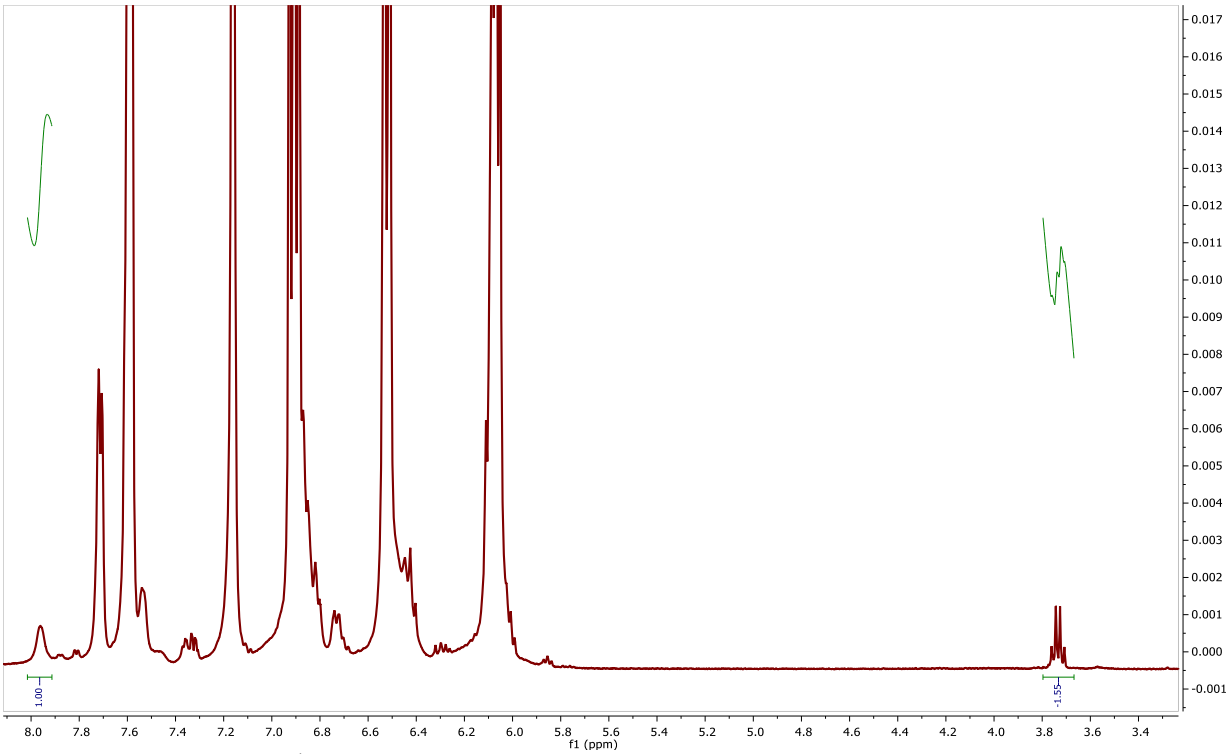

Figure C6. Truncated ^{1}H NMR spectrum of (2-pyridone-AlEt$_2$) after CO_2 addition (**9c**) in C_6D_6.

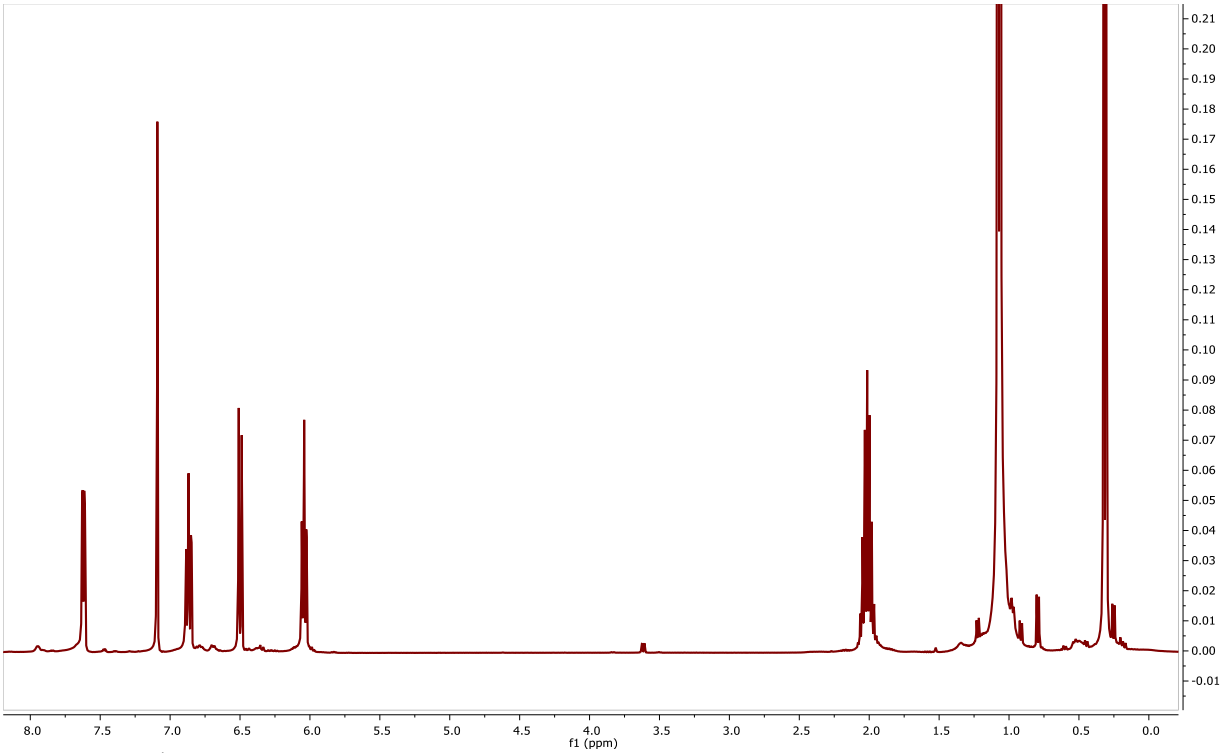

Figure C7. ^{1}H NMR spectrum of (2-pyridone-Al^{i}Bu$_2$) (**9b**) after CO_2 addition in C_6D_6 to yield (**9d**).

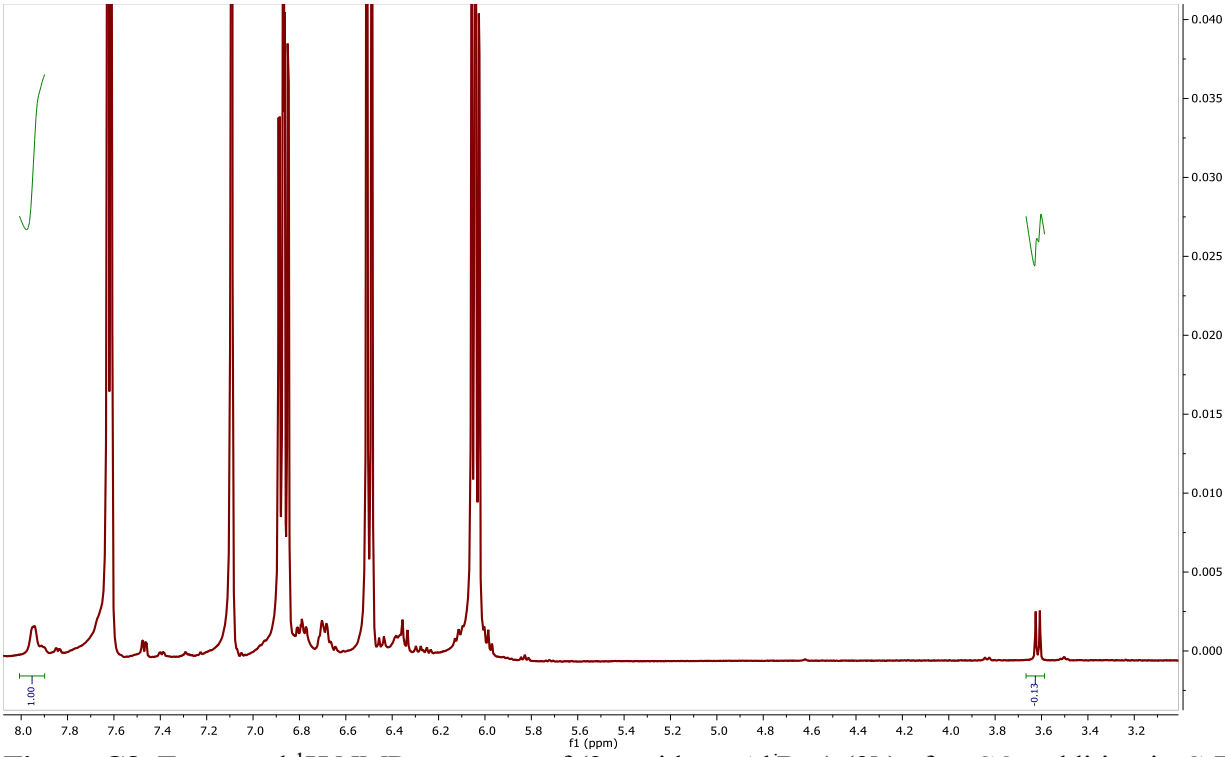

Figure C8. Truncated ^{1}H NMR spectrum of (2-pyridone-Al^{i}Bu$_2$) (**9b**) after CO_2 addition in C_6D_6 to yield (**9d**).

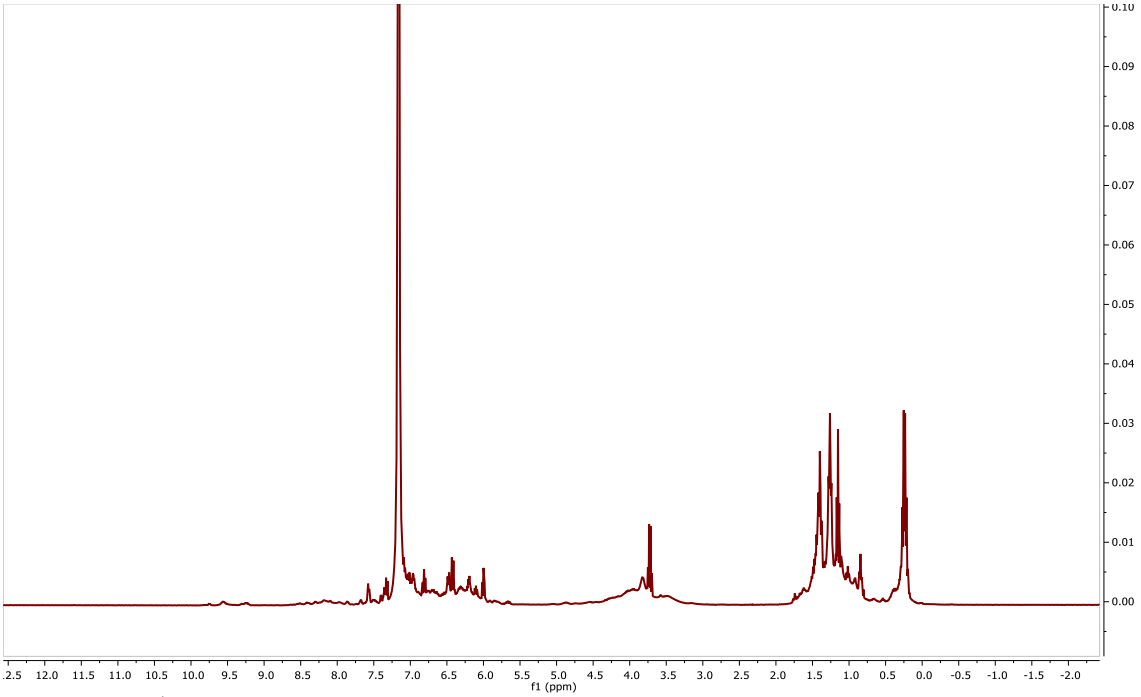

Figure C9. ^{1}H NMR spectrum of (2-pyridone-AlEt$_2$) (**9a**) after 1 eq of EtOH addition in C_6D_6.

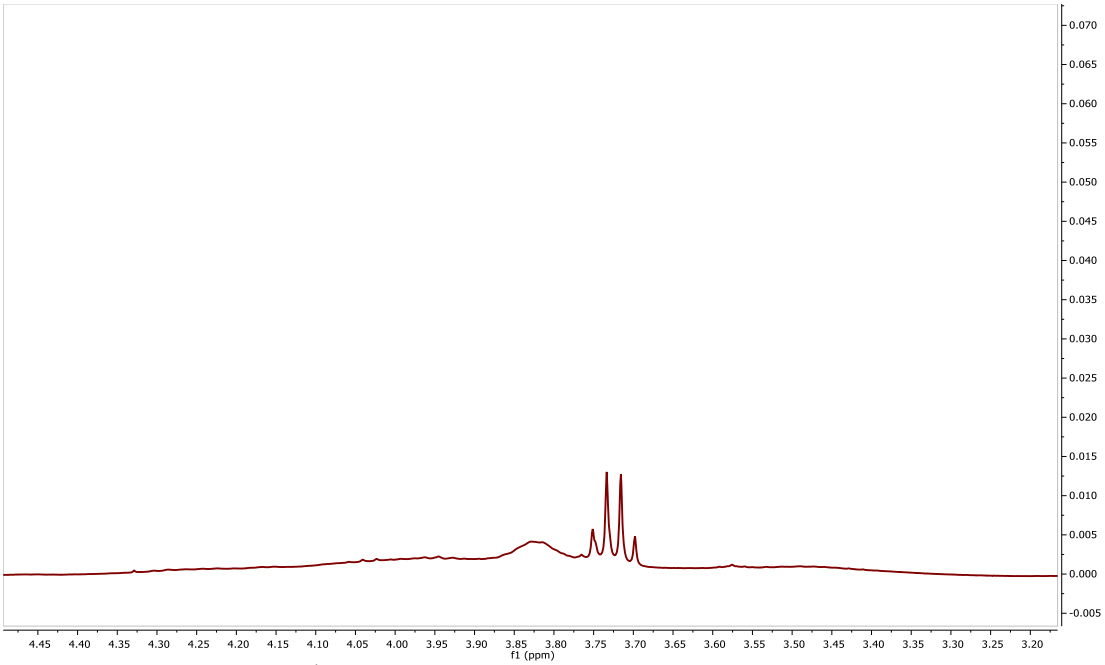

Figure C10. Truncated ^{1}H NMR spectrum of (2-pyridone-AlEt$_2$) (**9a**) after 1 eq EtOH addition in C_6D_6.

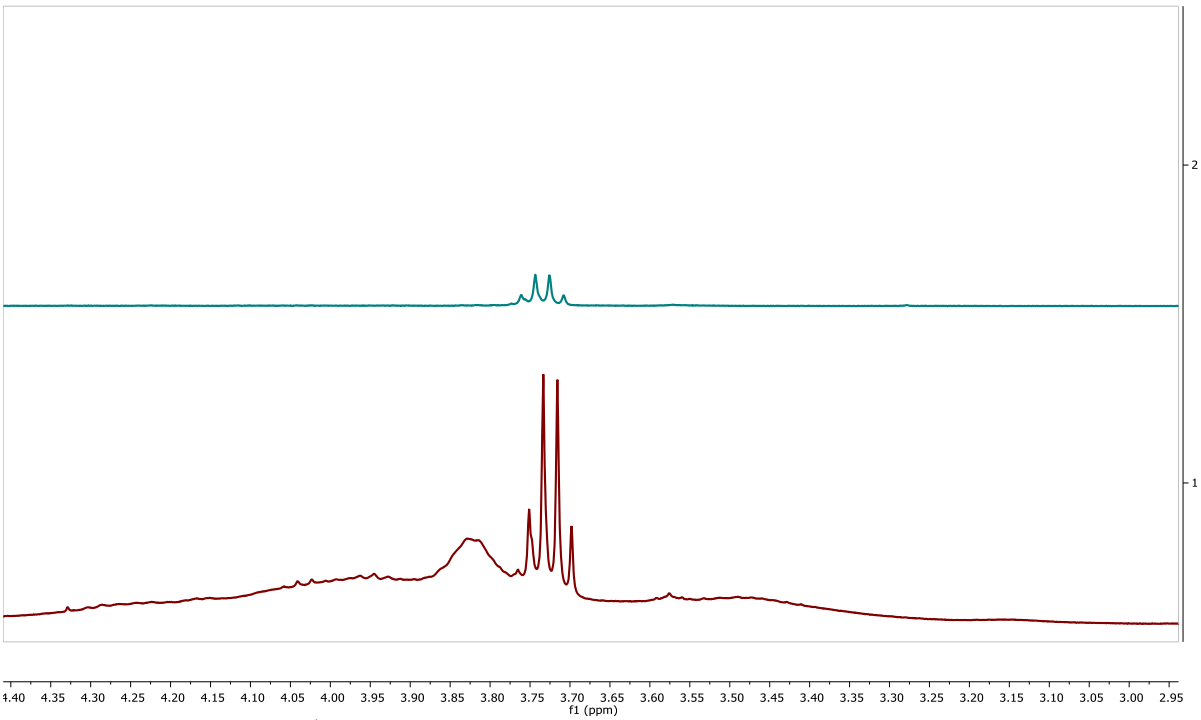

Figure C11. Truncated ^{1}H NMR spectrum of **9a** after CO_2 addition (top) and **9a** after 1 eq EtOH addition (bottom) in C_6D_6.

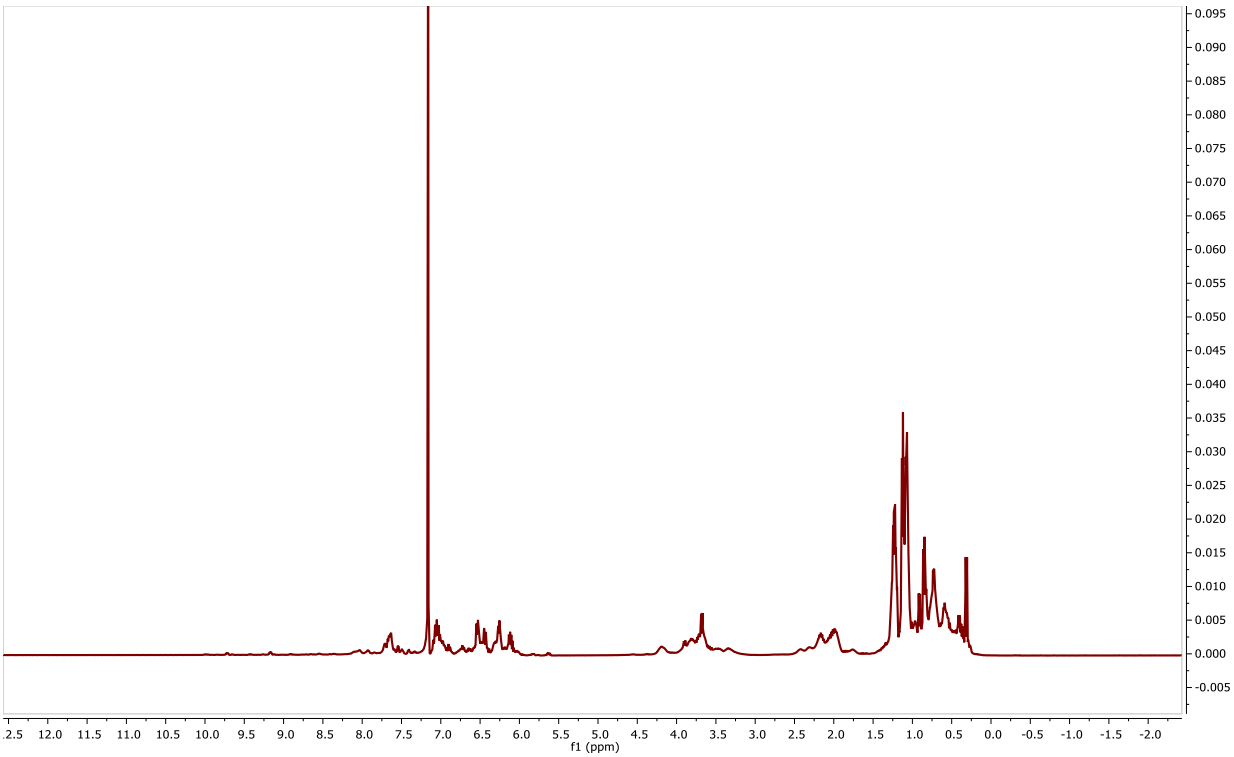

Figure C12. ^{1}H NMR spectrum of **9b** after ^{t}BuOH addition in C_6D_6.

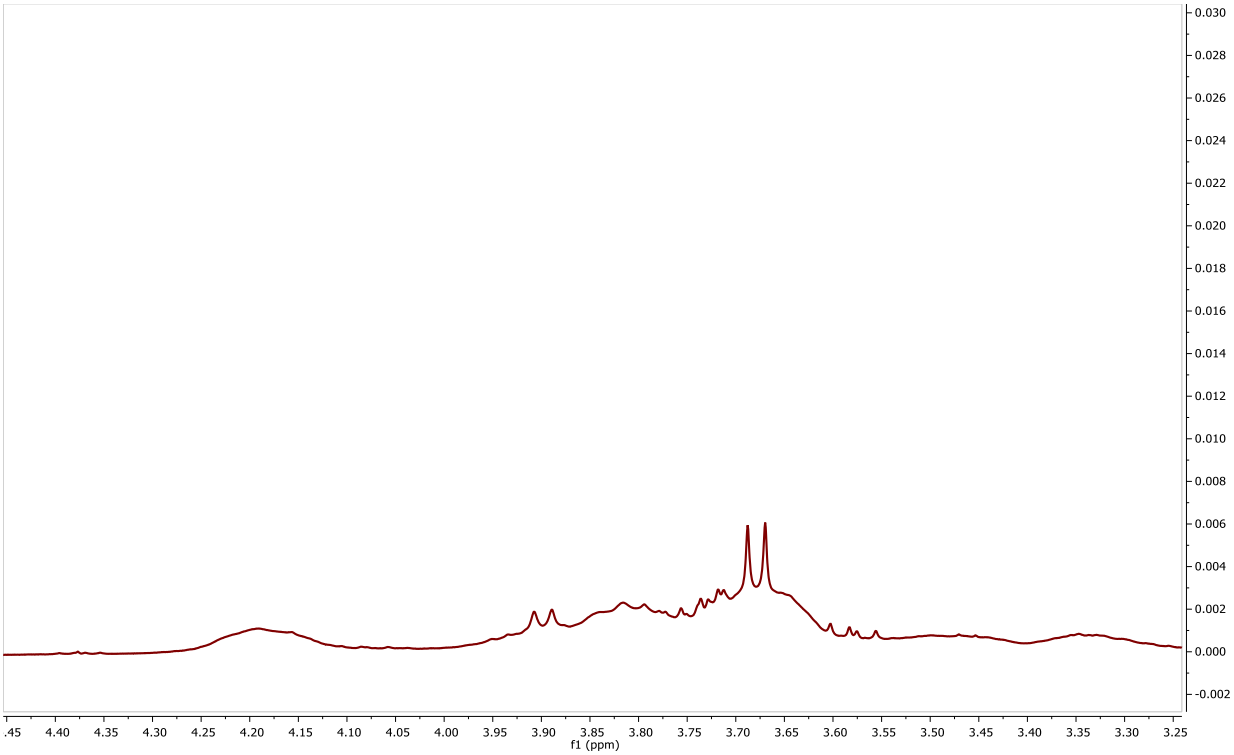

Figure C13. Truncated ^{1}H NMR spectrum of **9b** after 1 eq ^{i}BuOH addition in C_6D_6.

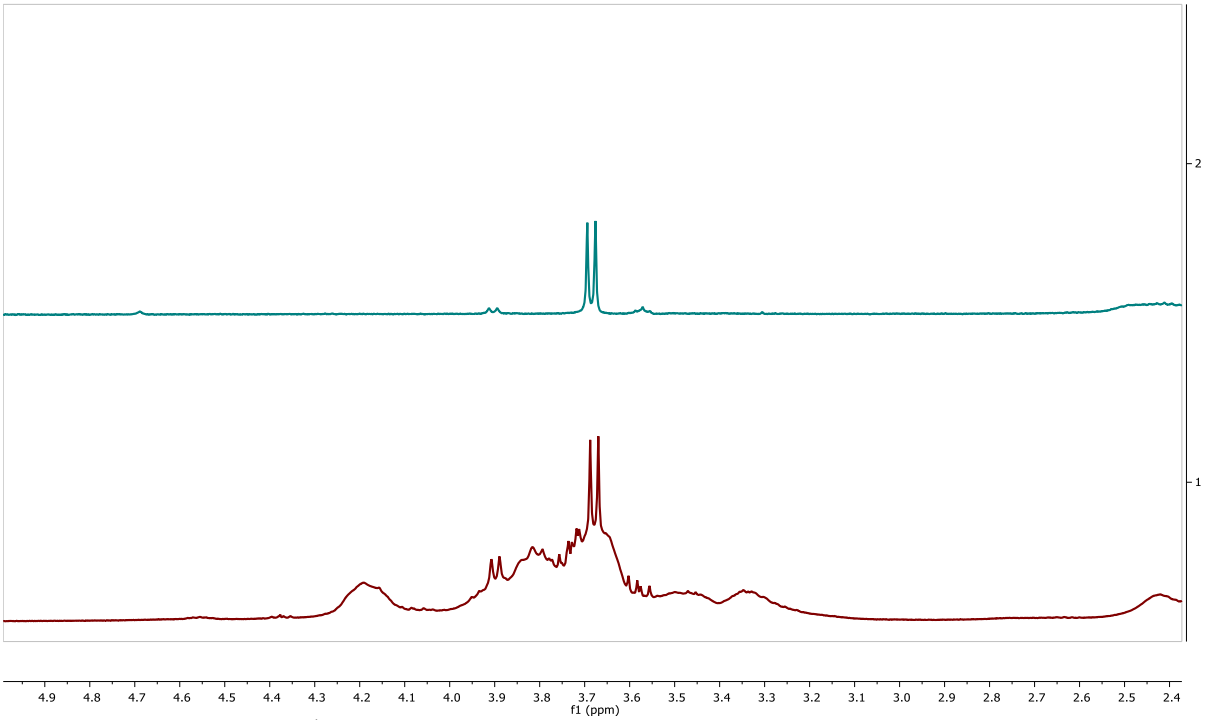

Figure C14. Truncated ^{1}H NMR spectrum of **9b** after CO_2 addition (top) and **9b** after 1 eq of ^{i}BuOH addition (bottom) in C_6D_6.

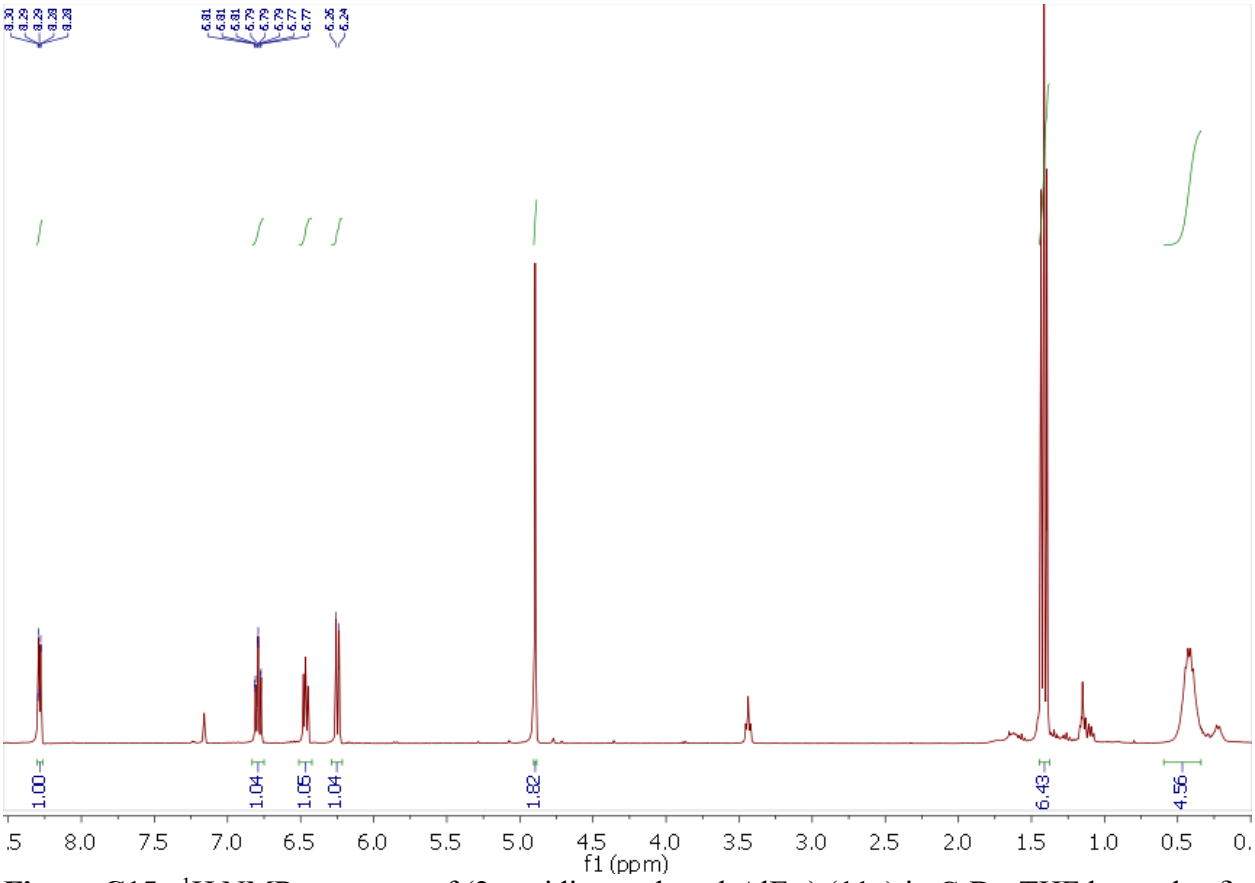

Figure C15. ^{1}H NMR spectrum of (2-pyridinemethanol-$AlEt_2$) (**11a)** in C_6D_6. THF located at δ 3.45 and δ1.25 ppm.

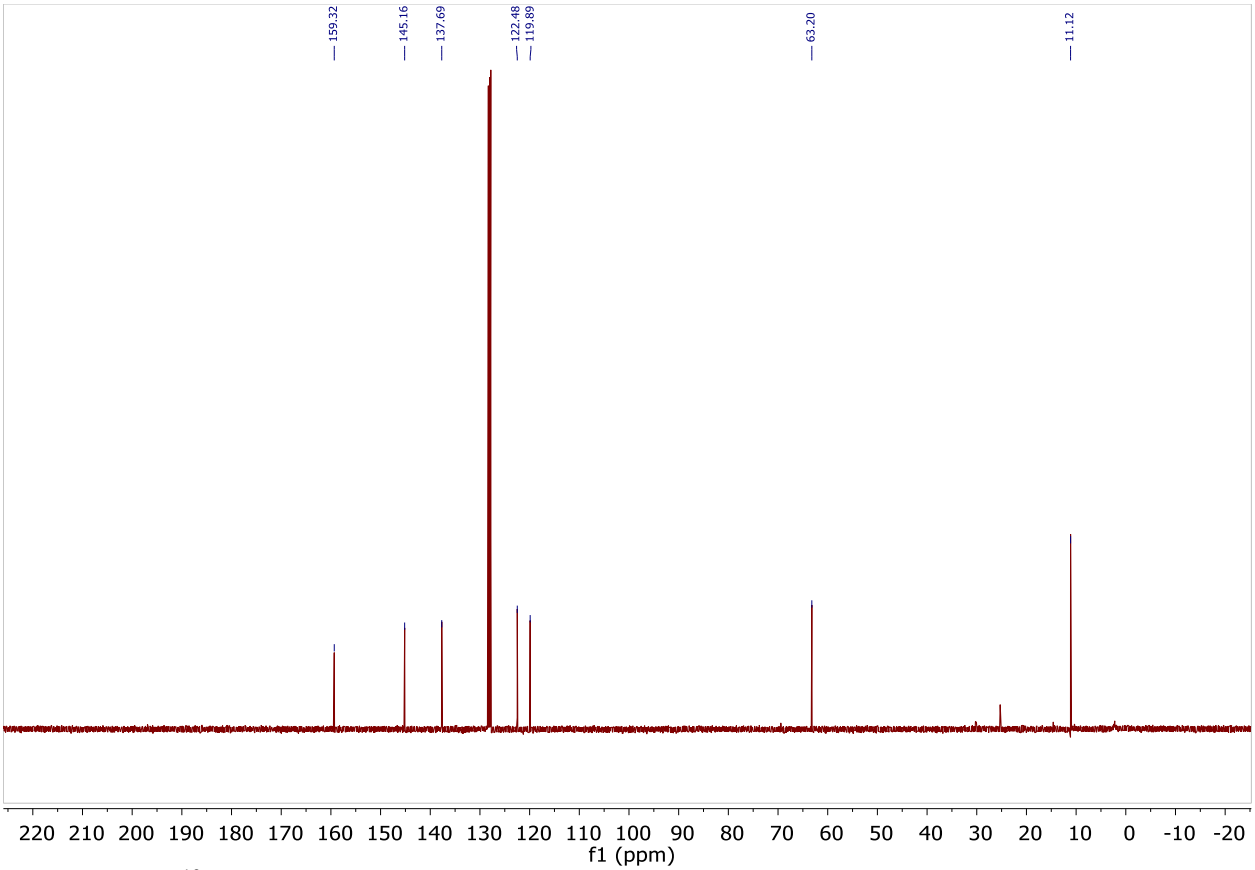

Figure C16. ^{13}C NMR spectrum of (2-pyridinemethanol-$AlEt_2$) (**11a**) in C_6D_6.

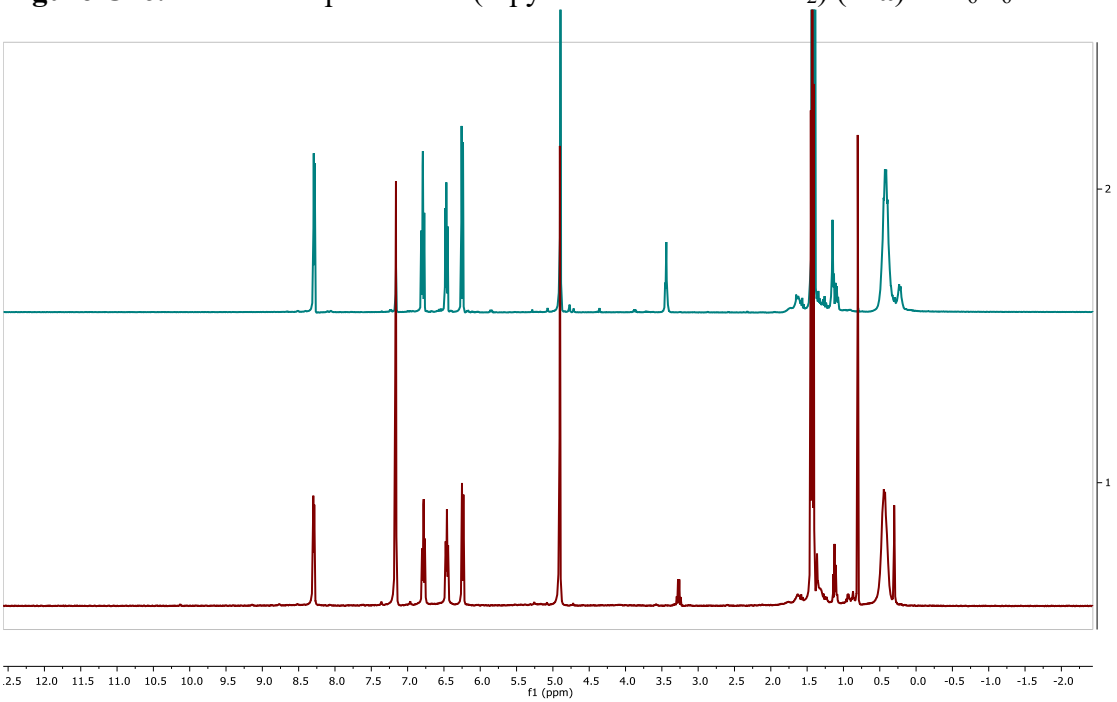

Figure C17. Stacked ^1H NMR spectrum of **11a** before CO_2 addition (top) and after CO_2 addition (bottom) in C_6D_6. THF impurity located at δ 3.57 and δ1.57 ppm. Et_2O impurity located at 3.25 ppm (bottom)

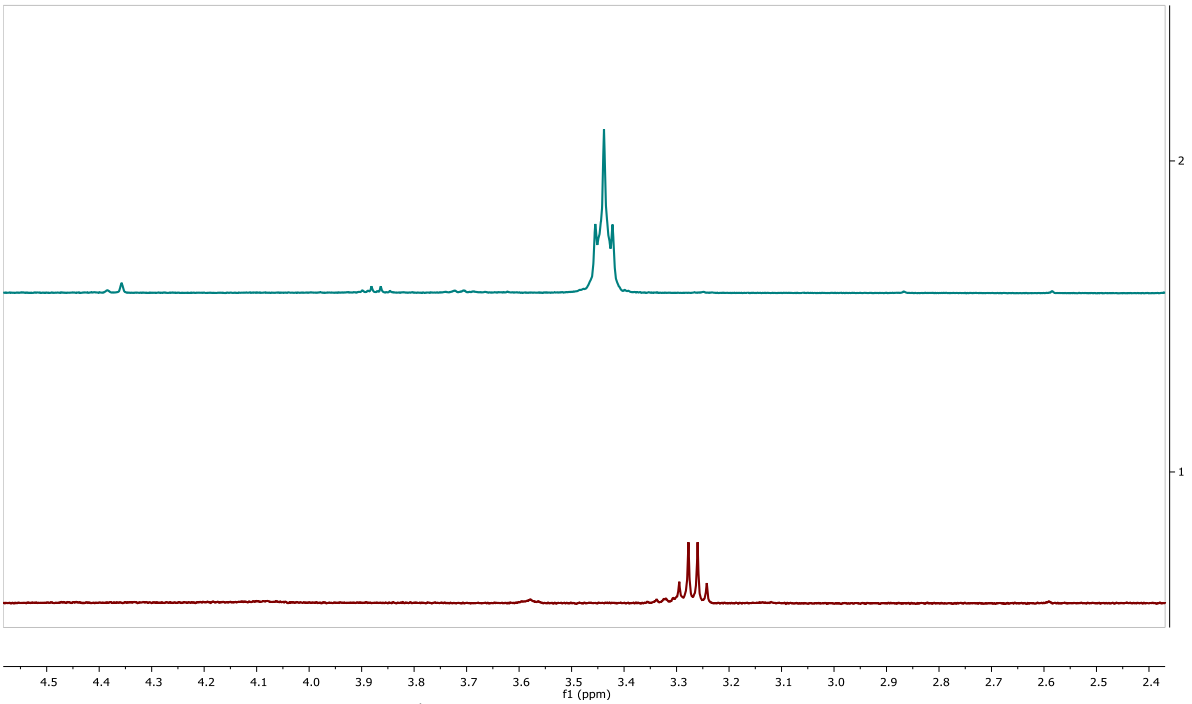

Figure C18. Truncated stacked ^{1}H NMR spectrum of **11a** before CO_2 addition (top) and after CO_2 addition in C_6D_6. THF impurity located at 3.45 ppm (top). Et_2O impurity located at 3.25 ppm (bottom).

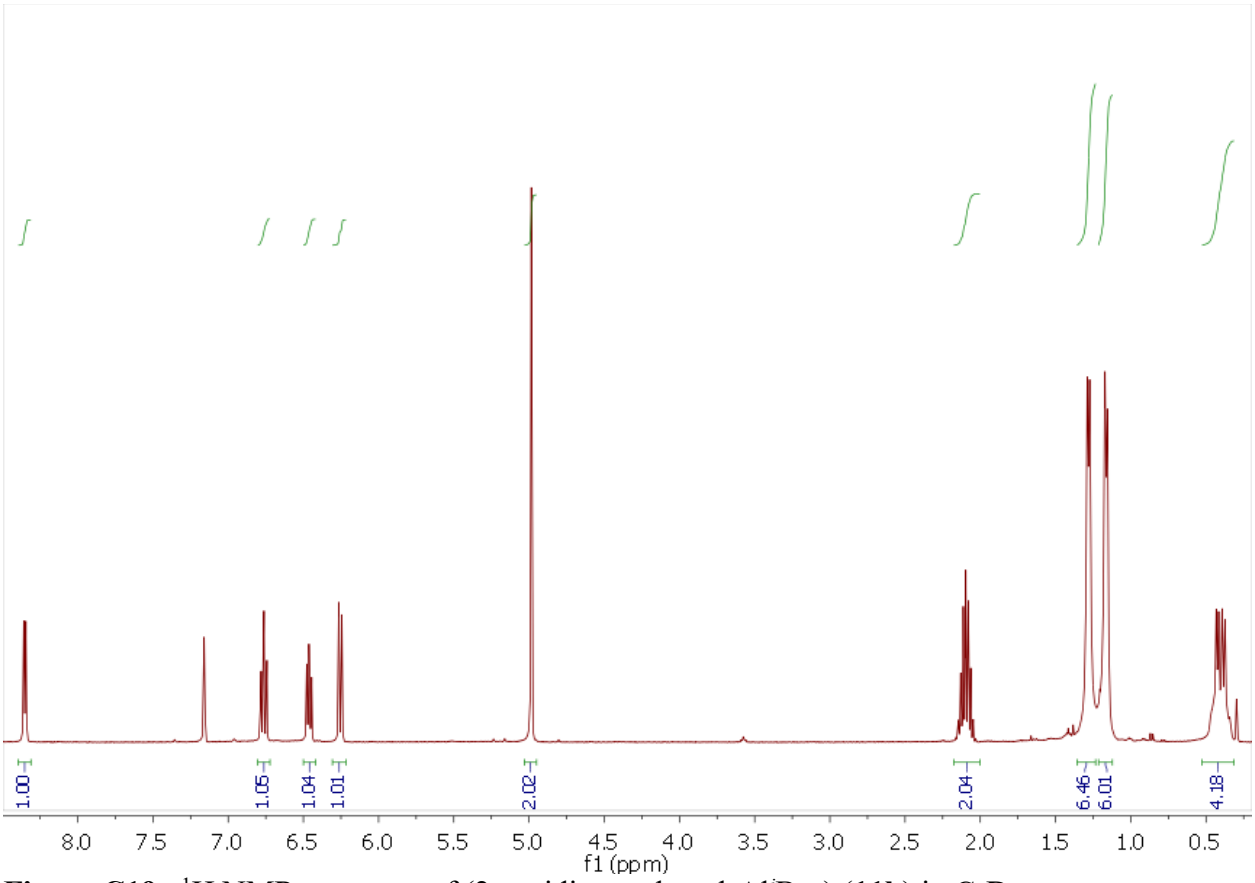

Figure C19. ^{1}H NMR spectrum of (2-pyridinemethanol-Al^{t}Bu$_2$) (**11b**) in C_6D_6.

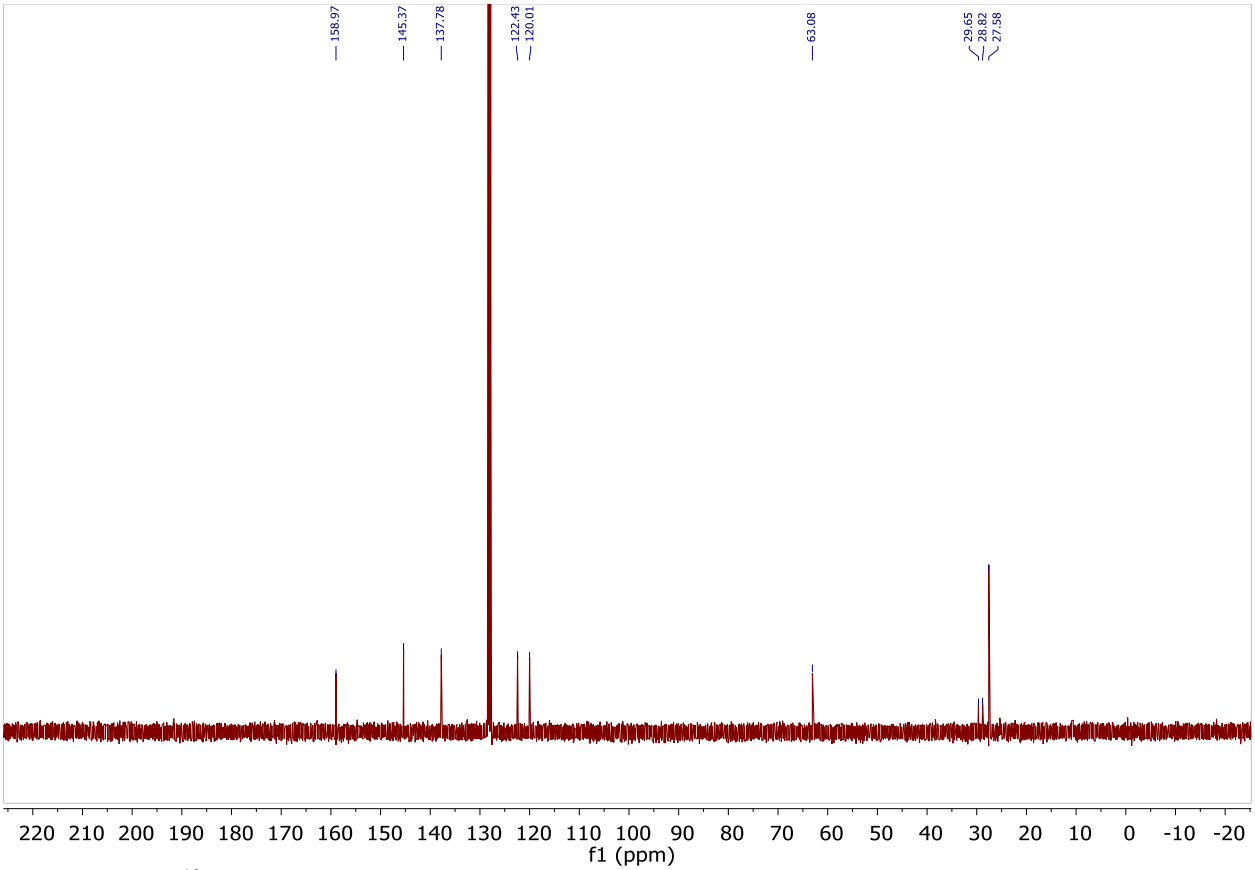

Figure C20. ^{13}C NMR spectrum of (2-pyridinemethanol-Al^{i}Bu$_2$) (**11b**) in C_6D_6.

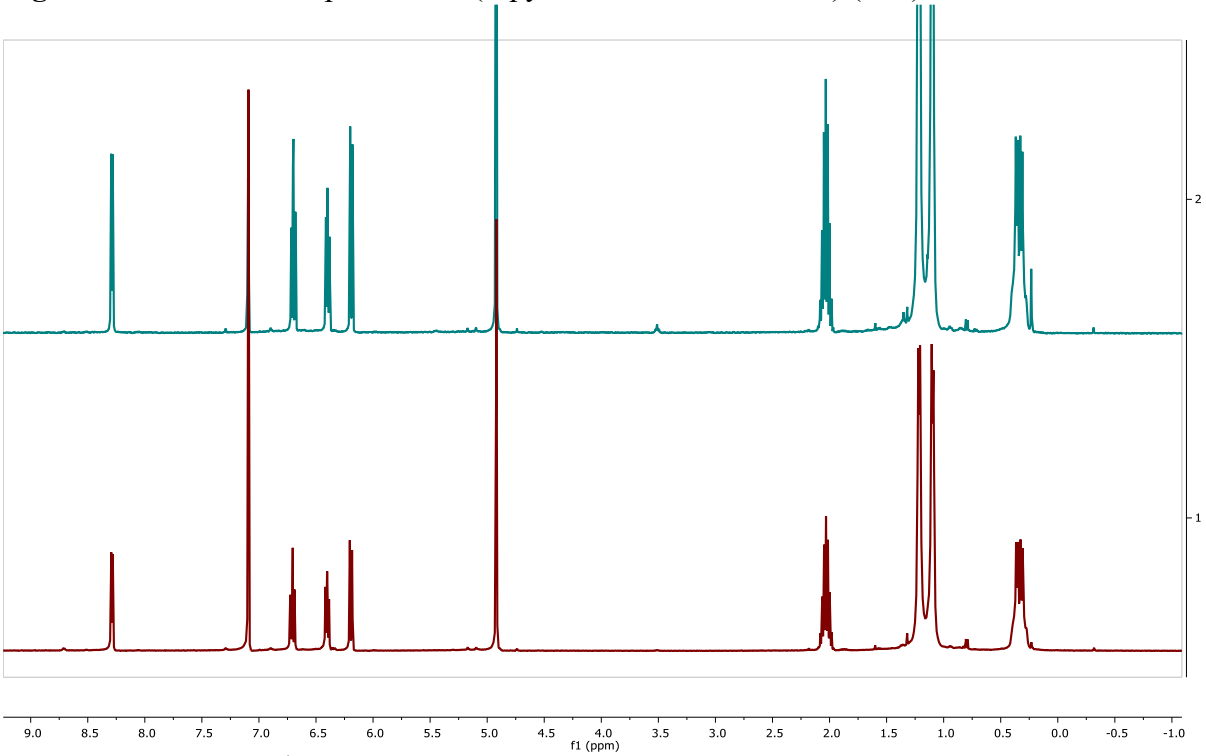

Figure C21. Stacked ^{1}H NMR spectrum of **(11b)** before CO_2 addition (top) and after CO_2 addition (bottom) in C_6D_6. THF impurity located at 3.45 ppm and δ1.57 ppm.

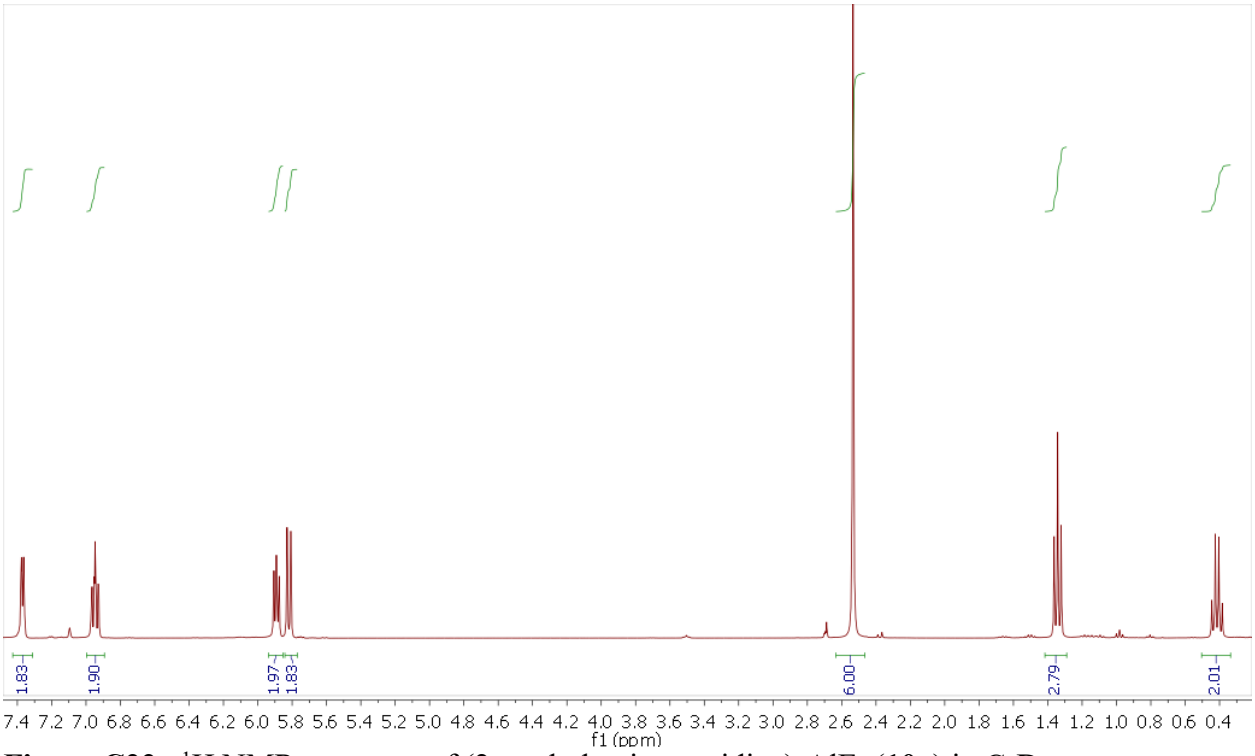

Figure C22. ^{1}H NMR spectrum of (2-methylamino pyridine)$_2$AlEt (**10a**) in C_6D_6.

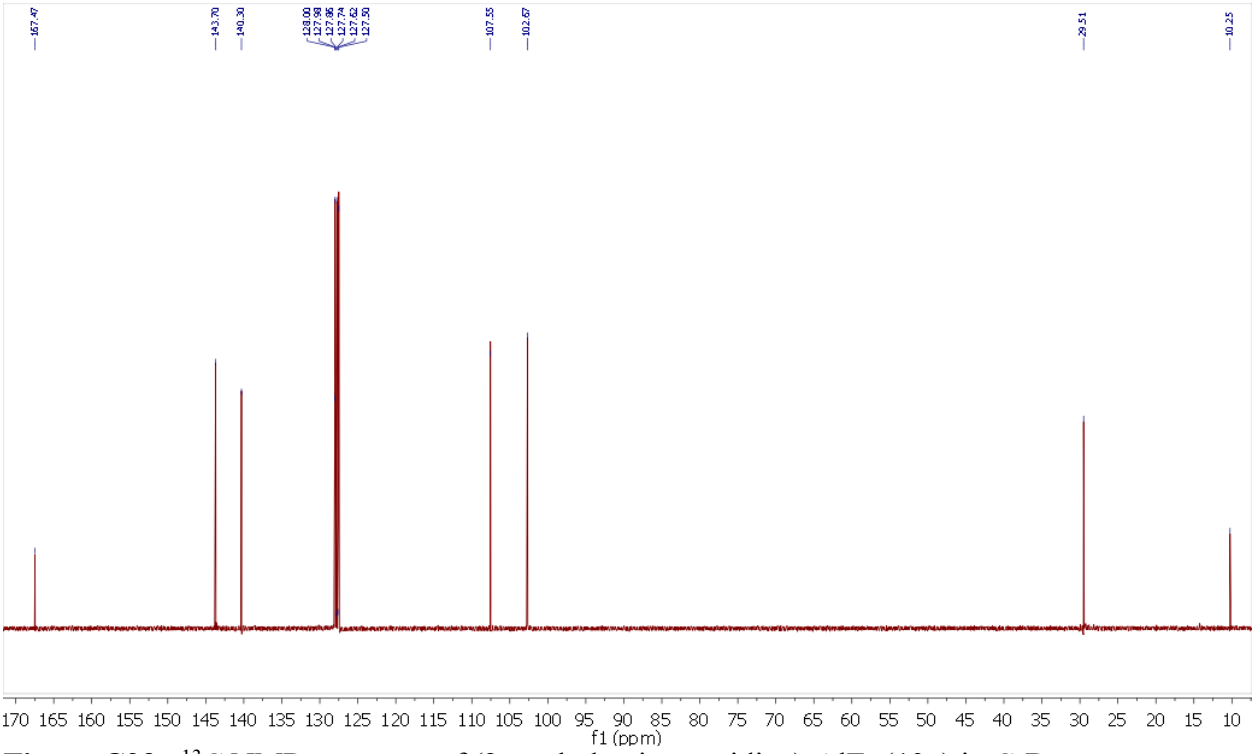

Figure C23. ^{13}C NMR spectrum of (2-methylamino pyridine)$_2$AlEt (**10a**) in C_6D_6.

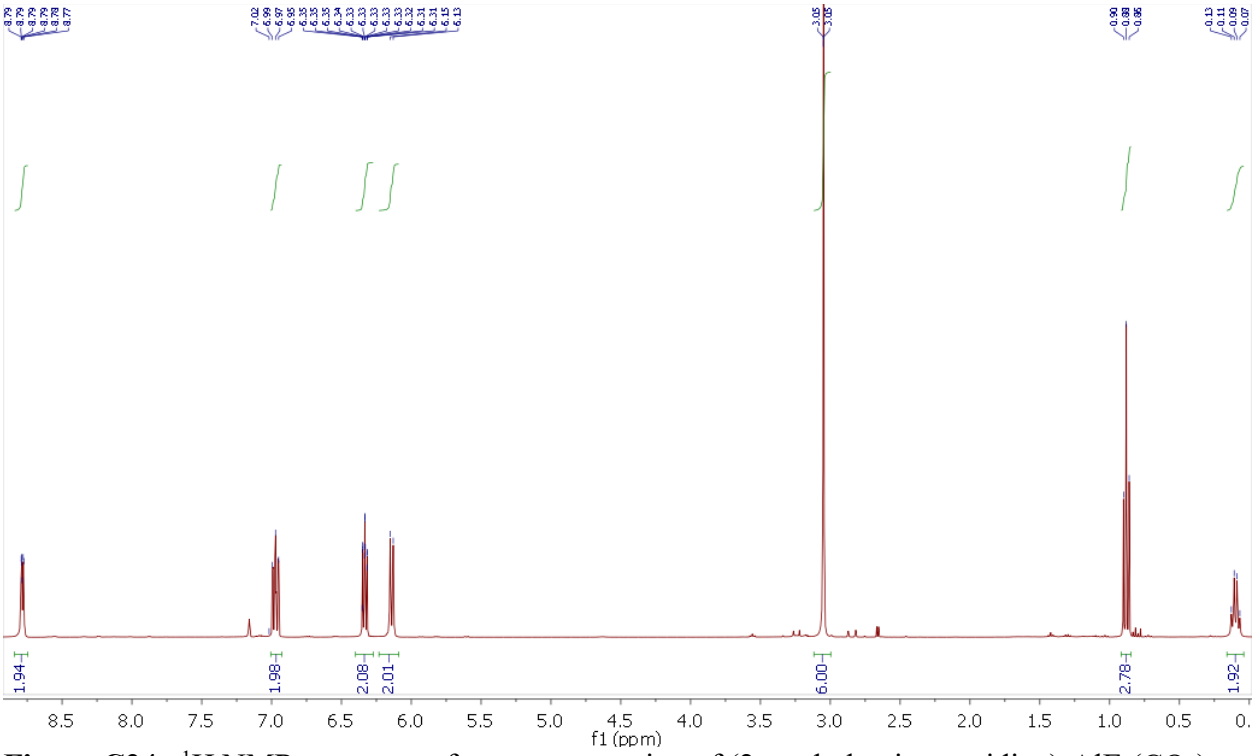

Figure C24. ^{1}H NMR spectrum of *in situ* generation of (2-methylamino pyridine)$_2$AlEt(CO$_2$)$_2$ (**10c**) in C_6D_6.

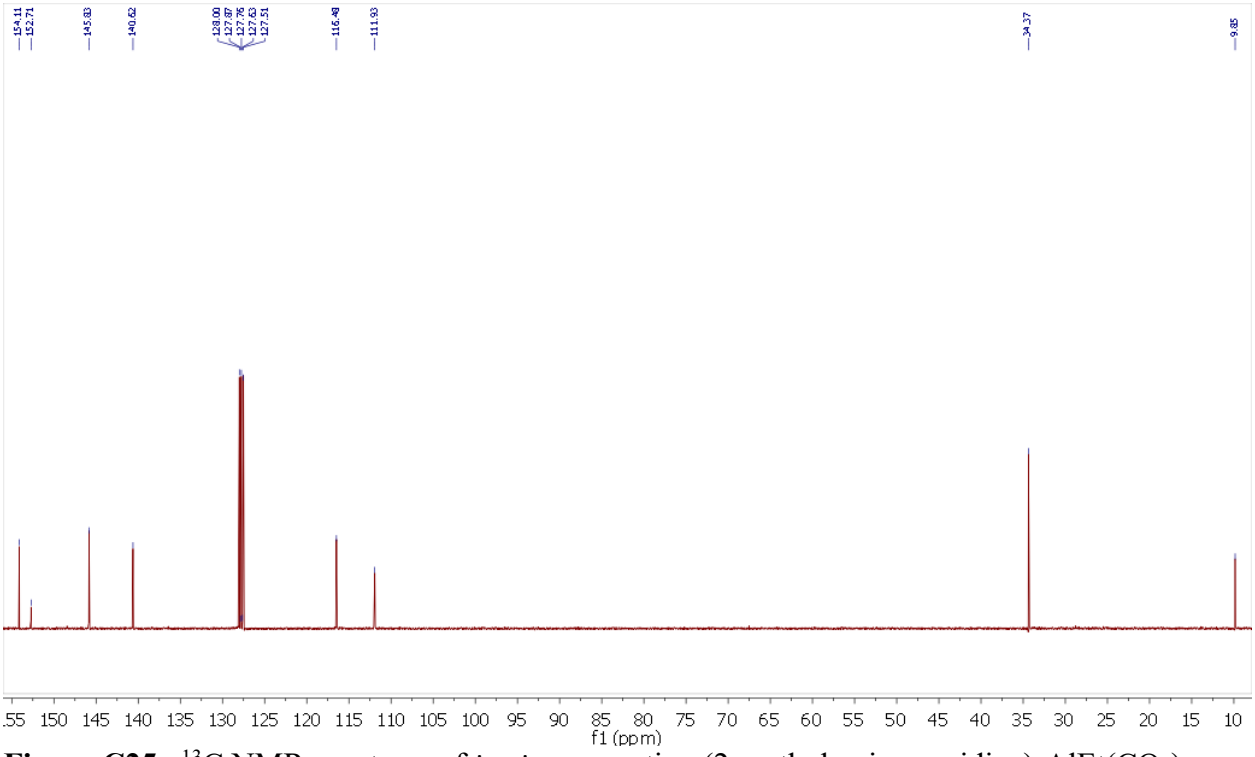

Figure C25. ^{13}C NMR spectrum of *in situ* generation (2-methylamino pyridine)$_2$AlEt(CO$_2$)$_2$ (**10c**) in C_6D_6.

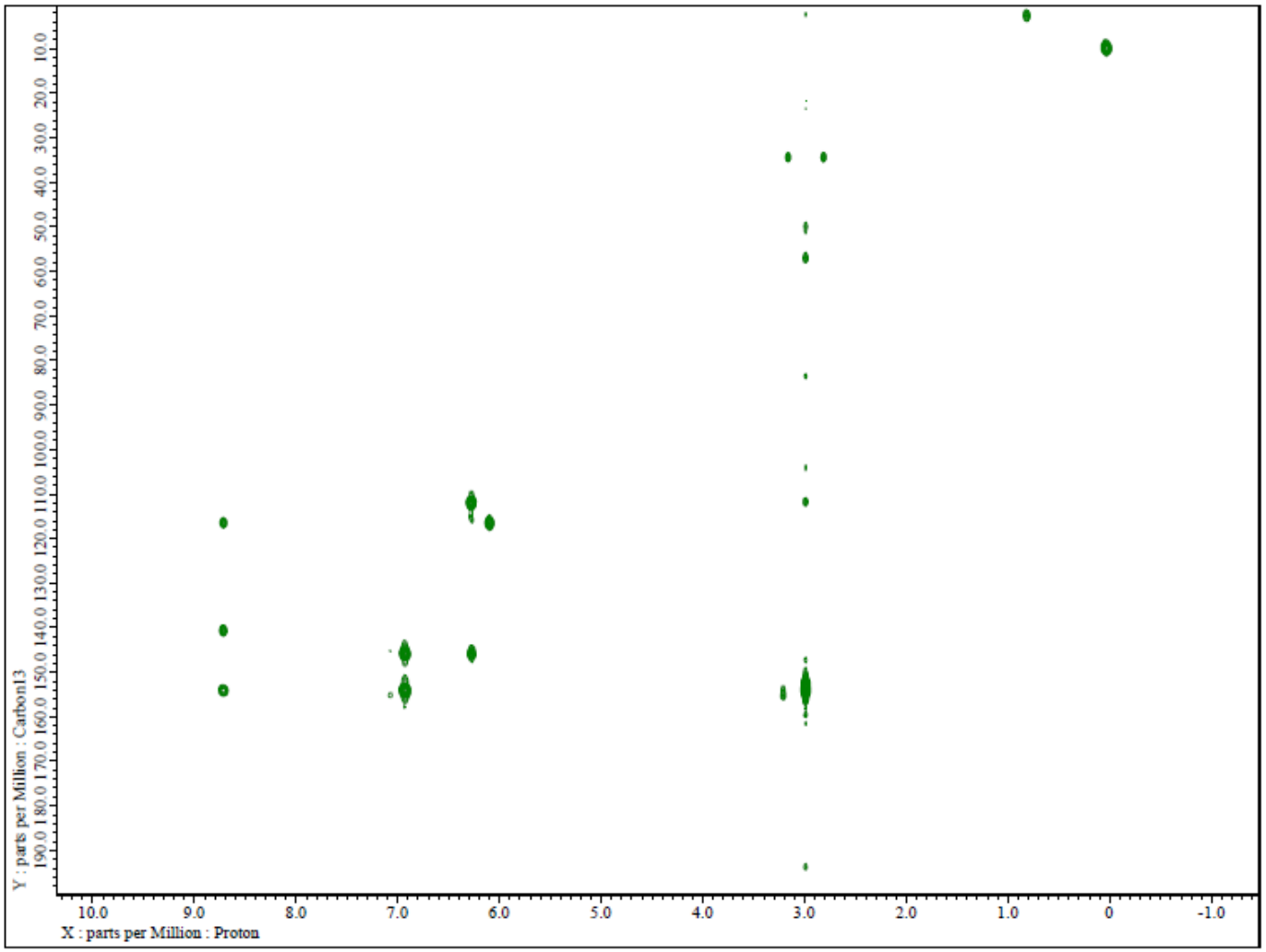

Figure C26. HMBC spectrum of (2-methylamino pyridine)$_2$AlEt(CO$_2$)$_2$ (**10c**) in C_6D_6. *Species generated *in situ*

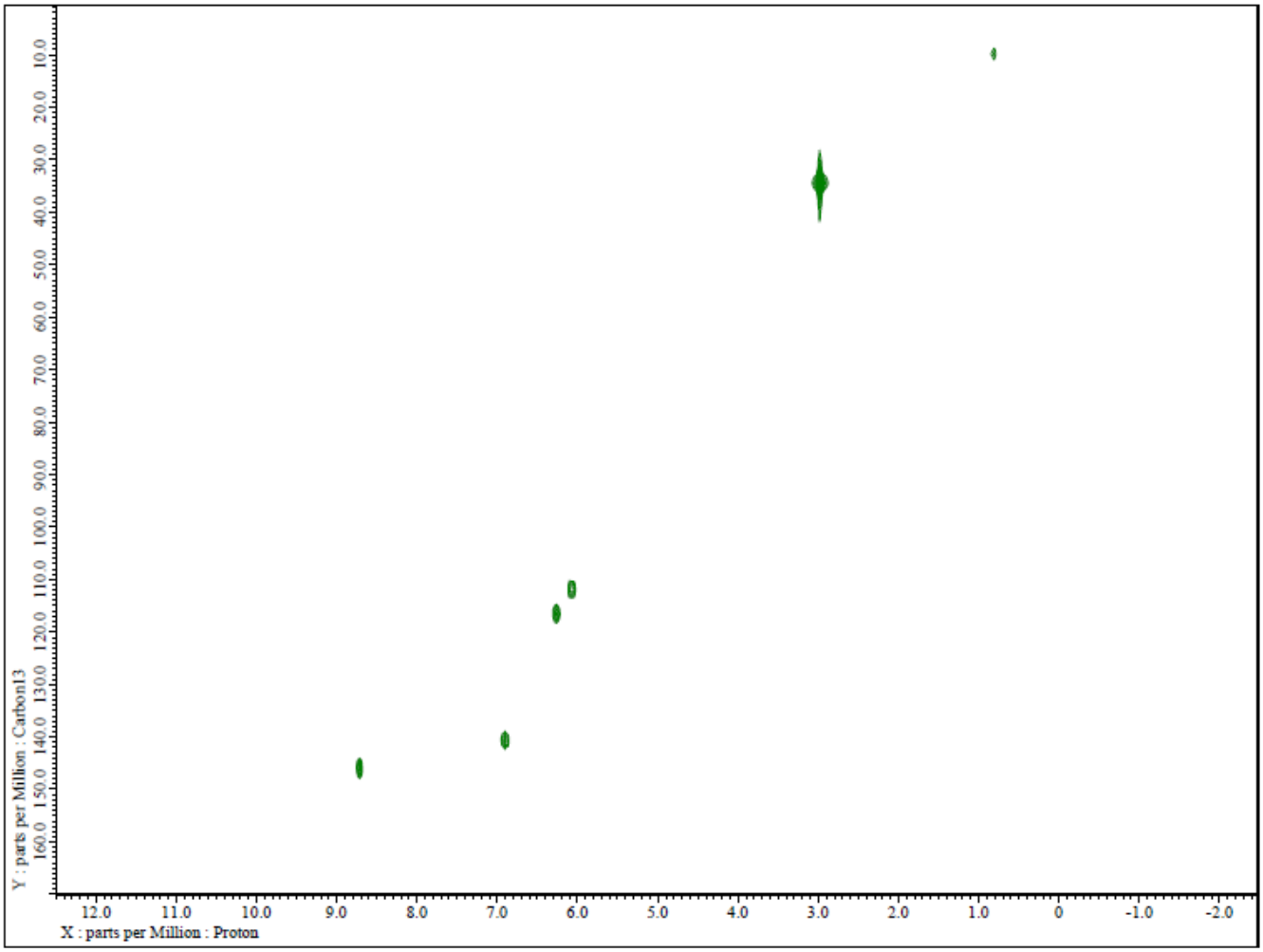

Figure C27. HMQC spectrum of (2-methylamino pyridine)$_2$AlEt(CO$_2$)$_2$ (**10c**) in C_6D_6. *Species generated *in situ*

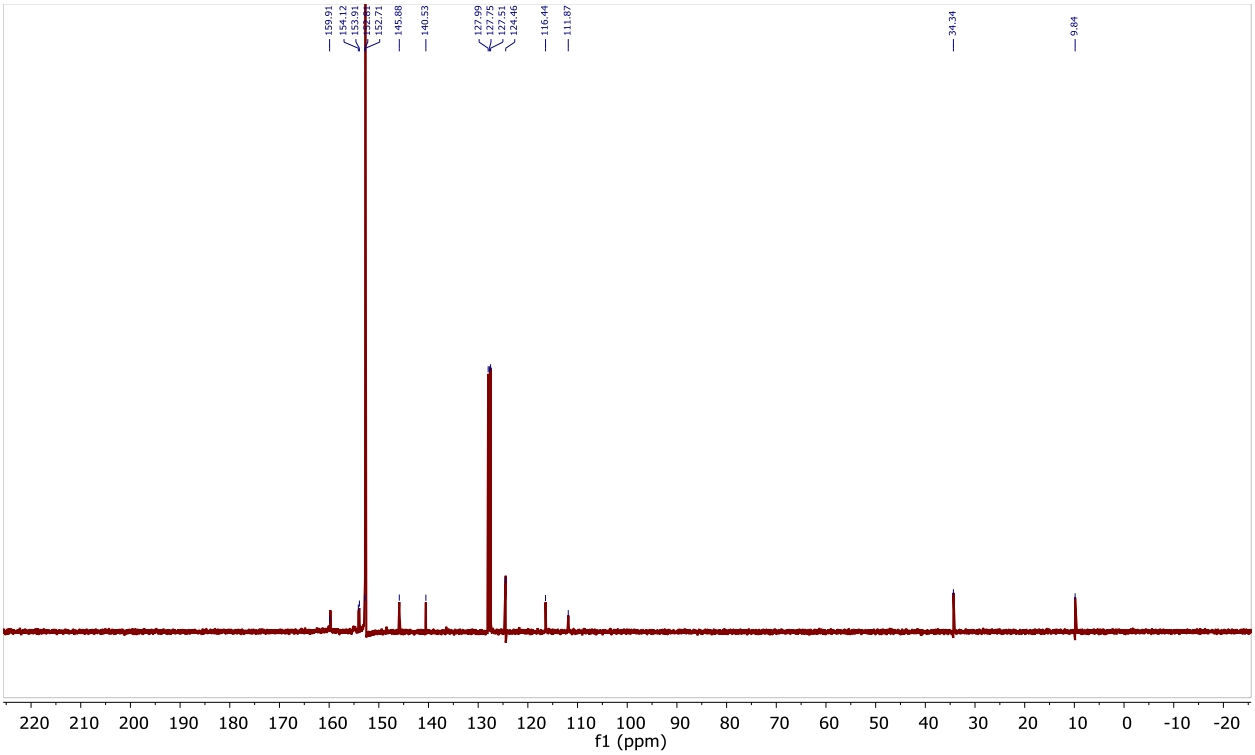

Figure C28. ^{13}C NMR spectrum of (2-methylamino pyridine)$_2$AlEt($^{13}CO_2$)$_2$ (**10c**) in C_6D_6 after 90 minutes.

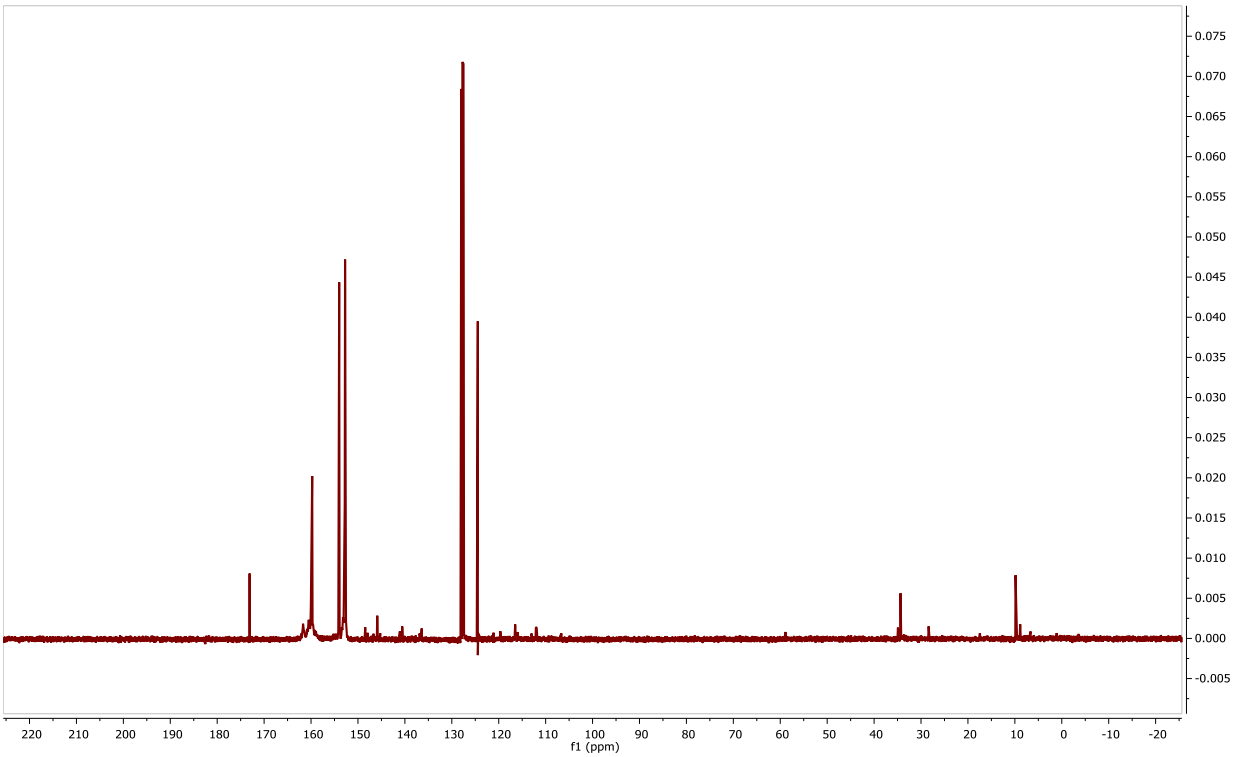

Figure C29. ^{13}C NMR spectrum of (2-methylamino pyridine)$_2$AlEt($^{13}CO_2$)$_2$ (**10c**) in C_6D_6 after 48 hours.

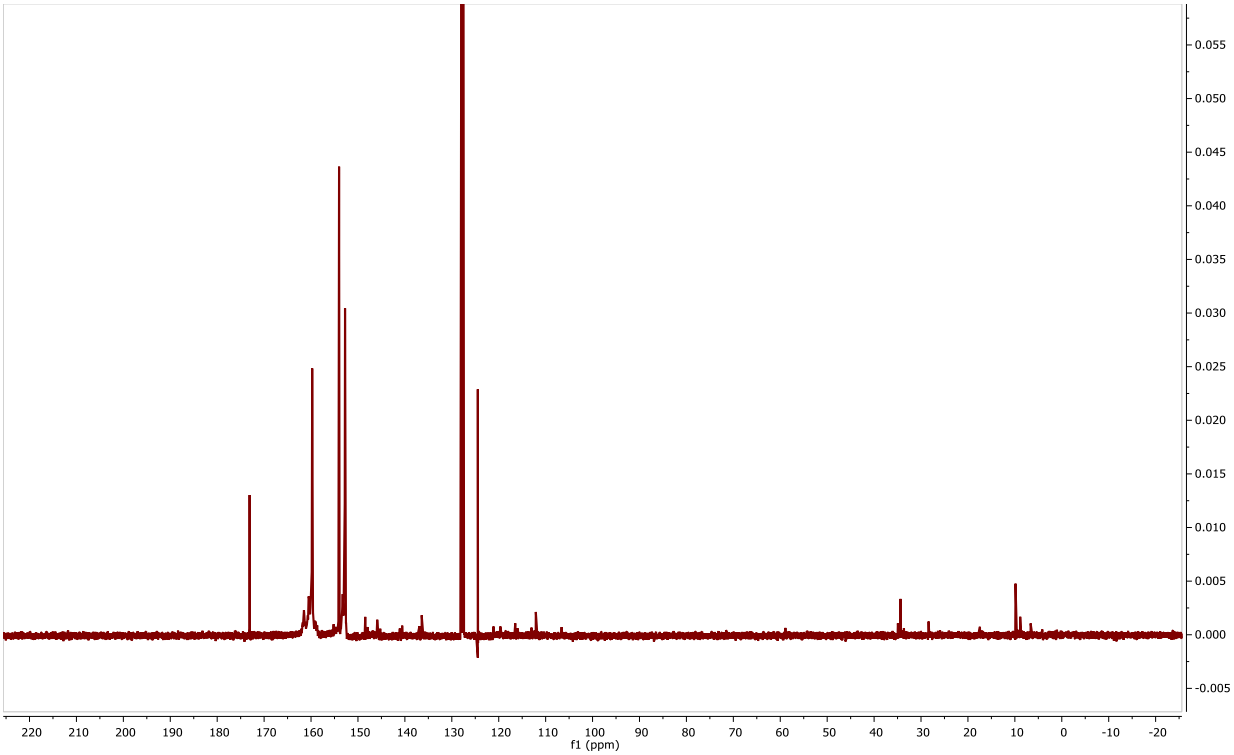

Figure C30. ^{13}C NMR spectrum of (2-methylamino pyridine)$_2$AlEt($^{13}CO_2$)$_2$ (**10c**) in C_6D_6 after 72 hours.

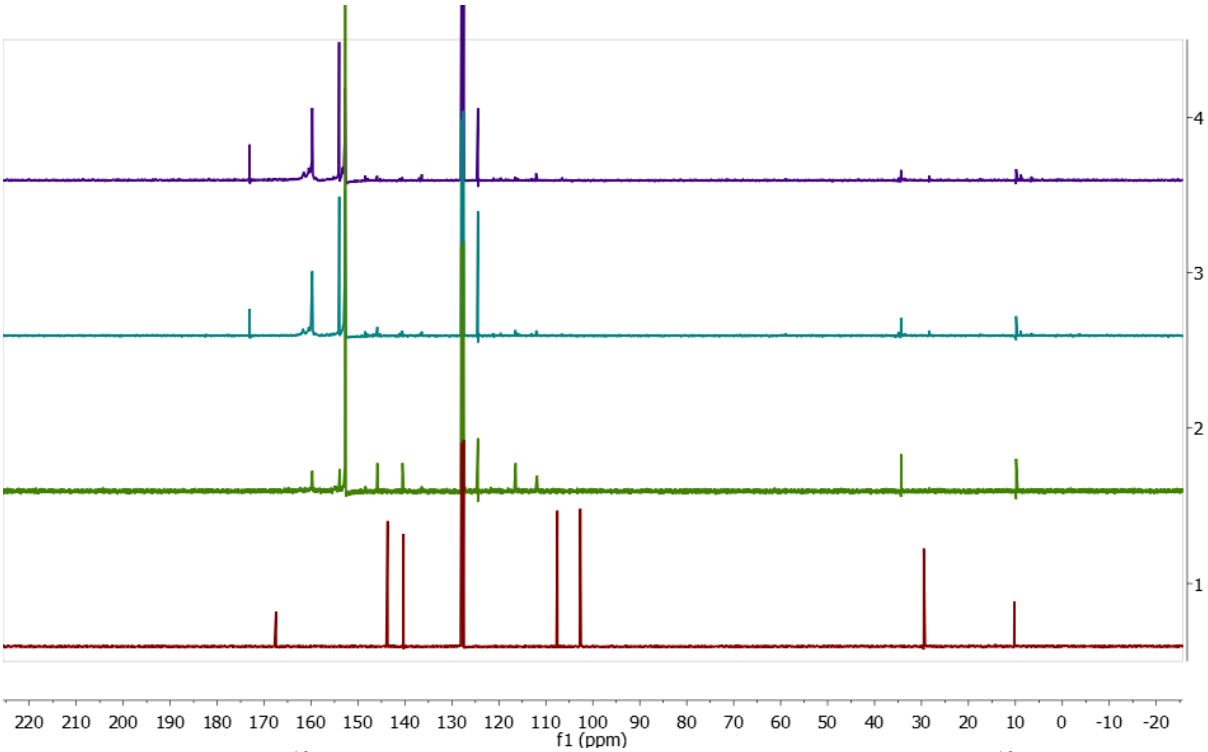

Figure C31. Stacked ^{13}C NMR spectrum of (2-methylamino pyridine)$_2$AlEt($^{13}CO_2$)$_2$ (**10c**) in C_6D_6 after to 72 hours.

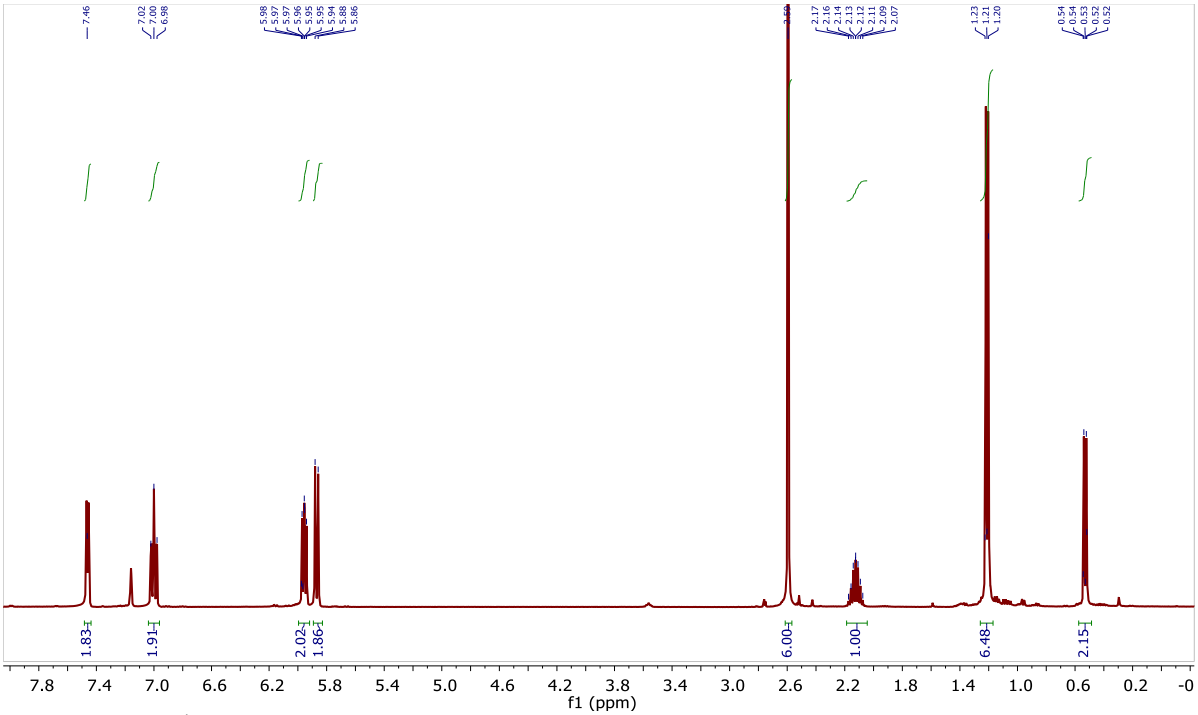

Figure C32. ^{1}H NMR spectrum of (2-methylamino pyridine)$_2$Al^{i}Bu (**10b**) in C_6D_6.

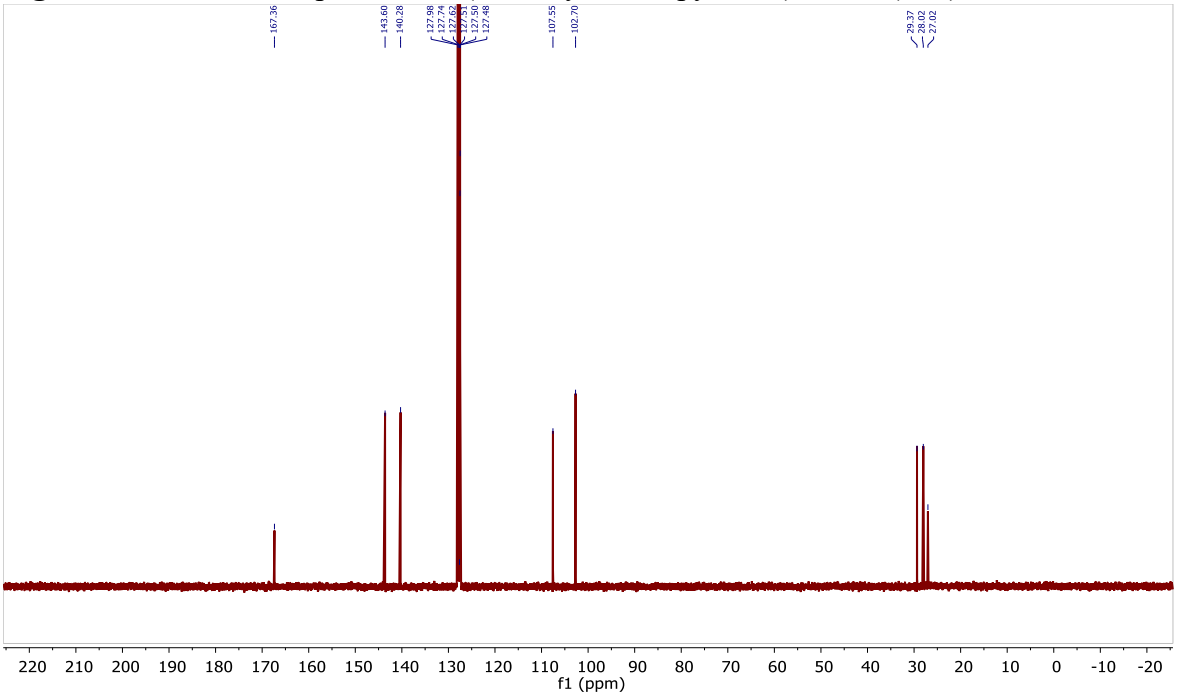

Figure C33. ^{13}C NMR spectrum of (2-methylamino pyridine)$_2$Al^{i}Bu (**10b**) in C_6D_6.

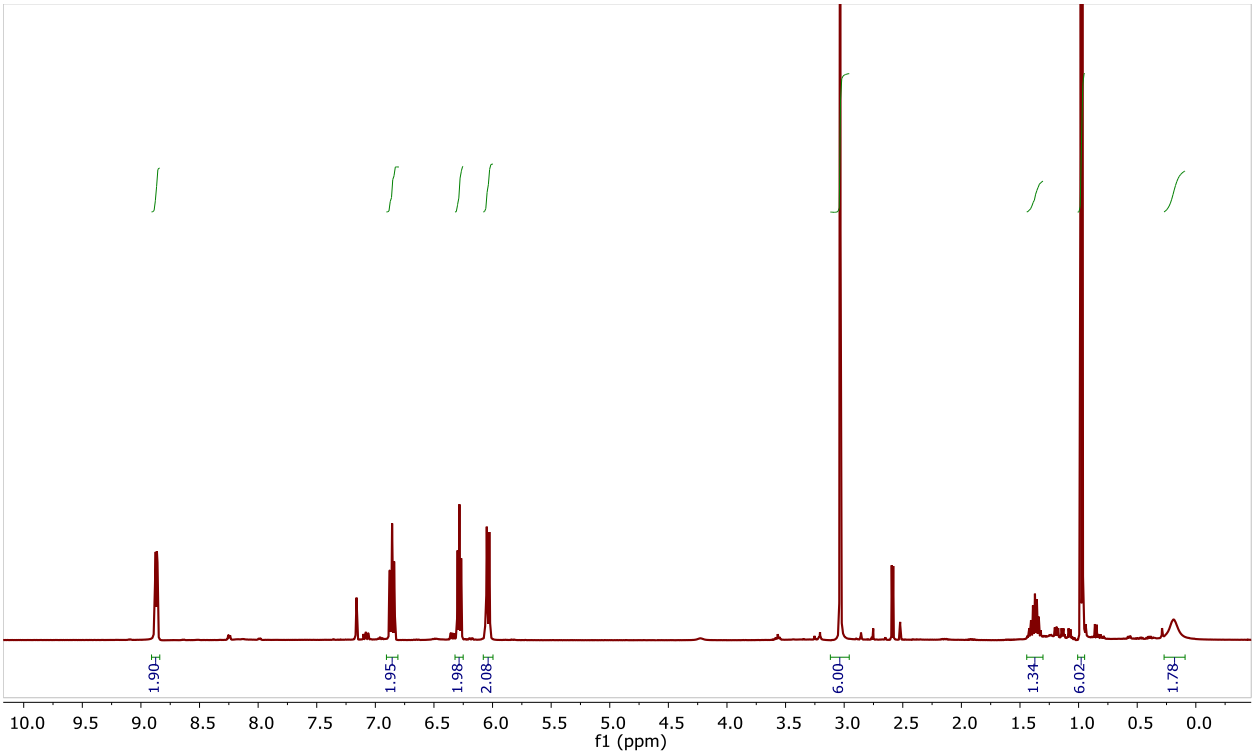

Figure C34. ^{1}H NMR spectrum of (2-methylamino pyridine)$_2$Al^{i}Bu(CO$_2$)$_2$ (**10d**) in C$_6$D$_6$. *Species generated *in situ*

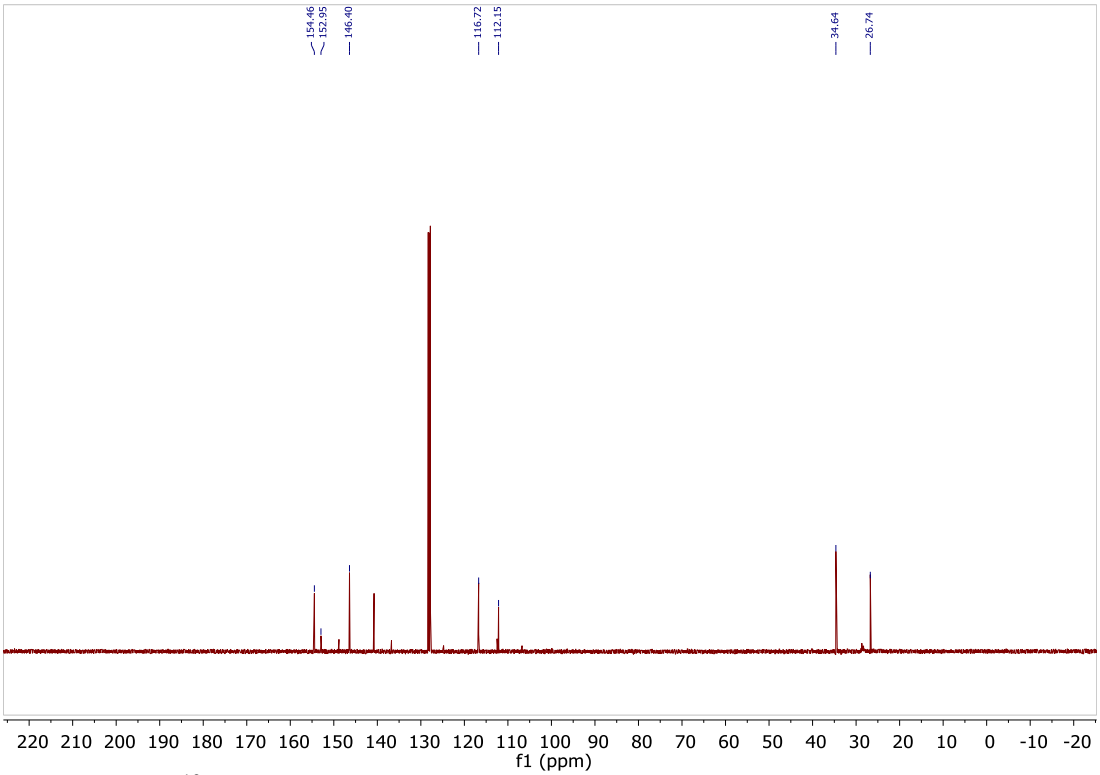

Figure C35. ^{13}C NMR spectrum of (2-methylamino pyridine)$_2$Al^{i}Bu(CO$_2$)$_2$ (**10d**) in C$_6$D$_6$. *Species generated *in situ*. Excess carbon peaks due to hydrolysis of 2-methylamino pyridine.

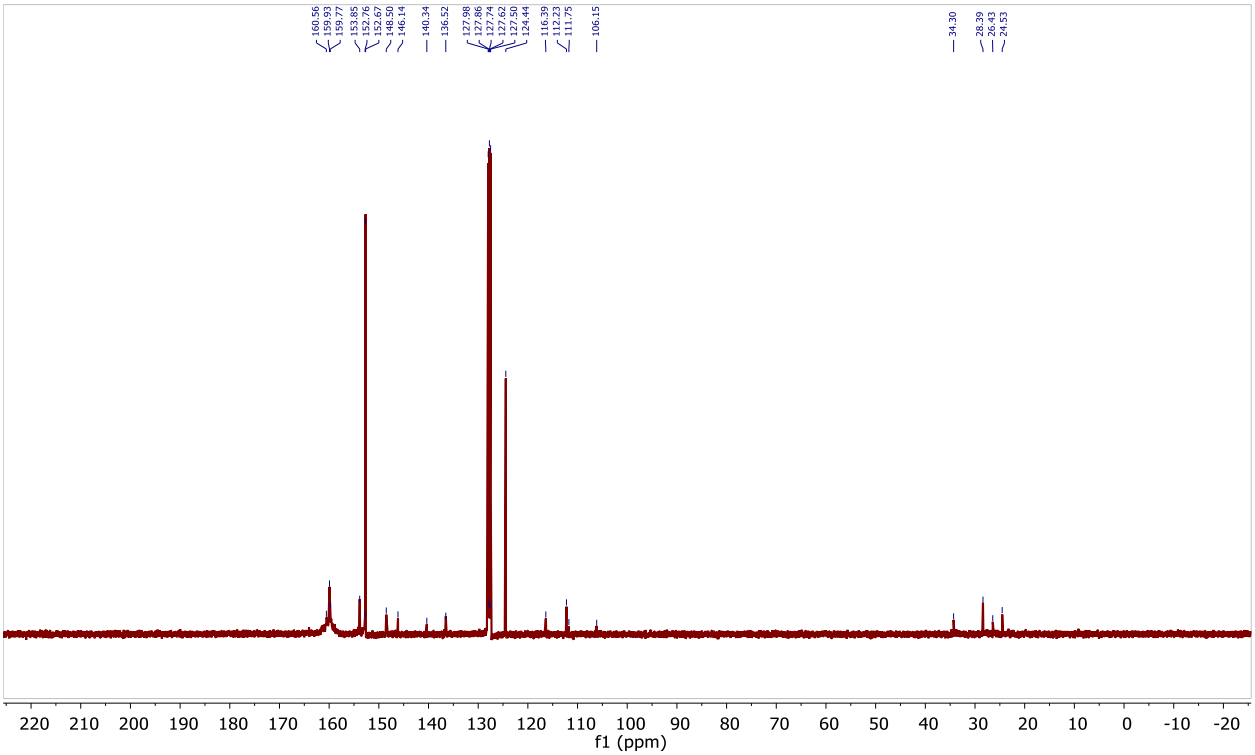

Figure C36. ^{13}C NMR spectrum of (2-methylamino pyridine)$_2$Al^{i}Bu($^{13}CO_2$)$_2$ (**10d**) in C_6D_6. *Species generated *in situ*

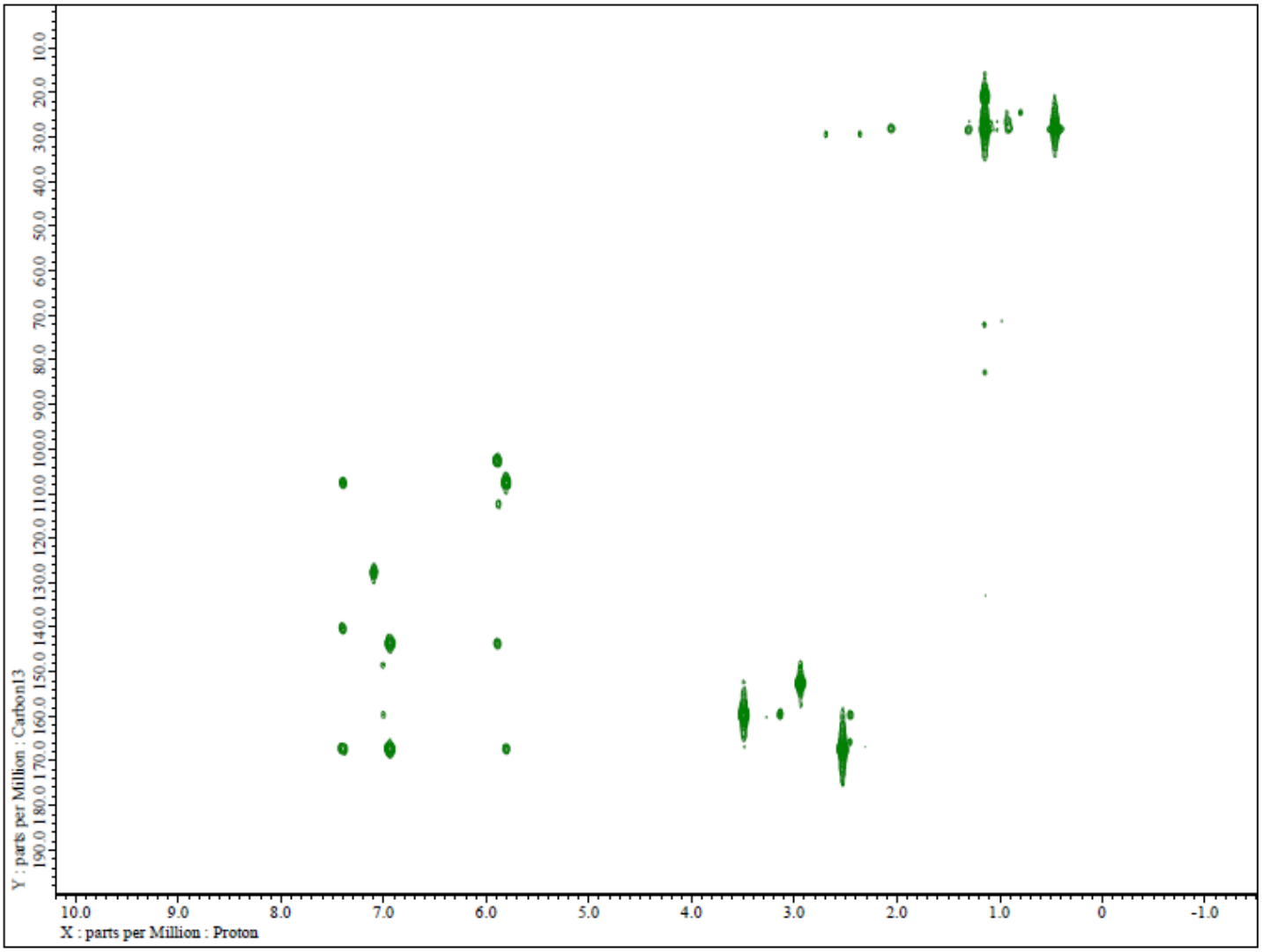

Figure C37. HMBC spectrum of (2-methylamino pyridine)$_2$Al^{t}Bu(CO$_2$)$_2$ (**10d**) in C_6D_6.*Species generated *in situ*

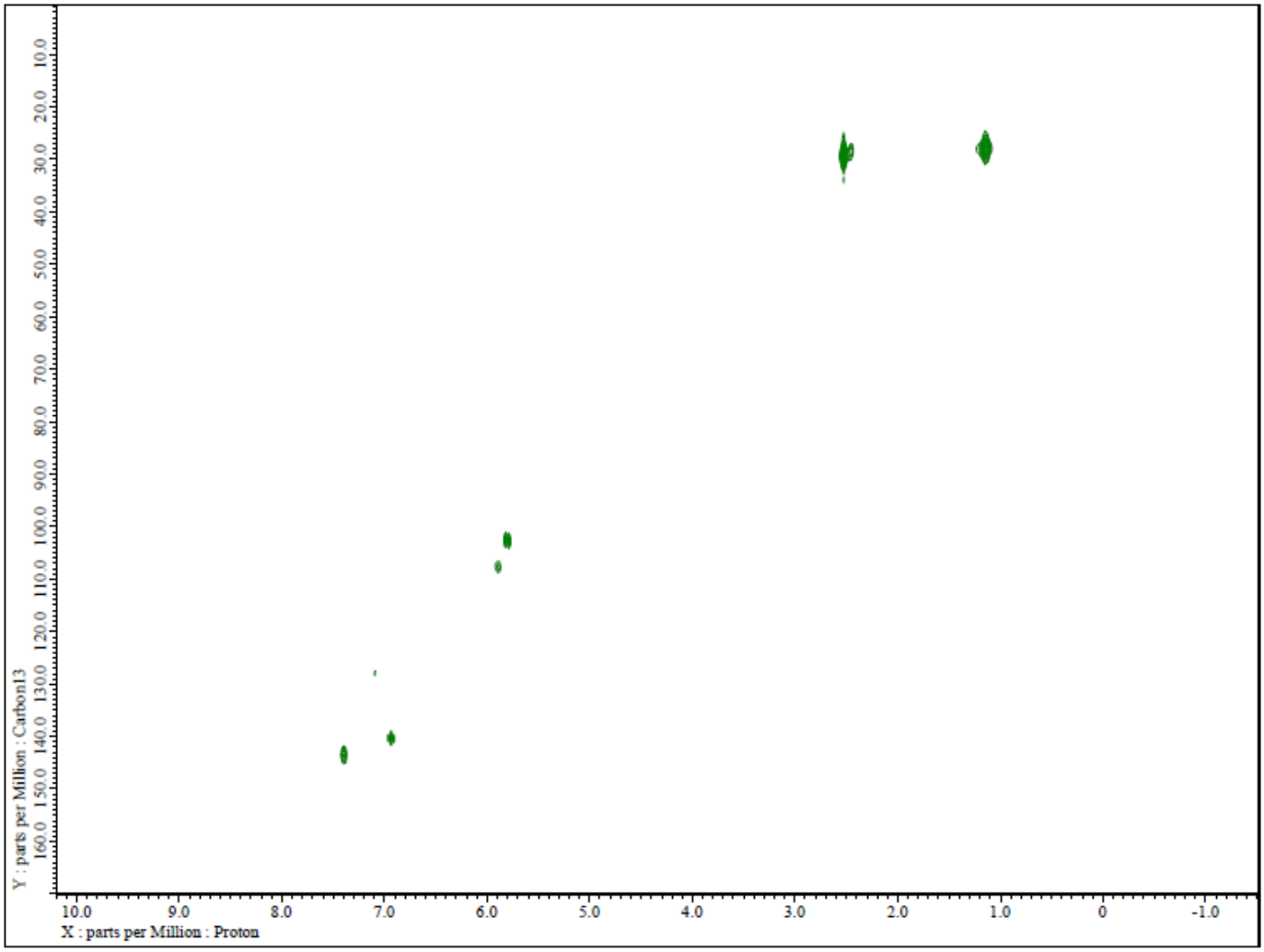

Figure C38. HMQC spectrum of (2-methylamino pyridine)$_2$Al^{i}Bu(CO$_2$)$_2$ (**10d**) in C_6D_6.*Species generated *in situ*

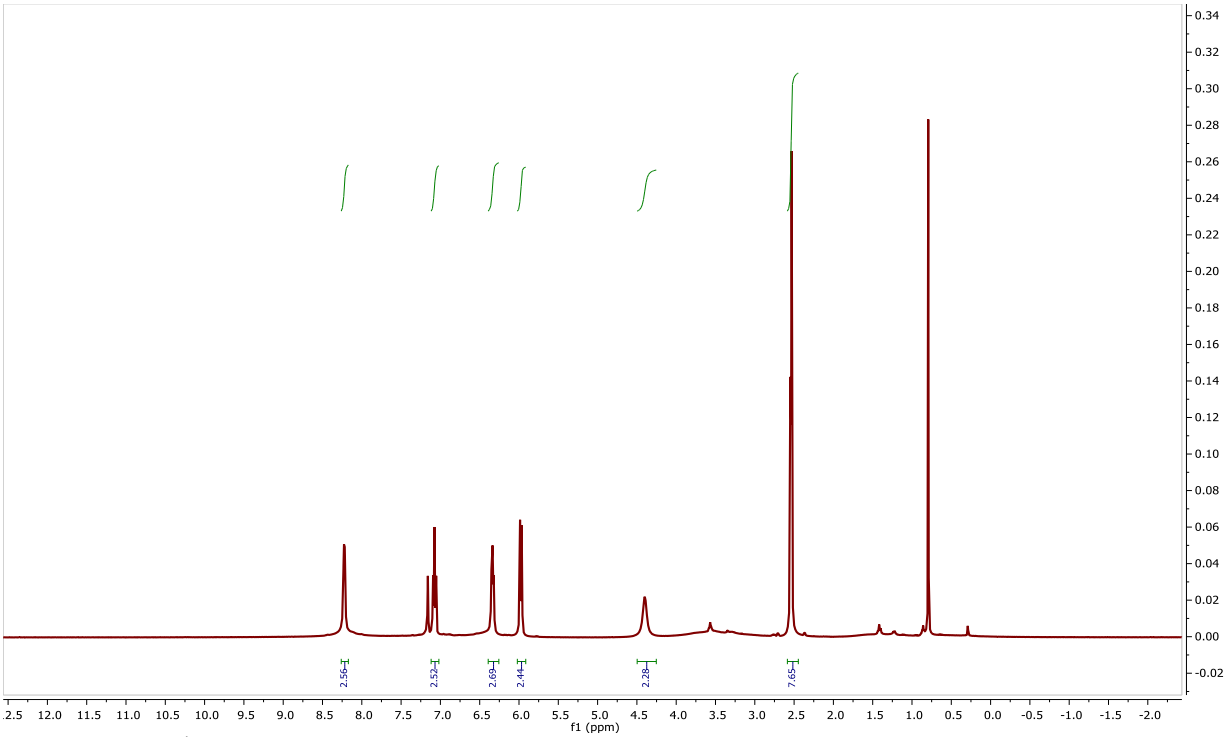

Figure C39. ^{1}H NMR spectrum of (2-methylamino pyridine)$_2$AlEt(CO$_2$)$_2$ (**10c**) after addition of 5µL of H_2O in C_6D_6.

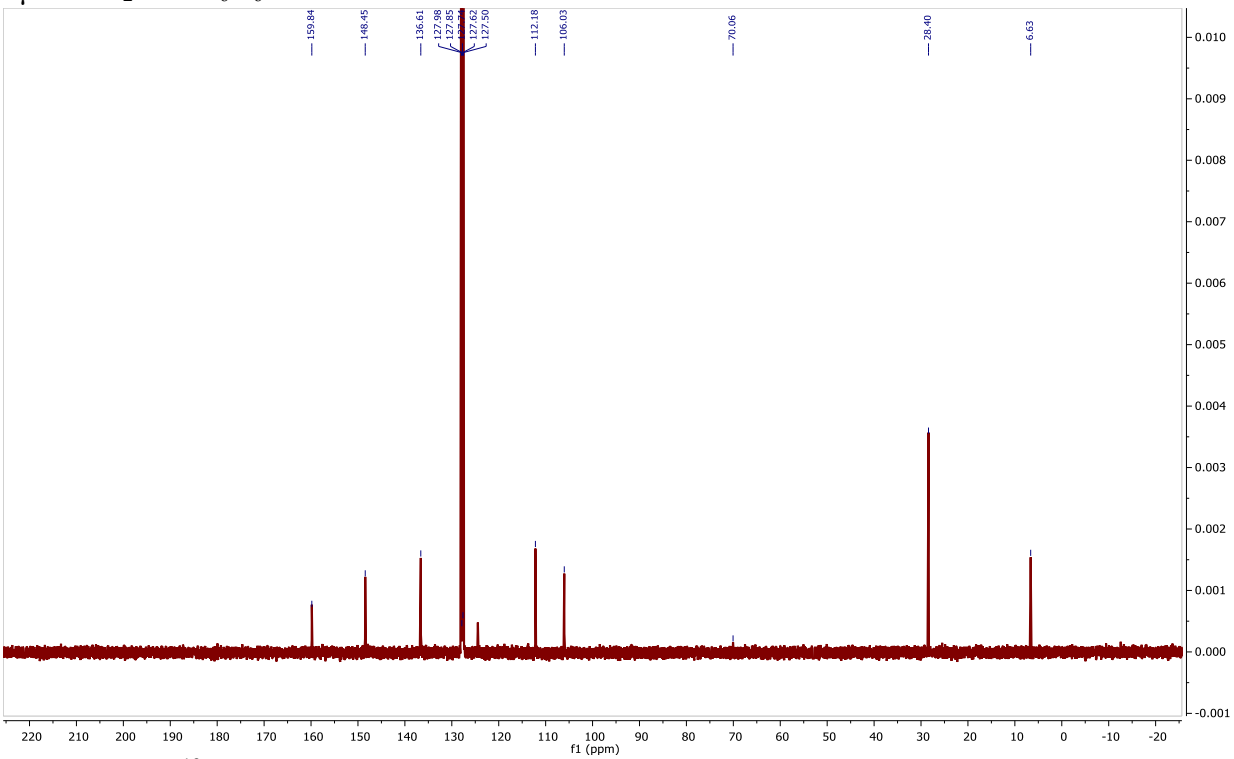

Figure C40. ^{13}C NMR spectrum of (2-methylamino pyridine)$_2$AlEt(CO$_2$)$_2$ (**10c**) after addition of 5µL of H_2O in C_6D_6.

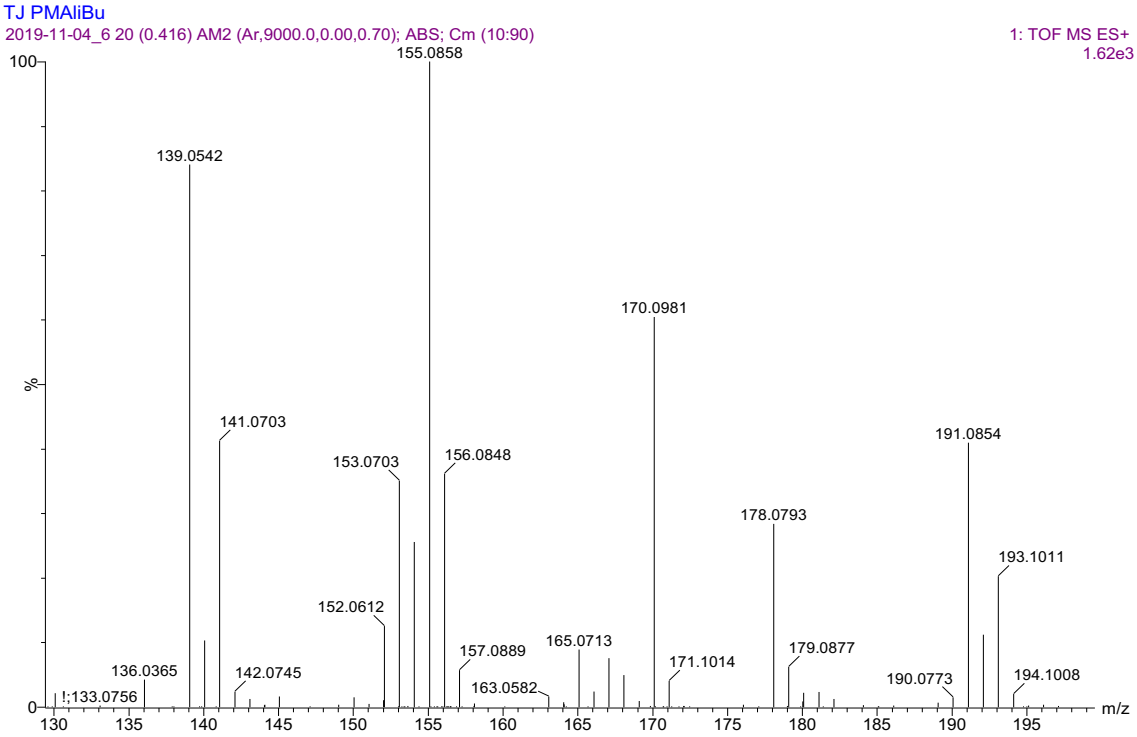

Figure C41. HRMS spectrum of **9b.**

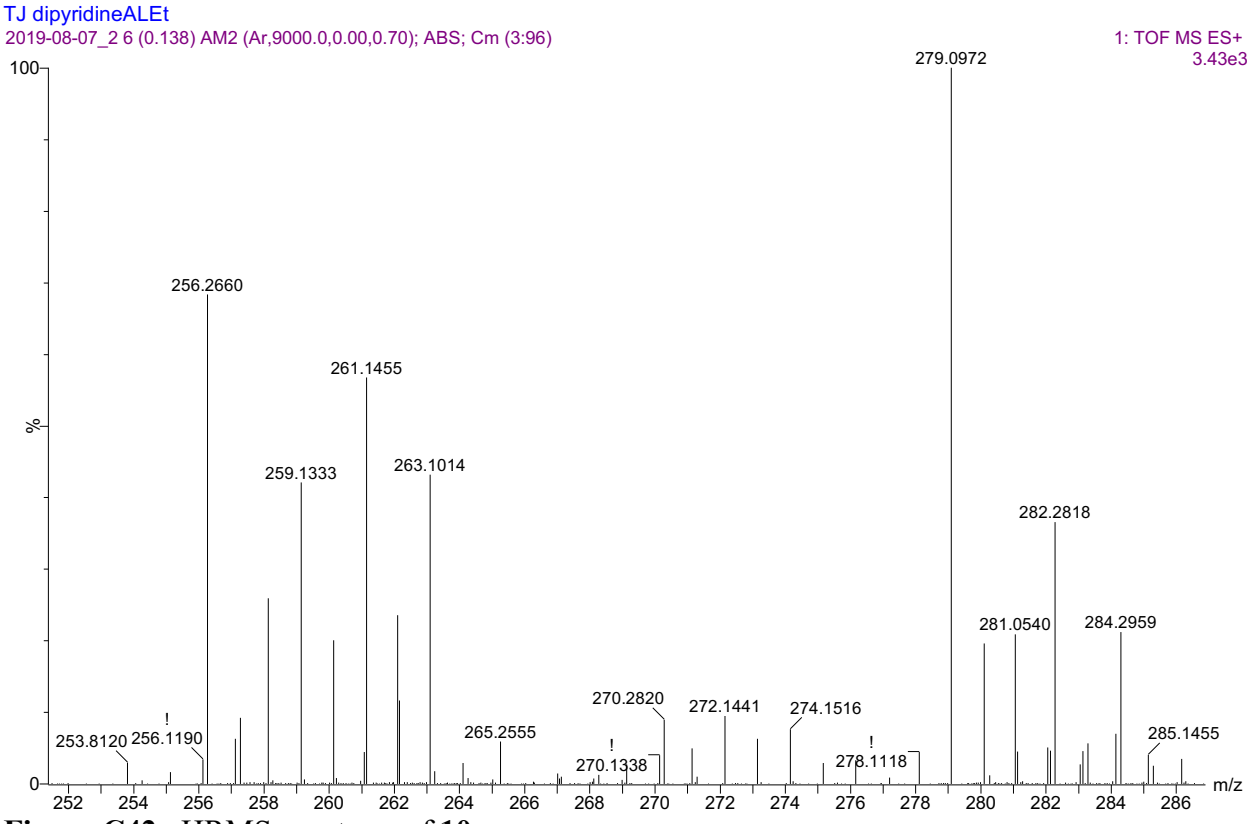

Figure C42. HRMS spectrum of **10a**.

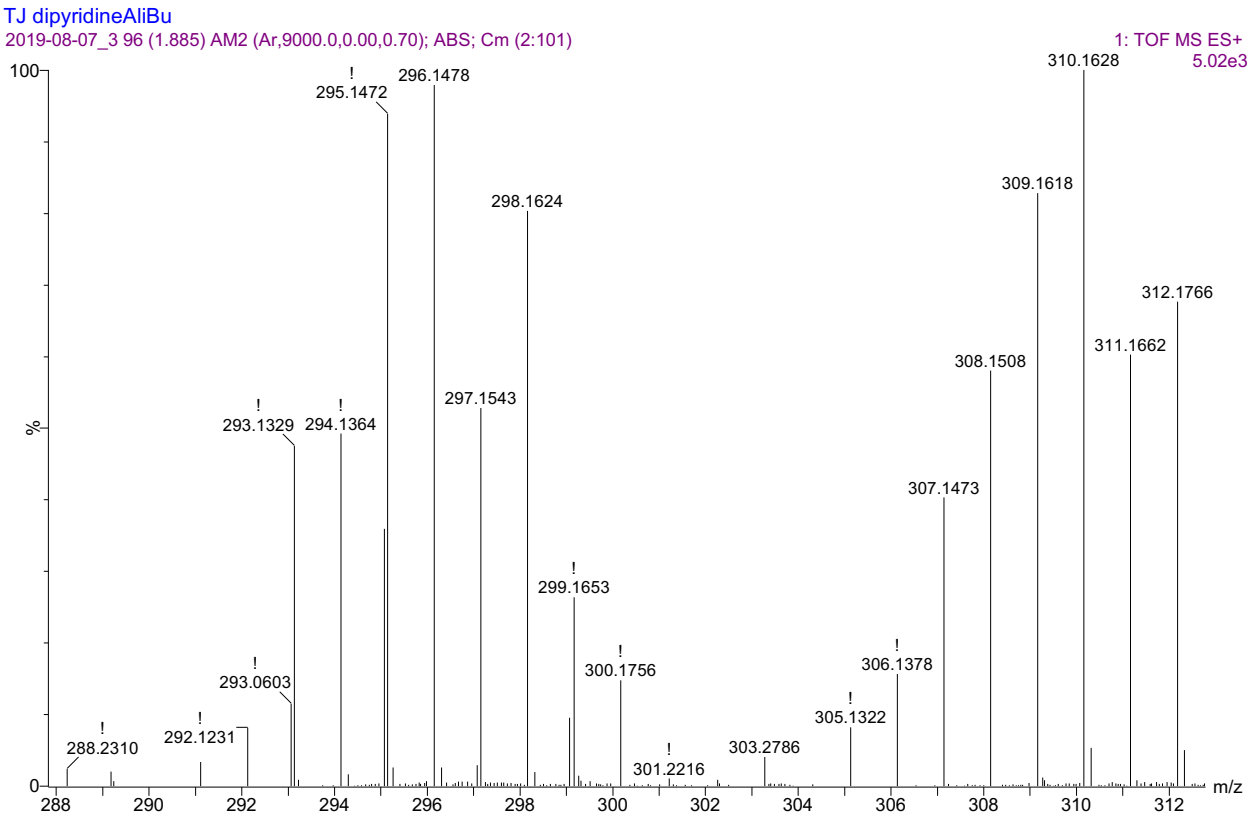

Figure C43. HRMS spectrum of **10b**.

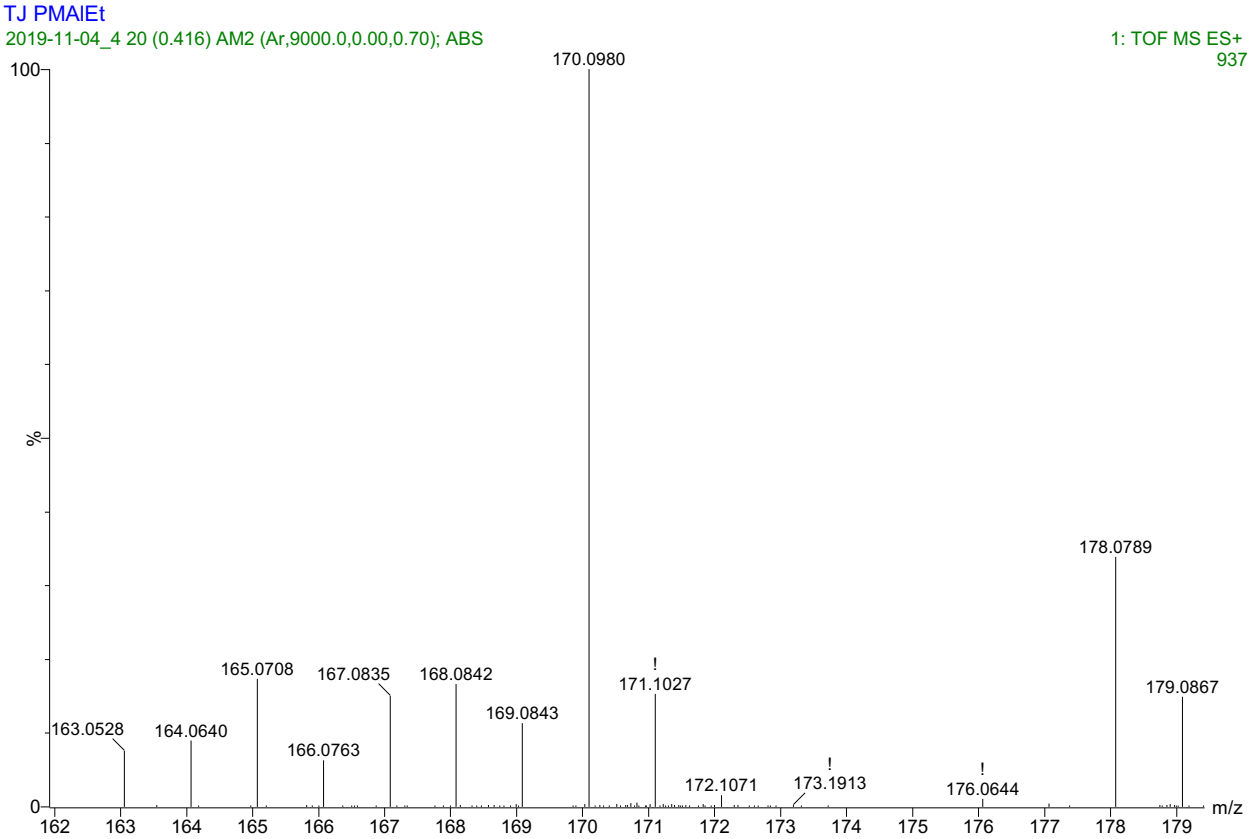

Figure C44. HRMS spectrum of **11a**.